

SELECTIVE LASER MELTING OF NICKEL
SUPERALLOYS FOR HIGH TEMPERATURE
APPLICATIONS

By

LUKE NELSON CARTER

A thesis submitted to the
University of Birmingham
for the degree of
DOCTOR OF PHILOSOPHY

School of Metallurgy and Materials
College of Engineering and Physical Sciences
University of Birmingham
May 2013

UNIVERSITY OF
BIRMINGHAM

University of Birmingham Research Archive

e-theses repository

This unpublished thesis/dissertation is copyright of the author and/or third parties. The intellectual property rights of the author or third parties in respect of this work are as defined by The Copyright Designs and Patents Act 1988 or as modified by any successor legislation.

Any use made of information contained in this thesis/dissertation must be in accordance with that legislation and must be properly acknowledged. Further distribution or reproduction in any format is prohibited without the permission of the copyright holder.

ABSTRACT

Selective Laser Melting (SLM) is of growing interest within the aerospace industry due to its ability to produce complex netshape components directly from CAD file allowing for increased design freedom without the constraints of traditional methods. There is currently a lack of knowledge regarding the influence of process variables on the integrity and properties of the as-fabricated material. The research presented investigates the SLM-fabrication of three nickel superalloys: Primarily CM247LC with CMSX486 and IN625 as secondary alloys.

CM247LC is Ni-base superalloy hardenable by the precipitation of the coherent γ' phase. It presents a particular challenge due to weld-crack susceptibility. This research aims to establish a processing route for CM247LC components via SLM: Parametric studies are presented to quantitatively assess the cracking behaviour based on microstructural observations and characterise the cracks by suggesting mechanisms for their formation. Hot Isostatic Pressing (HIPping) has been investigated as a retro-fix solution to cracking and further heat treatments have been implemented to refine the γ' structure for the best possible creep resistance; the γ' evolution through the manufacturing stages (SLM & Heat Treatment) has been examined.

Electron BackScatter Diffraction (EBSD), MicroCT Tomography and microscopy have been used to characterise the influence of the laser scan strategy on the SLM fabricated microstructure.

Research was extended to two additional alloys: CMSX486 and IN625. A statistical design of experiments methodology was used to rapidly establish process parameters for these two alloys.

Mechanical testing (creep/tensile) was performed for comparison against traditionally cast material. The poor creep performance of the SLM processed CM247LC and CMSX486 raise significant concerns regarding the future successful use of SLM in its current form as a viable manufacturing route. In contrast, IN625 performed well under room and elevated temperature tensile testing and highlight that appropriate alloy selection (or specific alloy development) is needed for future research in this area.

In conclusion a processing route capable of yielding fully dense material with a satisfactory γ' structure is presented; however, it involves significant post-fabrication processing and the resulting poor creep properties detract from the attractiveness of SLM as a viable manufacturing method. Further research is suggested, specifically into modelling and thermal measurement of SLM.

ACKNOWLEDGEMENTS

I am grateful to the Engineering & Physical Sciences Research Council (EPSRC) for my PhD scholarship and the financial support provided by our industrial collaborators Meggitt Sensing Systems and Microturbo (Safran Group) without whom this research could not have been carried out.

Acknowledgements for specific contributions go to: Dr. Noriko Read and Prof. Mike Loretto for their knowledge and expertise in TEM sample preparation and imaging using TEM; Frank Biddlestone for his expertise in DSC; Ian Brough for his knowledge and expertise performing EBSD; Prof. Martin Strangwood and David Routledge for their assistance and expertise in the generation of Thermo-Calc phase-diagram models; Wei Wang for the production of the simple scan strategy sample.

I would also like to thank the following individuals: Prof. Xinhua Wu for giving me this opportunity and for her support as my supervisor through the first 15 months of my PhD; Dr. Moataz Attallah for agreeing to be my supervisor upon Prof. Wu's departure and for the scientific direction, input and encouragement he has provided in that role; Prof. Mike Loretto for his time, knowledge and expertise when needed and his tireless effort to improve my use of the English language; Dr. Nick Adkins for his pragmatic approach and willingness for technical discussion; Dr. Noriko Read for her daily hard work and support and all other academic staff & colleagues who were willing to give their time when necessary.

I would also like to express my gratitude to all the technical staff for their time and expertise in assisting me in my practical work; particularly John Shurvinton and Mike Glynn for the technical support they have provided in the Netshape Building.

Finally, I would like to express my deep thanks for the support of my friends and family who have always shown me patience and kindness as well as encouraging and inspiring me in everything I do.

TABLE OF CONTENTS

CHAPTER 1: INTRODUCTION - AIMS, OBJECTIVES & SCOPE	1
1.1. A Brief Background on High-Temperature Materials	1
1.2. Additive Layer Manufacturing (ALM) as a Netshaping Technique	6
1.3. Research Aims & Objectives	7
1.4. References	9
CHAPTER 2: LITERATURE REVIEW	10
2.1. Categories of Superalloys	10
2.2. γ/γ' Structure	11
i. Atomic Structure	12
ii. Precipitate Morphology	13
iii. Strengthening Mechanism of the γ' Phase	17
iv. Heat Treatment Principles	22
2.3. The Role of Carbides	27
2.4. Roles of the Specific Elements within a Nickel Superalloy	31
i. The Role of Cobalt (Co)	32
ii. The Roles of Chromium (Cr), Molybdenum (Mo), Titanium (Ti) and Aluminium (Al) in Corrosion Resistance	37
iii. The Role of Tantalum (Ta)	39
iv. The Role of Tungsten (W)	41
v. The Role of Hafnium (Hf)	42
2.5. Detrimental Elements & Phases	45
2.6. Specific Metallurgy and Properties of CM247LC	46
2.7. Specific Metallurgy and Properties of CMSX486	52
2.8. Specific Metallurgy and Properties of IN625	55
2.9. DSC of Nickel Superalloys	57
2.10. Brief Overview of ALM Techniques	58
2.11. Early Attempts to Characterise the SLM Process	60
2.12. Microstructure within SLM Fabricated Nickel Superalloys	62
2.13. Residual Stress within SLM Fabricated Materials	66
2.14. The Welding of Nickel Superalloys: Cracking Mechanisms and Process Mapping	67
i. Solidification Cracking (Hot Tearing)	69
ii. Liquation Cracking	70
iii. Ductility-Dip Cracking (DDC)	73

iv.	Strain-Age Cracking (SAC) or Post Weld Heat Treatment (PWHT) Cracking	75
2.15.	Concluding Remarks	76
2.16.	References	79
CHAPTER 3: EXPERIMENTAL METHODS		86
3.1.	Materials	86
3.2.	Measurement of Powder Particle Size Distribution	87
3.3.	Chemical Composition Analysis	87
3.4.	Selective Laser Melting	88
3.5.	Hot Isostatic Pressing (HIPping)	94
3.6.	Heat Treatment	95
3.7.	Metallurgical Sample Preparation	98
3.8.	Optical Microscopy	100
3.9.	Scanning Electron Microscopy (SEM)	100
i.	Powder Characterisation	101
ii.	SLM Process Optimisation: CM247LC	102
iii.	SLM Process Optimisation: CMSX486	102
iv.	γ' Development Through the Processing Route	103
v.	Influence of Laser Scan Strategy on Grain Structure, Orientation and Cracking	104
3.10.	Image Analysis	104
i.	Crack Quantification of CM247C	105
ii.	Crack & Void Quantification of CMSX486	106
iii.	Porosity Quantification of IN625	106
iv.	Porosity Quantification of Powder Samples (CM247LC/CMSX486/IN625)	106
v.	γ' Particle Size Measurement	106
3.11.	Transmission Electron Microscopy (TEM)	107
3.12.	MicroCT	107
3.13.	Differential Scanning Calorimetry (DSC) Thermal Analysis	109
3.14.	Thermo Calc Phase Diagram Modelling	109
3.15.	Mechanical Testing	109
i.	Tensile Testing	110
ii.	Creep Testing	112
3.16.	Summary	113
3.17.	References	114
CHAPTER 4: PROCESS OPTIMISATION: INFLUENCE OF THE SLM PARAMETERS ON THE MICROSTRUCTURE & INTEGRITY		115

4.1	Introduction	115
4.2	CM247LC Parametric Studies	117
	i. Powder Chemical Analysis: Results & Discussion	117
	ii. Powder Size Analysis: Results & Discussion	119
	iii. SEM Powder Examination: Results & Discussion	120
	iv. SLM Parametric Study: Introduction	125
	v. SLM Parametric Study: Microstructural Results	126
	vi. SLM Parametric Study: Crack Quantification Results	133
	vii. SLM Parametric Study: Discussion	137
4.3	CMSX486 Parametric Studies	147
	i. Powder Size Analysis: Results & Discussion	147
	ii. SEM Powder Examination: Results & Discussion	148
	iii. Statistical DOE Introduction	152
	iv. SLM Parametric Study: Crack & Void Quantification Results	152
	v. SLM Parametric Study: Discussion	164
4.4	IN625 Parametric Studies	167
	i. Powder Size Analysis Results & Discussion	168
	ii. SEM Powder Examination: Results & Discussion	169
	iii. SLM Parametric Study: Void Quantification Results	171
	iv. SLM Parametric Study: Discussion	177
4.5	Validity & Limitations of the Image Analysis Method Used for the Quantification of Crack Density	179
4.6	Conclusions & Summary	181
4.7	References	183

CHAPTER 5: INFLUENCE OF LASER SCAN STRATEGY ON GRAIN STRUCTURE, ORIENTATION AND CRACKING

		184
5.1.	Introduction	184
5.2.	Grain Structure	184
5.3.	EBSD Mapping	188
5.4.	MicroCT & SEM Visualisation of Cracks and Voids	193
5.5.	Discussion	196
5.6.	Simple Scan Pattern: A Preliminary Study	202
	i. Results	203
	ii. Discussion	206
5.7.	Conclusions & Summary	207
5.8.	References	209

CHAPTER 6: HEAT TREATMENT, γ' STRUCTURE & MECHANICAL TESTING

		210
6. 1.	Establishing Solution Treatment for SLM & HIPped CM247LC	210

i.	Initial Gas Quench (GQ) Results (1230°C)	211
ii.	Oil Quench Investigation Results	212
iii.	DSC Results of CM247LC Powder	213
iv.	Phase Diagram Modelling of CM247LC (Thermo-Calc)	214
v.	Discussion	215
6. 2.	Evolution of γ' Structure through the Processing Route of CM247LC	217
i.	Microstructure Observations & Results	217
ii.	Quantification of Particle Size & Shape	221
iii.	HIPped & Rapidly Cooled Microstructure	223
iv.	Discussion	225
6. 3.	Mechanical Testing of CM247LC	229
i.	Tensile Results	229
ii.	Creep Results	233
iii.	Discussion	236
6. 4.	Mechanical Testing of CMSX486	239
i.	DSC Results	240
ii.	Tensile Results	240
iii.	Creep Results	242
iv.	Discussion	243
6. 5.	Mechanical Testing of IN625	244
i.	Tensile Results	244
ii.	Discussion	245
6. 6.	Overall Discussion & Conclusions	246
6. 7.	References	248

CHAPTER 7: CONCLUSIONS, EVALUATION & FUTURE WORK

7.1.	Overall Conclusions	249
7.2.	Evaluation of the SLM Processing Route	252
7.3.	Proposed Areas of Future Work	254
i.	Simulation of the SLM process	254
ii.	Specific Investigation into the Influence of the Laser Scan Strategy	255
iii.	Refinement of the SLM process to reduce residual stress	255
iv.	Further Cracking Mechanism Investigation	256
v.	Post Fabrication HIPping & Heat Treatment	256
vi.	Alloy Development for SLM	257
vii.	Engineering for SLM	257
7.4.	Final Remarks	258

7.5.	References	258
APPENDIX A: CONCEPT LASER M2 OPERATION		259
i.	File Preparation	259
ii.	Support Structures	260
iii.	Physical Setup and Operation of the M2 System	262
iv.	SLM Process Parameters	266
v.	References	269
APPENDIX B: CENTRAL COMPOSITE DESIGN METHODOLOGY		270
i.	Central Composite Design	270
ii.	Fitting Response Surface	271
iii.	Definitions of the P-Value and R^2 Value	272
iv.	References	272

LIST OF FIGURES

PAGE	CAPTION
2.	Figure 1.1: Diagram of a simple single spool gas-turbine jet engine with the key stages and components labelled.
4.	Figure 1.2: Temperature (T) - Entropy (S) diagram for the Brayton Cycle approximating to a simple gas-turbine engine; CW = Compressor Work, TW = Turbine Work, UW = Useful Work.
5.	Figure 1.3: Relationship between TET, capability of superalloys, introduction of blade cooling and thermal barrier coatings between 1940 and 2010.
12.	Figure 2.1: Diagram showing the f.c.c. structure of both the γ Ni phase and the γ' Ni ₃ Al phase. Black (and shaded black) circles denote the Ni atoms and red (and shaded red) circles denote the Al atoms.
13.	Figure 2.2: Diagram showing (a) the ordered plane structure within the γ' phase and (b) how these planes combine with the Ni planes.
14.	Figure 2.2: Spherical γ' morphology within a nickel superalloy.
14.	Figure 2.4: SEM micrograph. showing the idealised cuboidal γ' structure (DS CM247LC; solution treated & aged).
16.	Figure 2.5: Evolution of γ' particle shape from (a) spherical to (b) cuboidal, (c) arrowhead and finally (e, f) cuboidal array as presented by Ricks <i>et al.</i>
17.	Figure 2.6: SEM micrograph showing over-aged γ' particles displaying cuboidal array or "split-cube" morphology (CC'd and aged CM247LC).
18.	Figure 2.7: Diagram showing the ordered particle (a) before and (b) after dislocation cutting and the associated slip plane and APB; Figure adapted from Smallman.
19.	Figure 2.8: Micrographs showing (a) darkfield TEM micrographs of Nimonic 105 with the coupled glide planes marked by arrows and (b) a further TEM micrograph of Nimonic 105 showing clearly the coupling of dislocations.
20.	Figure 2.9: The process of Orowan looping around large particles.
21.	Figure 2.10: The influence of particle diameter on the critical resolved shear stress in terms of the different dislocation movement mechanisms and with respect to precipitate particle size. Initially Weak coupled dislocation pairs (1), then strongly coupled pairs (2) and finally Orowan looping (3). The peak stress occurs at the transition between weak and strong coupled pairs.
23.	Figure 2.11: Al-Ni phase diagram adapted from Chen <i>et al.</i>

25. Figure 2.12: Isothermal sections of the ternary system Al-Cr-Ni. Showing section at (a) 900°C and (b) 1200°C. Data adapted from work published by Raghavan.
26. Figure 2.13: SEM Micrographs showing very fine secondary γ' precipitates within the γ matrix channels as presented by (a) Kakehi and (b) Liao et al. in Mar-M247.
28. Figure 2.14: Diagram showing a typical grain boundary carbide structure; adapted from Sims.
29. Figure 2.15: Micrograph showing typical carbides structure within MAR-M247 (heat treated) with MC and $M_{23}C_6$ carbides labelled.
31. Figure 2.16: Micrographs showing script-like carbides occurring in (a) Mg-freeMAR-M247 and (b) particular carbides occurring in 80ppm Mg MAR-M247.
32. Figure 2.17: An overview of the role of each of the key elements within a typical nickel superalloy. Hatched elements denote minor beneficial elements whilst horizontally shaded elements show detrimental elements.
33. Figure 2.18: SEM showing carbide precipitates with varying Co levels: (a) 10 wt.% ; (b) 5 wt.% ; (c) 0 wt.% . Label 'C' showing the 'script-like' carbides Micrographs.
34. Figure 2.19: SEM showing the varying gamma' phase structure with different Co levels: (a) 10%; (b) 5%; (c) 0%. (wt.%) Label 'C' denotes carbides; Label ' γ' ' indicating the γ' structure.
35. Figure 2.20: Plot (reconstructed from source) showing yield Strength as a function of Temperature for MAR-M247 samples containing varying wt.% Co; arrows indicate estimates of the peak strength for each alloy composition.
36. Figure 2.21: Plot. (reconstructed from source) showing Ultimate Tensile Strength (UTS) and Yield Strength (YS) for MAR-M247 samples at 649°C with varying levels of Co.
37. Figure 2.22: Plot (*reconstructed from source*) showing creep rupture life at 871°C, 414MPa with varying %wt. Co.
38. Figure 2.23: SEM Micrograph showing the surface oxide layers and γ' depleted layer formed on DS GTD-111 resulting from atmospheric exposure at high temperature.
40. Figure 2.24: Plot (reconstructed from source) showing the variation of Ta and Hf within the extracted carbides of heat treated cast MAR-M247 with varying wt.% Ta in the alloy.
40. Figure 2.25: Plot (reconstructed from source) showing the variation of Ta/Hf within the carbides compared with Ta/Hf in the alloy both before as-cast and following heat treatment.
44. Figure 2.26: Micrograph showing the typical formation of 'blocky γ' ' with the addition of Hf to MAR-M200.

48. Figure 2.27: Data (*Reconstructed from source*) showing (a) the variation of UTS and (b) elongation with different casting and heat treatment techniques for CM247LC (CC: Conventionally Cast; DS: Directionally Solidified; HTA: Aged; HTSA: Solution Treated & Aged).
50. Figure 2.28: Compiled data presented by Kim (2008), Kim (2011) and Harris (1984) showing (a) UTS/YS and (b) elongation (%) for CM247LC cast and heat treated using different methods.
51. Figure 2.29: Creep data presented by (a) Maldini *et al.* and (b) Satyanarayana *et al.* (3mm test section) (*Reconstructed from source*) for DS cast and fully heat treated CM247LC.
51. Figure 2.30: Larson-Miller Parameter data for DS cast and fully heat treated CM247LC compiled from curves presented by Donachie & Donachie, Harris *et al.*, Maldini *et al.* and individual points based on the 3mm section creep tests presented by Satyanarayana *et al.* (Log scale on Y-axis)
53. Figure 2.31: SEM Micrograph showing as-cast microstructure of CMSX-486. γ' precipitates, γ/γ' eutectic and carbides are labelled.
54. Figure 2.32: Data (*Reconstructed from source*) showing creep curves for fully heat treated CMSX-486 for different temperatures.
54. Figure 2.33: Data (*Reconstructed from source*) showing Larson-Miller relationship of cast and heat treated CMSX-486.
55. Figure 2.34: Dark-field TEM Micrograph showing ellipsoidal γ'' precipitates in IN625.
56. Figure 2.35: Tensile data collated as presented by Donachie (wrought alloy data, no heat treatment provided) and Shankar *et al.* (solution annealed condition: 1150°C, time not provided) for IN625.
56. Figure 2.36: Data presented by Donachie showing a Larson-Miller plot for IN625.
57. Figure 2.37: Diagram presented by Sponseller showing a heating (10°C/min) DSC curve for MAR-M247 highlighting the key features around the γ' solvus temperature.
59. Figure 2.38: Schematic diagram showing the key operation of an SLM system.
61. Figure 2.39: Example of balling in a single line of laser deposited iron based powder.
61. Figure 2.40: Process map for the consolidation of single laser line scans of Fe based powder.
63. Figure 2.41: SEM Micrograph showing SLM fabricated IN263 with clearly visible columnar grains elongated in the build direction (Z) and 'fishscale' weld pattern.
64. Figure 2.42: Micrograph showing DLF deposited IN625 with columnar features inclined toward the direction of laser movement for each layer.

64. Figure 2.43: Micrograph showing columnar grains with ‘fishscale’ weld pattern (left) and the fine dendritic structure within the grains under higher magnification (right) within IN738 processed by DLF.
65. Figure 2.44: Micrograph showing regions of columnar and fine grains in DLF fabricated IN718.
67. Figure 2.45: Plot (Reconstructed from source) showing the Al and Ti contents of various nickel superalloys (including CM247LC, CMSX-486 and IN625). The dashed line indicates an empirical boundary between weldable and un-weldable material due to cracking susceptibility.
68. Figure 2.46: Typical (TIG) weldability map for IN718.
69. Figure 2.47: Micrograph showing dendritic structure on the wall of a solidification crack present in 308 stainless steel.
71. Figure 2.48: Micrograph showing interdendritic liquation of heated and quenched IN718.
72. Figure 2.49: SEM showing grain boundary liquation and crack propagation in the HAZ of Rene 80.
72. Figure 2.50: Micrograph showing laser deposited IN738 on a DS superalloy substrate. The liquation occurs in the HAZ of the substrate and the crack formed propagates along a grain boundary into the deposited material.
73. Figure 2.51: Micrograph showing the occurrence of liquation in the HAZ away from the fusion zone in IN718.
74. Figure 2.52: Diagram showing the high strain concentrations at triple point boundaries (a) the movement of the high strain regions with the addition of grain boundary particles (b) and finally the division of the high the inclusion of a tortuous grain boundary.
75. Figure 2.53: Diagram (*Reconstructed from source*) showing schematically the proposed mechanism for DDC by the formation of voids from localised stresses around carbides precipitated at grain boundaries.
75. Figure 2.54: SEM micrograph (*poor quality original*) showing DDC void formation along a line of carbides.
76. Figure 2.55: Diagram showing the potential sequence of events leading to SAC.
90. Figure 3.1: Diagrams illustrating the M2 laser scan regime: (a) shows the raster and contour regions for a simple square slice; (b) shows the island scan regime.
91. Figure 3.2: Diagram illustrating the scan spacing and island overlap parameters on a single island.
92. Figure 3.3: Diagrams illustrating the ‘pin-style’ supports: (a) pin spacings and dimensions; (b) as applied to a simple horizontal bar CAD model.

96. Figure 3.4: Detailed heating profiles for the three stage heat treatment of CM247LC.
97. Figure 3.5: Detailed heating profiles for the three stage heat treatment of CMSX486.
99. Figure 3.6: Apparatus for electrolytic etching of nickel superalloy samples.
102. Figure 3.7: Diagram (Not to Scale) illustrating; (a) the sectioning of the sample; (b) the image sampling method for the optimisation study of CM247LC (study (ii)).
103. Figure 3.8: Diagram (Not to Scale) illustrating; (a) the sectioning of the sample; (b) the image sampling method for the optimisation study of CMSX486 (study (iii)).
105. Figure 3.9: Diagram of a 'particle' showing the various measurements used in the image analysis.
107. Figure 3.10: Example of a γ' particle measurement. Arrows indicate the distances measured in order to present particles size data.
108. Figure 3.11: Schematic diagram of microCT equipment.
110. Figure 3.12: Dimensioned drawing of M8 threaded tensile test bar used for room temperature and elevated temperature tensile tests.
112. Figure 3.13: Dimensioned drawing showing 14G creep specimen.
116. Figure 4.1: Optical micrograph showing cracking within a preliminary SLM-fabricated sample of CM247LC (X-Z plane).
120. Figure 4.2: Powder size distribution plots for the CM247LC; the vertical dashed lines show the ideal +15-53 μ m size range.
121. Figure 4.3: Secondary SEM micrographs showing mounted CM247LC powder taken at (a) 130X, (b) 400X, (c) 1200X magnification. Some surface irregularities can be seen on the powder.
121. Figure 4.4: Backscattered SEM micrograph showing ground and polished CM247LC powder particles.
122. Figure 4.5: Backscattered SEM micrograph showing the grain structure in a single ground and polished CM247LC particle; bright intergranular carbides are labelled.
122. Figure 4.6: Backscattered SEM micrograph typical of the set taken to determine powder porosity via image analysis; key pore features labelled.
123. Figure 4.7: EDS linescan for a spherical CM247LC powder particle showing counts against distance across linescan (inset: micrograph of particle with linescan marked in yellow).
123. Figure 4.8: EDS linescan for an irregular CM247LC powder particle showing counts against distance across linescan (inset: micrograph of particle with linescan marked in yellow).

126. Figure 4.9: Typical set of samples produced during the SLM parametric study for CM247LC.
127. Figure 4.10: Typical BSE SEM micrograph from a VHE sample (200W, 400 mm/s) showing dense jagged cracking and large pores.
128. Figure 4.11: Typical BSE SEM micrograph showing HE sample (150 W, 600 mm/s) displaying dense ‘jagged’ cracks with limited directionality with respect to the build direction.
129. Figure 4.12: SE SEM micrograph showing dendritic protrusions from the internal surface of a ‘jagged’ crack.
129. Figure 4.13: SE SEM micrograph showing dendritic protrusions from a ‘jagged’ crack surface.
130. Figure 4.14: BSE SEM micrograph of a typical LE sample (150 W, 1000 mm/s) showing a low occurrence of the ‘jagged’ cracking and a dominant ‘clean’ style of cracking. These cracks show a strong directional alignment to the build direction.
130. Figure 4.15: SE SEM micrograph showing high magnification detail of a ‘clean’ crack.
131. Figure 4.16: BSE SEM micrographs showing grain boundary crack structure: (a) X-Z plane, showing void formation along very fine line of GB carbides; (b) X-Y plane, showing fine void formation along grain boundary next to GB carbides; (c) X-Y plane, showing fine crack tip with crack lying along a grain boundary originating at a triple point intersection; (d) X-Y plane, showing crack lying on a grain boundary displaying film-like formation of carbides.
132. Figure 4.17: IPF coloured EBSD maps of three typical ‘smooth’ style cracks in SLM deposited CM247LC.
132. Figure 4.18: BSE SEM micrograph of a typical VLE sample (150 W, 1500 mm/s) showing ‘clean’ style cracks and large volumetric defects.
135. Figure 4.19: Plot showing midline variation of crack density within SLM-fabricated CM247LC samples with respect to scan spacing for three different laser powers. Labels indicate the microstructural observations related to the crack/defect character.
135. Figure 4.20: Plot showing edgeline variation of crack density within SLM-fabricated CM247LC samples with respect to scan spacing for three different laser powers. Labels indicate the microstructural observations related to the crack/defect character
136. Figure 4.21: Plot showing ‘ Δ Cracking’ values between the edgeline and the midline of SLM-fabricated samples of CM247LC for different scan speeds and laser powers. ‘-ve’ values indicate a greater midline than edgeline cracking density.
136. Figure 4.22: Plot showing cracking density variation with energy density (midline samples). Samples previously denoted as VLE, LE, HE and VHE have been labelled.

137. Figure 4.23: Plot showing variation in crack density (midline only) for SLM-fabricated samples of CM247LC with varying scan spacing for two different power/speed parameter sets. Microstructural observations are labelled.
140. Figure 4.24: Schematic diagram showing typical melt pool shape and associated thermal field for (a) high n_3 and (b) low n_3 welding parameters.
141. Figure 4.25: Schematic illustration showing the difference in thermal fields between (a) short path and (b) long path raster filled areas in SLM fabrication.
147. Figure 4.26: Particle size distribution for argon gas atomised CMSX486 powder as supplied (Carpenters, Chain dashed line) and following re-sieving (Reclassified, Solid line); black dashed lines indicate the ideal size distribution boundaries. Key sizing data is provided in the inset table.
149. Figure 4.27: SE SEM micrographs of the as-supplied gas atomised CMSX486 powder at increasing magnifications ((a)-(c)).
150. Figure 4.28: BSE SEM micrograph showing an individual ground and polished powder particle of CMSX486.
151. Figure 4.29: EDS linescans across two CMSX486 particles (inset – linescan shown by yellow line) showing no significant variation across the particle diameter. Note the drop in Ni and increase in C due to the edge of the particle and the mounting Bakelite.
151. Figure 4.30: BSE SEM micrograph of a ground CMSX486 powder sample (Re-sieved). Note the irregular particle shapes from the joined of particles in the molten state and the crescent pores formed from droplets colliding with solidified particles.
154. Figure 4.31: Plot showing raw void fraction and cracking density data for SLM fabricated CMSX486 plotted against energy density (mm/mm^2).
154. Figure 4.32: Plot showing comparison of predicted values against actual results for the crack density of SLM-fabricated CMSX486.
156. Figure 4.33: Plot showing predicted influence of laser power on crack density for CMSX486 (scan speed = 1500 mm/s, scan Spacing = 0.5, island size = 5 mm). Red points indicate the design points measured and the dashed lines indicate the 95% confidence limits of the model.
156. Figure 4.34: Plot showing predicted influence of laser scan speed on crack density for CMSX486 (laser power = 150 W, scan Spacing = 0.5, island size = 5 mm). Red points indicate the design points measured and the dashed lines indicate the 95% confidence limits of the model.
157. Figure 4.35: Plot showing the predicted interaction between the scan spacing and the scan speed for CMSX486. The red plot indicates the predicted influence of scan speed on crack density for a scan spacing = 0.65 and the black for a scan spacing = 0.35. The dashed lines indicate the respective 95% confidence limits and the green dots are the measured design points.

159. Figure 4.26: Plot showing comparison of predicted values against actual results for the void fraction of SLM-fabricated CMSX486
159. Figure 4.37: Plot showing predicted influence of laser power on void fraction for CMSX486 (scan speed = 1500 mm/s, scan Spacing = 0.5, island size = 5 mm). Red points indicate the design points measured and the dashed lines indicate the 95% confidence limits of the model.
160. Figure 4.38: Plot showing predicted influence of laser scan speed on void fraction for CMSX486 (laser power = 150 W, scan Spacing = 0.5, island size = 5 mm). Red points indicate the design points measured and the dashed lines indicate the 95% confidence limits of the model.
160. Figure 4.39: Plot showing predicted influence of scan spacing on void fraction for CMSX486 (laser power = 150 W, Scan Speed = 1500 mm/s, island size = 5 mm). Red points indicate the design points measured and the dashed lines indicate the 95% confidence limits of the model.
161. Figure 4.40: Plot showing the predicted interaction between the scan speed and the laser power for CMSX486. The red plot indicates the predicted influence of laser power on void fraction for a scan speed = 2000 mm/s and the black for a scan speed = 1000 mm/s. The dashed lines indicate the respective 95% confidence limits and the green dots are the measured design points.
161. Figure 4.41: Plot showing the predicted interaction between the scan spacing and the scan speed for CMSX486. The red plot indicates the predicted influence of scan speed on void fraction for a scan spacing = 0.65 and the black for a scan spacing = 0.35. The dashed lines indicate the respective 95% confidence limits and the green dots are the measured design points.
162. Figure 4.42: Surface plot showing predicted crack density against scan speed and laser power for CMSX486. Scan spacing fixed at 0.63; island size fixed at 6.4 mm.
162. Figure 4.43: Surface plot showing predicted void area fraction against scan speed and laser power for CMSX486. Scan spacing fixed at 0.63; island size fixed at 6.4 mm.
163. Figure 4.44: Surface plot showing both predicted crack density (red) and void area fraction (blue) for CMSX486. Scan spacing fixed at 0.63; island size fixed at 6.4 mm.
168. Figure 4.45: Particle size distribution for argon gas atomised IN625 powder as; black dashed lines indicate the ideal size distribution boundaries. Key sizing data is provided in the inset table.
170. Figure 4.46: BSE SEM micrograph showing a typical sample of ground and polished IN625 as used for the porosity quantification. Note the misshapen particles due to particle joining during solidification and the 'crescent' shaped pores formed by particle collision during solidification.
170. Figure 4.47: BSE SEM micrograph of an individual ground and polished particle of IN625 argon gas atomised powder.

171. Figure 4.48: EDS linescans across two individual IN625 powder particles (Yellow line on micrograph denoting linescan profile). EDS results show no significant segregation across the particle. Note: The increase in C and decrease in Ni towards either end of the scan is due to the onset of the particle edge and the effect of the mounting Bakelite.
172. Figure 4.49: Plot showing porosity (%) against energy density (J/mm^2) for SLM of IN625.
173. Figure 4.50: Plot showing comparison of predicted values against actual results for the void fraction of SLM-fabricated IN625.
174. Figure 4.51: Plot showing predicted influence of laser power on void fraction for IN625. Dashed lines indicate the 95% confidence limits of the model.
174. Figure 4.52: Plot showing predicted influence of scan speed on void fraction for IN625. Dashed lines indicate the 95% confidence limits of the model.
175. Figure 4.53: Plot showing predicted influence of scan spacing on void fraction for IN625. Dashed lines indicate the 95% confidence limits of the model.
175. Figure 4.54: Plot showing the predicted limits of 0% void fraction for the SLM of IN625 for different laser powers in terms of scan speed and spacing. Processing parameters falling below the line specific to their laser power are predicted to produce fully dense material.
176. Figure 4.55: Predicted time-map for IN625 showing time to scan a single island for lines representing 0% void fraction samples for different laser powers and the corresponding required scan spacing. The corresponding scan speeds can be found by referring to Figure 4.54.
185. Figure 5.1: Optical Micrograph (Stitched) showing etched microstructure in the X-Y plane; vertical lines are an artefact of micrograph stitching.
185. Figure 5.2: Annotated optical micrograph showing the 1mm repeating 'square' pattern in the X-Y plane.
186. Figure 5.3: Backscattered SEM Micrograph showing the fine elongated grain structure at the pattern boundary region (Right of the dashed line) of the 1 mm pattern contrasting with the more equiaxed grains in the central region (Left of the dashed line).
187. Figure 5.4: Optical micrograph in the X-Z plane showing the long 'plumes' of elongated grains with the fine grained region running down the middle of the image in the build direction (between dashed lines).
187. Figure 5.5: Backscattered SEM micrograph showing the elongated and fine grained regions in the X-Z plane (denoted by dashed lines).
188. Figure 5.6: Diagram showing how the grain structure in the transverse (X-Y) and longitudinal (X-Z) planes relate to each other; (a) is a 3D representation constructed from micrographs and (b) shows this relationship schematically.

189. Figure 5.7: IPF EBSD map showing the X-Y plane of SLM fabricated CM247LC highlighting the repeating diamond pattern.
190. Figure 5.8: Localised pole figures corresponding to (a) area of strong texture, (b) less defined orientation.
191. Figure 5.9: Grain boundary misorientation of the EBSD mapped area for misorientation $> 5^\circ$; (a) shows the entire area; (b) shows a single unit of the repeating pattern.
192. Figure 5.10: Frequency distribution of grain boundary misorientation for the entire EBSD mapped area (misorientation $> 5^\circ$ only).
192. Figure 5.11: Relative frequency of grain boundary misorientation within the boundary and core regions of the repeating pattern (regions were divided using by author's judgement).
193. Figure 5.12: MicroCT 3 dimensional visualisation of SLM fabricated CM247LC showing cracks (red) and voids (yellow); note the band of heavy cracking running through the entire length of the sample.
194. Figure 5.13: MicroCT 3-dimensional visualisation of SLM fabricated CM247LC of the X-Y plane showing cracks (red) and voids (yellow). (a) standard visualisation; (b) annotated image showing the boundaries between the well defined heavily and less cracked regions denoted by the dashed lines.
194. Figure 5.14: BSE SEM micrograph showing the as-fabricated transverse (X-Y) plane with annotations indicating the heavily cracked and less cracked regions of the repeating pattern.
195. Figure 5.15: MicroCT 3-dimensional visualisation of SLM fabricated and HIPped CM247LC showing cracks (red).
195. Figure 5.16: BSE SEM Micrograph showing SLM fabricated and HIPped CM247LC. Note the elimination of cracks with only minor isolated porosity remaining.
196. Figure 5.17: Schematic representation of how the 5mm island pattern with a 1mm shift each layers can result in the observed 1mm repeating pattern in the grain structure caused by the effect of the edges of the islands realigning every 6 slices.
198. Figure 5.18: Diagram showing how a rapidly moving point heat source (a) could be considered to be a band of heat moving across the island (b) with a speed determined by the scan speed and scan spacing.
203. Figure 5.19: Schematic illustration showing the difference between (a) the island scan strategy and (b) the simple scan strategy for the laser path of a single slice.
203. Figure 5.20: Optical micrograph showing simple scan pattern produced CM247LC in the X-Y plane. Possible cracks and pores are labelled.

204. Figure 5.21: EBSD map of simple scan pattern CM247LC with IPF colouring showing crystallographic orientation with respect to the (a) Z (build) direction and (b) Y (laser scan) direction.
205. Figure 5.22: {100} pole figures for the simple scan pattern CM247LC with respect to the (a) Z (build) direction and (b) Y (laser scan) direction.
205. Figure 5.23: Frequency plot showing grain boundary misorientation frequency for the simple scan pattern CM247LC.
211. Figure 6.1: BSE SEM micrographs of etched CM247LC revealing coarse γ' structure. Sample was SLM-fabricated, HIPped and solution treated (1230°C, 2h, GQ); (a) 2000x magnification, (b) 6000x magnification.
212. Figure 6.2: BSE SEM micrograph of etched CM247LC revealing coarse 'raft like' γ' structure. Sample was SLM-fabricated, HIPped and solution treated (1230°C, 2h, GQ).
213. Figure 6.3: SE SEM micrographs showing oil quenched SLM-fabricated CM247LC & HIPped samples following 2h hold at (a) 1260°C, (b) 1280°C and (c) 1300°C. Samples are etched to reveal fine γ' structure.
214. Figure 6.4: DSC results for the heating (red) and cooling (blue) of CM247LC powder (UK1091) annotated with solidus, liquidus and onset of γ' formation (Heating/Cooling = 10°C/min).
215. Figure 6.5: Thermo-Calc temperature-phase fraction model of CM247LC.
217. Figure 6.6: Diagram illustrating the steps in the proposed processing route for SLM-fabricated CM247LC components.
218. Figure 6.7: BSE SEM micrograph of as fabricated CM247LC, etched to reveal γ' phase. Light phase represented fine carbide precipitates, γ' phase not visible.
218. Figure 6.8: TEM Micrographs of as-fabricated CM247LC. (a) Diffraction pattern showing the indexed weak 010 γ' superlattice spot. (b) Corresponding dark field TEM micrograph revealing γ' as the bright 'speckled' phase (obvious in the lower left corner).
219. Figure 6.9: SE SEM micrograph showing SLM-fabricated & HIPped CM247LC etched to reveal γ' phase; γ' shows a very coarse structure.
220. Figure 6.10: SE SEM micrograph showing SLM-fabricated, HIPped & solution treated CM247LC etched to reveal γ' phase; γ' shows reasonably fine cuboidal γ' structure.
220. Figure 6.11: SE SEM micrograph showing SLM-fabricated, HIPped, solution & 1st ageing treated CM247LC etched to reveal γ' phase; γ' shows cuboidal structure with some 'split cube' style particles.
221. Figure 6.12: SE SEM micrograph showing SLM-fabricated, HIPped, solution, 1st & 2nd ageing treated CM247LC etched to reveal γ' phase; γ' shows coarse with many irregular and 'split cube' style particles.

222. Figure 6.13: Frequency plots showing γ' particle size distributions in SLM-fabricated & HIPped CM247LC following (a) solution treatment, (b) 1st ageing and (c) 2nd ageing; plots are annotated with the maximum particle size, mean particle size and the mean aspect ratio. Black line shows moving average over 3 bins.
223. Figure 6.14: Plot showing moving average line for frequency of γ' particle size in the solution treated (red), 1st aged (blue) and 2nd aged (green) conditions.
224. Figure 6.15: Plot showing measured temperature against time for the gas-quenched solution treatment, HIP with jet-cooling and standard HIP cycles. Curves are annotated with cooling rates determined by the linear portions of the falling curve.
225. Figure 6.16: SE SEM micrograph showing SLM-fabricated, HIPped & jet-cooled CM247LC etched to reveal the coarse γ' structure.
225. Figure 6.17: Frequency plot showing γ' particle size distribution in SLM-fabricated, HIPped and jet-cooled CM247LC. Plot is annotated with the maximum & mean particle size; black line shows moving average over 3 bins.
230. Figure 6.18: Bar plot showing UTS at room temperature for SLM-fabricated CM247LC for 4 different processing conditions; 3 samples were tested for each condition. Dashed line shows data for CC'd CM247LC presented by Kim et al. for comparison. Hatched bars show samples SLM-fabricated in a 2nd batch and tested at a later date
230. Figure 6.19: Bar plot showing 0.2% proof stress at room temperature for SLM-fabricated CM247LC for 4 different processing conditions; 3 samples were tested for each condition. Dashed line shows data for CC'd CM247LC presented by Kim et al. for comparison. Hatched bars show samples SLM-fabricated in a 2nd batch and tested at a later date.
231. Figure 6.20: Bar plot showing % strain to failure at room temperature for SLM-fabricated CM247LC for 4 different processing conditions; 3 samples were tested for each condition. Dashed line shows data for CC'd CM247LC presented by Kim et al. for comparison. Hatched bars show samples SLM-fabricated in a 2nd batch and tested at a later date.
232. Figure 6.21: Elevated temperature tensile test results for vertically built SLM-fabricated, HIPped & heat treated CM247LC showing UTS (square points & solid line) and 0.2% proof stress (triangular points & dashed line). Data presented by Kim et al. for CC'd CM247LC (black lines) is also presented for comparison.
232. Figure 6.22: Elevated temperature tensile test results for vertically built SLM-fabricated, HIPped & heat treated CM247LC showing % strain to failure. Data presented by Kim et al. for CC'd CM247LC (black line) is also presented for comparison.
234. Figure 6.23: Creep curves for SLM-fabricated CM247LC in various conditions tested at 1050°C, 100MPa. Vertical sample results are shown in (a) and horizontal in (b); two samples tested for each condition (Note: Different time axis scale on (a) and (b)).

- 235. Figure 6.24: Bar plot showing 1050°C, 100 MPa creep life for SLM-fabricated CM247LC following various processing conditions.
- 235. Figure 6.25: Bar plot showing 1050°C, 100 MPa creep strain to failure for SLM-fabricated CM247LC following various processing conditions.
- 239. Figure 6.26: Photograph showing SLM-fabricated CMSX486 following HIPing, heat treatment and machining to test specimen geometry. Note the extensive cracking visible along the length of the sample.
- 240. Figure 6.27: DSC results for the heating (red) and cooling (blue) of a solid sample of CMSX486 annotated with solidus, liquidus and onset of γ' formation (Heating/Cooling = 10°C/min).
- 241. Figure 6.28: Bar plot showing UTS for SLM-fabricated and heat treated CMSX486. Three samples were tested in both vertical and horizontal build orientation.
- 241. Figure 6.29: Bar plot showing 0.2% proof stress for SLM-fabricated and heat treated CMSX486. Three samples were tested in both vertical and horizontal build orientation.
- 242. Figure 6.30: Bar plot showing % strain to failure for SLM-fabricated and heat treated CMSX486. Three samples were tested in both vertical and horizontal build orientation.
- 243. Figure 6.31: Creep curves for SLM-fabricated and fully heat treated CMSX486. Samples tested at 1050°C and 100 MPa loading. The plot is annotated with the creep life of each sample.
- 244. Figure 6.32: Plot showing UTS and 0.2% proof stress for as-fabricated IN625 in both the horizontal and vertical build conditions against temperature. Data published by Donachie for cast IN625 is shown in black.
- 245. Figure 6.33: Plot showing % strain to failure for as-fabricated IN625 in both the horizontal and vertical build conditions against temperature. Data published by Donachie for cast IN625 is shown in black.

Appendix A Figures:

- 261. Figure 1: Screenshot from Magics showing the automatically generated support structure attached to the actual component geometry.
- 263. Figure 2: Photograph showing different views of the Concept Laser M2 system: (a) Front view of machine showing handling chamber; (b) Exterior view of the processing chamber.
- 263. Figure 3: Schematic cross-section of the technology module of the Concept Laser M2 system.

- 266. Figure 4: Diagram defining the contour inset and beam compensation with respect to the defined part edge and scan vectors.
- 267. Figure 5: Screen capture showing parameters used when slicing in the Magics software.
- 268. Figure 6: Screen capture showing standard laser parameters assigned for the SLM of CM247LC
- 268. Figure 7: Screen capture showing standard process parameters assigned for the SLM of CM247LC
- 269. Figure 8: Screen capture showing standard machine parameters assigned for the SLM of CM247LC

Appendix B Figures:

- 271. Figure 1: CCD space for three factors

LIST OF TABLES

PAGE	CAPTION
15.	Table 2.1: Results presented by Ricks et al. showing lattice misfit of various nickel superalloys and the particle size at which γ' departs from a spherical to a more cuboidal morphology.
43.	Table 2.2: Data (Units converted from source) showing the influence of 2 wt.% Hf addition on the creep properties of MAR-M200.
47.	Table 2.3: Nominal composition of CM247LC (wt.%).
50.	Table 2.4: Heat treatments applied to mechanical test samples for various sources.
52.	Table 2.5: Nominal composition of CMSX486 (wt.%).
55.	Table 2.6: Nominal composition of IN625 (wt.%).
86.	Table 3.1: Powder Batch Details
89.	Table 3.2: Technical Specifications for both Concept Laser M2 and EOS EOSint M270 SLM.
92.	Table 3.3: Summary of SLM operating parameters for the different investigation stages.
94.	Table 3.4: Technical specifications of the HIP vessel.
95.	Table 3.5: HIPing parameters for the consolidation of SLM fabricated CM247LC and CMSX486 samples.
95.	Table 3.6: Heat treatment parameters for samples of CM247LC and CMSX486.
98.	Table 3.7: Approximate guide for relative convective heat transfer coefficients for gas, oil and water quenching.
101.	Table 3.8: Details of the SEMs used and the studies they correspond to.
111.	Table 3.9: Tensile testing conditions for SLM fabricated CM247LC samples.
111.	Table 3.10: Tensile testing conditions for SLM fabricated CMSX486 samples.
112.	Table 3.11: Tensile testing conditions for SLM fabricated IN625 samples.
113.	Table 3.12: Creep test conditions for CM247LC specimens.
113.	Table 3.13: Creep test conditions for CMSX486 specimens.

- 117. Table 4.1: Chemical analysis result for CM247LC powder, 150 W, 1500 mm/s SLM sample and 200 W, 400 mm/s SLM sample compared against nominal composition (wt.% unless otherwise stated).
- 122. Table 4.2: Summary of porosity data calculated by image analysis of ground CM247LC powder.
- 126. Table 4.3: Parameters used to produce samples for analysis within the parametric study of SLM-fabricated CM247LC.
- 133. Table 4.4: Empirical observations of cracking character within SLM-fabricated samples of CM247LC.
- 152. Table 4.5: Porosity quantification results for CMSX486 (re-sieved) powder.
- 153. Table 4.6: Raw experimental results for the parametric study of CMSX486.
- 154. Table 4.7: ANOVA for crack density of CMSX486. Blue rows indicate significant terms and red row indicates overall model significance.
- 158. Table 4.8: ANOVA for void fraction of CMSX486. Blue rows indicate significant terms and red row indicates overall model significance.
- 163. Table 4.9: Crack density and void fraction results from the three validation samples compared against the model results for CMSX486.
- 171. Table 4.10: Porosity quantification results for In625 powder.
- 172. Table 4.11: Parametric DOE study results for the SLM processing of IN625 investigating 3 parameters measuring porosity only.
- 173. Table 4.12: ANOVA for void area fraction of IN625. Blue rows indicate significant terms and red row indicates overall model significance.
- 177. Table 4.13: Validation results for the optimised IN625 SLM parameters based.

Appendix A Tables:

- 262. Table 1: Typical automatic support parameters used for SLM of CM247LC, CMSX486 & IN625

CHAPTER 1: INTRODUCTION - AIMS, OBJECTIVES & SCOPE

This chapter introduces high-temperature materials and provides a brief background as to their importance within gas-turbine engines. Additive Layer Manufacturing (ALM) is introduced, and the potential advantages and disadvantages of this technique are discussed. Finally the industrial impetus for this research is presented and the research aims and objectives identified.

1.1. A Brief Background on High-Temperature Materials

With the advent of the jet engine also came the need for high-temperature materials able to withstand the extreme temperatures, stresses and atmospheres within them. The gas flow route within a typical gas-turbine engine can be broken down into two key sections: the ‘cold’ section consisting of the region between the intake and the fuel injection and the ‘hot’ section consisting of the combustion chamber out to the exhaust nozzle; this distinction is shown in Figure 1.1 [1].

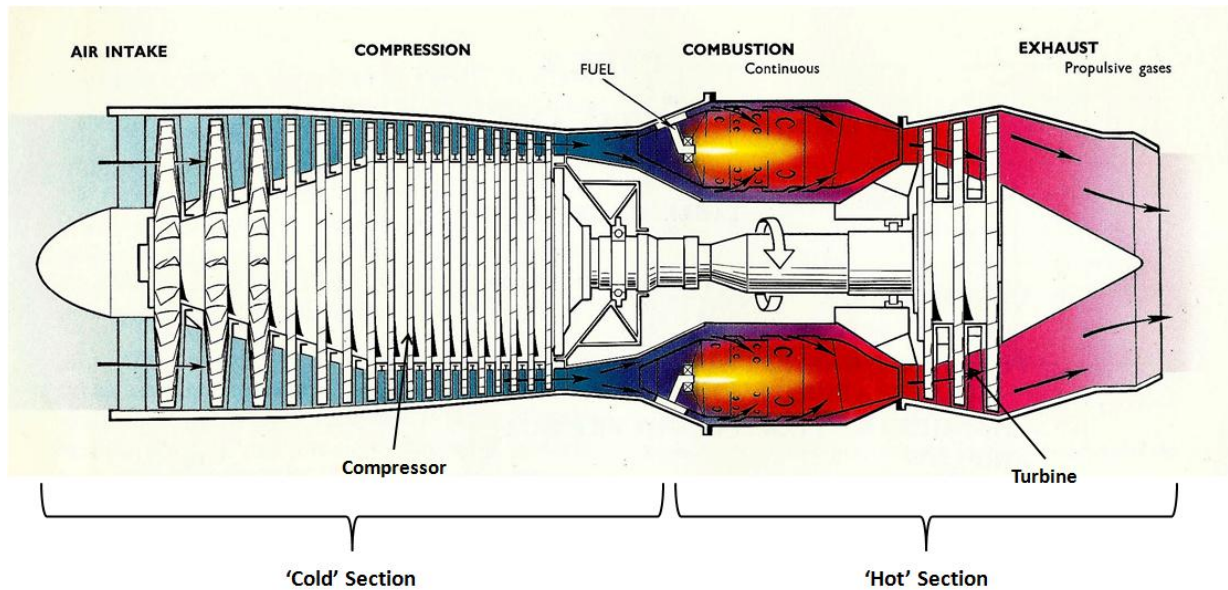


Figure 1.1: Diagram of a simple single spool gas-turbine jet engine with the key stages and components labelled [1].

Within the ‘cold’ section, the key components that come into contact with the gas stream (mainly the rotary and static parts of the compressor) can be made out of lightweight and strong titanium alloys as the temperatures experienced are relatively low.

In the hot section however a high-temperature material is required which must be able to fulfil the following three criteria [2]:

- Maintain mechanical properties under operating temperatures close to material melting point ($T_{\text{operating}}/T_{\text{melting}} > 0.6$).
- Resistance to mechanical degradation caused by loading over extended periods of time (ie. creep resistance) and cyclic loading.
- Tolerance of severe environments (ie. corrosion/oxidation resistance).

The key components within this stage of the gas-turbine are those that extract the work from the gas stream: the turbine disk, the static nozzle guide vanes and above all the rotating turbine blades which are subject to the highest temperatures, greatest forces and harshest environments. Nickel superalloys have been developed to meet these requirements; the

improvements in their properties and forming methods have been pivotal in the continuing evolution of gas turbine engines.

By considering the basic thermodynamic cycle at work within a gas turbine engine, it becomes apparent why these high temperatures are necessary and why there is continuing drive to develop materials to withstand even higher temperatures. Figure 1.2 shows the temperature (T) – entropy (S) diagram for the Brayton cycle which approximates to what occurs in a simple gas-turbine engine (assuming isentropic compression/expansion and heat input at constant pressure). The cycle occurs as follows:

- Gas is taken in at atmospheric conditions: T_1 , P_1 . (1)
- Gas pressure is increased to P_2 having undergone work by the compressor (CW).
(1→2)
- Combustion takes place raising the temperature of the gas at a constant pressure to T_3 .
(2→3)
- Gas expands through the turbine back to atmospheric pressure (P_1) during which work is extracted to drive the turbine (TW) with the remainder providing the useful work (UW) of the system (either thrust for a jet engine, or further turbine stages for power generation). (3→4)
- As the turbine and the compressor are directly connected, $CW = TW$.

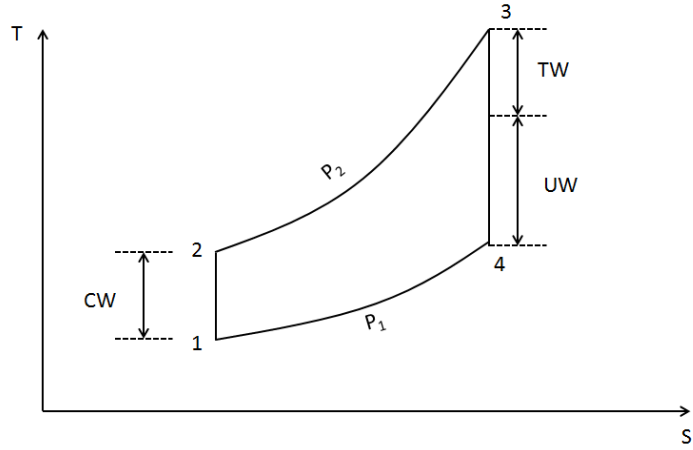


Figure 1.2: Temperature (T) - Entropy (S) diagram for the Brayton Cycle approximating to a simple gas-turbine engine; CW = Compressor Work, TW = Turbine Work, UW = Useful Work.

From basic thermodynamics it is known [3]:

$$\text{Work (per unit mass flow)} = C_p \Delta T$$

$$C_p = \text{Specific heat of gas; } \Delta T = \text{Temperature change}$$

Therefore:

$$\text{Heat in, } q_{in} = C_p (T_3 - T_2)$$

$$\text{Heat out, } q_{out} = C_p (T_4 - T_1)$$

Thermodynamic efficiency, η_{th} is defined as:

$$\eta_{th} = 1 - \frac{q_{out}}{q_{in}} = 1 - \frac{C_p (T_4 - T_1)}{C_p (T_3 - T_2)} = 1 - \frac{T_1 \left(\frac{T_4}{T_1} - 1 \right)}{T_2 \left(\frac{T_3}{T_2} - 1 \right)}$$

As 2-3 and 4-1 are both constant pressure and the compression is adiabatic then:

$$\frac{T_2}{T_1} = \frac{P_2^{\frac{k-1}{k}}}{P_1^{\frac{k-1}{k}}} = \frac{P_3^{\frac{k-1}{k}}}{P_4^{\frac{k-1}{k}}} = \frac{T_3}{T_4}$$

By substituting:

$$\eta_{th} = 1 - \frac{T_4}{T_3}$$

From here it becomes apparent that as T_4 cannot be easily controlled. The best way to improve the thermodynamic efficiency is to increase T_3 also known as ‘Turbine Entry Temperature’ (TET) (further details can be found elsewhere [2, 4]). Figure 1.3 [2] shows how the drive to increase TET has directly influenced alloy development, casting techniques, development of thin-film cooling and the introduction of thermal barrier coatings for high temperature components.

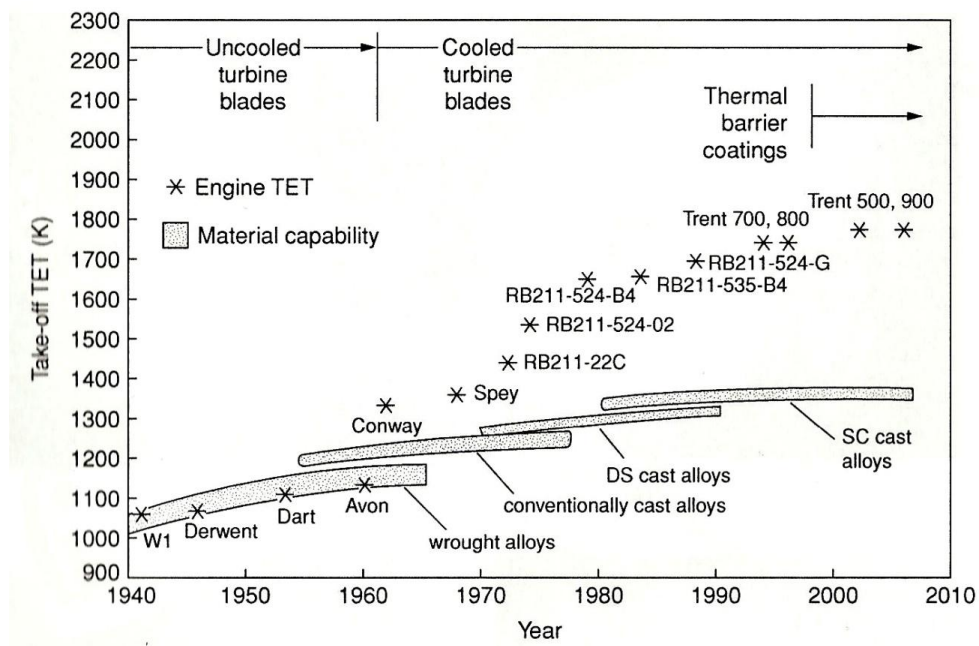


Figure 1.3: Relationship between TET, capability of superalloys, introduction of blade cooling and thermal barrier coatings between 1940 and 2010 [2].

1.2. Additive Layer Manufacturing (ALM) as a Netshaping Technique

ALM encompasses a wide range of netshaping techniques where a 3-dimensional object is directly made from an input stock material and CAD file. All ALM technologies follow the same basic steps:

- A 3-dimensional CAD model is produced.
- The model is ‘virtually-sliced’ into a sequence of 2-dimensional geometries of a specific thickness.
- Each slice is then physically made and combined with previous ones until the entire shape is produced.

The different techniques included within the term ALM are further discussed in the literature review (Chapter 2). In principle, ALM has a number of attractive advantages with the potential for industrial exploitation:

- Ability to produce complex shapes, including internal geometries without the constraints of traditional machining or the expensive setup costs associated with investment casting.
- Manufacturing freedom allows for a ‘design-for-functionality’-philosophy rather than one based on ‘design-for-manufacture’.
- Ability to dramatically shorten the ‘design-to-component’ time allowing for more design iterations and actual physical testing of components.
- Reduction in material waste as the majority of processed material is in the final component.

As with all technologies however there are a number of drawbacks associated with ALM processing:

- Processing time can be long making large production runs unfeasible with current technology.
- Geometries are subject to a specific set of constraints concerning build orientation and support structures during building.
- Current technology has strict maximum build-size limitations. (*Typically 250 mm cubed*)
- Post-processing may be required to obtain the desired finish/properties reducing the appeal of the ALM processing route.
- Necessity to qualify materials suitable for ALM.
- Necessity to develop methods for assessing quality and reproducibility of components.
- Current facility costs (*>£400,000 for SLM*)

All these factors need to be taken into account when selecting ALM as the processing route for a specific component.

1.3. Research Aims & Objectives

A manufacturer of aerospace components has proposed research into the possibility of producing several high temperature components directly by the Selective Laser Melting (SLM) route from the nickel based superalloy CM247LC; additionally there is a secondary interest in the alloys CMSX486 and IN625 which are also to be assessed. The potential components are of high geometric complexity and as production is typically limited to small volumes each year an ALM solution is economically viable. The research presented within this thesis focuses solely on the material science element to this project and no discussion will be made of the component geometry or the practical challenges of producing them by SLM.

The overall aim of this project can be stated as:

To establish a processing route for the nickel-base superalloy CM247LC using SLM and to evaluate against conventional cast CM247LC in terms of microstructure and mechanical properties. Furthermore, based on the results for CM247LC, to assess the processability and mechanical properties of SLM-fabricated CMSX486 and IN625.

This aim can be broken down into a series of concise objectives for the research:

- To optimise the SLM processing parameters for CM247LC, CMSX486 and IN625 using parametric studies to reduce defects and produce a fully dense material (Chapter 4).
- To investigate and characterise the influence of SLM on the grain structure and defects within CM247LC (Chapter 5).
- To investigate the use of a post-processing technique to eliminate remaining defects within the SLM-fabricated CM247LC (Chapters 5, 6).
- To establish post-processing heat treatments to refine the γ' microstructure in CM247LC to maximise the creep properties (Chapter 6).
- To characterise the γ' structure of CM247LC throughout the processing route (Chapter 6).
- Finally to mechanically test the SLM-fabricated CM247LC, CMSX486 and IN625 following all processing steps based on the operational requirements of the components and compare against conventionally formed material (Chapter 6).

Final conclusions and an evaluation of the proposed processing route will be presented; recommendations for future research to further understand and develop this technique will also be made.

1.4. References

- [1] Rolls-Royce. The Jet Engine. Derby, 1966.
- [2] Reed RC. The Superalloys: Fundamentals and Applications: Cambridge, 2006.
- [3] Bathie WW. Fundamentals of Gas Turbines. New York; Chichester: Wiley, 1996.
- [4] Van Wylen G, Sonntag R, Borgnakke C. Fundamentals of Classical Thermodynamics. New York; London: John Wiley, 1994.

CHAPTER 2: LITERATURE REVIEW

This chapter presents a review of the relevant literature outlining the fundamental metallurgy of nickel superalloys; the roles of specific elements within those alloys; the physical metallurgy of CM247LC, CMSX486 and IN625; ALM techniques; early studies to characterise SLM-fabricated material; the SLM of nickel alloys and finally the weld cracking mechanisms in nickel superalloys.

2.1. Categories of Superalloys

Superalloys can be traditionally categorised into one of three main classes. The first to be developed are known as iron-nickel-base alloys. These alloys are typified in the Incoloy 800 series [1], and contain high wt.% Fe which acts as a joint base material with Ni [2]. Most of these alloys display a solid-solution strengthening mechanism similar to nickel-base superalloys yet show a spherical rather than cuboidal precipitation of the strengthening γ' phase [2] and are typically used as wrought rather than cast materials [1, 2].

The second category is nickel-base superalloys which contains the majority of currently used blade alloys and can themselves be subcategorised depending on microstructure (i.e. strengthening mechanism) and composition. They are typified by the use of nickel as the sole base-material [2] and can be used in both cast and wrought form depending on the application.

The final category is cobalt-base superalloys which use cobalt as the base material. These alloys typically rely on strengthening by elements within solid-solution and the formation of carbides for their high temperature properties. Some elements are able to form an inter-metallic (of the form Co_3M) phase equivalent to the γ' phase found in nickel-base superalloys

however practical application for these has yet to be found due to their limited temperature range (See ref. [3] - *Section IX*).

The research presented in this thesis relates to nickel-base superalloys which themselves can be further subdivided:

- **γ' strengthened:** Hardened by the precipitation of the coherent γ' phase (Ni_3Al) typically heat treated to form in a fine cuboidal structure; these alloys are the main focus of this thesis and as such the specific details of this structure are discussed in subsequent sections.
- **γ'' strengthened:** These Nb-containing alloys are hardened by the precipitation of the Body-Centred Tetragonal (BCT) γ'' phase (Ni_3Nb) as typified by IN718 where the γ'' phase is precipitated as coherent disc shaped particles [1]. γ' strengthening can occur in addition to that provided by γ'' .
- **Solid-solution strengthened nickel-base superalloys:** Typified by IN625 and HastelloyX where material strength is achieved through solid-solution strengthening elements (e.g. Co, Cr, Fe, Mo, W, Ta, Re) [2].

2.2. γ/γ' Structure

The γ' phase and how it is precipitated within the γ matrix is the key to the high temperature creep resistance of this type of precipitate hardenable nickel-base superalloy. It is therefore necessary to fully discuss the relationship between these two phases before considering the other factors, phases and elements within these complex alloy systems.

i. Atomic Structure

The γ (Ni) and γ' (Ni_3Al) phases exhibit a face-centred cubic (f.c.c.) structure. The crystal structures of both the γ and γ' phases are shown in Figure 2.1 [2]. The γ' phase shows an ordered structure: taking the unit cell illustrated in Figure 2.1, it can be seen that the upper and lower planes consist of a Ni atom surrounded by Al atoms at each corner of the square. Extending this pattern out in all directions would result in an ordered plane of Ni and Al atoms. The middle plane, lying between the upper and lower face of the unit cell, shows simply four Ni atoms lying in the face-centred positions. These atoms form an entire plane of Ni which separates each plane of ordered Ni and Al. A diagram showing the ordered plane is given in Figure 2.2 (a) and how this combines with the Ni planes is shown in Figure 2.2 (b).

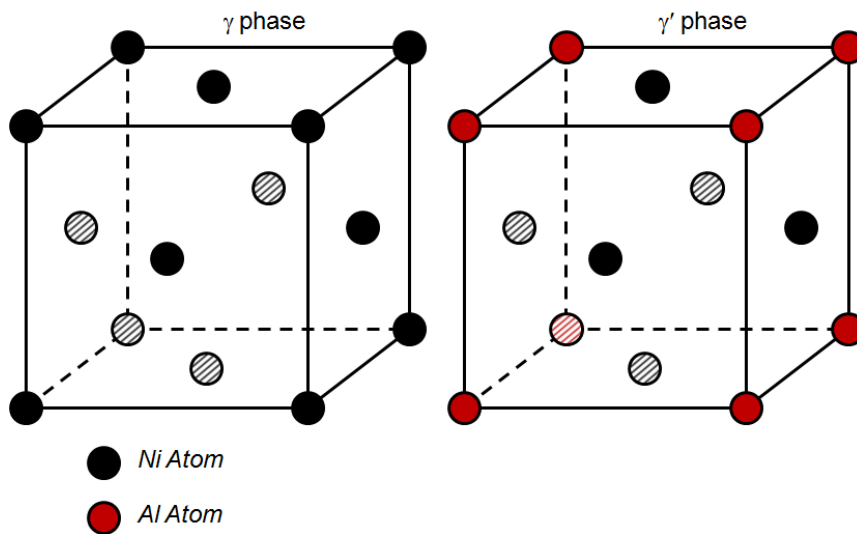


Figure 2.1: Diagram showing the f.c.c. structure of both the γ Ni phase and the γ' Ni_3Al phase. Black (and shaded black) circles denote the Ni atoms and red (and shaded red) circles denote the Al atoms [2].

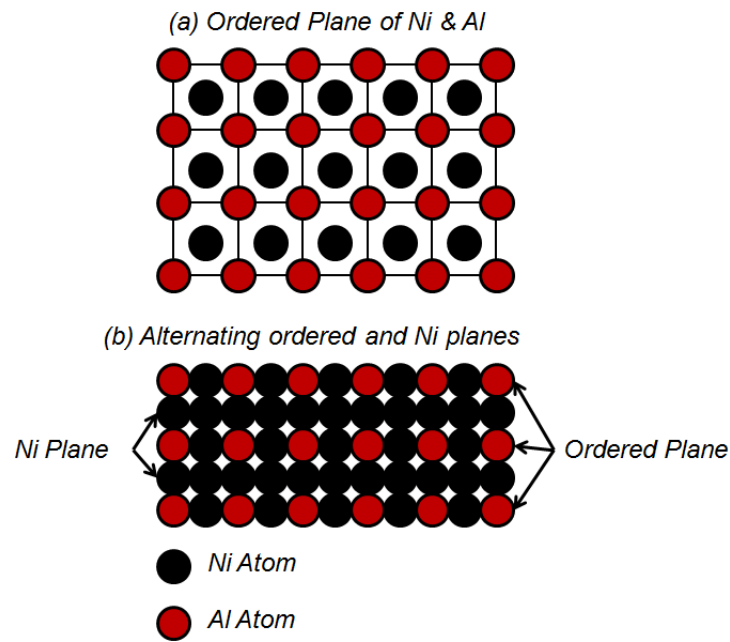


Figure 2.2: Diagram showing (a) the ordered plane structure within the γ' phase and (b) how these planes combine with the Ni planes.

ii. Precipitate Morphology

Assuming a fully homogenised, solutionised and stress-free material, an ageing heat treatment can be used to precipitate the γ' phase in the form of discrete particles. This particulate structure is desirable as it confers good creep properties.

Initially within the ageing treatment, the γ' phase will form as small spherical particles as is characterised by the early superalloys (e.g. Incoloy 800), however further ageing will produce cuboidal precipitates as are characteristic of more recent alloys. Figure 2.3 shows typical spherical γ' morphology as presented by MacKay & Nathal [4]. Figure 2.4 shows a micrograph presented by Kim *et al.* [5] of the characteristic cuboidal γ' structure within the nickel-base superalloy, CM247LC, following a full heat treatment.

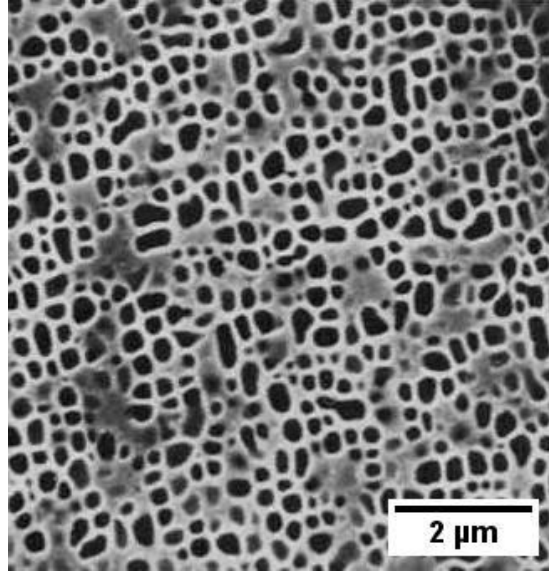


Figure 2.3: Spherical γ' morphology within a nickel superalloy [4].

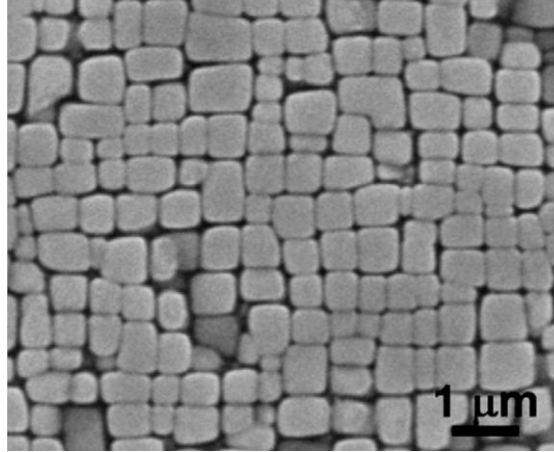


Figure 2.4: SEM micrograph. showing the idealised cuboidal γ' structure (DS CM247LC; solution treated & aged) [5].

The transition from spherical particle to cuboidal during ageing is discussed in standard texts [1], however the key research was published in 1982 by Ricks *et al.* [6]. This transition is dependent directly on the lattice misfit parameter (δ) between the γ and γ' phases, as given in equation 1 where a_γ and $a_{\gamma'}$ are the lattice parameters of the γ and γ' phase respectively; lattice misfit is described as positive if $a_{\gamma'} > a_\gamma$.

$$\delta = 2 \times \left[\frac{a_{\gamma'} - a_\gamma}{a_{\gamma'} + a_\gamma} \right] \quad \text{-Eq. 1 [1]}$$

Assuming that the γ' phase maintains coherency within the γ matrix, the stress field surrounding the γ' particles, induced by the deformation of the surrounding γ matrix depends on the size of the particle and the lattice misfit parameter. At some threshold point this stress field will become great enough in magnitude to deform the γ' particle from spherical to cuboidal in shape. Table 2.1 presents the result published by Ricks *et al.* [6] showing the lattice misfit of five alloys and the particle size at which the γ' structure departed from spherical to cuboidal.

Table 2.1: Results presented by Ricks et al. [6] showing lattice misfit of various nickel superalloys and the particle size at which γ' departs from a spherical to a more cuboidal morphology

Alloy	Lattice Misfit (%)	Particle size threshold for spherical/cuboidal transition (μm)
Udimet 720	<0.02	0.7
Nimonic 105	-0.04	0.7
Nimonic 115	-0.18	0.5
Nimonic 80A	+0.32	0.3
Nimonic 90	+0.34	0.3

If further ageing takes place then the particles continue to grow through a very distinctive sequence. Ricks *et al.* [6] state that the coherency strains associated with a positively misfitting particle are in tension parallel to the faces of the cube and compressive normal to the faces. This results in a region of low strain at the corners where the compressive strain from the face is nullified by the tension strains of the other two faces at that corner. As such, further growth of the γ' particle takes place at the corners, along the $\langle 111 \rangle$ directions. Growth continues at the eight corners until they are also subject to a shift in shape due to the coherency strains and are deformed into cuboidal shapes. This results in the cuboidal array of γ' particles associated with over-aged nickel superalloys materials. This evolution of particle shape due to ageing is shown diagrammatically in Figure 2.5.

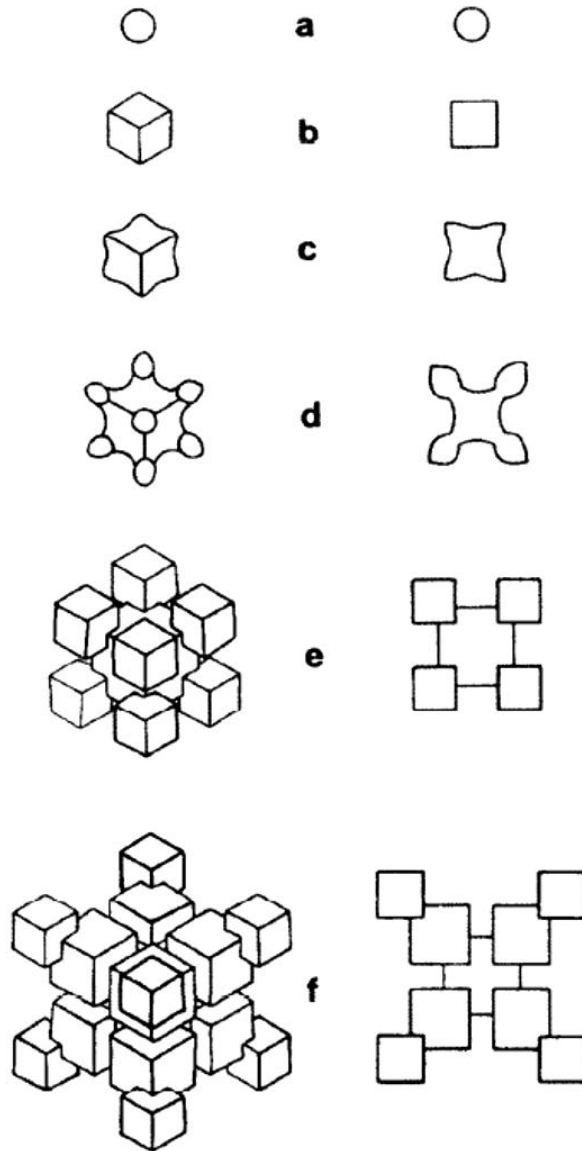


Figure 2.5: Evolution of γ' particle shape from (a) spherical to (b) cuboidal, (c) arrowhead and finally (e, f) cuboidal array as presented by Ricks et al. [6].

Cuboidal-array morphology is seen in micrographs illustrating an over-aged γ' structure as in Figure 2.6 (Kim et al. [5]); often referred to as “split-cube” morphology.

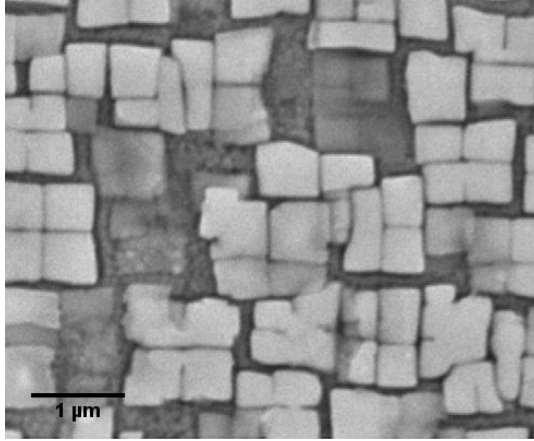


Figure 2.6: SEM micrograph showing over-aged γ' particles displaying cuboidal array or "split-cube" morphology (CC'd and aged CM247LC).

iii. Strengthening Mechanism of the γ' Phase

The key strengthening mechanism due to the γ' particles is documented in traditional texts on the subject [1, 2, 7] and referred to as 'order strengthening' [1] or sometimes 'chemical hardening' [7]. For a dislocation to move through the ordered γ' particle, it is necessary for an Anti-Phase Boundary (APB) to be formed and the associated anti-phase boundary energy (γ_{APB}) overcome. This process is shown diagrammatically in Figure 2.7 both (a) before and (b) after the dislocation has moved through the ordered particle; the APB and slip plane are indicated.

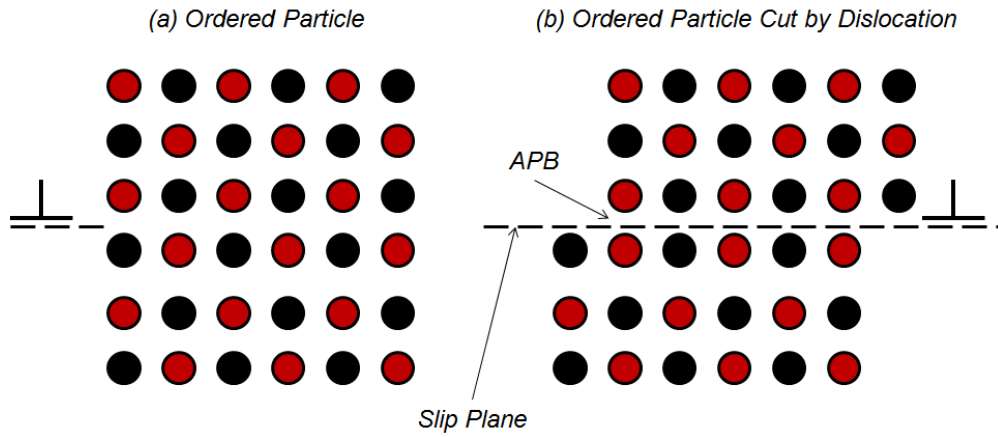


Figure 2.7: Diagram showing the ordered particle (a) before and (b) after dislocation cutting and the associated slip plane and APB; Figure adapted from Smallman [7].

There is some disagreement in traditional text on the most significant mechanism due to γ' strengthening:

Reed [1] suggests that as the particle cutting stress will be approximately of the order γ_{APB}/b where b is the Burgers vector and given typical values of $\gamma_{\text{APB}} \approx 0.1 \text{ J/m}^2$ and $b = 0.25 \text{ nm}$, the cutting stress will be in the order of 400 MPa. Reed goes on to state that this will form the most substantial contribution to the γ' particulate strengthening and outweighs the other mechanisms.

Smallman [7] however, includes three mechanisms for the hardening effect of the ordered particles. Firstly the APB effect as described above; secondly the work required to create additional particle matrix interface due to the increased perimeter of the particle following the dislocation cutting and finally the energy associated with the change in width of a dissociated dislocation as it passes through a particle of different stacking fault energy.

It is agreed between both texts [1, 7] that dislocation movement through the particles must take place in coupled pairs with the second dislocation restoring the ordered structure of the particle. The theoretical basis of these dislocation pairs is discussed by Reppich [8] and is

demonstrated in the corresponding experimental paper by Reppich et al. [9] which shows examples of this dislocation couple effect as shown in Figure 2.8.

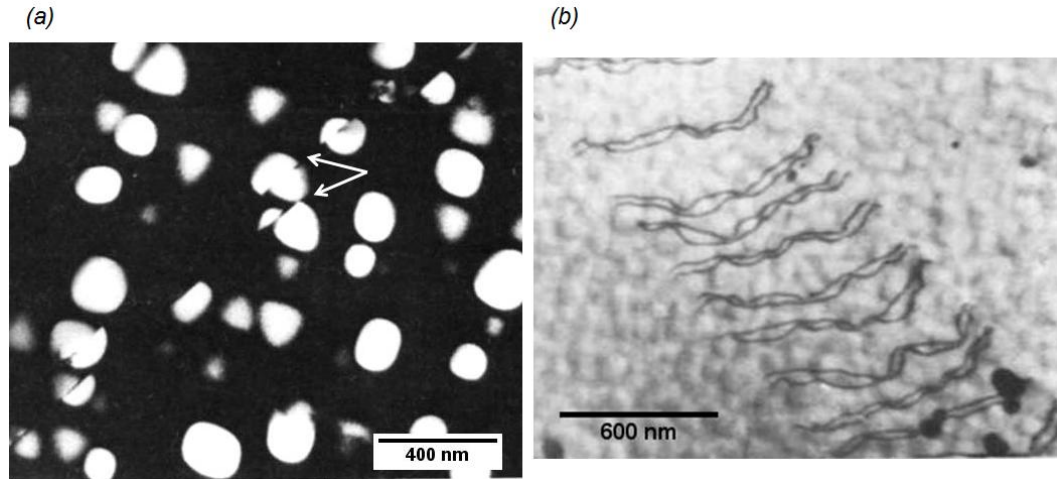


Figure 2.8: Micrographs showing (a) darkfield TEM micrographs of Nimonic 105 with the coupled glide planes marked by arrows and (b) a further TEM micrograph of Nimonic 105 showing clearly the coupling of dislocations [9].

A distinction is made between the weak and strong coupling of these dislocation pairs [8, 9] and is defined such that weak coupling occurs when the spacing between the two dislocation is large compared with the particle diameter so that there may be a cut particle containing APB between the two. Strongly coupled dislocations occur when the particle size is comparable to the distance between the dislocations. A full theoretical derivation of the differences in the energy required in each of these situations can be obtained in the comprehensive review of the subject by Ardell [10], however at this point it is sufficient to appreciate that at some threshold particle size, dislocation pairs move from weak to strong coupling.

At larger particle sizes, Orowan looping is suggested as the mechanism for the movement of dislocations past precipitate particles. Sufficiently large particles are required such that the energy for looping is less than that for particle shearing and that the particles must lie

sufficiently far apart to allow bowing in the low stress valleys between them [7]. This process is shown schematically in Figure 2.9.

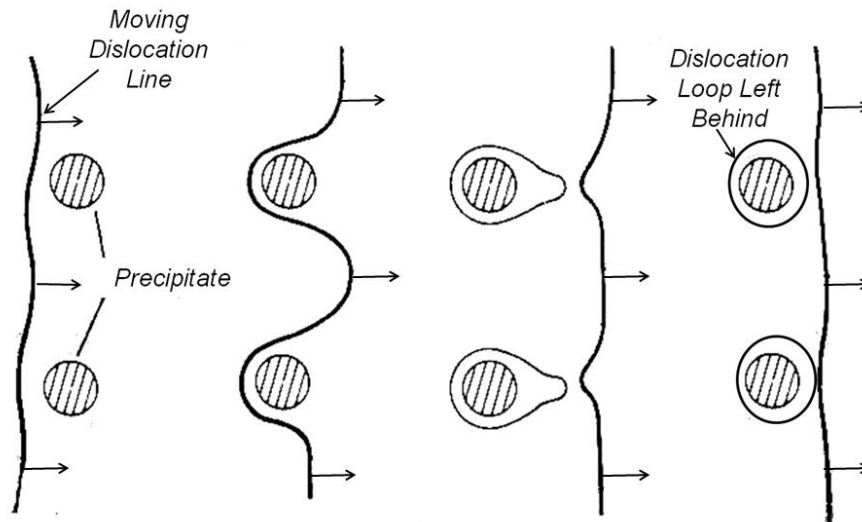


Figure 2.9: The process of Orowan looping around large particles [7].

This kind of dislocation looping has been observed around γ' precipitates within nickel superalloys and is shown in research presented by Plumtree & Persson relating to Alloy 800 [11].

By considering all the mechanisms of creep strength in terms of particle size, Reppich *et al.* [8, 9] were able to map the key creep deformation mechanisms. The generalised form of their results is presented in Figure 2.10. At small particle sizes, it is the weakly coupled dislocations cutting through the particles that result in creep damage, (1); at larger particle sizes, the key mechanism is the strongly coupled dislocations (2) and finally Orowan looping is responsible for the passage of dislocations around the precipitate particles (3). The peak material strength occurs at the transition between weak and strong coupled dislocations, however the particle size of this transition varies depending on the material composition.

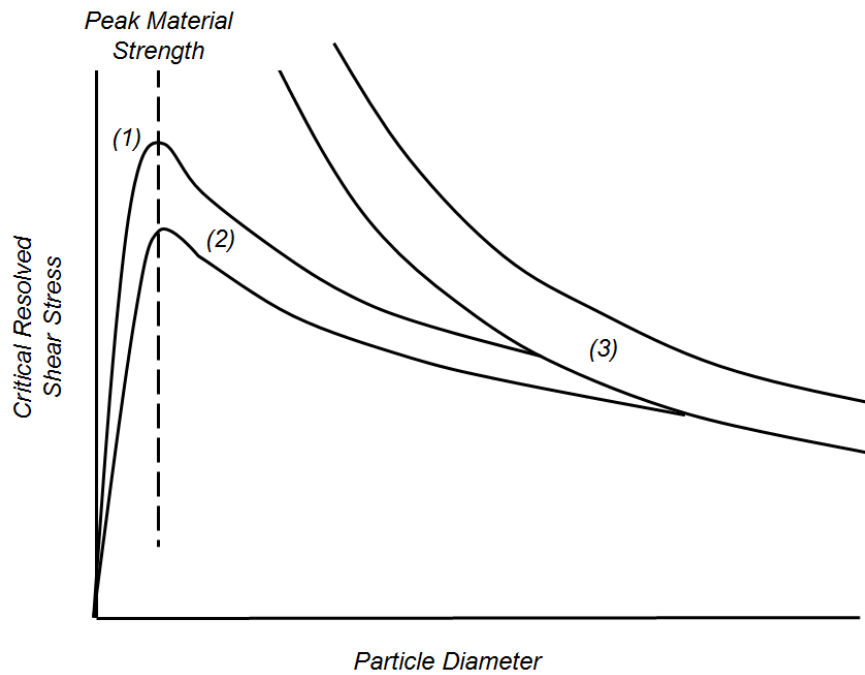


Figure 2.10: The influence of particle diameter on the critical resolved shear stress in terms of the different dislocation movement mechanisms and with respect to precipitate particle size. Initially Weak coupled dislocation pairs (1), then strongly coupled pairs (2) and finally Orowan looping (3). The peak stress occurs at the transition between weak and strong coupled pairs [8, 9].

It should be noted that this research differs from traditional material science which states that the peak stress occurring within a precipitate hardened material occurs at the transition between particle shearing and looping [12]. This justification is also used by Nathal et al. [13, 14] when discussing the peak strength in MAR-M247 with varying amounts of Co. Nathal et al. conclude that the increasing γ' particle size due to the Co additions move the material through the shearing/looping transition. Whilst that may be the cause of their observed peak in strength, the more complete view presented by Reppich et al. [8, 9] suggests that this may be smaller than an earlier peak strength occurring at the transition between weak/strongly coupled dislocation pairs.

In practical application however, precipitates tend to grow under service conditions [15] so the ideal size is not generally maintained. Additionally, within published research on the subject, there is a mismatch between particle size of the peak strength obtained at the

transition between weak and strong coupling as presented by Reppich *et al.* [9] (<100nm) and those typically used in the investigation of the tensile properties of nickel-base superalloys (0.2-0.7 μm published by Kakehi [16]; 0.3-0.5 μm published by Kim [5] *et al.* and 0.2-0.9 μm published by Sluytman & Pollock [17]). This disparity is likely to be caused by the physical limitations of furnace equipment and cooling rates within larger samples of material.

A further note on precipitate shape has been presented by Sluytman & Pollock [17]. This research uses image analysis to define a mean 'shape parameter', η , for the particles observed with a microstructure where η tends to 1 as the particle shape tends to cuboidal. As the lattice misfit is directly responsible for the formation of the cuboidal precipitate shape, the research shown that the shape parameter is directly related to the lattice misfit. The paper concludes that peak shape parameter occurs at a misfit of 0.4% which also corresponds to good high-temperature creep properties of the material. This work stands out as it aims to link the shape to the lattice misfit therefore providing a further way to evaluate potential mechanical properties of the overall material rather than relying on the tradition measurement of γ' particle size.

iv. Heat Treatment Principles

In order to obtain the γ/γ' structure discussed, the correct heat treatment must be applied to the material. In generic terms, this would be a solution treatment followed by an ageing treatment and can be explained by considering the Ni rich side of the Al-Ni phase diagram as shown in Figure 2.11 (Al-Ni phase diagram adapted from research presented by Chen *et al.* [18]).

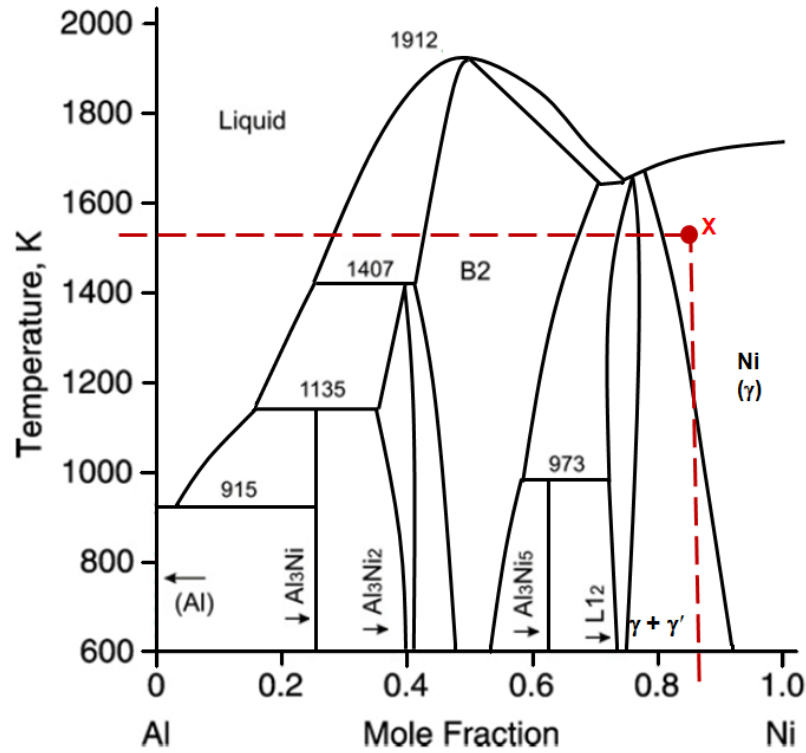


Figure 2.11: Al-Ni phase diagram adapted from Chen et al. [18].

Taking a hypothetical Ni-Al binary alloy represented by the red dashed line in Figure 2.11 existing in $\gamma + \gamma'$ state at ambient conditions, the alloy is heated to point 'X' during the solution treatment in order to homogenise the structure and fully dissolve the γ' phase into solution. The material is then rapidly quenched to suppress the formation of the γ' phase. During the ageing treatment the material is then heated to a temperature below the γ' solvus (represented at the boundary between the $\gamma + \gamma'$ and γ regions) to allow the γ' particles to form by diffusion.

In reality nickel-base superalloys contain many elements making them difficult to represent on a phase diagram, however due to the levels of chromium, most alloys could be considered as ternary systems of Ni-Cr-Al with the addition of minor elements to refine and modify that microstructure [15]. Two isothermal sections of the Ni-Cr-Al system are shown in Figure 2.12; adapted from the phase diagrams collated by Raghavan [19]. The composition marked

by the red 'X' represents the region where a typical nickel-base superalloy may exist. At higher temperature (1200°C - Figure 2.12 (b)) the γ' is dissolved into solution and the material lies in the purely γ region likewise at lower temperatures the γ' phase can be precipitated out as the material falls into the $\gamma+\gamma'$ region (Figure 2.12(a)).

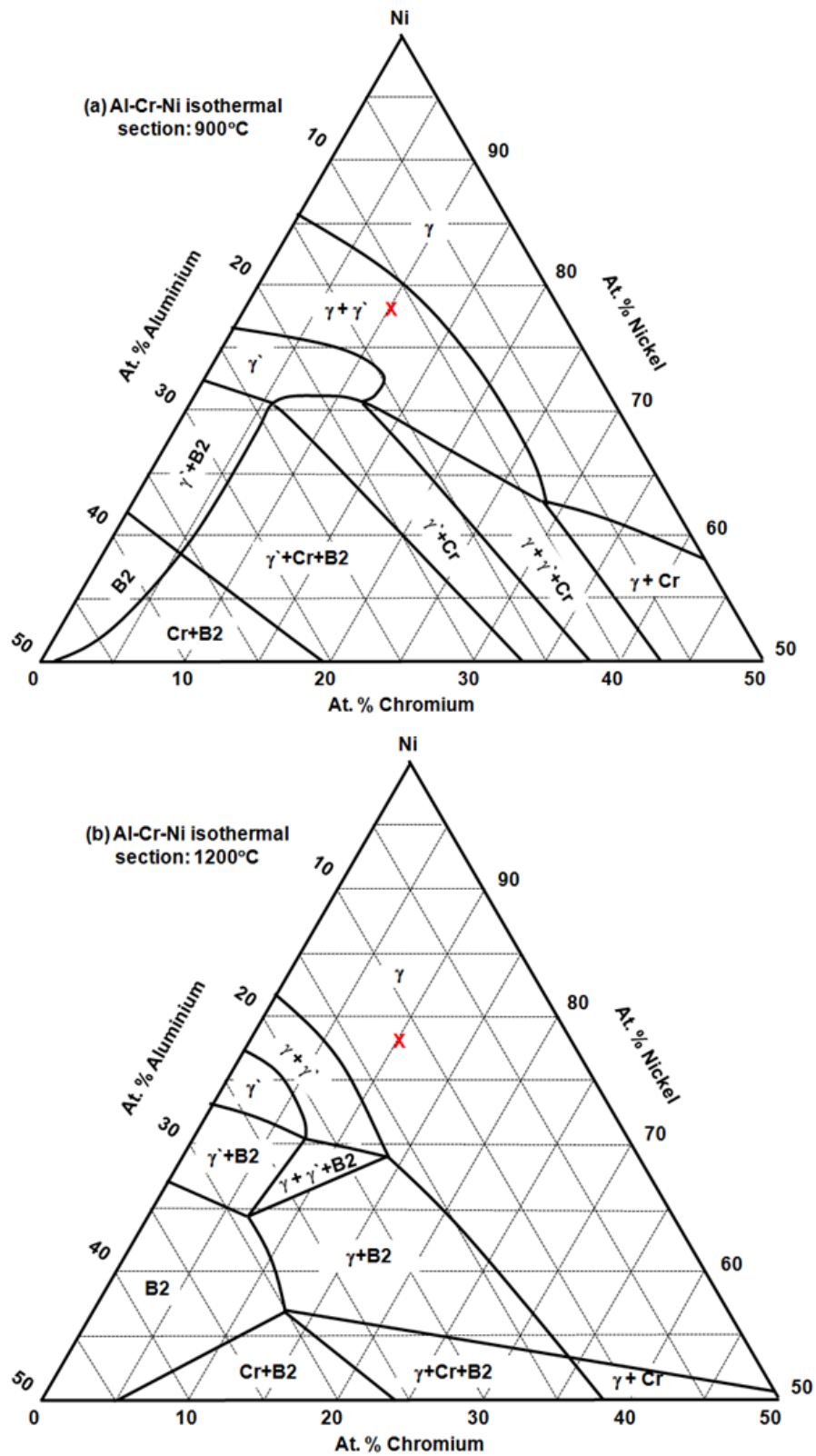


Figure 2.12: Isothermal sections of the ternary system Al-Cr-Ni. Showing section at (a) 900°C and (b) 1200°C. Data adapted from work published by Raghavan [19].

Heat treatments in practice do not produce the perfect idealised results as might be expected from examination of phase diagrams; one of these ‘imperfections’ is the occurrence of secondary γ' . During the quenching following heat treatment, the cooling rate may not be fast enough to hold the γ' phase fully in solution and very fine secondary γ' may be precipitated. This can remain in the γ matrix channels between the larger primary γ' precipitates and has been observed by several researchers including Kakehi [16] and Liao *et al.* [20] as shown in Figure 2.13.

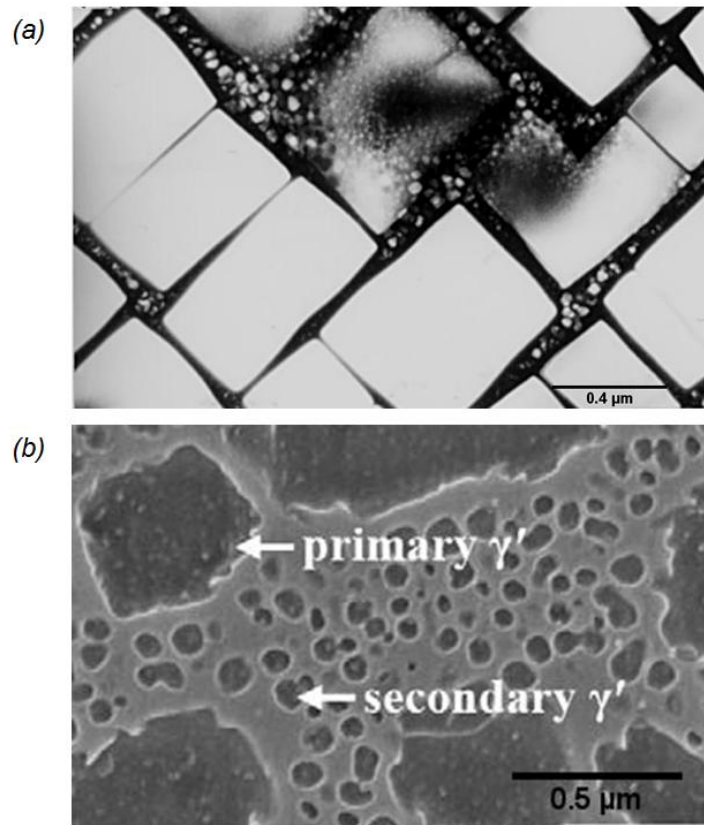


Figure 2.13: SEM Micrographs showing very fine secondary γ' precipitates within the γ matrix channels as presented by (a) Kakehi [16] and (b) Liao *et al.* [20] in Mar-M247.

Liao *et al.* [20] suggests that the secondary γ' precipitate size is too small to provide any real resistance to the dislocations and therefore adds little in terms of creep strength. Conversely, the research by Kakehi [16] shows that the occurrence of secondary γ' within the γ matrix

channels can have a large impact on the creep strength of the material due to the net reduction in channel width for dislocation passage. Additionally, research presented by Kim et al. [5] suggests that fine secondary γ' has a positive influence on the low temperature tensile deformation on CM247LC.

Traditional texts acknowledge the existence of secondary γ' , but its full influence is not understood and furthermore due to its fine nature it can make determining the γ' volume fraction by microscopy problematic.

Many practical heat treatments have been developed within industry which consist of a solution and two-stage ageing treatment. Anecdotal reasoning for this two-stage approach, as in Donachie [2], states that the 2nd stage may further increase γ' precipitate size or further refine grain-boundary carbide formations, however actual evidence supporting these claims is difficult to find. Additionally the lower temperature heat treatment may reduce the occurrence of secondary γ' within the γ matrix channels as shown by Kakehi [16] in the research regarding heat treatment cooling rates within a nickel base superalloy.

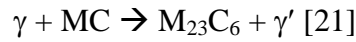
2.3. The Role of Carbides

Carbides play an important role within polycrystalline nickel-base superalloys and can perform three specific functions:

- Grain-boundary carbides (when properly formed) can strengthen grain boundaries by preventing or impeding grain-boundary sliding.
- Carbides can ‘tie-up’ detrimental elements within the alloy.
- Fine carbides precipitated within the matrix can potentially have strengthening effects, although this is most important in cobalt-base alloys.

Typically carbides form at high temperatures in the form of MC carbides (where ‘M’ represents any number of metals depending on the composition) with $M_{23}C_6$ and M_6C being formed at lower temperatures under ageing or in service conditions [2].

Some of the fundamental understanding of the structure of carbides within nickel-base superalloys is presented by Sims [21] who states that the larger MC carbides break down into ‘blocky’ (or particulate) $M_{23}C_6$ carbides at the grain boundaries via the movement of metal atoms from the carbide to the γ phase by the following reaction:



This leaves the carbides typically surrounded by a layer of grain boundary γ' as shown schematically in Figure 2.14 and as a micrograph illustrating both typical MC and $M_{23}C_6$ carbide formations presented by Bor *et al.* [22] in Figure 2.15.

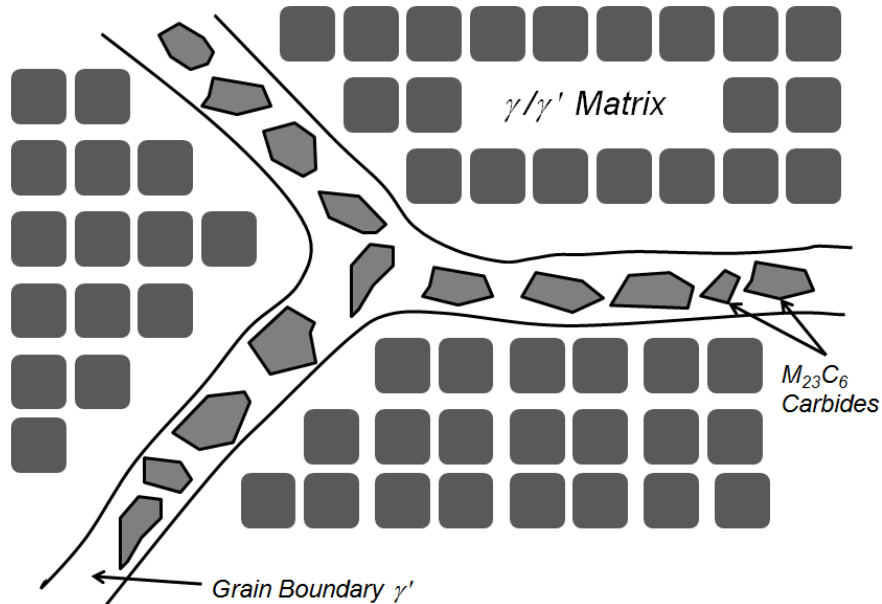


Figure 2.14: Diagram showing a typical grain boundary carbide structure; adapted from Sims [21].

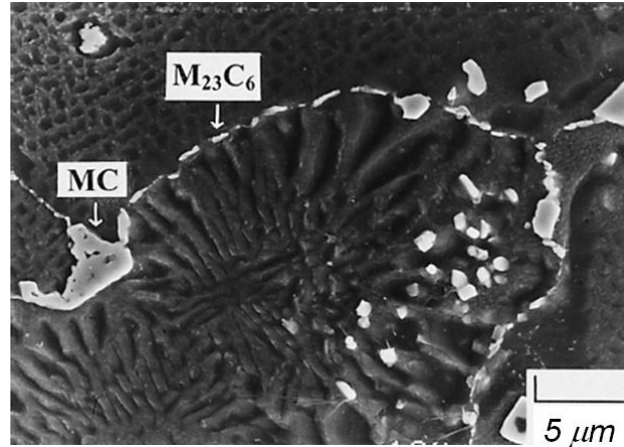


Figure 2.15: Micrograph showing typical carbides structure within MAR-M247 (heat treated) with MC and M₂₃C₆ carbides labelled [22].

Sims goes on to state that the particulate grain boundary carbides may improve material properties by inhibiting grain boundary sliding, however other formations of carbides may significantly harm both low and high temperature ductility. M₂₃C₆ carbides ultimately provide common sites for crack and rupture initiation points when the material fails [21].

The research presented by Doherty *et al.* [23] suggests that the grain boundary carbides not only act to prevent sliding, but the associated surrounding γ' regions (as seen in Figure 2.14) also allow for plastic accommodation to the localised stress concentrations surrounding the carbides. This is supported by the research presented by Bor *et al.* [24] examining the effect of a double ageing treatment on the alloy MAR-M247, which shows that the thickening of this localised γ' region could be a factor in the improved elongation performance of the material.

The role of carbides as crack initiation points is heavily documented notably in the research by Engler-Pinto *et al.* [25] on creep and thermo-mechanical fatigue, however it is the suggestion by Doherty *et al.* [23] that it is the ‘thin-film’ carbides formations which are most detrimental in terms of crack initiation and propagation (supported by the results presented by

Kaufman [26] regarding fatigue of MAR-M247 and those presented by Bor *et al.* [24] regarding creep of MAR-M247) which is of particular importance. These films of carbides are later referred to as script-like or ‘Chinese-script’ carbides.

Due to the role of carbide morphology, there have been several studies into the effect of the addition of various elements into an alloy in order to refine the carbide structure. Research presented by Kotval *et al.* [27] examines the influence of hafnium additions into a nickel-base superalloy (713-LC) and shows that 1.5% (wt.) additions of Hf can improve room-temperature ductility from 3-5% upto 12-15%. This is attributed to the Hf additions reducing the occurrence of the script-like carbides and promoting particulate carbide morphology.

The research presented by Bor *et al.* [22, 28, 29] examining the influence of Mg on the formation of carbides is also significant in showing the relationship between the lower occurrence of the script-like carbides (with increasing Mg additions) and an improvement to material ductility (Three times the elongation of MAR-M247 with 80 ppm Mg compared with un-doped MAR-M247 in creep at 1172K [28]). This transition between script-like to particulate morphology can be seen in the micrographs presented in Figure 2.16. A similar transition was observed by Nathal *et al.* [14] when examining the influence of cobalt on the microstructure of MAR-M247 (discussed further in section 2.4.i.).

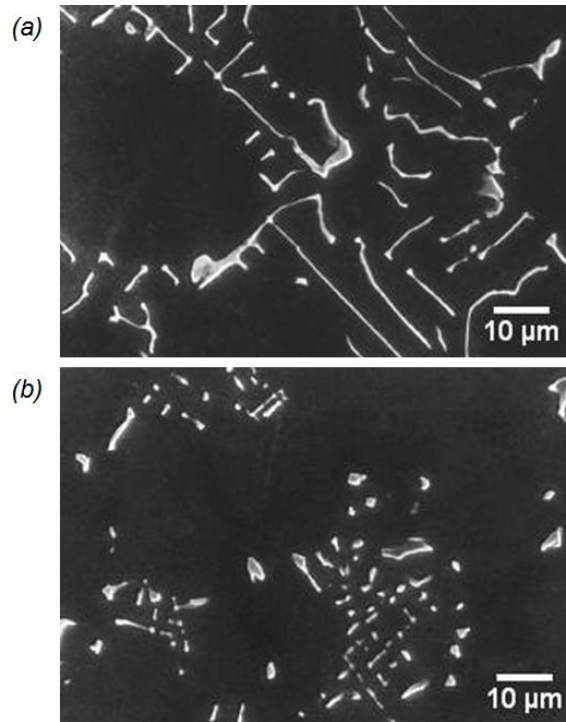


Figure 2.16: Micrographs showing script-like carbides occurring in (a) Mg-free MAR-M247 and (b) particular carbides occurring in 80ppm Mg MAR-M247 [28].

Bor *et al.* [28] states that not only does the improved carbide structure improve the rupture-life and elongation properties of the Mg-doped material, but also that the Mg is found at the carbide-matrix interface suggesting that it improves cohesion between the two phases and so reduces the influence of the carbide particle as a crack-initiation point.

2.4. Roles of the Specific Elements within a Nickel Superalloy

Thus far the structure of a nickel superalloy has been discussed in terms of the formation of the key phases and their roles within the alloy. This section will focus on the influence of the individual elements within the alloy, how they affect the formation of these phases and their influence on the mechanical properties.

A typical nickel superalloy may contain in excess of 10 constituent elements, each of which was added during the alloy design stage in order to fulfil a specific role or enhance a certain

material property. The text by Donachie [2] gives a simple overview to the role of each common element as shown in Figure 2.17.

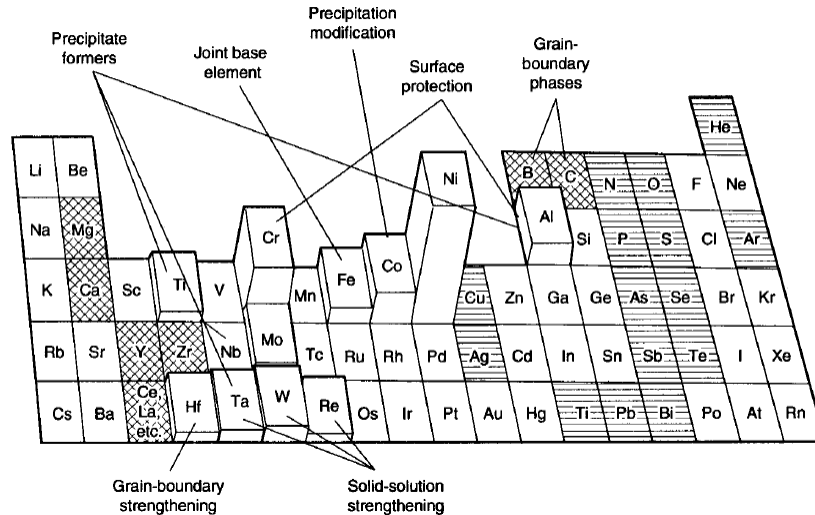


Figure 2.17: An overview of the role of each of the key elements within a typical nickel superalloy. Hatched elements denote minor beneficial elements whilst horizontally shaded elements show detrimental elements [2].

i. The Role of Cobalt (Co)

Cobalt plays a role both in shaping the morphology of the carbides present and the γ/γ' structure. The role of cobalt within nickel-base superalloys was the subject of some interest in the early 1980's. Tien *et al.* published a report examining its availability and role within the alloys based on the data available at that time [30]. The cobalt supply was primarily from politically unstable countries and was predicted to run out early in the next century. This instability coupled with growing demand from the aerospace industry prompted study into the exact role of cobalt and the possibility of substituting another element to perform the same role; this influence is also reported by Mackay & Nathal [4] in a review paper.

Research presented by Nathal *et al.* [14] initially looks at the influence of cobalt on the microstructure of MAR-M247. The study used Ni to substitute the Co content of standard MAR-M247 and examination was carried out on 0 wt.%, 5 wt.% and the standard 10 wt.% Co

versions of the alloy. The influence of the Co content on the carbide structure in commercially heat treated samples is shown clearly in Figure 2.18. The increase in Co from 0 wt.% to 10 wt.% shows a dramatic change from the script-like (thin-film) carbide morphology to the particulate type occurring at the grain boundaries. Additionally, the 10 wt.% Co prompted a reduction of approximately 1 wt.% of the overall carbides compared with the sample containing 0 wt.%. This change did not reflect any alteration of the composition or relative proportions of the two dominant carbide types: one rich in Ta and one rich in Hf.

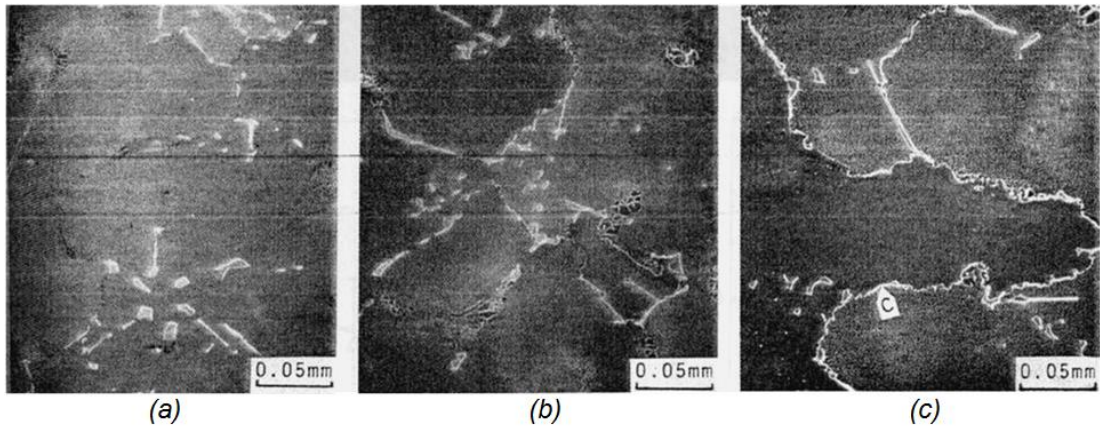


Figure 2.18: SEM showing carbide precipitates with varying Co levels: (a) 10 wt.% ; (b) 5 wt.% ; (c) 0 wt.% . Label 'C' showing the 'script-like' carbides Micrographs [14].
(Reproduced from hard-copy)

Figure 2.19 shows the reduction in γ' precipitate size (decrease from 0.8 μm to 0.6 μm) with increasing Co levels. There is an overall increase of γ' from 41 wt.% to 59 wt.% as the Co levels increase from 0 wt.% to 10 wt.%. The increase in Co also influenced the chemistry of the γ and γ' phases. W and Ti content of the γ' phase decreased from 8 wt.% \rightarrow 5 wt.% and 3 wt.% \rightarrow 2 wt.% respectively whilst Cr and Al content in the γ matrix increased from 13 wt.% \rightarrow 17 wt.% and 12 wt.% \rightarrow 15 wt.% respectively [14].

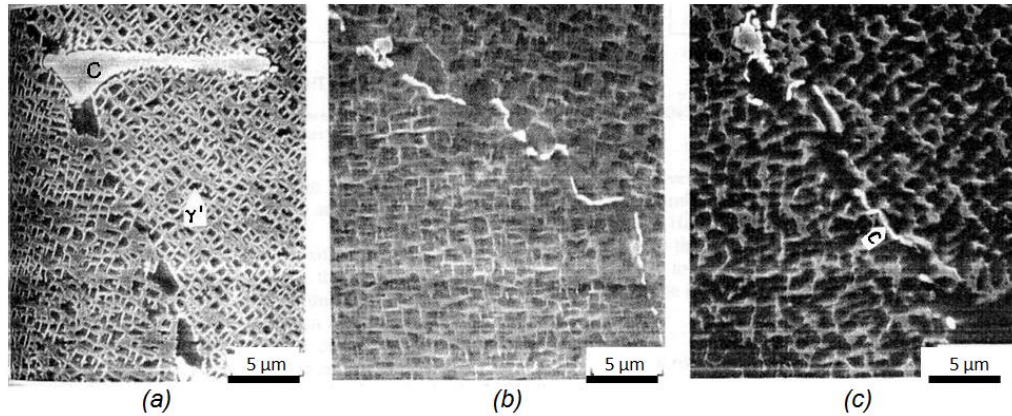


Figure 2.19: SEM showing the varying gamma' phase structure with different Co levels: (a) 10%; (b) 5%; (c) 0%. (wt.%) Label 'C' denotes carbides; Label ' γ' ' indicating the γ' structure [14]. (Reproduced from hard-copy)

In a companion paper, Nathal et al. [13] go on to discuss the influence of these microstructure changes to the overall mechanical properties demonstrated by the prepared samples. It is important to note that Co itself has very little direct impact on the mechanical properties; it is the influence of Co on the phases within the alloy that alters the mechanical properties.

To emphasise the point made in the previous paragraph, Nathal et al. [13] state that when considering the yield strength variation with changing Co level, it should first be noted that the Co addition results in a very small change to the lattice parameter of the γ/γ' phases and therefore Co acts as a weak solid solution hardener in this case. Figure 2.20 shows the variation of yield strength with temperature for the three different Co level samples. There is an approximately -80°C shift in the peak yield strength as the Co level is decreased from 10 wt.% to 0 wt.%. Nathal et al. [13] suggests that the decrease can be attributed to the increase in W and Ti levels in the γ' phase. W and Ti both act as solid solution hardeners (Rawlings & Staton-Bevan [31]) increasing the γ' strength at lower temperatures. However, this leads to a more rapidly attained critical resolved shear stress for primary cube slip which, once active, decreases the γ' strength as the temperature increases. Therefore as Co is added, the resulting reduction in W and Ti in the γ' phase increases the peak strength temperature.

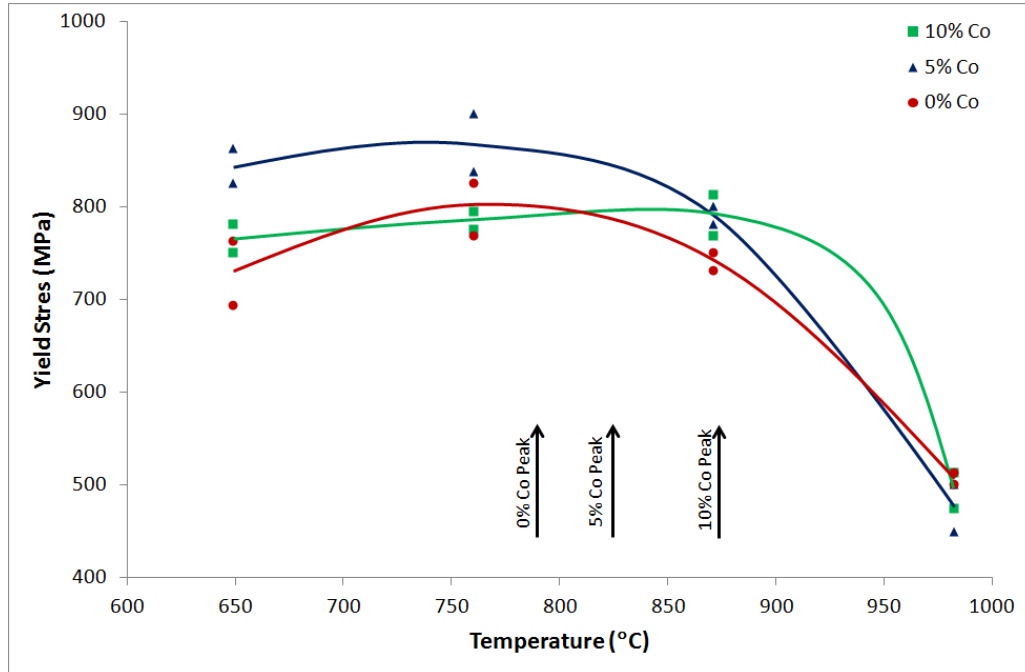


Figure 2.20: Plot (reconstructed from source) showing yield Strength as a function of Temperature for MAR-M247 samples containing varying wt.% Co; arrows indicate estimates of the peak strength for each alloy composition [13].

The research by Nathal *et al.* [13] also highlights an interesting result when examining the YS and UTS variation with Co for a single temperature (649°C) as shown in Figure 2.21 or the peak strengths as shown in Figure 2.20. The strength of the material does appear to increase overall between 0 wt.% and 10 wt.% Co however the peak strength lies around the 5% region. Nathal *et al.* propose that this peak strength is due to the change in γ' precipitate size caused by the Co addition (from 0.8 μm \rightarrow 0.6 μm mean size with increasing Co from 0 wt% to 10 wt.% and that the peak lies at the transition between dislocation cutting and looping. The γ' particle size would suggest this peak is secondary to that caused by the transition between strongly and weakly coupled dislocations (See Reppich [8, 9]) as discussed previously in Section 2.2.

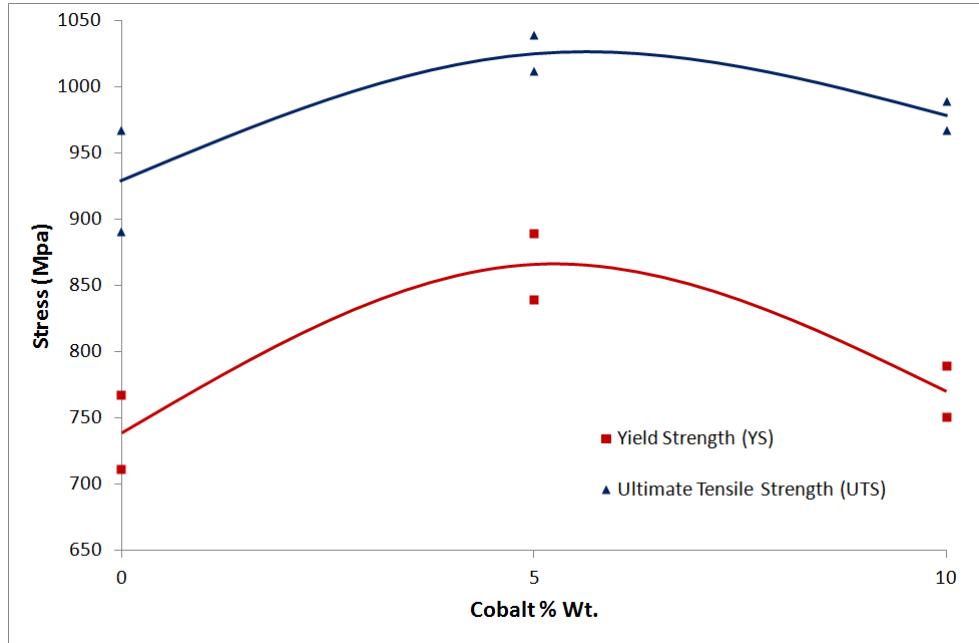


Figure 2.21: Plot. (reconstructed from source) showing Ultimate Tensile Strength (UTS) and Yield Strength (YS) for MAR-M247 samples at 649°C with varying levels of Co [13].

Nathal *et al.* [13] also shows the influence of cobalt on the creep life of MAR-M247 as presented in Figure 2.22. It can clearly be seen that Co has a positive effect on the creep life of the material; however this is once again an indirect influence of the addition. Nathal *et al.* suggest that it is most likely a combination of the reduction in γ' precipitate size and the transition of the grain boundary carbides to a particulate form therefore reducing their ability to act as rupture initiation points whilst inhibiting grain boundary sliding as discussed previously.

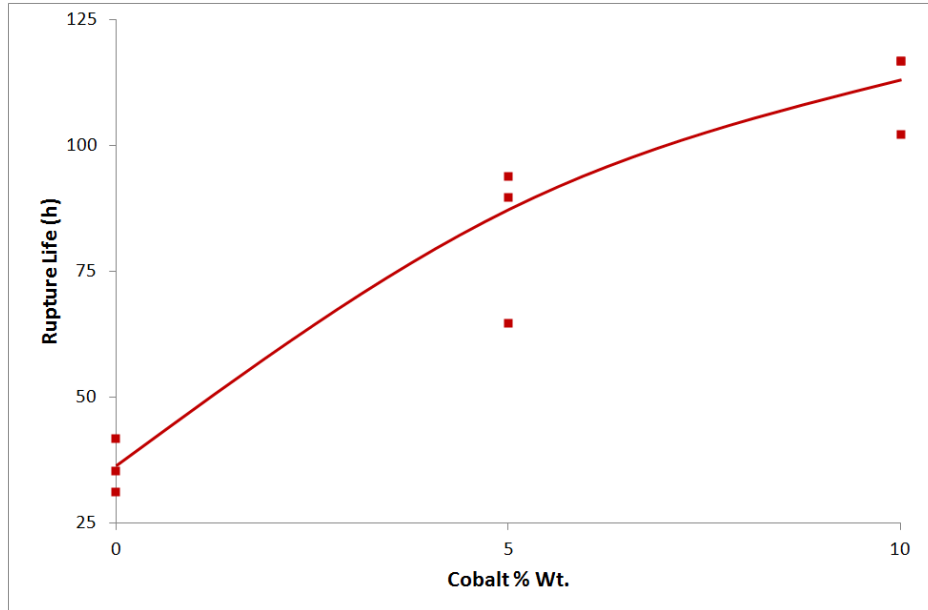


Figure 2.22: Plot (*reconstructed from source*) showing creep rupture life at 871°C, 414MPa with varying %wt. Co [13].

ii. The Roles of Chromium (Cr), Molybdenum (Mo), Titanium (Ti) and Aluminium (Al) in Corrosion Resistance

Traditional literature [2, 15] states that although most nickel superalloys contain chromium, its primary role depends on composition. In the case of precipitate hardenable nickel-base superalloys Cr addition is primarily to provide hot-corrosion resistance achieved by the formation of a protective oxide coating (Cr_2O_3) on the surface preventing the reaction between nickel and sulphurous gases (Sims [21]). Cr also acts as a solid-solution strengthener, however this is considered as a secondary effect in superalloys with low Cr content (between 6 wt.% and 22 wt.%; CM247LC contains 8 wt.% Cr [32]). Cr also acts as an MC carbide forming element [2].

Several researchers [3, 33-36] report the development of a ‘layered’ surface structure due to these oxides. This is most clearly described in the research presented by Gordon *et al.* [35] who state that both Al and Cr oxides form on the exposed surfaces. A layer of Al_2O_3 forms by the diffusion of Al from the γ' precipitates near the surface; this results in a layer of

γ' -depleted material below the oxide. Cr is transported through the layer of Al_2O_3 via diffusion forming an external layer of Cr_2O_3 (TiO_2 may also form depending on alloy composition). The micrograph in Figure 2.23 shows these surface layers; the research by Gordon *et al.* [35] supports this microstructural evidence with EDX data showing the presence of elements in each layer.

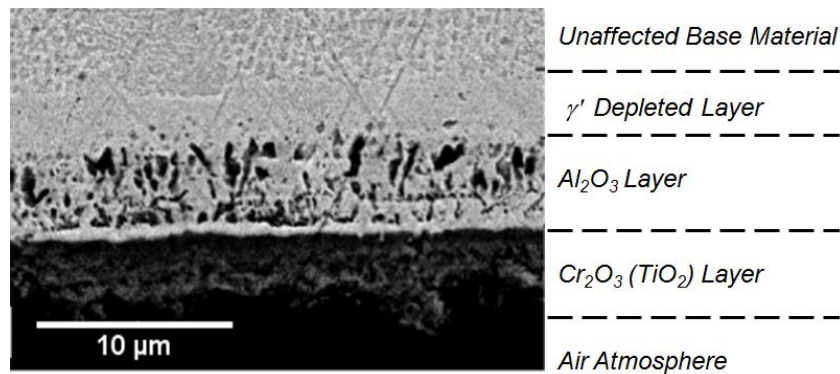


Figure 2.23: SEM Micrograph showing the surface oxide layers and γ' depleted layer formed on DS GTD-111 resulting from atmospheric exposure at high temperature [35].

The influence of this surface oxide layer however is not straightforward and is the subject of some debate depending on how it is evaluated. Research on the fatigue properties of Ni-superalloys has shown that oxides act as crack initiation points (Antolovich *et al.* [37]) and in the research regarding fatigue of MAR-M247 by Boismier & Sehitoglu [33] it is stated that the oxide and γ' -depleted layer form a region of weaker material ahead of the advancing crack tip during fatigue failure. In a companion paper, Boismier & Sehitoglu [34], continue to state that additional material damage may occur due to the differing thermal expansion coefficients of the layers under thermal cycling. This is not straightforward however as the research presented by Coffin [38] suggests that ‘crack blunting’ caused by the formation of the oxides at the crack tip may reduce the localised stresses and actually improve fatigue performance under low-frequency fatigue; this is supported by a similar suggestion of Donachie & Sullivan ([3] - Section VIII).

The final point to note with regards to the oxide layer is presented by Pandey *et al.* [36] which examines the effect of the heat treatment atmosphere on the surface layer formation and the creep performance of the material. The research shows that the samples heat treated in air show a better creep life performance than those in a reduced pressure atmosphere. This was attributed to the formation of an oxide layer during heat treatment preventing further oxygen ingress and so limiting oxide damage during creep testing.

Small amounts of molybdenum are typically included in nickel-base superalloys to provide wet corrosion resistance and also to act as a solid solution strengthener [2]. Titanium can substitute for Aluminium in the γ' phase strengthening as a function of atomic misfit parameter [31], however in small amounts within nickel-base superalloys it is included to provide hot corrosion resistance and remove nitrogen by the formation of TiN [2, 15].

iii. The Role of Tantalum (Ta)

The influence of tantalum within a nickel-base superalloy system has been detailed in two key pieces of research; that presented by Janowski *et al.* [39] and the more complicated study carried out by Nathal & Ebert [40, 41] which also investigated the influence of cobalt and tungsten.

There are two key influences of tantalum within the alloy; the first is the changes to the carbide composition. This is documented in the research by Janowski *et al.* [39] and shows that Ta can substitute for Hf within the carbides. Figure 2.24 shows the variation of Ta and Hf in the extracted carbides from the heat treated MAR-M247 with increasing additions of Ta to the alloy.

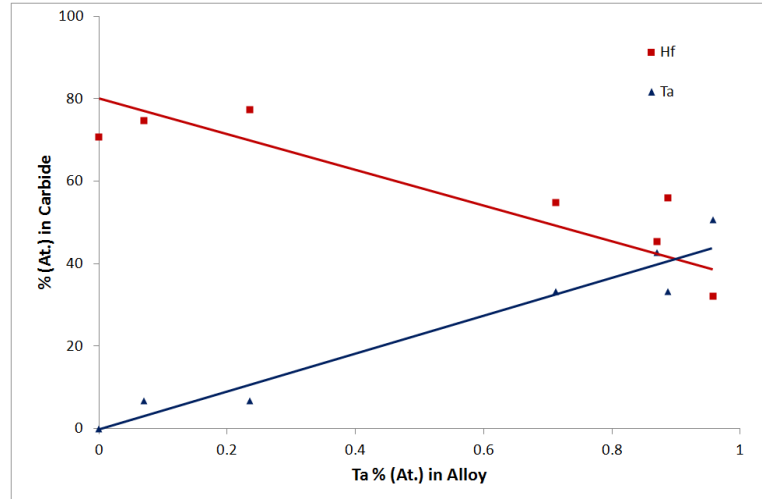


Figure 2.24: Plot (reconstructed from source) showing the variation of Ta and Hf within the extracted carbides of heat treated cast MAR-M247 with varying wt.% Ta in the alloy [39].

Janowski *et al.* [39] go further to show that Ta-containing carbides are not as stable as Hf carbides. Figure 2.25 shows the variation of Ta/Hf ratio in the carbides with Ta/Hf in the alloy. The >1 gradient of the line in the as-cast state shows that initially Ta is a stronger carbide former than Hf, however following heat treatment this gradient is significantly reduced. Janowski *et al.* [39] suggest that it is the greater thermodynamic stability of Hf-rich carbides compared with the Ta-rich carbides which is the cause of this effect.

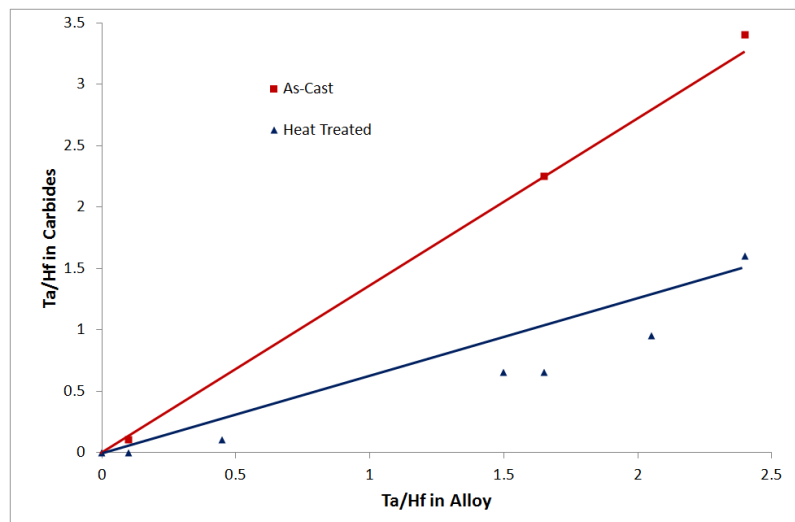


Figure 2.25: Plot (reconstructed from source) showing the variation of Ta/Hf within the carbides compared with Ta/Hf in the alloy both before as-cast and following heat treatment [39].

The second and more significant effect is that of the influence of Ta on the γ' phase. The research by Janowski *et al.* [39] reports that Ta not only has an affinity to the γ' phase, but also encourages precipitation of the γ' phase. It is reported that a 1 wt.% addition of Ta results in a 2 wt.% increase in the γ' phase and corresponding decrease in the γ phase. This reduction is confirmed by Nathal & Ebert [40] who report that reducing Ta in MAR-M247 from standard composition, 2.8 wt.% to 0 wt.% resulted in a 6% reduction in γ' volume-fraction. Nathal & Ebert [40] also use differential thermal analysis to show that Ta removal from MAR-M247 reduces the γ' solvus temperature and also reduces the lattice misfit significantly (although due to the experimental details it is difficult to attribute it entirely to the Ta removal).

The companion paper presented by Nathal & Ebert [41] examining the influence of Ta, Co and W on the elevated temperature mechanical properties of MAR-M247 shows that the creep performance is significantly reduced by the removal of Ta (as above it is difficult to attribute values to this due to the experimental details). This reduction is linked to the microstructural changes and is attributed to the change in γ' fraction, lattice misfit and possibly solution hardening of the γ' phase by Ta. The suggestion of solution hardening of the γ' phase by tantalum is also supported by the research presented by Chakravorty & West [42] as the reason for improved high temperature tensile/creep properties in their study of Ni-Al-Ta-Hf quaternary alloys, however the results here relate to overall mechanical properties and do not examine the microstructural influence of these different compositions.

iv. The Role of Tungsten (W)

The influence of tungsten is more straightforward than that of Ta and can be succinctly categorised as a solid solution strengthener [2]. Early research presented by Rawlings &

Staton-Bevan [31] showed that tungsten preferentially segregates to the γ' phase, however it can substitute for both Ni and Al in the f.c.c. structure. The research concludes that the strengthening occurs due to the substitution with Al and the resulting impact on the lattice misfit parameter.

Later research presented by Nathal & Ebert [40] verified this result by showing a larger lattice misfit of W-containing alloys. Additionally it was found that the removal of W lowered the γ' solvus temperature which would have an impact on the high-temperature performance of the material. Finally, in a companion paper, Nathal & Ebert [41] examining the mechanical property implications of these composition changes, it is shown that the W improves creep resistance and is concluded that this is due to the increased lattice misfit parameter.

v. The Role of Hafnium (Hf)

In general terms hafnium's role within nickel base superalloys is that of a grain boundary refiner [2]. In addition to this, it is also considered important in reducing the susceptibility to cracking in thin-walled investment castings [43].

The research presented by Heck *et al.* [43] showed that CM247LC (containing 1.4 wt.% Hf) showed no cracking in contrast to the high levels of cracking in IN792 (containing 0.5% wt. Hf) during the casting of a thin walled cylinder. Hf additions to the base IN792 material showed a distinct reduction in cracking susceptibility when considered in categories defined by crack length. Based on microstructural evidence, the authors suggest that the cracking mechanism is that of hot tearing initiating the crack during solidification followed by cold cracking propagating along grain boundaries.

Heck *et al.* [43] suggest that it is the improvements to the tensile properties (due to the addition of Hf) of the alloy which are responsible for its ability to resist cracking under the

solidification stresses. Research investigating the mechanical properties of Hf-enriched MAR-M200 presented by Duhl & Sullivan [44] supports this conclusion. Table 2.2 shows creep results of DS cast bars of MAR-M200 both with and without Hf additions loaded transverse to the direction of grain elongation. In all cases, there is a marked improvement in the Hf-containing alloy suggesting greater grain boundary cohesion due to Hf. Duhl & Sullivan [44] also presented tensile data showing a similar trend in the transverse direction and also that the mechanical properties in the longitudinal direction seem to be largely unaffected by the Hf addition, again supporting the suggestion that Hf improves grain boundary strength rather than the overall material strength.

Table 2.2: Data (*Units converted from source*) showing the influence of 2 wt.% Hf addition on the creep properties of MAR-M200 [44].

Temperature (°C)	Stress (MPa)	Rupture life (h)		Elongation (%)	
		2wt.% Hf	No Hf	2wt.% Hf	No Hf
760	586	780	0.3	4.2	0.8
760	690	170	Failed on Load	5.3	0.1
871	414	120	15	9.8	1.6
982	172	125	75	7.6	1.9

The improvements to creep performance with Hf addition is confirmed by the mechanical testing results presented by Chakravorty & West [42]. They show that the creep resistance of the material increases with Hf addition.

Some of the fundamental research regarding the influence of Hf on the microstructure of MAR-M200 is presented by Doherty *et al.* [23] which shows two distinct microstructural effects of Hf. Firstly there is a distinctive formation of ‘blocky γ' ’ at the grain boundaries in the as-cast material; this is potentially due to segregation of Hf during solidification and its affinity to the γ' phase. The typical formation of ‘blocky γ' ’ can be seen in Figure 2.26.

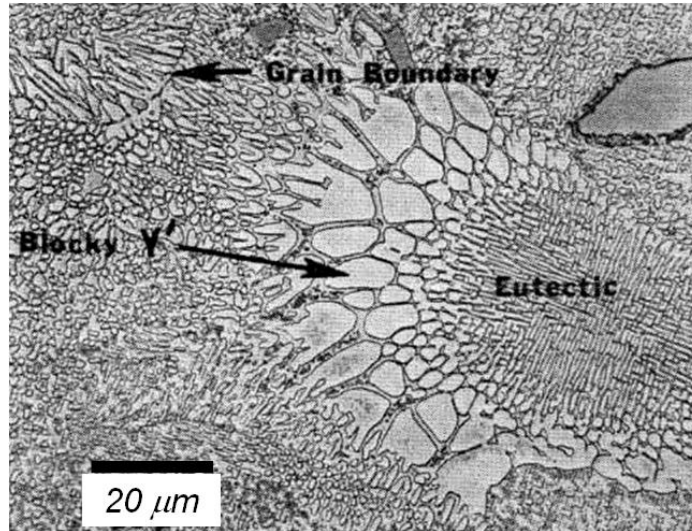


Figure 2.26: Micrograph showing the typical formation of ‘blocky γ' ’ with the addition of Hf to MAR-M200 [23]. (Reproduced from hard copy)

It is reported that the γ' lining the grain boundaries is responsible for the second observed change. The carbides appear to be more irregular, finer and less likely to form thin script-like films. Doherty *et al.* suggest that as Cr has an affinity for the γ phase, the γ' lining the grain boundaries reduces the available Cr for the formation of the Cr-rich $M_{23}C_6$ carbides. Doherty *et al.* [23] conclude that the enhanced properties due to Hf additions can be attributed to the solid solution strengthening of Hf within the ‘blocky γ' ’ (as supported by Chakravorty & West [42]) providing greater intergranular cohesion and accommodation of stress around the grain boundary carbides. Additionally, the smaller carbides due to the Hf addition provide less attractive crack initiation sites.

Supporting these suggestions is the research presented by Kotval *et al.* [27] which examines the influence of Hf addition on alloy 713-LC and draws the same conclusions (i.e. Script-like carbides broken into particulate forms and γ' lining grain-boundaries). The one further point is the observation that the γ' forms at the grain boundaries in a dendritic-like structure resulting in convoluted grain-boundaries within the Hf-modified alloy compared with the unmodified

material. These interlocking γ' dendrites across the grain boundary are also believed to resist grain boundary sliding.

A secondary effect of Hf is that discussed by Doherty *et al.* [45] and shows that Hf additions can be useful to produce stable sulphides and so reduce the influence of embrittlement caused by sulphur in solid solution.

Finally, it should be noted that Hf can have detrimental effects such as reactivity with casting shells (producing inclusions), reducing the solution heat treatment window and freckle formation. Research presented by Rösler *et al.* [46] investigates the possibility of eliminating Hf in a castable corrosion-resistant nickel-base superalloy.

2.5. Detrimental Elements & Phases

Some elements and phases are particularly detrimental to the mechanical properties of nickel-base superalloys and will briefly be outlined.

Sulphur proves to be one of the most detrimental elements and its influence is concisely presented by Doherty *et al.* [45, 47]. The low solubility of S within the Ni matrix results in its segregation to the grain boundaries where it forms a low melting-point eutectic which provides a crack propagation route and poor intergranular cohesion. The impact of S contamination can be reduced if certain minor elements can produce stable sulphides (typically Hf or Zr) as previously discussed.

Other elements known to segregate, or to form brittle phases are as follows [2]:

- Silicon, Si
- Phosphorus, P
- Lead, Pb
- Bismuth, Bi
- Tellurium, Te
- Selenium, Se
- Silver, Ag

It should be noted that the property-sensitivity to these elements is not universal; research presented by Shekhar *et al.* [48] shows that the properties of CM247LC are not as sensitive to minor additions of Fe, Mn, Si and Sn as previously believed.

In addition to these detrimental elements, it is possible for the formation of detrimental phases from the addition of the minor beneficial elements as follows [2]:

- μ phase – Rhombohedral in structure and generally formed by high levels of Molybdenum or Tungsten. $(Co_2W_6, (Fe, Co)_7(Mo, W)_6)$
- Laves phase – Hexagonal in structure, not generally found in Ni-base superalloys, formed after extended high temperature exposure. $(Fe_2Nb, Fe_2Ti, Fe_2Mo, Co_2Ta, Co_2Ti)$
- σ phase – Tetragonal in structure, not commonly found in Ni-base superalloys, formed after extended exposure between 540°C and 980°C. $(FeCr, FeCrMo, CrFeMoNi, CrCo, CrNiMo)$

2.6. Specific Metallurgy and Properties of CM247LC

The nickel base superalloy CM247LC is the primary focus of the work presented within this thesis. The alloy composition is as listed in Table 2.3:

Table 2.3: Nominal composition of CM247LC (wt.%) [32]

C	Cr	Ni	Co	Mo	W	Ta
0.07	8	Bal.	9	0.5	10	3.2
Ti	Al	B	Zr	Hf	Si[49]	S[49]
0.7	5.6	0.015	0.01	1.4	0.03 (Max)	15 ppm (Max)
Density (g/cm³)		M.P. Range (°C)				
8.54		1310 - 1375				

CM247LC was developed in the 1970's and is a derivative of the more commonly used MAR-M247 with minor chemistry changes originally implemented to tailor the alloy to Directionally Solidified (DS) casting application. The general structure follows that as outlined in the previous sections consisting of a γ matrix hardenable by the precipitation of the coherent γ' phase with discrete particulate carbides acting as grain boundary strengtheners. The key differences between the old MAR-M247 and the modified CM247LC are presented by Harris *et al.* [49].

Tighter controls were imposed on the detrimental elements Si and S when compared with MAR-M247 (0.1 wt.% Max \rightarrow 0.03 wt.% Max and 150ppm \rightarrow 15ppm respectively); this reduced the tendency for grain boundary cracking. Zr and Ti were lowered (0.03 wt.% \rightarrow 0.01 wt.% and 1 wt.% \rightarrow 0.7 wt.% respectively) to reduce its segregation to the grain boundaries and to accommodate for the tighter S controls.

The 'LC' (low-carbon) denotes a reduction in carbon (0.15 wt.% \rightarrow 0.07 wt.%) which is to accommodate the reduction in grain boundaries in DS castings compared with equiaxed structures and also to reduce the formation of large carbides which act as weak point within the structure. The corresponding reductions in Ti, W and Mo accommodate the lower C and reduce the chance of the formation of σ phase.

Figure 2.27 shows data presented by Kim *et al.* [5] highlighting the influence of the casting technique and heat treatment on the tensile properties of cast CM247LC. The bars were cast

either conventionally (CC) or directionally (DS) and subjected either to an ageing only treatment (HTA: 871°C, 20h) or a full solution and ageing treatment (HTSA: Solution, 1260 °C, 2h; 1st age, 1079 °C, 4h; 2nd age, 871 °C, 20h). The DS material shows improved UTS over the CC material and the full heat treatment (HTSA) shows an improvement over the aged only (HTA) condition as shown in Figure 2.27 (a). Figure 2.27 (b) also illustrates that the DS material displays greater high temperature ductility (tested longitudinally) compared with the CC material.

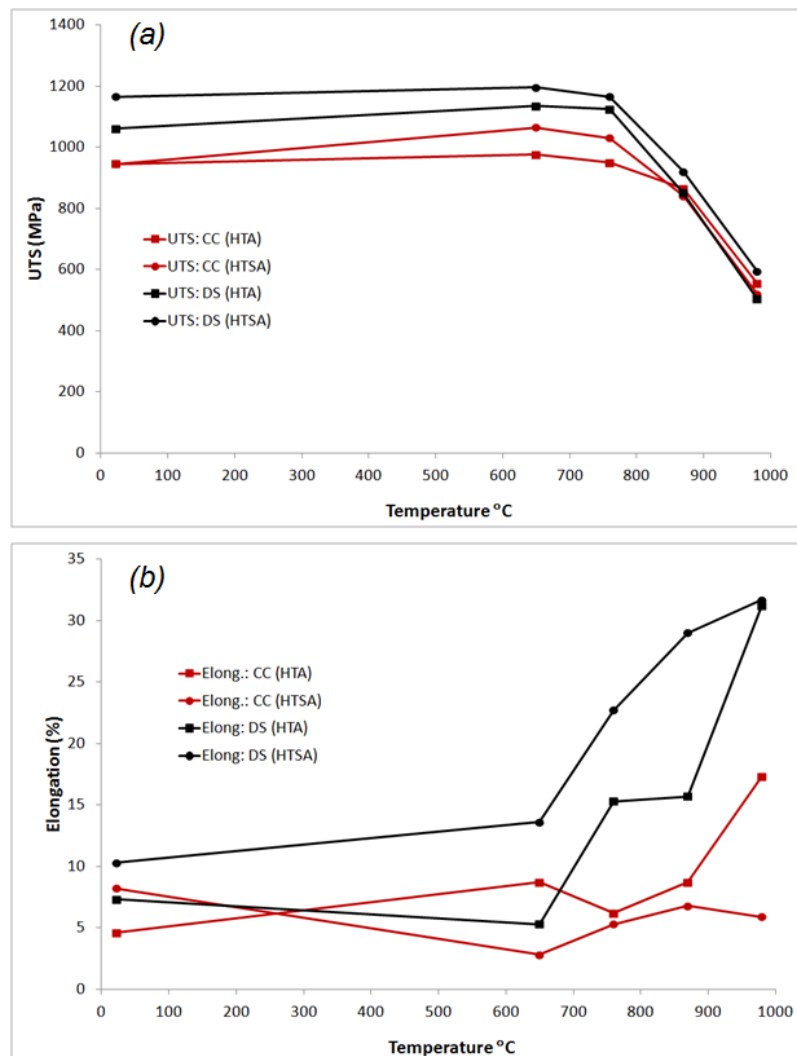


Figure 2.27: Data (Reconstructed from source) showing (a) the variation of UTS and (b) elongation with different casting and heat treatment techniques for CM247LC (CC: Conventionally Cast; DS: Directionally Solidified; HTA: Aged; HTSA: Solution Treated & Aged) [5].

Further tensile data for CM247LC is presented in a later paper by Kim *et al.* [50] based upon conventionally cast (equiaxed) material following a full heat treatment. Very early tensile data on DS cast but aged only CM247LC is presented by Harris *et al.* [49]. Figure 2.28 shows a comparison of these three data sources. The UTS of the material seems to be greatly improved by DS and full heat treatment; this is likely to be due to the improved high temperature ductility of this material as shown in Figure 2.28 (b).

Figure 2.29 shows some individual creep curves presented by (a) Maldini *et al.* [51] and (b) Satyanarayana *et al.* [52] for DS cast CM247LC. It should be noted that CM247LC shows mainly an extended tertiary creep regime in the curves showing data above 800°C and at lower temperatures displays a short region of primary creep preceding this, as is typical of Ni-base superalloys [1] .

Larson-Miller Parameter (LMP) plots are useful as they combine the time and temperature parameters allowing for direct comparison between sources. LMP is calculated by Equation 2:

$$\text{LMP} = T(20 + \log_{10}t) \quad - \text{Eq. 2}$$

$$T = \text{Temperature (K)}; t = \text{Time (h)}$$

Figure 2.30 shows LMP curves/data presented by various authors [2, 49, 51, 52] for DS cast and fully heat treated CM247LC; these appear to show good agreement with each other and provide a basis for literature comparisons. The heat treatments relating to each of the sources is presented in Table 2.4:

Table 2.4: Heat treatments applied to mechanical test samples for various sources.

Source	Heat Treatment
Kim <i>et al.</i> [5, 50]	1260°C, 2h; 1079°C, 4h; 871°C, 20h (unspecified cooling)
Harris <i>et al.</i> [49]	1250°C, 5h; 982°C, 4h; 871°C, 20h (unspecified cooling)
Maldini <i>et al.</i> [51]	1260°C, (unspecified time); 1079°C, 4h; 871°C, 20h (All Rapid Fan Quenched)
Satyanarayana <i>et al.</i> [52]	1260°C, 3h (Argon Quench); 1080°C, 4h (Argon Quench); 870°C, 20h
Donachie [2]	1232°C, 2h; 1260°C, 2h; 1079°C, 4h; 871°C, 20h (All Air cooled)

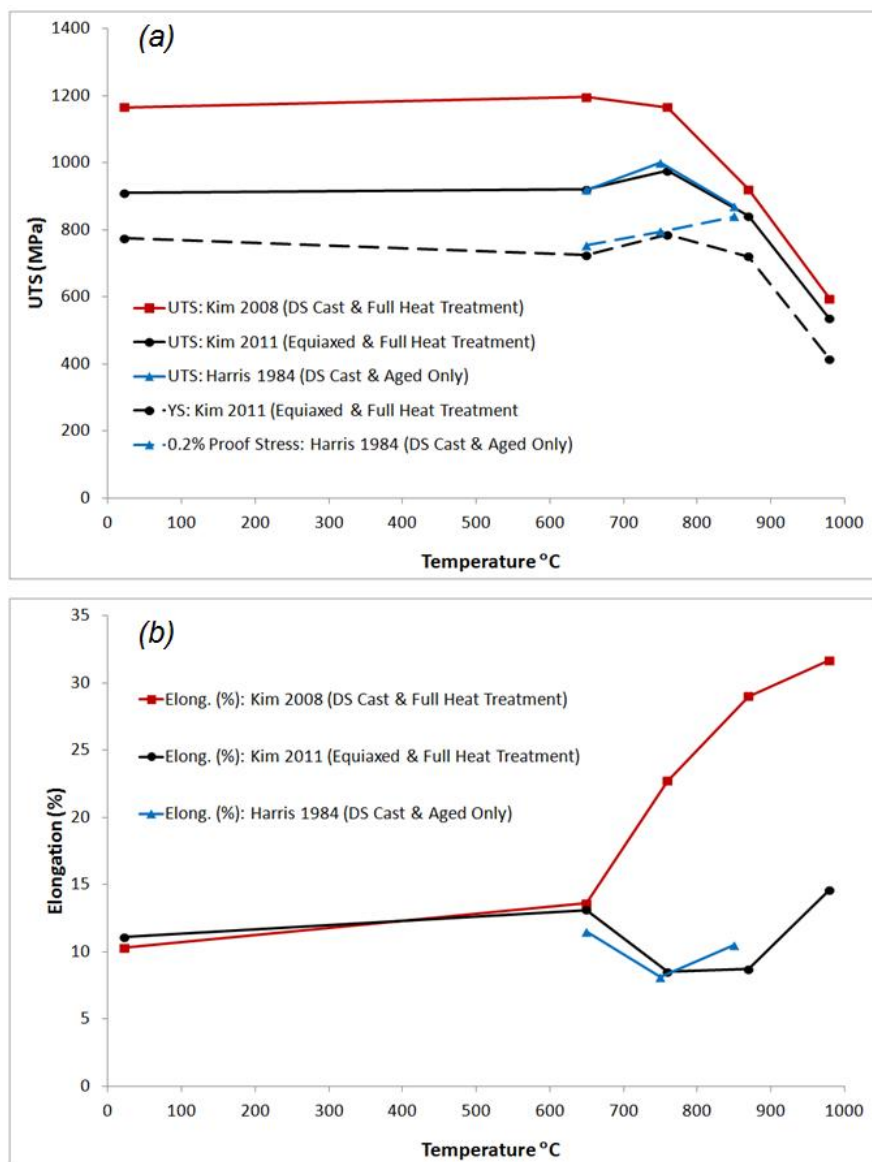


Figure 2.28: Compiled data presented by Kim (2008) [5], Kim (2011) [50] and Harris (1984) [49] showing (a) UTS/YS and (b) elongation (%) for CM247LC cast and heat treated using different methods.

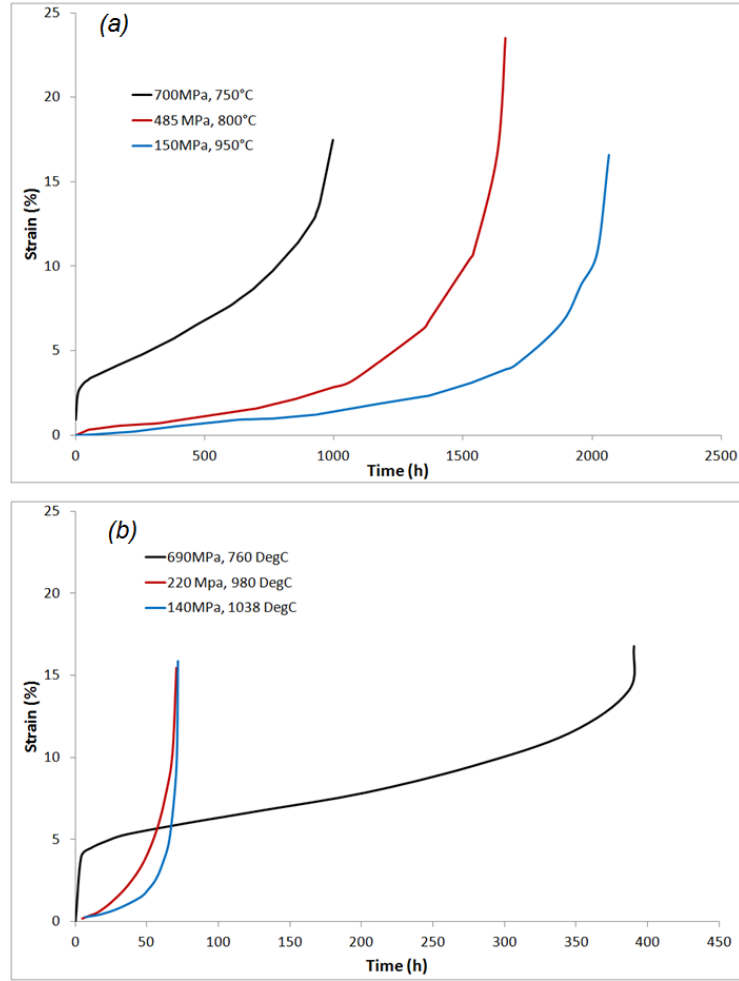


Figure 2.29: Creep data presented by (a) Maldini *et al.* [51] and (b) Satyanarayana *et al.* [52] (3mm test section) (Reconstructed from source) for DS cast and fully heat treated CM247LC

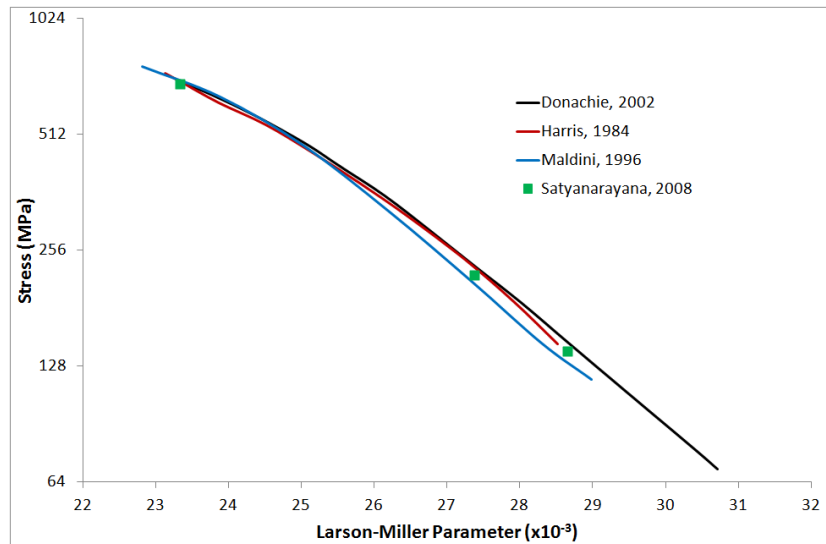


Figure 2.30: Larson-Miller Parameter data for DS cast and fully heat treated CM247LC compiled from curves presented by Donachie & Donachie [2], Harris *et al.* [49], Maldini *et al.* [51] and individual points based on the 3mm section creep tests presented by Satyanarayana *et al.* [52]. (Log scale on Y-axis)

2.7. Specific Metallurgy and Properties of CMSX486

The alloy CMSX486 is of secondary focus within this thesis. The composition is listed in Table 2.5 [53]:

Table 2.5: Nominal composition of CMSX486 (wt.%) [53]

C	Cr	Ni	Co	Mo	W	Ta
0.07	5	Bal.	9.3	0.7	8.6	4.5
Ti	Al	B	Zr	Hf	Re	
0.7	5.7	0.015	0.005	1.2	3	

Due to its unusual nature, there is relatively little published research on the alloy CMSX486. The alloy background, chemistry and creep data can be obtained from two papers presented by Harris & Wahl [53, 54]. CMSX-486 is a derivative of the widely used CMSX-4 which has been modified to contain grain boundary strengthening elements (C, B); this modification allowed for ‘single-crystal’ castings able to accommodate some higher angle grain boundaries (upto 9°-12° misorientation).

The chemistry of CMSX486 is very similar to CM247LC. The higher levels of Al and Ta encourage a greater γ' volume fraction and some W has been substituted for Rhenium (Re). Early research published on the addition of Re to a nickel-base superalloy is presented by Giamei & Anton [55] in 1985 and concludes that Re segregates to the γ matrix conferring addition strength through solid solution hardening. It is also shown that Re slows γ' coarsening at higher temperatures and so improves component life. The hardening effect of Re on the γ matrix is confirmed by nano-indentation in the research presented by Durst & Göken [56] examining three single crystal alloys with increasing Re levels (CMSX-6, CMSX-4 and CMSX-10). Finally, recent work by Liao *et al.* [20] shows that 3 wt.% Re addition to MAR-M247 can improve the UTS, YS and creep (150h \rightarrow 260h at 871°C 379MPa) significantly due to finer γ' precipitation and solid solution hardening of the γ matrix. A

typical as-cast microstructure for CMSX-486 is presented by Ola *et al.* [57] in Figure 2.31. A publication by Wilson *et al.* [58] suggests an appropriate heat treatment (1318°C, 2h, gas quenched; 1140°C, 6h, air cooled; 871°C, 20h, air cooled).

Creep curves of cast and heat treated CMSX486 are presented by Harris & Wahl [53], Figure 2.32, for temperatures 982°C, 1038°C and 1093°C. These are accompanied by a Larson-Miller plot (also presented by Harris & Wahl [54]) of cast and heat treated CMSX486 as show in Figure 2.33.

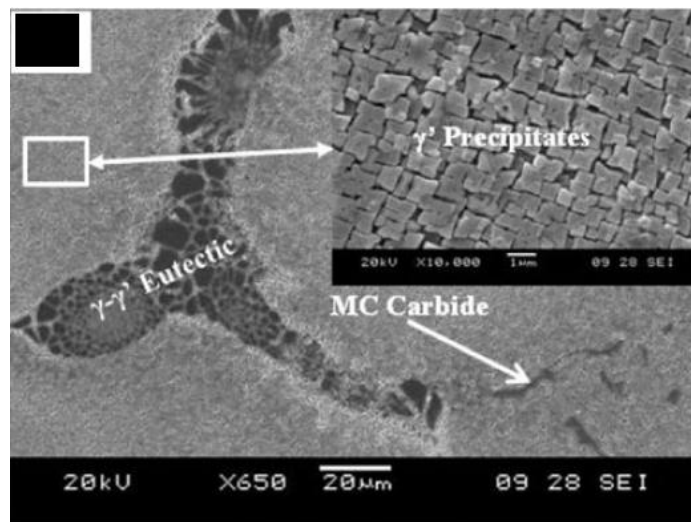


Figure 2.31: SEM Micrograph showing as-cast microstructure of CMSX-486. γ' precipitates, γ/γ' eutectic and carbides are labelled [57].

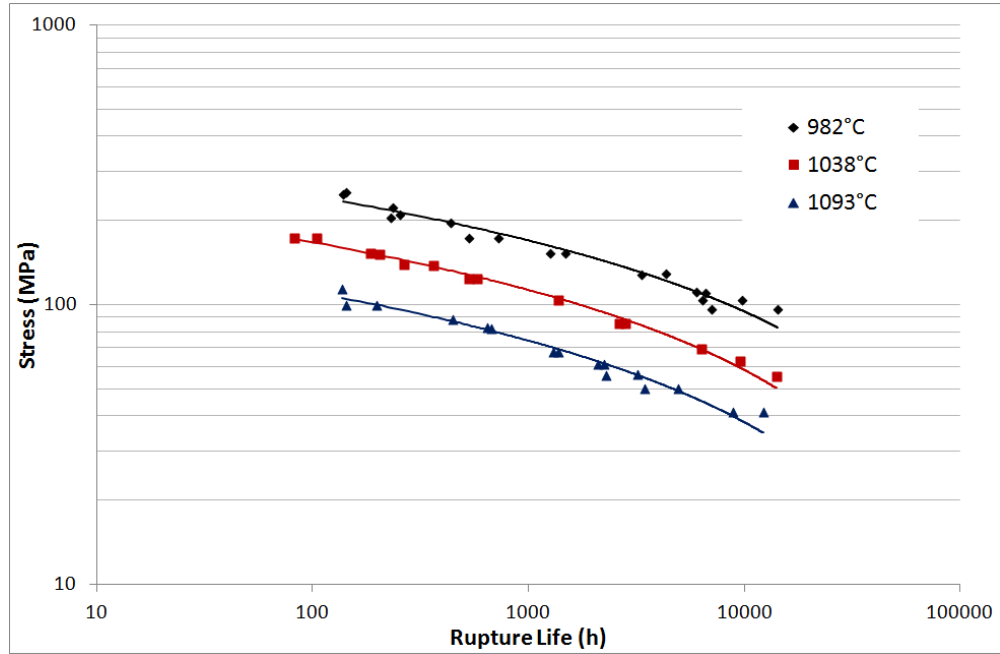


Figure 2.32: Data (*Reconstructed from source*) showing creep curves for fully heat treated CMSX-486 for different temperatures [53].

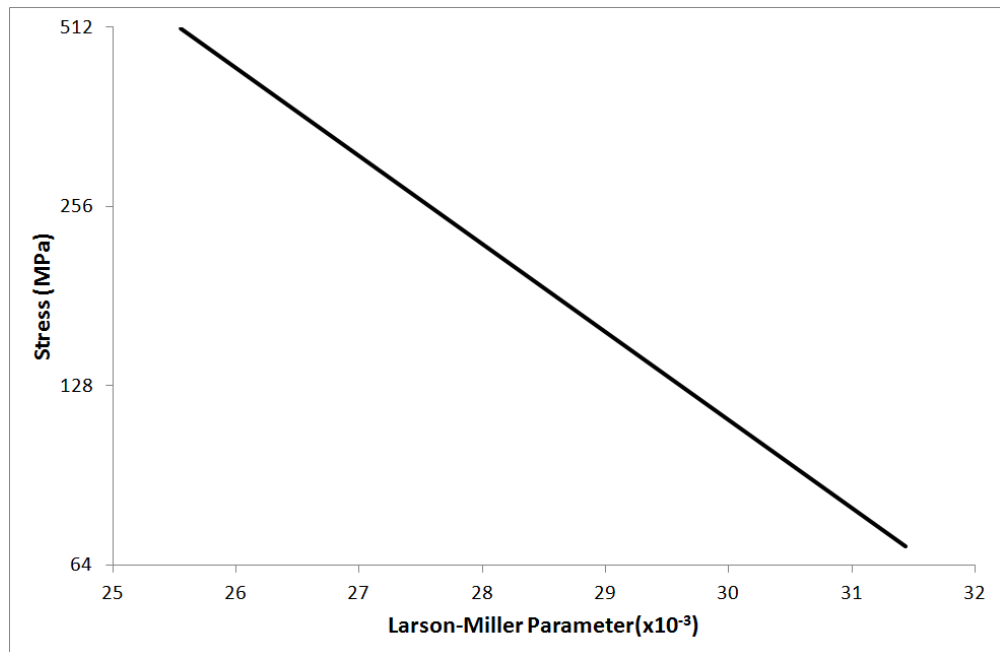


Figure 2.33: Data (*Reconstructed from source*) showing Larson-Miller relationship of cast and heat treated CMSX-486 [54]. (*log scale on Y-axis*)

2.8. Specific Metallurgy and Properties of IN625

IN625 is also a secondary focus of some of the research presented in this thesis. Its composition is listed in Table 2.6 [1]:

Table 2.6: Nominal composition of IN625 (wt.%) [1]

Cr	Mo	Nb	Al	Ti	Fe	C	Ni
21.5	9.0	3.6	0.2	0.2	2.5	0.05	Bal.

IN625 differs from CM247LC and CMSX-486 in that strength is obtained mainly through the solid-solution strengthening of the γ matrix through the elements C, Cr and Mo [59]. Typically there is no observed precipitation of the γ' rather precipitation hardening occurs through the precipitation of the body-centred tetragonal γ'' phase ($\text{Ni}_3(\text{Nb}, \text{Ti}, \text{Al})$) [59, 60]. This is precipitated as ellipsoidal particles as presented by Shankar *et al.* [59], Figure 2.34.

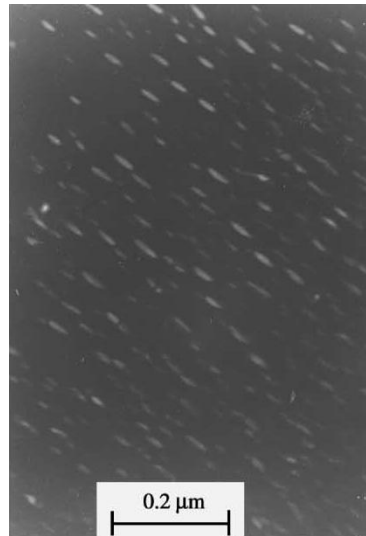


Figure 2.34: Dark-field TEM Micrograph showing ellipsoidal γ'' precipitates in IN625 [59].

The research presented by Shankar *et al.* [59, 60] concludes that in-service ageing can significantly improve the mechanical (creep) properties of IN625 through precipitation of the γ'' phase.

Tensile data for IN625 is presented in Figure 2.35 [2, 59]; the room temperature properties presented by Shankar *et al.* show similar yield strength to the Donachie data, but a much greater ductility.

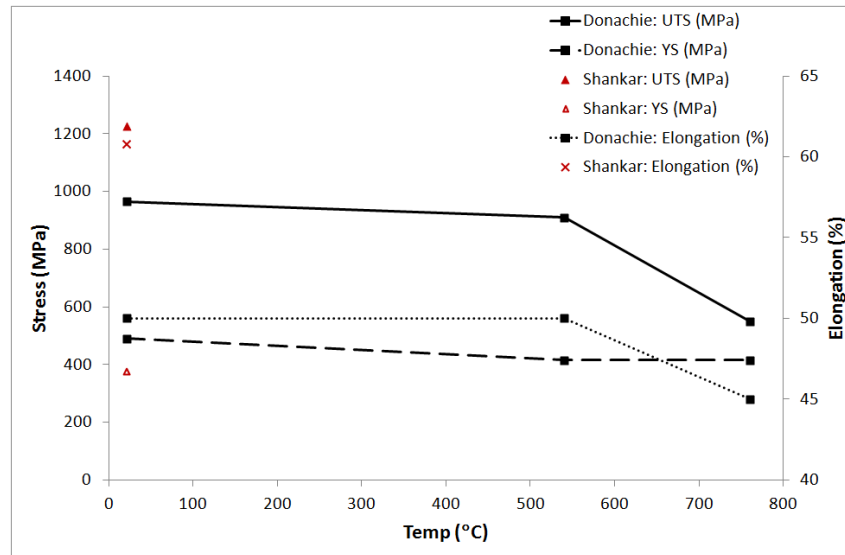


Figure 2.35: Tensile data collated as presented by Donachie [2] (wrought alloy data, no heat treatment provided) and Shankar et al. [59] (solution annealed condition: 1150°C, time not provided) for IN625.

A Larson-Miller plot for IN625 (collated from data presented by Donachie [2]) is presented in Figure 2.36.

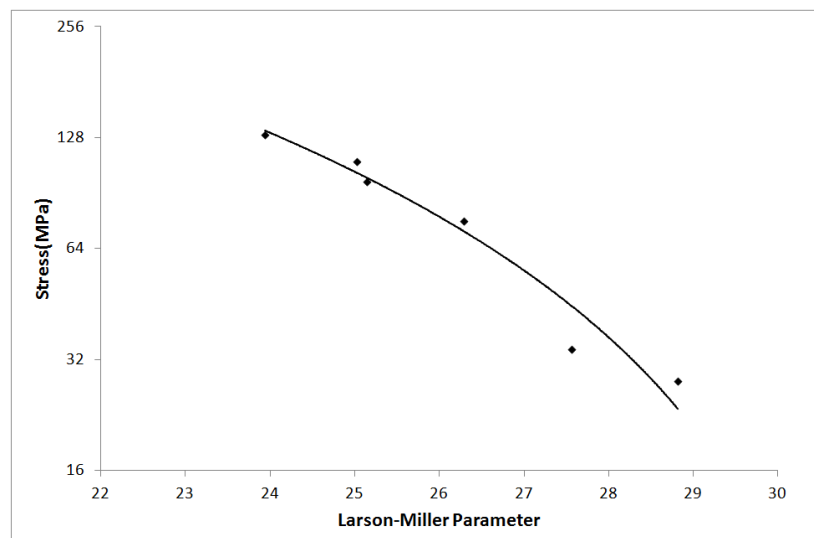


Figure 2.36: Data presented by Donachie [2] showing a Larson-Miller plot for IN625.

2.9. DSC of Nickel Superalloys

Differential Scanning Calorimetry (DSC) is a technique that uses the difference between energy change during heating of a material sample and reference sample pan. This technique can be used to calculate various energies and physical characteristics for the sample material; the technique is extensively documented in traditional texts [61].

Within nickel-base superalloy metallurgy one of the key uses of DSC is to identify the solution treatment window which lies between the γ' solvus temperature and solidus of the material. This application of DSC is detailed in two papers by Sponseller [62] and Chapman [63]. Figure 2.37 shows the key features of the DSC curve for MAR-M247.

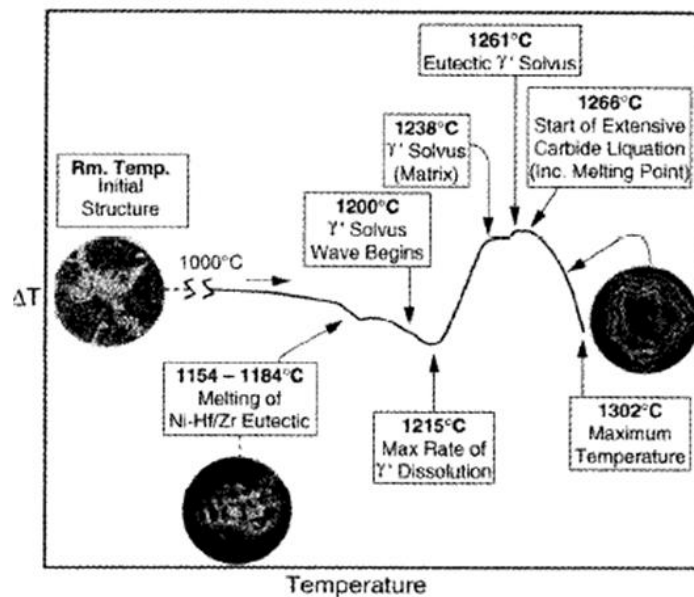


Figure 2.37: Diagram presented by Sponseller [62] showing a heating (10°C/min) DSC curve for MAR-M247 highlighting the key features around the γ' solvus temperature.

This schematic representation is supported by the annotated DSC results presented by Zhao *et al.* [64] (investigating the effect of Nb addition to a Ni superalloy); additionally Wang *et al.* [65] present DSC curves for CMSX486.

2.10. Brief Overview of ALM Techniques

‘Additive Layer Manufacturing’ (ALM) is an overall term that refers to a collection of manufacturing techniques which all share the following general methodology. Initially a 3-dimensional shape in the form of a CAD file is virtually broken down and approximated to a sequence of 2-dimensional slices of a fixed thickness. Some physical process then forms each of these slices in turn and bonds it to the previous; the physical shape is formed by the repetition of this process.

Early ALM techniques are typically known as rapid prototyping (RP) technologies and emerged in the late 1980’s. These generally revolve around the formation of polymer shapes and demonstration pieces and include 3D-printing, stereolithography and plastic selective laser sintering (SLS). A comprehensive review of these techniques is presented elsewhere [66].

The evolution of these technologies into Rapid Manufacturing (RM) techniques has occurred in the past decade and involves the movement towards fully dense, metallic and functional components. During this evolution there has emerged a certain amount of overlap between the different techniques particularly around SLS (Selective Laser Sintering) (polymers), SLS (metals), SLS (metal with binder) and SLM (Selective Laser Melting) techniques; this ambiguity is clarified in technology reviews by Levy *et al.* [67] and Santos *et al.* [68].

Emerging are the two key ALM techniques for the production of fully dense and functional parts: Direct Laser Fabrication (DLF or LENS) and SLM. DLF is similar to a laser cladding process where metal powder is injected via an argon gas stream into the focal point of a laser all mounted on a CNC style actuator system. The volume of research on the DLF process is

too large to summarise here, however the fundamentals of the process can be obtained in the papers by Wu & Mei [69], Lewis & Schlienger [70] and Mazumder *et al.* [71].

The SLM process is very similar to an SLS process in terms of principle and equipment with the key difference being that the metal passes through a fully molten state and so fully dense material is produced (See the review by Kruth *et al.* [72] for a full explanation of SLS consolidation mechanisms). A schematic arrangement of an SLM system can be seen in Figure 2.1.

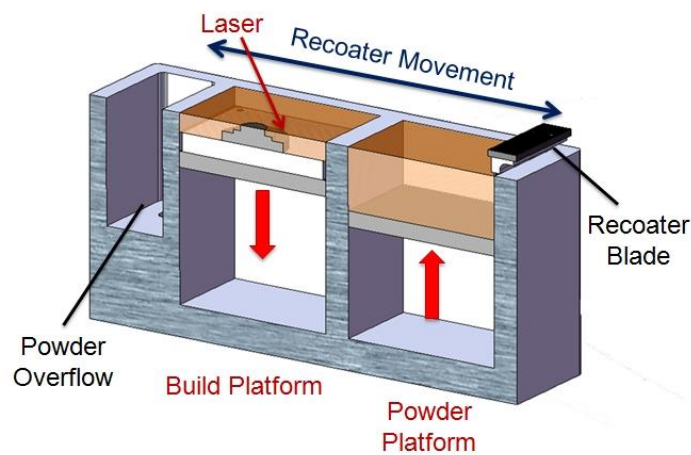


Figure 2.38: Schematic diagram showing the key operation of an SLM system

The essential stages of operation are as follows:

- The powder platform is raised presenting a small amount of powder proud of the build surface.
- The recoater blade moves across the powder and build platforms; spreading a thin layer of powder across the build plate and previously built layers.
- A computer controlled laser selectively melts the current build slice and re-melts some of the previous layer ensuring good bonding between the two.
- The build platform moves down by the thickness of a single slice.

- The process is repeated until the component has been completely fabricated.

A comparison between the DLF and SLM techniques is presented by Wu [73] and finds the following key differences: SLM has the ability to produce very complicated shapes at high dimensional accuracy with a ‘good’ surface finish, although the build sizes are limited to the dimensions of the machine; DLF can produce at much higher material deposition rates, gives the possibility for component repair/additive methodology & functionally graded materials (Wu *et al.*[74]) and can typically operate on a larger scale than SLM although it shows much poorer surface finish and low dimensional control (as such is limited to relatively simple shapes) and poor powder capture rates. This makes the re-use of powder problematic due to partial melting or oxidation of the un-captured particles. Both processes suffer from residual stress issues in the fabricated material due to localised rapid heating/cooling.

The work presented in this thesis concerns SLM.

2.11. Early Attempts to Characterise the SLM Process

Early/fundamental attempts to examine the SLM process have revolved around single laser line scan tracks across (typically steel) powder. It is difficult to resolve the findings of these studies with the complex behaviour observed in the wider SLM process however the key publications are summarised here:

‘Balling’ is typically a focus of these studies and occurs when the laser scan path forms a broken series of ‘ball-like’ deposits rather than continuous material, Figure 2.39. Process maps produced by Childs *et al.* [75] examining steel powders show that scan speed is a significant parameter governing this behaviour. The research concludes that there is an upper threshold of scan speed at which balling will occur with laser power having very little influence. The later research presented by Kruth *et al.* [76] (Fe based powder) disagreed with

this, showing a continuous line of deposited material can be achieved using higher laser power at faster scan speeds; this is attributed to the rapidly solidifying melt pool following the laser spot.

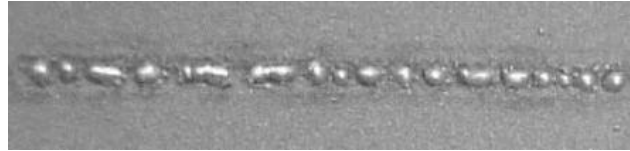


Figure 2.39: Example of balling in a single line of laser deposited iron based powder [77].

Realistically, the study by Childs *et al.* [75] used impractically slow scan speeds (<15 mm/s), therefore it is the research presented by Kruth *et al.* [76] that is of greater practical interest and this overall process map can be seen in Figure 2.40.

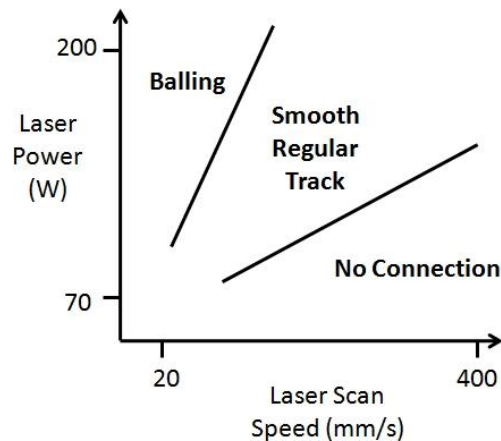


Figure 2.40: Process map for the consolidation of single laser line scans of Fe based powder [76].

It is commonly recognised that balling of the material is caused by the surface tension of the melt pool and poor wetting of the substrate material [75, 76, 78, 79]. Additionally, studies by Kruth *et al.* [76] (Fe based powder), Abe *et al.* [78] (Ni based powder) and Niu *et al.* [79] (steel powder) state that oxide layers reduce the wetting ability of the solidifying material and as such SLM is typically carried out under inert atmosphere.

Further research by Childs *et al.* [80] (steel) examine the raster scanning of a single layer of powder to map the onset of porosity with respect to power and scan speed. It is suggested that porosity onset is due to balling, however research by Rombouts *et al.* [81] argues that balling is a feature of single laser scan experiments and that the same principles do not apply in SLM.

2.12. Microstructure within SLM Fabricated Nickel Superalloys

Much of the early research attempting to characterise microstructure within laser-fabricated materials (both SLM and DLF) was carried out in the early 2000's revolving around Ti-6Al-4V [82-85]. One of the consistent microstructural features from these studies is the occurrence of columnar grains elongated in the build (or 'Z') direction.

Following these studies there has been an increased interest in the laser-fabrication of nickel superalloys and specifically IN718 [86-90], which proved to be a good candidate material due to low weld-cracking susceptibility and good mechanical properties (75% of wrought RT-tensile properties according to Tabernero *et al.* [88]) and IN625 [91-94] which also shows low weld-cracking susceptibility and good mechanical properties when laser-fabricated. Similar to the research regarding Ti-6Al-4V, both of these alloys (and the various other nickel alloys investigated) show columnar grains elongated in the build direction. These columnar grains can be clearly seen in the micrograph presented by Vilaro *et al.* [95] in Figure 2.41 showing SLM-fabricated IN263.

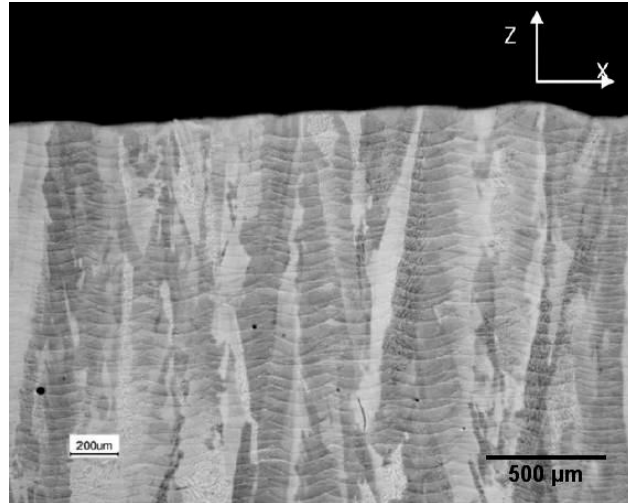


Figure 2.41: SEM Micrograph showing SLM fabricated IN263 with clearly visible columnar grains elongated in the build direction (Z) and ‘fishscale’ weld pattern [95].

Also visible in Figure 2.41 is the ‘fishscale’-like weld pattern caused by each scan pass of the laser. This weld pattern is a common feature of SLM-fabricated nickel alloys and is also reported in research on IN718 [86] regarding IN718 and Hastelloy X [96]. In all cases, the columnar grains were shown to grow epitaxially across these weld patterns from one layer to the next. This epitaxial growth can be related to the partial re-melting of the grains in the previous build layer and the directionality is due to the preferential heat transfer route down through the deposited material rather than outwards into the surrounding powder (or atmosphere in the case of DLF). The theory behind epitaxial growth in SLM is presented elsewhere [97].

Further proof that this columnar structure is caused by the heat flow within the material is presented by Dinda *et al.* [93] regarding the DLF of IN625 where the columnar structure is clearly shown to incline towards the direction of the laser head and alternate with each layer as the laser passes back and forth as shown in Figure 2.42.

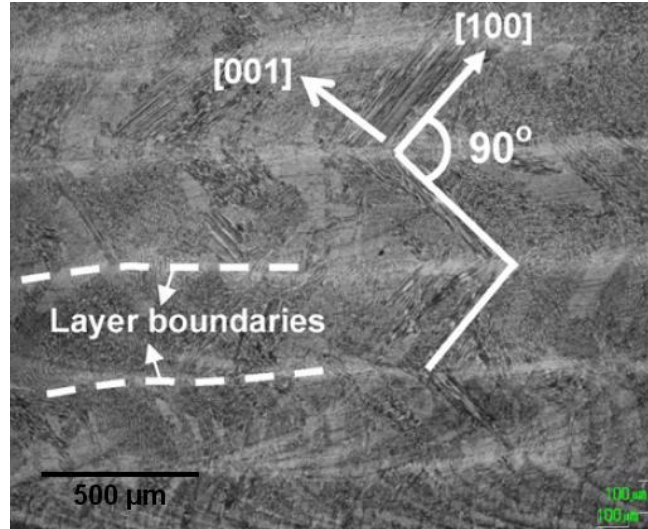


Figure 2.42: Micrograph showing DLF deposited IN625 with columnar features inclined toward the direction of laser movement for each layer [93].

Research by Chen & Xue [98], Zhao *et al.* [87] and Amato *et al.* [86] all show a further fine columnar dendritic structure within the elongated grains. The micrograph presented by Chen & Xue [98] in Figure 2.43 shows this structure clearly with the columnar grains visible under low magnification and the fine dendritic structure visible under a higher magnification.

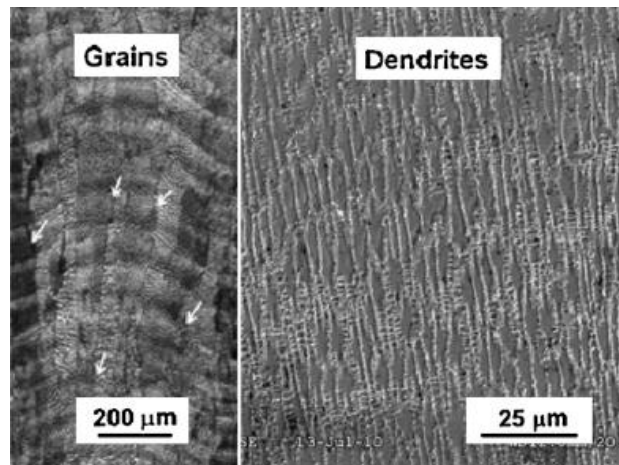


Figure 2.43: Micrograph showing columnar grains with ‘fishscale’ weld pattern (left) and the fine dendritic structure within the grains under higher magnification (right) within IN738 processed by DLF [98].

Similar structures observed in the DLF samples of Zhao *et al.* [87] show a $\langle 100 \rangle$ orientation and in the study based around the deposition of IN738 by Zhong *et al.* [99] fine carbide chains can be seen decorating the borders of these features.

Interesting grain structures have been observed in DLF fabricated material resulting from rapid cooling at the edge of laser scan lines. Research published by Moat *et al.* [100] (Waspaloy) and Liu *et al.* [101] (IN718) show fine grained regions lying between the large columnar regions at the edge and centre of the laser scan path respectively. This bimodal structure can be seen in the micrograph presented by Liu *et al.* [101] in Figure 2.44.

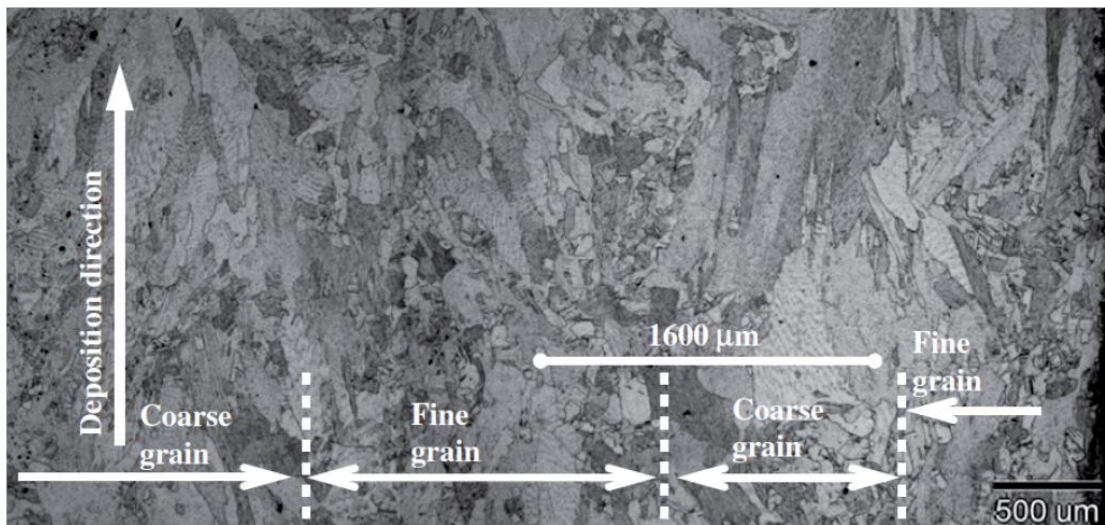


Figure 2.44: Micrograph showing regions of columnar and fine grains in DLF fabricated IN718 [101].

Most of the research into the laser fabrication of nickel superalloys revolves around solution-strengthened (or γ'' hardenable material) however an interesting result is shown in research by Chen & Xue [98] regarding the γ' structure in IN738. It is stated that in the as-fabricated condition the γ' is suppressed due to the high cooling rates that material shows effectively a solution treated structure with a super-saturated γ matrix. This is a key point in understanding what further heat treatments must be carried out in order to produce the ideal microstructure and good material properties.

A final point to note is research into the use of a post-fabrication HIPping (Hot Isostatic Pressing) treatment to close internal defects. Research by Blackwell [90] shows that in DLF deposited IN718, the HIP treatment can improve material properties by eliminating the

defects between build layers. Wu *et al.* [96] uses this technique to eliminate porosity within SLM-fabricated Hastelloy X to produce a higher density material and finally Zhao *et al.* [102] utilises this method to successfully close internal cracks in DLF fabricated Rene88DT.

2.13. Residual Stress within SLM Fabricated Materials

The occurrence of high and detrimental residual stresses within laser fabricated components due to localised heating/melting and cooling/solidification is well known. For the DLF process, various researchers have measured [100, 101, 103] and attempted to model [104, 105] these stresses, although this is generally for simple thin walls and a simple scan path. The complicated scan paths used in SLM-fabrication make drawing conclusions from measurements and modelling very difficult.

Some meaningful conclusions have been drawn and may prove useful in the future removal or control of these residuals. Research presented by Kruth *et al.* [76] shows that the residual stress is dependent on the laser scan strategy; a simple raster scanning appears to show high stress in one direction (transverse to the path) but almost zero longitudinally to the path; conversely an ‘island’ style shows a greater, but much more balanced residual stress level.

Research presented by Abe *et al.* [78] examining the SLM of steels shows that a 2nd laser following the first has the ability to reduce the residual stress and improve the ductility by either reducing the cooling rate, or reheating to provide in-situ stress relief. The research by Shiomi *et al.* [106] goes further stating that the highest residual stresses lie at the top of the fabricated material as the top layers have had fewer subsequent heating/cooling cycles and suggests three different methods of heat treatment for stress-relaxation: A post-fabrication heat treatment resulted in a 70% reduction in residual stress; the laser rescanning of each layer

during fabrication resulted in a 55% reduction in residual stresses and a pre-heated substrate resulted in a 40% reduction in residual stresses.

2.14. The Welding of Nickel Superalloys: Cracking Mechanisms and Process Mapping

Due to the localised heating/melting of material, laser processing (both SLM and DLF) can be considered analogous to welding. It is well documented that precipitation hardenable nickel superalloys with a high γ' fraction are susceptible to weld cracking. Figure 2.45 shows a plot presented by Donachie [2] illustrating the Al and Ti (γ' forming elements) and an empirical line representing the boundary between materials considered to be weldable and un-weldable due to their cracking susceptibility. This method of weldability assessment is also supported by Henderson *et al.* [107] although it must be emphasised that this does not take into account the mechanisms or the complex microstructural effects governing weldability; the values for CM247, CMSX486 and IN625 have been added to the plot. Note that CM247 and CMSX-486 lie firmly in the ‘un-weldable’ region whereas IN625 appears in the weldable portion of the plot.

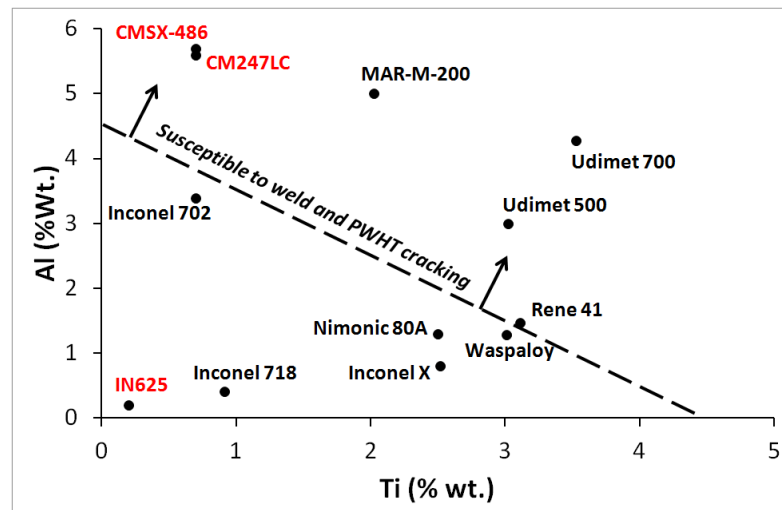


Figure 2.45: Plot (Reconstructed from source) showing the Al and Ti contents of various nickel superalloys (including CM247LC, CMSX-486 and IN625). The dashed line indicates an empirical boundary between weldable and un-weldable material due to cracking susceptibility [2].

Work by Dye *et al.* [108] has shown it is possible to construct a map for welding of Ni-superalloys by identifying the potential defects which may occur as a function of the effective weld power and weld speed. An example of this type of weldability map (developed for IN718) is shown in Figure 2.46.

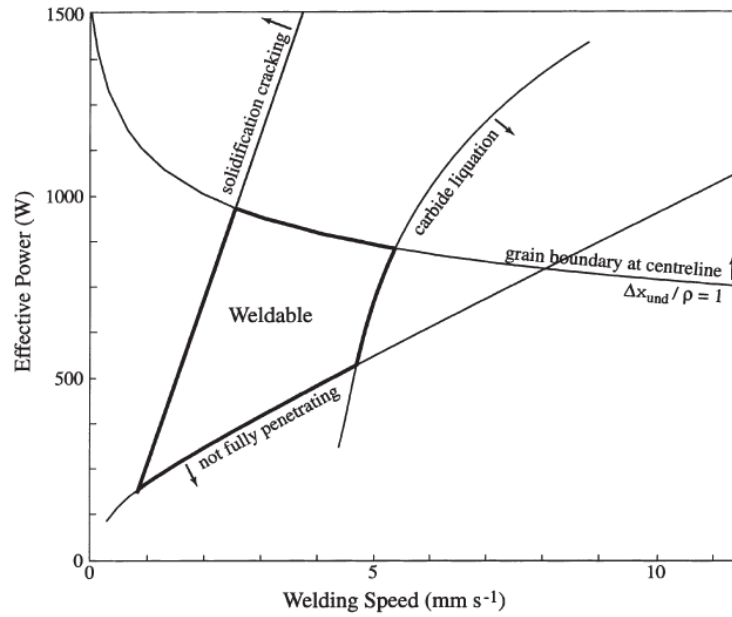


Figure 2.46: Typical (TIG) weldability map for IN718 [108]

The research by Rush *et al.* [109] also presents a parametric study aimed to map the process parameters of laser welding to cracking within Rene 80. The research presented by Egbewande *et al.* [110] and Zhong *et al.* [99] (both regarding IN738) are less complete, but still show some attempt to relate to the process parameters to the crack occurrence within the material. In general terms all three of these studies show that by reducing the heat input the occurrence of cracking is reduced.

Based on a review of the relevant literature, four cracking mechanisms associated with the welding of nickel superalloys have been identified; these mechanisms are identified, discussed and documented relationships to processing parameters identified:

i. Solidification Cracking (Hot Tearing)

This mechanism is described in general by traditional texts on the subject such as that of Kou [111] or DuPont *et al.* [112] as occurring in the partially liquid phase during the solidification of the material. Dye *et al.* [108] present an extensive numerical analysis of weld cracking in nickel superalloys and describe solidification cracking succinctly as occurring when the solid fraction (f_s) is in the range of 0.7-0.9 (depending on material and sources). During this range, the movement of the remaining liquid is restricted by the growing dendrites and, under the action of the solidification stress, it is unable to backfill into the contracting regions causing cracks to open. Kou [111] expands on this by stating that the solidification cracking susceptibility is increased with increasing solidification range (i.e. Difference between solidus and liquidus of material). It is also stated that the crack wall shows a distinctive dendritic morphology where the crack has formed between the solidifying dendrites; Figure 2.47 shows a micrograph presented by Kou [111] of this phenomenon in a steel solidification crack. Similar observations of an “unusual cellular structure” on the crack wall of thin walled castings of the nickel superalloy MAR-M246 were reported by Winstone & Northwood [113].

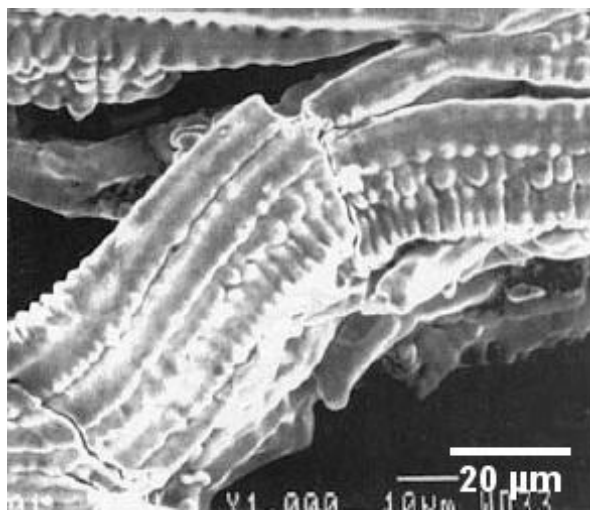


Figure 2.47: Micrograph showing dendritic structure on the wall of a solidification crack present in 308 stainless steel [111].

The weld mapping performed by Dye *et al.* [108], regarding IN718, shows that solidification cracking tends to occur under low welding speeds and high effective power (i.e. high heat input; Figure 2.46). The research presented by Rush *et al.* [109] identifies the occurrence of solidification cracking to be restricted to cracks showing a very high Average Crack Length (ACL) occurring under high power/small beam diameter (i.e. high heat input) laser welds of Rene 80. Egbewande *et al.* [110] also supports the idea of solidification cracking under high heat input (in laser welded IN 738) as a significant reduction in cracking is shown when moving from 0.5 – 1 m/min weld speed. This reduction in cracking is linked to the elimination of cracks which appear to be caused during solidification (based on the micrographs presented).

ii. Liquation Cracking

Grain boundary liquation in nickel superalloys is widely reported; The papers presented by Henderson *et al.* [107] and Attallah *et al.* [114] summarise this phenomenon by describing it as occurring when material is heated rapidly to a high temperature, but not above the overall melting point of the bulk material. Under these conditions some grain boundary phases are unable to dissolve rapidly enough into solid solution and can form low-melting point phases (such as eutectics) at the grain boundaries. These phases can melt and form liquid grain boundary films which can act as crack initiation points under residual or thermal stresses.

The precise composition of the liquid phases varies from alloy to alloy. In solid-solution and γ'' -strengthened alloys, liquation is generally attributed to carbides [109, 115, 116], however in γ' -strengthened, grain boundary γ' (or the formation of a γ/γ' eutectic under rapid heating) has been attributed to liquation [99, 110, 117].

Figure 2.48 shows a micrograph presented by Thompson & Radhakrishnan [116] revealing the interdendritic liquation in a sample of IN718 following heating and quenching. In this situation stress was not applied so the liquated phase resolidified in the interdendritic region without cracking. Figure 2.49 shows a micrograph presented by Sidhu & Chaturvedi [117] of the HAZ (Heat Affected Zone) in welded Rene80; here the thermal stress imposed by the weld has shown that the liquation film acts as a crack initiation point along the grain boundary. The propagation of cracks along grain boundaries is further explored by Zhong *et al.* [99] in laser deposited IN738 onto a DS superalloy substrate. The micrograph in Figure 2.50 shows the liquation occurring in the HAZ of the substrate and the crack propagating along a grain boundary into the deposited IN738.

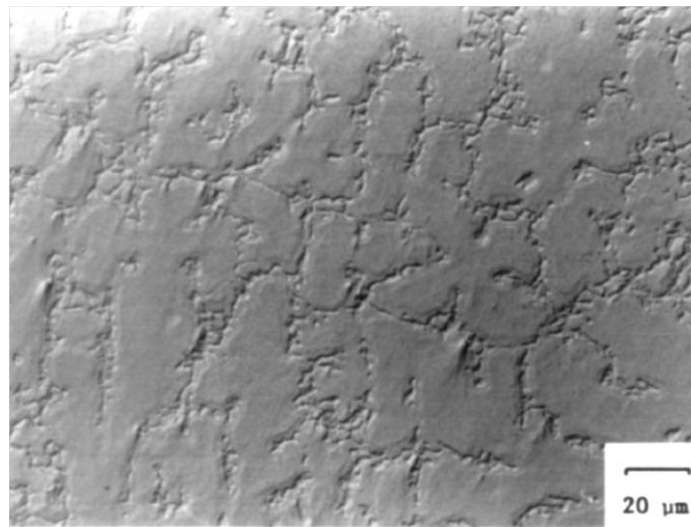


Figure 2.48: Micrograph showing interdendritic liquation of heated and quenched IN718 [116].

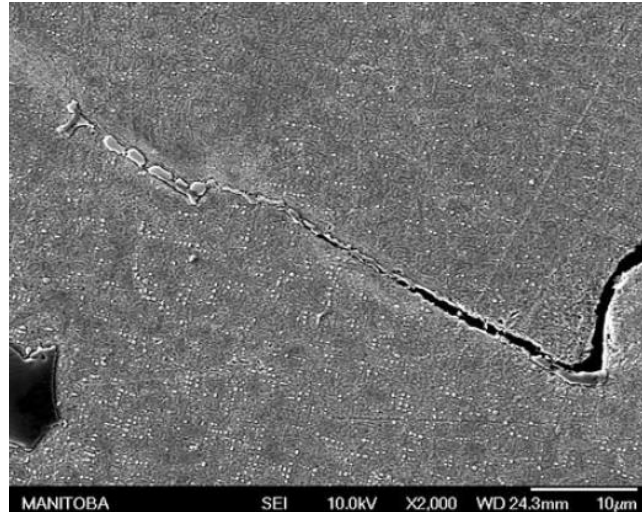


Figure 2.49: SEM showing grain boundary liquation and crack propagation in the HAZ of Rene 80 [117].

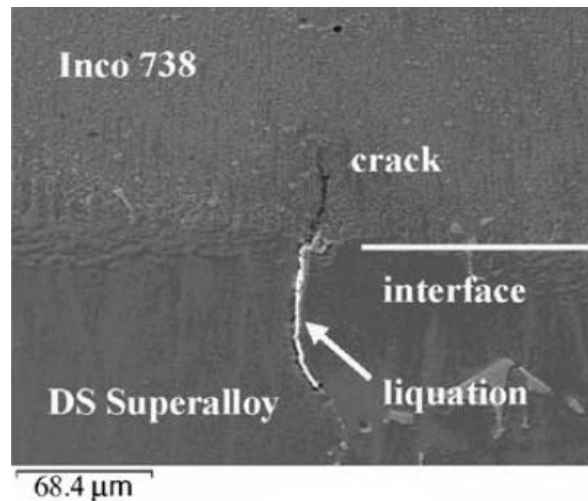


Figure 2.50: Micrograph showing laser deposited IN738 on a DS superalloy substrate. The liquation occurs in the HAZ of the substrate and the crack formed propagates along a grain boundary into the deposited material [99].

The micrograph presented by Odabaşı *et al.* [118] in Figure 2.51 confirms the region subject to liquation to be in the HAZ rather than in the fusion zone (laser-welding of IN718). The research also shows that liquation is more distinct in samples welded under lower energy conditions (i.e. faster weld speed) rather than the higher energy input conditions. This is supported by the weld map for IN718 presented by Dye *et al.*[108] (Figure 2.46) showing liquation cracks to occur under low power and high speed welding conditions.

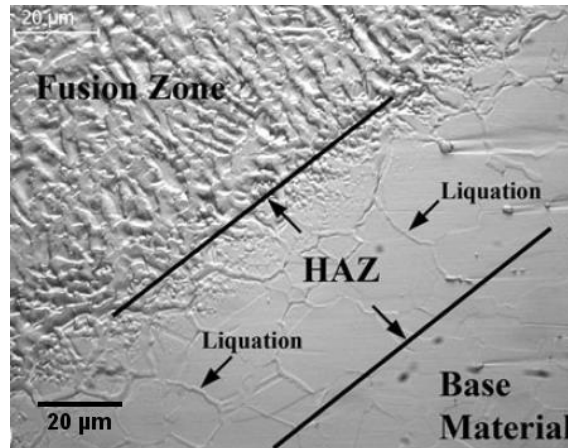


Figure 2.51: Micrograph showing the occurrence of liquation in the HAZ away from the fusion zone in IN718 [118].

iii. Ductility-Dip Cracking (DDC)

DDC is not clearly separated in the literature and is often included in the general categories of ‘reheat cracking’ and ‘hot cracking’; but recently research by Dupont *et al.* [112] has clarified DDC as a separate mechanism. Lippold and co-workers define it as a cracking caused by the reduction in ductility occurring in nickel alloys at intermediate temperatures ($0.4-0.7 T_m$) [112, 119]. Much of the literature referring to DDC is in relation to weld filler materials; however research by Kim *et al.* [50] shows a ‘ductility-dip’ in tensile data presented for CM247LC in the range 700°C - 900°C.

Two differing microstructural mechanisms have been suggested for the occurrence of DDC within the literature: That suggested by Lippold *et al.* and Young *et al.*

Lippold *et al.* [119-123] suggest DDC to be a ‘creep-like’ mechanism which operates at a high enough temperature to promote grain boundary sliding, but below the threshold of dynamic recrystallisation [119, 122]. It is concluded that the grain boundary sliding leads to stress concentrations and ultimately the formation of voids on grain boundary features. Within these, papers by Lippold *et al.* [119, 120, 122] discuss the factors influencing DDC occurrence. Triple point boundary intersections were shown to be points of severe stress

concentrations in material showing relatively smooth/straight grain boundaries. Fine grain boundary particles (carbides) were able to provide some grain boundary locking in order to reduce the occurrence of voids at the triple point intersections; however the particles themselves became sources of stress concentration. Tortuous grain-boundaries can also provide greater resistance to DDC when combined with the effect of fine grain boundary particles and ultimately larger grain boundary particles added a microstructural locking effect further adding to the DDC resistance. Figure 2.52 presented by Lippold & Ramirez [122] shows the general scheme from ‘triple point stress’ to ‘particle stress’ to the division of stress between the particles and the ‘tortuous grain boundaries’.

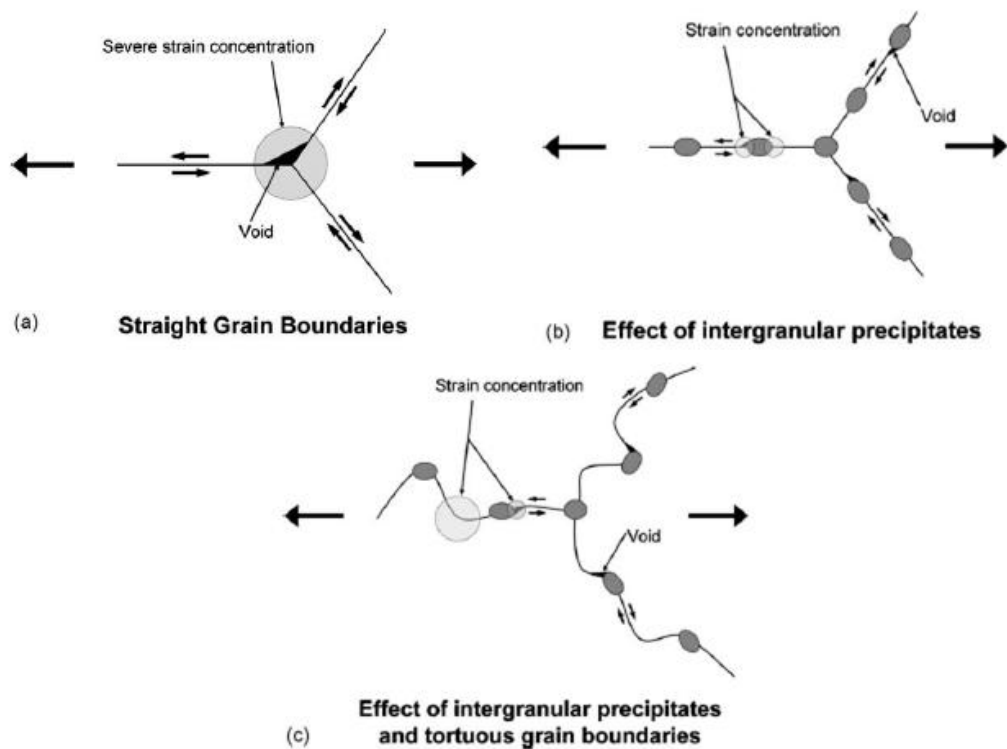


Figure 2.52: Diagram showing the high strain concentrations at triple point boundaries (a) the movement of the high strain regions with the addition of grain boundary particles (b) and finally the division of the high the inclusion of a tortuous grain boundary [122].

The final point to note is that Lippold *et al.* [120] also concluded that the susceptibility to DDC is increased at high angle grain boundaries.

Research presented by Young *et al.* [124] suggests a different mechanism that is due to the precipitation of partially coherent carbides at grain boundaries under intermediate temperatures; the stress imposed by these carbides acts upon the grain boundaries forming microscopic voids which act as crack initiation points under larger stresses. This is shown schematically in Figure 2.53.

Regardless of the formation mechanism, the onset of DDC can be characteristically seen as a series of voids lying on a grain-boundary between carbide particles, Figure 2.54.

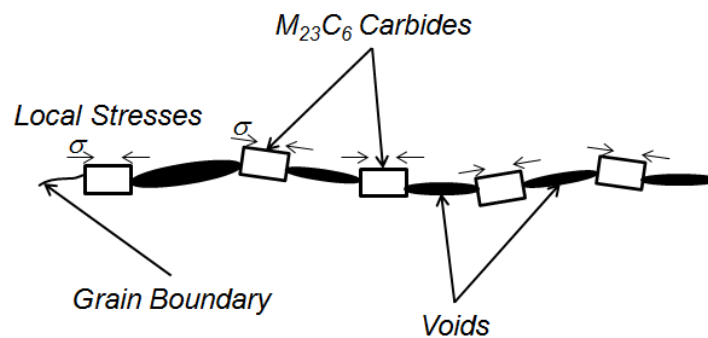


Figure 2.53: Diagram (Reconstructed from source) showing schematically the proposed mechanism for DDC by the formation of voids from localised stresses around carbides precipitated at grain boundaries [124].

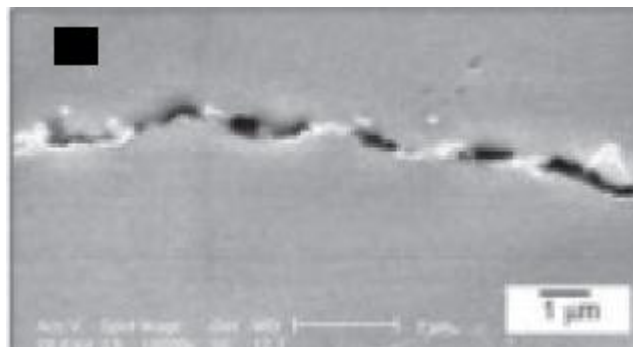


Figure 2.54: SEM micrograph (poor quality original) showing DDC void formation along a line of carbides [124].

iv. Strain-Age Cracking (SAC) or Post-Weld Heat Treatment (PWHT) Cracking

SAC is not typically associated with the welding process, but is associated with a post-weld heat-treatment (PWHT) of a γ' precipitation hardenable Ni-base superalloy and is well

documented. SAC may occur during stress-relief treatment following a weld, during an ageing treatment or in the ramp phase of a solution treatment. When heated to within the ageing region of the alloy, two competing actions occur; the precipitation of the γ' phase and the much slower relaxation of residual stress due to welding. The precipitation of γ' increases the material strength whilst reducing ductility [2, 107]). Rowe [125] reports that an additional stress is induced due to the reduction in volume inherent in the precipitation of γ' from solid solution. The combination of these two stresses combined with the reduction in ductility can exceed the material strength causing cracks to open. Henderson *et al.* [107] reports that these cracks typically open at grain boundaries with particulate carbides acting as initiation points.

Figure 2.55 presented by Donachie [2] graphically shows this sequence of events:

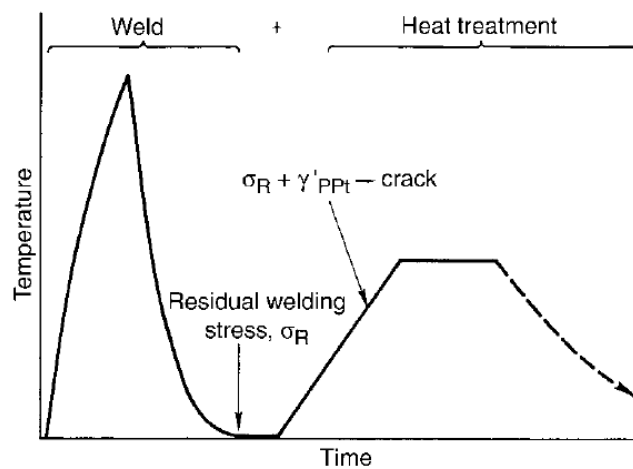


Figure 2.55: Diagram showing the potential sequence of events leading to SAC [2].

2.15. Concluding Remarks

This literature review has summarised the factors controlling structure and mechanical properties of nickel-base superalloys focussing on CM247LC, CMSX486 and IN625 as they are the subject of this research into SLM-fabricated nickel superalloys. Relevant literature on

weld cracking has also been summarised due to the similarity between welding and the SLM process as well as relevant literature in the field of laser fabrication in general.

Based on this review it is clear that the thermal history of the material and therefore the process parameters will control the microstructure, internal stresses and the tendency for crack formation. It is also apparent that further post-fabrication treatments will be necessary to refine the as-fabricated structure in order to produce the optimum material properties.

The literature review has identified the following knowledge gaps and how they are to be addressed by the research contained within this thesis:

- General lack of research regarding the SLM fabrication of γ' hardenable Ni-base superalloys.
 - The γ' hardenable alloys CM247LC and CMSX486 have been the subject of investigation within this thesis.
- Lack of research relating SLM process parameters on the defect formation (specifically cracking) within Ni-base Superalloys.
 - Parametric studies into the influence of processing parameters on defect formation within Ni-base superalloys CM247LC, CMSX486 and IN625 are presented.
- Lack of research attempting to characterise cracks within SLM fabricated Ni-base superalloys.
 - Microstructural evidence is presented to characterise and suggest cracking mechanisms within SLM fabricated CM247LC.
- Lack of research investigating the influence of the laser scan strategy during SLM on the microstructure of the final materials.

- Grain structure observations and EBSD data for SLM fabricated CM247LC are presented to illustrate the influence of the 'island' scanning strategy on the material.
- The γ' structure of SLM fabricated Ni superalloys has not been fully addressed
 - The evolution of the γ' structure throughout the proposed processing route of SLM fabricated CM247LC is presented.
- Limited research detailing the mechanical properties of SLM fabricated Ni-base superalloys.
 - Tensile (CM247LC, CMSX486 & IN625) and Creep (CM247LC & CMSX486) properties for the SLM fabricated alloys are presented with some insight into the influence of the processing route.

2.16. References

- [1] Reed RC. The Superalloys: Fundamentals and Applications: Cambridge, 2006.
- [2] Donachie MJ, Donachie SJ. Superalloys: A Technical Guide. Ohio: ASM International, 2002.
- [3] Source Book on Materials for Elevated-Temperature Applications. Ohio: American Society for Metals, 1979.
- [4] Mackay RA, Nathal MV. Microstructure-Property Relationships in Directionally Solidified Single-Crystal Nickel-Base Superalloys. MiCon 86: Optimization of Processing Properties, and Service Performance Through Microstructural Control: ASTM, 1988. p.202.
- [5] Kim IS, Choi BG, Seo SM, Kim DH, Jo CY. Influence of heat treatment on microstructure and tensile properties of conventionally cast and directionally solidified superalloy CM247LC. Materials Letters 2008;62:1110.
- [6] Ricks RA, Porter AJ, Ecob RC. Growth of Gamma Prime Precipitates in Nickel-Baase Superalloys. Acta Metallurgica 1983;31:43.
- [7] Smallman RE. Modern Physical Metallurgy. London: Butterworths, 1985.
- [8] Reppich B. Some New Aspects Concerning Particle Hardening Mechanisms Gamma Prime Precipitating Ni-Base Alloys- 1. Theoretical Concept. Acta Metallurgica 1982;30:87.
- [9] Reppich B, Schepp P, Wehner G. Some New Aspects Concerning Particle Hardening Mechanisms in Gamma Prime Precipitating Nickel-Base Alloys - 2. Experiments. Acta Metallurgica 1982;30:95.
- [10] Ardell AJ. Precipitation Hardening. Metallurgical and Materials Transactions A (Physical Metallurgy and Materials Science) 1985;16 A:2131.
- [11] Plumtree A, Persson NG. Influence of Gamma Prime Precipitation on the Creep Strength and Ductility of an Austenitic Fe-Ni-Cr Alloy. Metallurgical and Materials Transactions A (Physical Metallurgy and Materials Science) 1976;7 A:1743.
- [12] Tien JK, Ansell GS. Alloy and microstructural design: Academic Press, 1976, 1976.
- [13] Nathal MV, Maier RD, Ebert LJ. The Influence of Cobalt on the Tensile and Stress-Rupture Properties of the Nickel-Base Super-Alloy MAR-M247. Metallurgical and Materials Transactions A (Physical Metallurgy and Materials Science) 1982;13:1767.
- [14] Nathal MV, Maier RD, Ebert LJ. The Influence of Cobalt on the Microstructure of the Nickel-Base Super-Alloy MAR-M247. Metallurgical and Materials Transactions A (Physical Metallurgy and Materials Science) 1982;13:1775.
- [15] Betteridge W. Nickel and its Alloys: Ellis Horwood, 1984.
- [16] Kakehi K. Effect of primary and secondary precipitates on creep strength of Ni-base superalloy single crystals. Materials Science and Engineering A 2000;A278:135.
- [17] Van Sluytman JS, Pollock TM. Optimal precipitate shapes in nickel-base - Alloys. Acta Materialia 2012;60:1771.
- [18] Chen HL, Doernberg E, Svoboda P, Schmid-Fetzer R. Thermodynamics of the Al₃Ni phase and revision of the Al-Ni system. Thermochemica Acta 2010;512:189.
- [19] Raghavan V. Al-Cr-Ni (aluminum-chromium-nickel). Journal of Phase Equilibria and Diffusion 2006;27:381
- [20] Liao J-H, Bor H-Y, Wei C-N, Chao C-G, Liu T-F. Influence of microstructure and its evolution on the mechanical behaviour of modified MAR-M247 fine-grain superalloys at 871C. Materials Science and Engineering A 2012;539:93.
- [21] Sims CT. Contemporary view of nickel-base superalloys. Journal of Metals 1966;18:1119.

- [22] Bor HY, Chao CC, Ma CY. The influence of Mg on creep properties and fracture behaviors of Mar-M247 superalloy under 1255 K/200 MPa. *Metallurgical and Materials Transactions A (Physical Metallurgy and Materials Science)* 2000;31:1365.
- [23] Doherty JE, Kear BH, Giamei AF. On the origin of the ductility enhancement in Hf-doped Mar-M200. *Journal of Metals* 1971;23:59.
- [24] Bor HY, Wei CN, Jeng RR, Ko PY. Elucidating the effects of solution and double ageing treatment on the mechanical properties and toughness of MAR-M247 superalloy at high temperature. *Materials Chemistry and Physics* 2008;109:334.
- [25] Engler-Pinto CC, Jr., Nosedo C, Nazmy MY, Rezai-Aria F. Interaction between creep and thermo-mechanical fatigue of CM247LC-DS. Warrendale, PA, USA: TMS, 1996. p.319.
- [26] Kaufman M. Properties of Cast MAR-M-247 for Turbine Blisk Applications. In: Gell M, Kortovich CS, Bricknell RH, Kent WB, Radavich JF, editors. *Superalloys 1984*. Seven Springs Mountain Resort, Champion, Pennsylvania, USA: AIME, 1984. p.43
- [27] Kotval PS, Venables JD, Calder RW. Role of hafnium in modifying the microstructure of cast nickel- base superalloys. 1972;3:453.
- [28] Bor HY, Chao CG, Ma CY. The effects of Mg microaddition on the mechanical behavior and fracture mechanism of MAR-M247 superalloy at elevated temperatures. *Metallurgical and Materials Transactions A (Physical Metallurgy and Materials Science)* 1999;30:551.
- [29] Bor HY, Chao CG, Ma CY. The influence of magnesium on carbide characteristics and creep behavior of the Mar-M247 superalloy. *Scripta Materialia* 1997;38:329.
- [30] Tien JK, Howson TE, Chen GL, Xie XS. Cobalt availability and superalloys. *Journal of Metals* 1980;32:12.
- [31] Rawlings RD, Staton-Bevan AE. The alloying behaviour and mechanical properties of polycrystalline Ni3Al (' phase) with ternary additions. *Journal of Materials Science* 1975;10:505.
- [32] Cannon-Muskegon. C-M Group Website. www.c-mgroup.com, vol. 2009, 2009.
- [33] Boismier DA, Sehitoglu H. Thermomechanical Fatigue of MAR-M247.1. Experiments. *Journal of Engineering Materials and Technology-Transactions of the Asme* 1990;112:68.
- [34] Sehitoglu H, Boismier DA. Thermomechanical Fatigue of MAR-M247. 2. Life Prediction. *Journal of Engineering Materials and Technology-Transactions of the Asme* 1990;112:80.
- [35] Gordon AP, Trexler MD, Neu RW, Sanders TJ, McDowell DL. Corrosion kinetics of a directionally solidified Ni-base superalloy. *Acta Materialia* 2007;55:3375.
- [36] Pandey MC, Taplin DMR, Ashby MF, Dyson BF. Effect of Prior Exposure-Time on Air-Environment/Creep Interactions. *Acta Metallurgica* 1986;34:2225.
- [37] Antolovich SD, Liu S, Bauer R. Low Cycle Fatigue Behaviour of Rene 80 at Elevated Temperature. *Metallurgical and Materials Transactions A (Physical Metallurgy and Materials Science)* 1981;12 A:473.
- [38] Coffin Jr LF. Effect of Frequency on the Cyclic Strain and Fatigue Behaviour of Cast Rene at 1600 degree F. *Metallurgical and Materials Transactions A (Physical Metallurgy and Materials Science)* 1974;5:1053.
- [39] Janowski GM, Heckel RW, Pletka BJ. The effects of tantalum on the microstructure of two polycrystalline nickel-based superalloys: B-1900+Hf and MAR-M247. *Metallurgical and Materials Transactions A (Physical Metallurgy and Materials Science)* 1986;17A:1891.

- [40] Nathal MV, Ebert LJ. Influence of Cobalt, Tantalum, and Tungsten on the Microstructure of Single Crystal Nickel-Base Superalloys. *Metallurgical and Materials Transactions A (Physical Metallurgy and Materials Science)* 1985;16 A:1849.
- [41] Nathal MV, Ebert LJ. Influence of Cobalt, Tantalum, and Tungsten on the Elevated Temperature Mechanical Properties of Single Crystal Nickel-Base Superalloys. *Metallurgical and Materials Transactions A (Physical Metallurgy and Materials Science)* 1985;16 A:1863.
- [42] Chakravorty S, West DRF. High-Temperature Strength of Nickel Alloys Based on Gamma Prime Phase. *Metals technology London* 1980;7:414.
- [43] Heck K, Blackford JR, Singer RF. Castability of directionally solidified nickel base superalloys. *Materials Science and Technology* 1999;15:213.
- [44] Duhl DN, Sullivan CP. Some effects of hafnium additions on the mechanical properties of a columnar-grained nickel-base superalloy. *Journal of Metals* 1971;23:38.
- [45] Doherty JE, Giamei AF, Kear BH. Importance of Grain Boundary Morphology and Cohesion on Intergranular Strength. *Canadian Metallurgical Quarterly* 1974;13:229.
- [46] Rosler J, Konter M, Tonnes C. On the castability of corrosion resistant DS-superalloys. *Champion, PA, United states*, 1996. p.515.
- [47] Johnson WC, Doherty JE, Kear BH, Giamei AF. Confirmation of Sulphur Embrittlement in Nickel Alloys. *Scripta Metallurgica* 1974;8:971.
- [48] Shekhar R, Arunachalam J, Das N, Murthy AMS. Chemical and structural characterisation of nickel based superalloys doped with minor and trace elements. *Materials Science and Engineering A* 2006;435-436:491.
- [49] Harris K, Erickson GL, Schwer RE. MAR M 247 Derivations - CM 247 LC DS Alloy, CMSX Single Crystal Alloys: Performance and Properties. *Superalloys* 1984 1984:221
- [50] Kim IS, Choi BG, Hong HU, Yoo YS, Jo CY. Anomalous deformation behavior and twin formation of Ni-base superalloys at the intermediate temperatures. *Materials Science and Engineering A* 2011;528:7149.
- [51] Maldini M, Marchionni M, Nazmy M, Staubli M, Osinkolu G. Creep and fatigue properties of a directionally solidified nickel base superalloy at elevated temperature. *Warrendale, PA, USA: TMS*, 1996. p.327.
- [52] Satyanarayana DVV, Omprakash CM, Jagadeesan B, Das N. Effect of section thickness on creep and stress rupture behaviour of DS CM247 nickel base superalloy. *Materials at High Temperatures* 2008;25:17.
- [53] Harris K, Wahl JB. Improved single crystal superalloys, CMSX-4 (SLS)[La+Y] and CMSX-486. *Champion, PA, United states: Minerals, Metals and Materials Society*, 2004. p.45.
- [54] Harris K, Wahl JB. Developments in superalloy castability and new applications for advanced superalloys. *Materials Science and Technology* 2009;25:147.
- [55] Giamei AF, Anton DL. Rhenium Additions to a Ni-Baase Superalloy: Effects on Microstructure. *Metallurgical and Materials Transactions A (Physical Metallurgy and Materials Science)* 1985;16 A:1997.
- [56] Durst K, Goken M. Micromechanical characterisation of the influence of rhenium on the mechanical properties in nickel-base superalloys. *Materials Science and Engineering A* 2004;387-389:312.
- [57] Ola OT, Ojo OA, Wanjara P, Chaturvedi MC. A study of linear friction weld microstructure in single crystal CMSX-486 superalloy. *Metallurgical and Materials Transactions A (Physical Metallurgy and Materials Science)* 2012;43:921.
- [58] Wilson BC, Hickman JA, Fuchs GE. The effect of solution heat treatment on a single-crystal Ni-based superalloy. *Journal of Metals* 2003;55:35.

- [59] Shankar V, Bhanu Sankara Rao K, Mannan SL. Microstructure and mechanical properties of Inconel 625 superalloy. *Journal of Nuclear Materials* 2001;288:222.
- [60] Shankar V, Valsan M, Bhanu Sankara Rao K, Mannan SL. Room temperature tensile behavior of service exposed and thermally aged service exposed alloy 625. *Scripta Materialia* 2001;44:2703.
- [61] Höhne G, Hemminger W, Flammersheim H-J. Differential scanning calorimetry. London: Springer, 2003.
- [62] Sponseller DL. Differential thermal analysis of nickel-base superalloys. Warrendale, PA, USA: TMS, 1996. p.259.
- [63] Chapman LA. Application of high temperature DSC technique to nickel based superalloys. vol. 39. USA: Kluwer Academic Publishers, 2004. p.7229.
- [64] Zhao K, Lou LH, Ma YH, Hu ZQ. Effect of minor niobium addition on microstructure of a nickel-base directionally solidified superalloy. *Materials Science and Engineering A* 2008;476:372.
- [65] Wang YL, Ojo OA, Ding RG, Chaturvedi MC. Weld metal cracking in laser beam welded single crystal nickel base superalloys. *Materials Science and Technology* 2009;25:68.
- [66] Conley JG, Marcus HL. Rapid Prototyping and Solid Free Form Fabrication. *Journal of Manufacturing Science and Engineering, Transactions of the ASME* 1997;119:B.
- [67] Levy GN, Schindel R, Kruth JP. Rapid manufacturing and rapid tooling with layer manufacturing (LM) technologies, state of the art and future perspectives. *CIRP Annals - Manufacturing Technology* 2003;52:589.
- [68] Santos EC, Shiomi M, Osakada K, Laoui T. Rapid manufacturing of metal components by laser forming. *International Journal of Machine Tools and Manufacture* 2006;46:1459.
- [69] Wu X, Mei J. Near net shape manufacturing of components using direct laser fabrication technology. *Journal of Materials Processing Technology* 2003;135:266.
- [70] Lewis GK, Schlienger E. Practical considerations and capabilities for laser assisted direct metal deposition. *Materials and Design* 2000;21:417.
- [71] Mazumder J, Dutta D, Kikuchi N, Ghosh A. Closed loop direct metal deposition: Art to Part. *Optics and Lasers in Engineering* 2000;34:397.
- [72] Kruth JP, Levy G, Klocke F, Childs THC. Consolidation phenomena in laser and powder-bed based layered manufacturing. *CIRP Annals - Manufacturing Technology* 2007;56:730.
- [73] Wu X. A review of laser fabrication of metallic engineering components and of materials. *Materials Science and Technology* 2007;23:631.
- [74] Wang F, Mei J, Wu X. Microstructure study of direct laser fabricated Ti alloys using powder and wire. *Applied Surface Science* 2006;253:1424.
- [75] Childs THC, Hauser C, Badrossamay M. Mapping and modelling single scan track formation in direct metal selective laser melting. *CIRP Annals - Manufacturing Technology* 2004;53:191.
- [76] Kruth JP, Froyen L, Van Vaerenbergh J, Mercelis P, Rombouts M, Lauwers B. Selective laser melting of iron-based powder. *Journal of Materials Processing Technology* 2004;149:616.
- [77] Childs THG, Hauser G, Badrossamay M. Selective laser sintering (melting) of stainless and tool steel powders: Experiments and modelling. *Proceedings of the Institution of Mechanical Engineers, Part B: Journal of Engineering Manufacture* 2005;219:339.

- [78] Abe F, Osakada K, Shiomi M, Uematsu K, Matsumoto M. The manufacturing of hard tools from metallic powders by selective laser melting. *Journal of Materials Processing Technology* 2001;111:210.
- [79] Niu HJ, Chang ITH. Instability of scan tracks of selective laser sintering of high speed steel powder. *Scripta Materialia* 1999;41:1229.
- [80] Childs THC, Hauser C. Raster scan selective laser melting of the surface layer of a tool steel powder bed. *Proceedings of the Institution of Mechanical Engineers, Part B: Journal of Engineering Manufacture* 2005;219:379.
- [81] Rombouts M, Kruth JP, Froyen L, Mercelis P. Fundamentals of selective laser melting of alloyed steel powders. *CIRP Annals - Manufacturing Technology* 2006;55:187.
- [82] Wu X, Liang J, Mei J, Mitchell C, Goodwin PS, Voice W. Microstructures of laser-deposited Ti-6Al-4V. *Materials and Design* 2004;25:137.
- [83] Thijs L, Verhaeghe F, Craeghs T, Humbeeck JV, Kruth J-P. A study of the microstructural evolution during selective laser melting of Ti-6Al-4V. *Acta Materialia* 2010;58:3303.
- [84] Kelly SM, Kamper SL. Microstructural evolution in laser-deposited multilayer Ti-6Al-4V builds: Part 1. Microstructural characterization. *Metallurgical and Materials Transactions A (Physical Metallurgy and Materials Science)* 2004;35 A:1861.
- [85] Kelly SM, Kampe SL. Microstructural evolution in laser-deposited multilayer Ti-6Al-4V builds: Part II. Thermal Modeling. *Metallurgical and Materials Transactions A (Physical Metallurgy and Materials Science)* 2004;35 A:1869.
- [86] Amato KN, Gaytan SM, Murr LE, Martinez E, Shindo PW, Hernandez J, Collins S, Medina F. Microstructures and mechanical behavior of Inconel 718 fabricated by selective laser melting. *Acta Materialia* 2012;60:2229.
- [87] Zhao X, Chen J, Lin X, Huang W. Study on microstructure and mechanical properties of laser rapid forming Inconel 718. *Materials Science and Engineering A* 2008;478:119.
- [88] Tabernero I, Lamikiz A, Martinez S, Ukar E, Figueras J. Evaluation of the mechanical properties of Inconel 718 components built by laser cladding. *International Journal of Machine Tools and Manufacture* 2011;51:465.
- [89] Liu F, Lin X, Huang C, Song M, Yang G, Chen J, Huang W. The effect of laser scanning path on microstructures and mechanical properties of laser solid formed nickel-base superalloy Inconel 718. *Journal of Alloys and Compounds* 2011;509:4505.
- [90] Blackwell PL. The mechanical and microstructural characteristics of laser-deposited IN718. *Journal of Materials Processing Technology* 2005;170:240.
- [91] Paul CP, Ganesh P, Mishra SK, Bhargava P, Negi J, Nath AK. Investigating laser rapid manufacturing for Inconel-625 components. *Optics and Laser Technology* 2007;39:800.
- [92] Ganesh P, Kaul R, Paul CP, Tiwari P, Rai SK, Prasad RC, Kukreja LM. Fatigue and fracture toughness characteristics of laser rapid manufactured Inconel 625 structures. *Materials Science and Engineering A* 2010;527:7490.
- [93] Dinda GP, Dasgupta AK, Mazumder J. Laser aided direct metal deposition of Inconel 625 superalloy: Microstructural evolution and thermal stability. *Materials Science and Engineering A* 2009;509:98.
- [94] Mumtaz K, Hopkinson N. Selective laser melting of Inconel 625 using pulse shaping. *Rapid Prototyping Journal* 2010;16:248.
- [95] Vilaro T, Colin C, Bartout JD, Naze L, Sennour M. Microstructural and mechanical approaches of the selective laser melting process applied to a nickel-base superalloy. *Materials Science and Engineering A* 2012;534:446.

- [96] Wu X, Wang F, Clark D. On direct laser deposited Hastelloy X: dimension, surface finish, microstructure and mechanical properties. *Materials Science and Technology* 2011;27:344
- [97] Das S. Physical Aspects of Process Control in Selective Laser Sintering of Metals. *Advanced Engineering Materials* 2003;5:701.
- [98] Chen J, Xue L. Process-induced microstructural characteristics of laser consolidated IN-738 superalloy. *Materials Science and Engineering A* 2010;527:7318.
- [99] Zhong M, Hongqing S, Wenjin L, Xiaofeng Z, Jinjiang H. Boundary liquation and interface cracking characterization in laser deposition of Inconel 738 on directionally solidified Ni-based superalloy. *Scripta Materialia* 2005;53:159.
- [100] Moat RJ, Pinkerton AJ, Li L, Withers PJ, Preuss M. Residual stresses in laser direct metal deposited Waspaloy. *Materials Science and Engineering A* 2011;528:2288.
- [101] Liu F, Lin X, Yang G, Song M, Chen J, Huang W. Microstructure and residual stress of laser rapid formed Inconel 718 nickel-base superalloy. *Optics and Laser Technology* 2011;43:208.
- [102] Zhao X, Lin X, Chen J, Xue L, Huang W. The effect of hot isostatic pressing on crack healing, microstructure, mechanical properties of Rene88DT superalloy prepared by laser solid forming. *Materials Science and Engineering A* 2009;504:129.
- [103] Rangaswamy P, Griffith ML, Prime MB, Holden TM, Rogge RB, Edwards JM, Sebring RJ. Residual stresses in LENS components using neutron diffraction and contour method. *Materials Science and Engineering A* 2005;399:72.
- [104] Vasinonta A, Beuth JL, Griffith M. Process maps for predicting residual stress and melt pool size in the laser-based fabrication of thin-walled structures. *Journal of Manufacturing Science and Engineering, Transactions of the ASME* 2007;129:101.
- [105] Finnie S, Cheng W, Finnie I, Drezet JM, Gremaud M. The computation and measurement of residual stresses in laser deposited layers. *Journal of Engineering Materials and Technology, Transactions of the ASME* 2003;125:302.
- [106] Shiomi M, Osakada K, Nakamura K, Yamashita T, Abe F. Residual stress within metallic model made by selective laser melting process. *CIRP Annals - Manufacturing Technology* 2004;53:195.
- [107] Henderson MB, Arrell D, Larsson R, Heobel M, Marchant G. Nickel based superalloy welding practices for industrial gas turbine applications. *Science and Technology of Welding & Joining* 2004;9:13.
- [108] Dye D, Hunziker O, Reed RC. Numerical analysis of the weldability of superalloys. *Acta Materialia* 2001;49:683.
- [109] Rush MT, Colegrove PA, Zhang Z, Broad D. Liquation and post-weld heat treatment cracking in Rene 80 laser repair welds. *Journal of Materials Processing Technology* 2012;212:188.
- [110] Egbewande AT, Buckson RA, Ojo OA. Analysis of laser beam weldability of Inconel 738 superalloy. *Materials Characterization* 2010;61:569.
- [111] Kou S. *Welding Metallurgy*: Wiley, 2003.
- [112] DuPont JN, Lippold JC, Kiser SD. *Welding Metallurgy and Weldability of Nickel-Base Alloys*: Wiley, 2009.
- [113] Winstone MR, Northwood JE. *Structure and Properties of Directionally Solidified Superalloys in Thin Sections. Solidification Technology in the Foundry and Cast House*. University of Warwick: The Metals Society, 1980. p.298

- [114] Attallah MM, Terasaki H, Moat RJ, Bray SE, Komizo Y, Preuss M. In-Situ observation of primary melting in Ni-base superalloy using confocal laser scanning microscopy. *Materials Characterization* 2011;62:760.
- [115] Radhakrishnan B, Thompson RG. Liquid film migration (LFM) in the weld heat affected zone (HAZ) of a NI-base superalloy. *Scripta metallurgica et materialia* 1990;24:537.
- [116] Radhakrishnan B, Thompson RG. Quantitative microstructural study of intergranular liquation and its relationship to hot cracking. *Metallography* 1988;21:453.
- [117] Sidhu RK, Ojo OA, Chaturvedi MC. Microstructural response of directionally solidified Rene 80 superalloy to gas-tungsten arc welding. *Metallurgical and Materials Transactions A (Physical Metallurgy and Materials Science)* 2009;40:150.
- [118] OdabasI A, Unlu N, Goller G, Eruslu MN. A study on laser beam welding (LBW) technique: Effect of heat input on the microstructural evolution of superalloy inconel 718. *Metallurgical and Materials Transactions A (Physical Metallurgy and Materials Science)* 2010;41:2357.
- [119] Collins MG, Lippold JC. An investigation of ductility dip cracking in nickel-based filler materials - Part I. *Welding Journal (Miami, Fla)* 2003;82:288/S.
- [120] Collins MG, Ramirez AJ, Lippold JC. An investigation of ductility-dip cracking in nickel-based weld metals - Part III. *Welding Journal (Miami, Fla)* 2004;83:39/S.
- [121] Collins MG, Ramirez AJ, Lippold JC. An Investigation of Ductility Dip Cracking in Nickel-Based Weld Metals - Part II. *Welding Journal (Miami, Fla)* 2003;82:348S.
- [122] Ramirez AJ, Lippold JC. High temperature behavior of Ni-base weld metal Part II - Insight into the mechanism for ductility dip cracking. *Materials Science and Engineering A* 2004;380:245.
- [123] Ramirez AJ, Lippold JC. High temperature behavior of Ni-base weld metal Part I. Ductility and microstructural characterization. *Materials Science and Engineering A* 2004;A380:259.
- [124] Young GA, Capobianco TE, Penik MA, Morris BW, McGee JJ. The mechanism of ductility dip cracking in nickel-chromium alloys. *Welding Journal (Miami, Fla)* 2008;87:31.
- [125] Rowe MD. Ranking the resistance of wrought superalloys to strain-age cracking. *Welding Journal (Miami, Fla)* 2006;85:27S.

CHAPTER 3: EXPERIMENTAL METHODS

This chapter details the experimental methods used in the processing, sample preparation and characterisation of materials investigated within this thesis.

3.1. Materials

The processability of three different nickel-base superalloys was investigated in this study. The materials contained varying levels of the γ' forming elements: IN625 (Low γ'), CM247LC (High γ') and CMSX486 (Very High γ'). CM247LC is the primary focus of the study, as stated in Chapter 2, however IN625 and CMSX486 were also investigated to show the influence of the γ' content.

All investigated powders were produced by argon gas atomisation (details regarding gas atomisation can be found elsewhere [1]) and supplied by either LPW Technology Ltd. (UK) or Carpenter Technology Corporation (USA). The powders are defined by batch as shown in Table 3.1 with the relevant material names, particle size classification and date of purchase.

Table 3.1: Powder Batch Details

Material	Manufacturer Material Name	Batch No.	Particle Size Range	Supplier	Weight Supplied	Date of Order
CM247LC	LPW247LC-2	P100511C01	+15-53 μm	LPW	25 Kg	01/2010
CM247LC	LPW247LC-2	UK1091	+15-53 μm	LPW	18 Kg	02/2011
CM247LC	LPW247LC-2	UK1152	+15-53 μm	LPW	82 Kg	02/2011
CMSX486	N/A	CPP 486	-50 μm	Carpenter	N/A	N/A
IN625	LPW625-2	UK1180	+15-45 μm	LPW	25 Kg	01/2012

For the SLM process, Concept Laser has advised the use of powder within the size range +15-53 μm to ensure good spreading within the machine; this size range is empirical. Following SLM, all powders were re-sieved to 65 μm before being reused; this was in an

effort to eliminate any larger contaminants and any particles formed due to weld spatter during SLM; powder size verification is discussed in Chapter 4.

3.2. Measurement of Powder Particle Size Distribution

Measurement of the powder size distribution was carried out before SLM processing to verify the supplied size fraction and assess the ‘spreadability’ of the powder prior to processing.

The particle size distribution was measured using the CoulterLS230 laser diffraction particle size analyser (technique details can be found elsewhere [1]) fitted with small-volume module located in the School of Metallurgy and Materials, University of Birmingham (Met. & Mat. UoB). A small quantity of powder (approx. 2-3 g) was suspended in distilled water before being inserted into the machine. A pump speed of 38% (of the maximum) showed a good result without any obvious indication of powder settling within the machine.

3.3. Chemical Composition Analysis

Chemical analysis of the supplied CM247LC powder and two SLM fabricated samples using the same material was performed externally by Incotest UK in order to confirm the alloy composition and quantify any compositional changes due to SLM.

Carbon and Sulphur contents were measured using a LECO CS444 infrared (IR) gas analysis system. This method involves the combustion of the material in oxygen followed IR analysis in order to determine the levels of CO₂ and SO₂ in the resultant gas [2]. Nitrogen and Oxygen contents were measured using a LECO TC436AR inert gas fusion analysis system. In this process the material sample is heated in a graphite crucible under inert atmosphere (typically helium). The oxygen bonds with the carbon to form either CO or CO₂, which is measured using IR analysis, whereas nitrogen is released as N₂ and measured using thermal conductivity [3]. All the remaining elements (Cr, Ni, Co, Mo, W, Ta, Ti, Al, B, Zr, Hf, Si, P,

Fe, Mg) were measured using Inductively Coupled Plasma (ICP) Optical Emission Spectrometry (OES). This technique involves heating of a sample by gas plasma resulting in light energy emissions from the sample of different characteristic wavelengths. This radiation is analysed by spectrometry to determine the composition of the original sample. Further explanation of the principles and practice of these techniques can be readily found in literature relating to chemical analysis [4].

3.4. Selective Laser Melting

The SLM fabrication of final demonstrator components delivered to the industrial sponsor and specimens for the microstructural examination and mechanical testing studies within this thesis was carried out using the Concept Laser M2 system (Met. & Mat. UoB). Some preliminary investigations into the feasibility of using the SLM process to build complex geometries within industrial specified dimensional tolerances were carried out using the EOSint M270 system (University of Wolverhampton). Whilst these preliminary studies do not form a part of the scientific component of this thesis, they did give valuable insight into the practical application of SLM.

This section focuses on the key variables and experimental parameters. Further details on file preparation and standard operating procedures and practices are detailed in Appendix A. The surface of the powder-bed is defined as the X-Y with recoater blade moving parallel to the X-axis. As the recoater movement cannot be established from microstructural examination, 'X' and 'Y' labels on micrographs are for indication of the view-plane only and do not relate to the sample orientation within the M2. The build direction lies perpendicular to the X-Y plane and is defined as the Z-axis.

The technical specifications of the two SLM systems are listed in Table 3.2 (Note: The Concept Laser M2 has a fixed focus and as such the beam diameter is not a variable parameter):

Table 3.2: Technical Specifications for both Concept Laser M2 [5] and EOS EOSint M270 [6] SLM systems.

SLM System	Concept Laser M2	EOS EOSint M270
Laser Type	Yb-fibre Continuous Wave	Yb-fibre Continuous Wave
Laser Power	Variable 200W	Variable 200W
Max. Scan Speed	7000 mm/s	7000 mm/s
Spot Size	150 μm (fixed)	100 – 500 μm
Default Scan Strategy	Randomised Islands	Simple Raster Scan (Rotating with layers)
Slice Thickness	20 – 50 μm	20 – 100 μm
Build Plate Dimensions	250 mm \times 250 mm	250 mm \times 250 mm
Max. Build Height	280 mm	215 mm
Operating Atmosphere	Ar (<0.1% O ₂)	Ar (<0.1% O ₂)
Powder Handling	Integrated inert (Ar) chamber	Air
Recoater Type	Flexible Rubber	Solid Steel/Ceramic
Build Plate	Mild Steel or Nickel (IN625)	Mild Steel

A general overview of the SLM process is provided in Chapter 2. The laser scanning strategy unique to the Concept Laser M2 is referred to as the ‘island strategy’ and is defined as follows:

- For each slice the raster filled area is selectively melted followed by a single laser track outlining the slice referred to as the contour. This scheme is illustrated in Figure 3.1(a) for a simple square slice.
- The raster filled area is subdivided into square ‘islands’ which lie at a 45° angle to the X-axis.

- Within the islands a simple back and forth laser scan pattern is used with the scan vectors being perpendicular to those in the adjacent islands. This island scheme is illustrated in Figure 3.1(b).
- The order in which these islands is selectively melted is randomised; This is a patented Concept Laser technique which claims to reduce the residual stress within the component [7].
- With each subsequent layer the island pattern is shifted by 1 mm in both the X and Y directions.

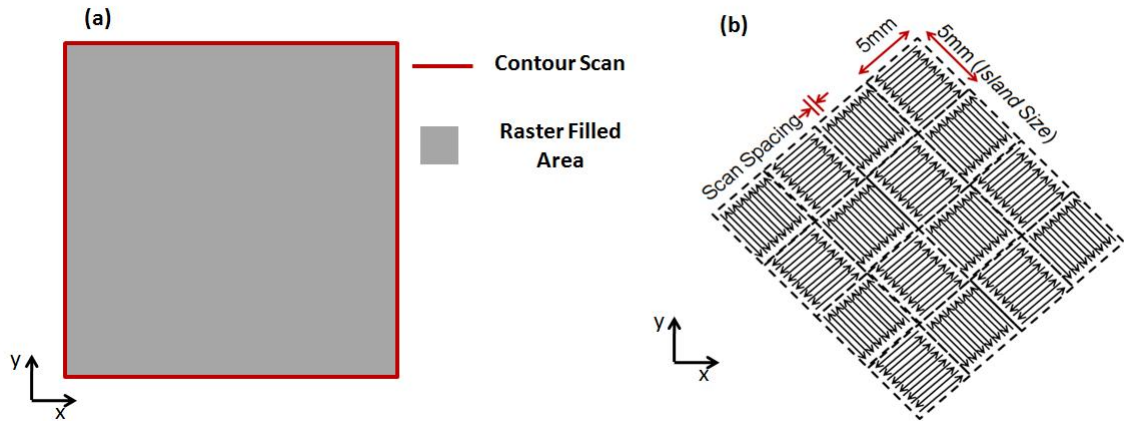


Figure 3.1: Diagrams illustrating the M2 laser scan regime: (a) shows the raster and contour regions for a simple square slice; (b) shows the island scan regime.

The scan spacing (a1) and island overlap (a2) parameters are illustrated in Figure 3.2 and can be defined as follows where d is the laser spot diameter:

$$\text{Scan Spacing } (\mu\text{m}) = a1 \times d$$

$$\text{Island Overlap } (\mu\text{m}) = a2 \times d$$

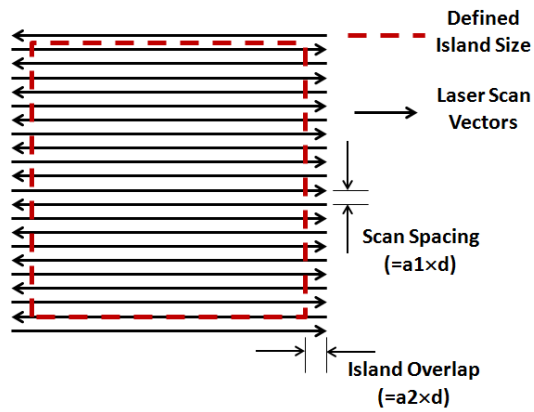


Figure 3.2: Diagram illustrating the scan spacing and island overlap parameters on a single island.

The island scan strategy was used for all samples other than a single sample produced using a simple back-and-forth laser scanning strategy (presented as a preliminary study in Chapter 5); for this lone sample all laser parameters were as listed in Appendix A.

This thesis focuses on the ‘bulk’ material and therefore all process parameters refer to the raster scanned area. Contour scan parameters are listed in Appendix A.

All specimens SLM processed were supported 3 mm from the build plate. This was done either using the automated ‘Magics’ generated supports or using a modified CAD model containing custom ‘pin-style’ supports. Details on the ‘Magics’ support generation are provided in Appendix A. Dimensions for the ‘pin-style’ supports can be seen in Figure 3.3 (a) and shown in Figure 3.3 (b) as applied to a simple horizontal bar.

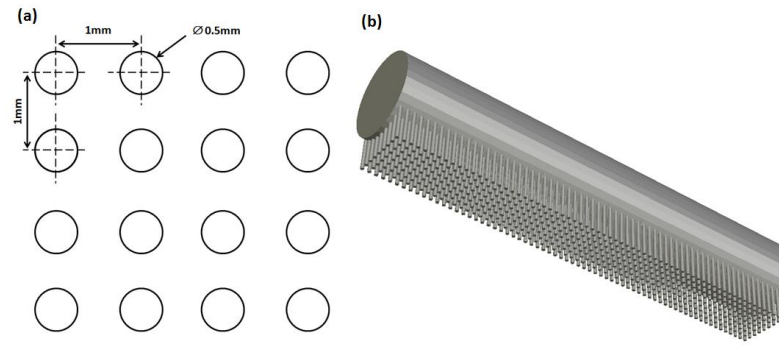


Figure 3.3: Diagrams illustrating the ‘pin-style’ supports: (a) pin spacings and dimensions; (b) as applied to a simple horizontal bar CAD model.

The SLM investigations were performed in seven stages which can be summarised as:

- I. Assessment of SLM process to produce complex geometry
- II. CM247LC parametric study and process optimisation
- III. CMSX486 parametric study and process optimisation
- IV. IN625 parametric study and process optimisation
- V. CM247LC mechanical testing and final component production
- VI. CMSX486 mechanical testing and final component production
- VII. IN625 mechanical testing and final component production

For each of the stages the key parameters or parameter ranges are listed in Table 3.3:

Table 3.3: Summary of SLM operating parameters for the different investigation stages.

Stage	System	Laser Power (W)	Scan Speed (mm/s)	Spacing (a1)	Island Overlap (a2)	Island Size (mm)	Material
I	EOS	195	1000	0.8	N/A	N/A	CM247LC
II	M2	150-200	400-2000	0.53-0.2	0.15	5	CM247LC
III	M2	100-200	500-2000	0.2-0.8	0.15	2-8	CMSX486
IV	M2	100-200	1000-3000	0.2-0.8	0.15	5	IN625
V	M2	150	1500	0.3	0.15	5	CM247LC
VI	M2	128	1007	0.63	0.15	6.4	CMSX486
VII	M2	200	1700	0.525	0.15	5	IN625

A brief overview of the SLM processing undertaken for each stage is provided:

Stage I – Several demonstration components were SLM fabricated using the EOS system with Magics supports in order to assess the feasibility of the process to produce particular features.

Stage II – Cuboidal coupons (10×10×20 mm) of CM247LC were SLM fabricated using ‘pin-style’ supports in order to investigate the influence of the parameters laser power, scan speed and scan spacing on the structural integrity and cracking behaviour within the material.

Stage III – Cuboidal coupons (10×10×20 mm) of CMSX486 were SLM fabricated using ‘pin-style’ supports in order to investigate the influence of the parameters laser power, scan speed, scan spacing and island size on the structural integrity and cracking behaviour within the material. The parameters for each coupon were selected using a central composite statistical design of experiments methodology as summarised in Appendix B.

Stage IV – Cuboidal coupons (10×10×20 mm) of IN625 were SLM fabricated using ‘pin-style’ supports in order to investigate the influence of the parameters laser power, scan speed and scan spacing on the structural integrity of the material. The parameters for each coupon were selected using a central composite statistical design of experiments methodology as summarised in Appendix B.

Stage V – Utilising the optimised process parameters found in Stage II, cylindrical mechanical test bars ($\varnothing = 12$ mm, length = 65mm) were SLM fabricated using ‘pin-style’ supports for testing. Additionally at this stage, any components to be delivered to the industrial sponsor were also fabricated using ‘Magics’ style supports.

Stage VI – Utilising the optimised process parameters found in Stage III, cylindrical mechanical test bars ($\varnothing = 12$ mm, length = 65mm) were SLM fabricated using ‘pin-style’

supports for testing. Additionally at this stage, any components to be delivered to the industrial sponsor were also fabricated using ‘Magics’ style supports.

Stage VII – Utilising the optimised process parameters found in Stage IV, cylindrical mechanical test bars ($\varnothing = 12$ mm, length = 65mm) were SLM fabricated using ‘pin-style’ supports for testing. Additionally at this stage, any components to be delivered to the industrial sponsor were also fabricated using ‘Magics’ style supports.

3.5. Hot Isostatic Pressing (HIPping)

HIPping was employed as a ‘retro-fix’ solution to close any cracks/porosity within the SLM fabricated samples. The influence of HIPping was studied in CM247LC and CMSX486 mechanical test samples; the IN625 study aimed to assess the as-fabricated mechanical properties so HIPping was not carried out on those specimens. A small extension to the HIPping investigation examined the effect of an increased cooling rate on the γ' structure of CM247LC.

The specifications of the HIP vessel are provided in Table 3.4 and the details of the two different HIP cycles performed at given in Table 3.5.

Table 3.4: Technical specifications of the HIP vessel.

HIP Name/Manufacturer	EPSI HIP
Location	Met. & Mat. UoB
Chamber Dimensions	\varnothing 145 mm, height 300 mm
Max. Pressure	200 MPa
Max. Temperature	1450°C
Gas	Argon

Table 3.5: HIPing parameters for the consolidation of SLM fabricated CM247LC and CMSX486 samples.

Cycle Name	Heating Rate	Cooling Rate	Hold Temperature	Hold Pressure	Hold Time	Description
Standard	5°C/min	5°C/min	1180°C	150 MPa	4h	Standard HIP for mechanical test bars and microstructural examination
Jet-Cooled	5°C/min	93°C/min (Gas Jet Cooled)	1260°C	150 MPa	4h	Investigation into the effect of HIP cooling rate on γ' structure

3.6. Heat Treatment

Heat treatment was performed on the mechanical test samples of CM247LC and CMSX486 in order to homogenise and refine the γ' structure in order to produce the best possible creep and tensile properties. These heat treatments were based on standard practice for castings of these materials. Heat treatments for the mechanical samples were carried out in the TAV furnace (Met. & Mat. UoB) under vacuum with forced gas quench using argon. All temperatures were monitored by in-situ thermocouples to $\pm 1^\circ\text{C}$. Details for the heat treatments are provided in Table 3.6 with specific heating profiles shown in Figure 3.4 and Figure 3.5 for CM247LC and CMSX486 respectively.

Table 3.6: Heat treatment parameters for samples of CM247LC and CMSX486.

Alloy	Solution Treatment	1st Ageing	2nd Ageing
CM247LC [8, 9]	1230°C - 1260°C, 2h, Gas Quench	980°C, 5h, Air Cooled	870°C, 20h, Air Cooled
CMSX486 [10]	1318°C, 2h, Gas Quench	1140°C, 5h, Air Cooled	871°C, 20h, Air Cooled

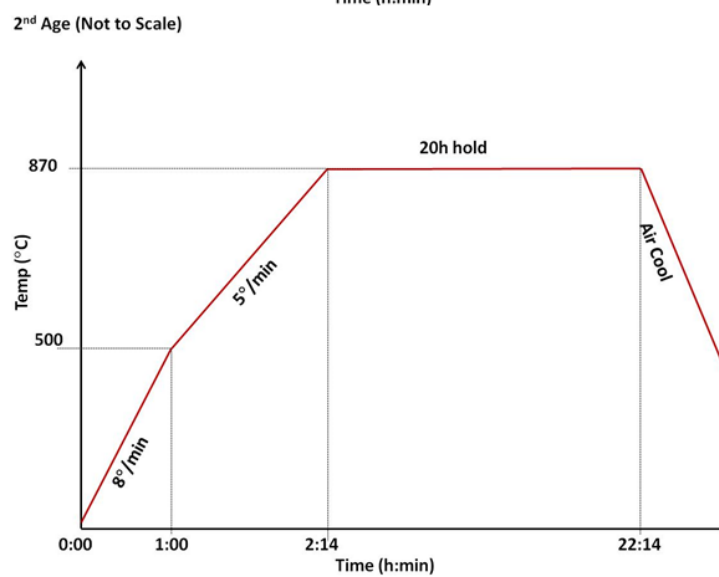
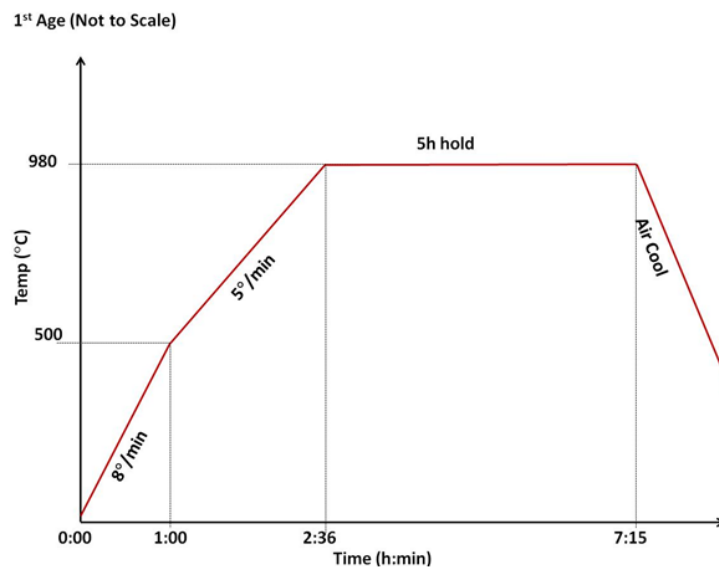
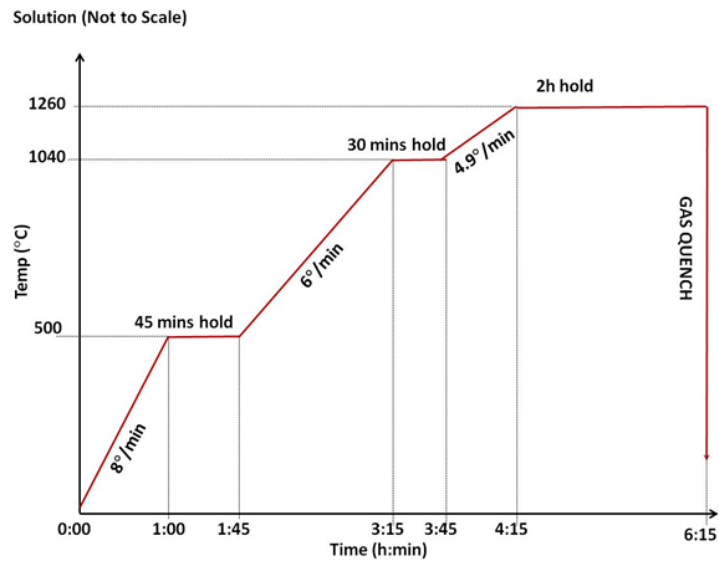


Figure 3.4: Detailed heating profiles for the three-stage heat treatment of CM247LC.

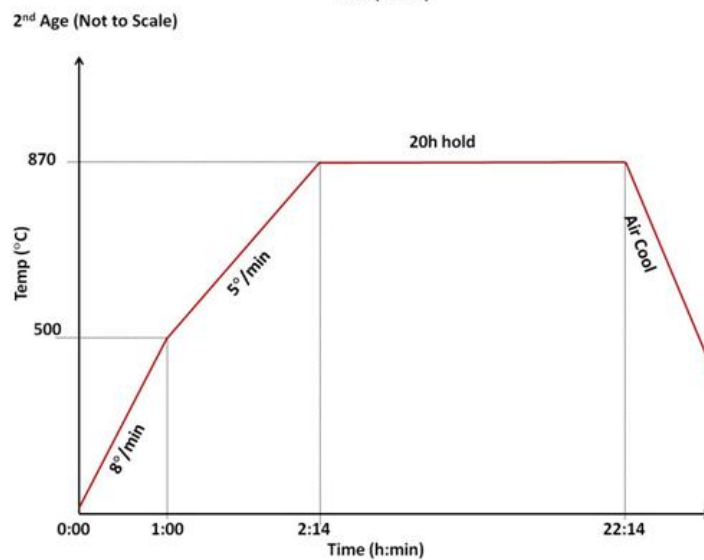
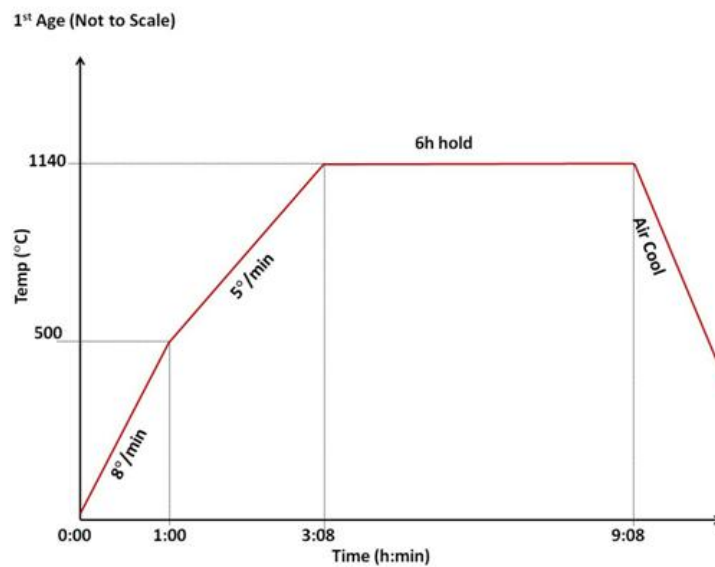
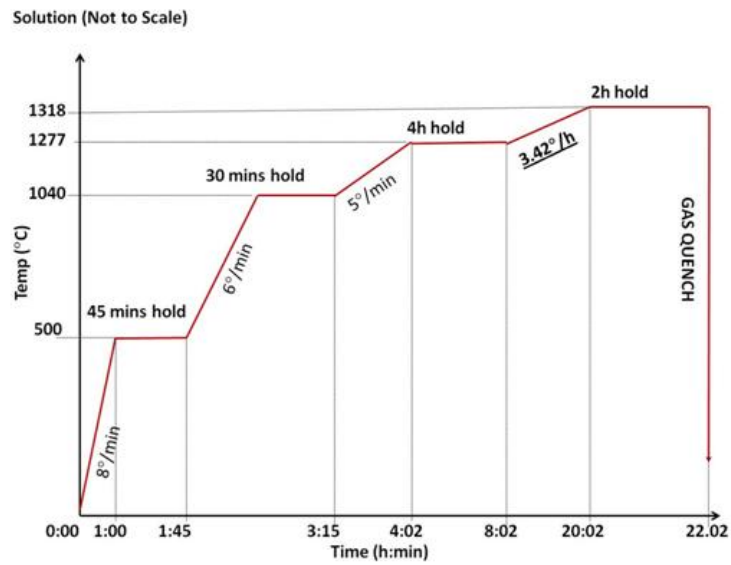


Figure 3.5: Detailed heating profiles for the three stage heat treatment of CMSX486.

A small investigation into the solution treatment temperature for CM247LC was conducted using a standard air furnace and an R-type thermocouple (Pt-Rh) positioned close to the sample (monitored to $\pm 2^\circ$). Three SLM fabricated and HIPed samples were heated to 1260°C, 1280°C and 1300°C, held for 2h and manually oil quenched. Oil was used as a quenching medium, as a rough approximation to gas in this investigation. Gauging the similarity is difficult and depends on the exact nature of the gas flow within the furnace, pressure and the gas used. However approximate figures show the heat transfer of oil quenching to be much closer to that of high velocity gas than water quenching. These approximate values are provided in Table 3.7 [11].

Table 3.7: Approximate guide for relative convective heat transfer coefficients for gas, oil and water quenching [11].

Quenching Medium	Approximate Convective Heat Transfer Coefficient (W/m² K)
Gas (Over-Pressure, High Velocity)	400
Oil	1000
Water	3000

3.7. Metallurgical Sample Preparation

Metallurgical samples were sectioned using either a precision cutter fitted with a SiC cutting wheel or by wire EDM. Depending on the investigation being carried out, samples were either sectioned longitudinally to the build direction (Z), to view the X-Z plane, or transversely to the build direction (to view the X-Y plane). Samples were hot-mounted in conductive Bakelite or cold mounted using resin in the case of the DOE due to the large number of samples.

Initially, all mounted specimens were ground using a coarse grit paper (p240) in order to produce a level surface and remove contamination from the cutting procedure. Further grinding was carried out in steps down to a p2500 finish, followed by polishing with diamond suspensions of 9 μm , 6 μm and final polishing by a 0.05 μm colloidal alumina suspension.

Two different etchants were used depending on the features of interest:

To reveal the grain structure, samples were etched by submersion for 5-10 in waterless Kalling's reagent (5 g CuCl_2 ; 100 ml HCl ; 100 ml ethanol [12]) then rinsed with ethanol and dried.

To reveal the γ' structure, samples were electrolytically etched in a 10% (volume) phosphoric acid (H_3PO_4) solution in H_2O . This etchant attacks the nickel γ matrix leaving the γ' structure intact [13]. The samples were immersed in a glass beaker containing etchant and connected to the anode with the cathode being submerged in the solution. Etching was performed using a voltage of 4V D.C. for approximately 4 s as illustrated in Figure 3.6.

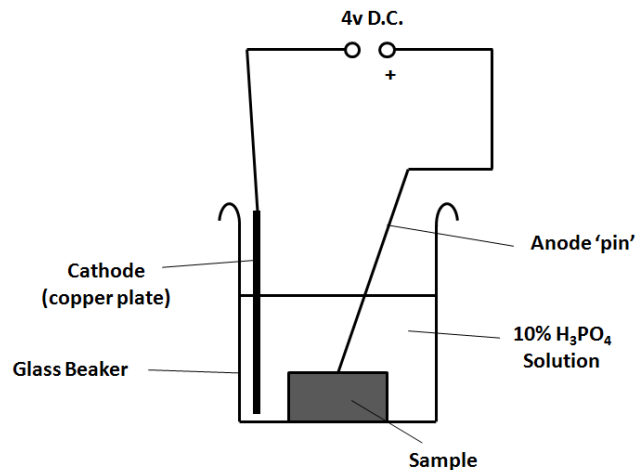


Figure 3.6: Apparatus for electrolytic etching of nickel superalloy samples.

3.8. Optical Microscopy

Optical microscopy was employed to characterise the grain structure within the SLM fabricated samples and the porosity within the SLM fabricated IN625. Imaging was performed using a Zeiss Axioskop 2 optical microscope equipped with monochrome CCD camera. Large area imaging was achieved through the use of the motorised stage and the images being reconstructed using the Axiovision (Carl Zeiss) software.

To quantify the porosity in IN625 samples, 12 images (covering an area of 5.6 mm²) were taken for each sample at 200X magnification at the mid-thickness of the X-Z section using the motorised stage.

3.9. Scanning Electron Microscopy (SEM)

SEM and the associated microstructural analysis tools; Energy Dispersive X-Ray Spectroscopy (EDX) and Electron Backscattered Diffraction (EBSD), were used to study the microstructural development, features, texture and composition (further details on these techniques can be found elsewhere [14]). The studies within this thesis that employed SEM microscopy are listed below:

- i. Powder Characterisation
- ii. SLM Process Optimisation: CM247LC
- iii. SLM Process Optimisation: CMSX486
- iv. γ' Development Through the Processing Route
- v. Influence of Laser Scan Strategy on Grain Structure, Orientation and Cracking

Technical details of the SEMs used and which of the above studies they were utilised in are listed in Table 3.8. Imaging was typically carried out using an accelerating voltage of 20 keV.

Table 3.8: Details of the SEMs used and the studies they correspond to.

Name	Investigation	Location	Electron Source	Detectors
Jeol 6060	i, v	Met. & Mat. UoB	Tungsten Filament	SE, BSE, Oxford INCA EDX
Phillips XL-30	i, ii, iii, iv	Met. & Mat. UoB	LaB ₆	SE, BSE, Oxford INCA EDX
Phillips XL-30 (ESEM)	ii	Met. & Mat. UoB	FEG	SE, BSE, Oxford INCA EDX
Jeol 7000	ii	Met. & Mat. UoB	FEG	SE, BSE, Oxford INCA EDX. WDX, EBSD
FEI Sirion	v	Materials Science Centre; Manchester University	FEG	SE, BSE, HKL Channel 5 EBSD

Details for the use of SEM within each of the studies making up this thesis are provided below.

i. Powder Characterisation

Powder characterisation was performed to assess the powder morphology, chemical composition and microstructure. Powder particles were mounted on conductive tape and imaged using the Jeol 6060 to observe their external morphology. Bakelite mounted ground samples were imaged using the XL-30 to observe grain structure and signs of chemical segregation due to gas atomisation. EDX linescans across particles were used to support these observations.

Powder porosity was quantified using a sample set of SEM images taken of the ground samples using the BSE detector. 15 images were captured at 500X magnification, allowing for several hundred particles to be analysed.

ii. SLM Process Optimisation: CM247LC

The imaging of individual cracks under high magnification was carried out using both the Philips XL-30 (FEG ESEM) and the Jeol 7000. Additionally, several small EBSD maps covering individual cracks were produced using the Jeol 7000 system.

The image sampling for the quantification of defects was carried out using the XL-30. Samples were sectioned to reveal the X-Z plane as shown in Figure 3.7 (a) and examined as polished. 30 BSE images (covering an area of 7.2 mm^2) were taken at 0.5 mm intervals along each of two lines; the 'midline' running down the centre of the sample and the 'edgeline' running closer to the edge of the sample allowing for comparison between the two regions, as illustrated in Figure 3.7 (b).

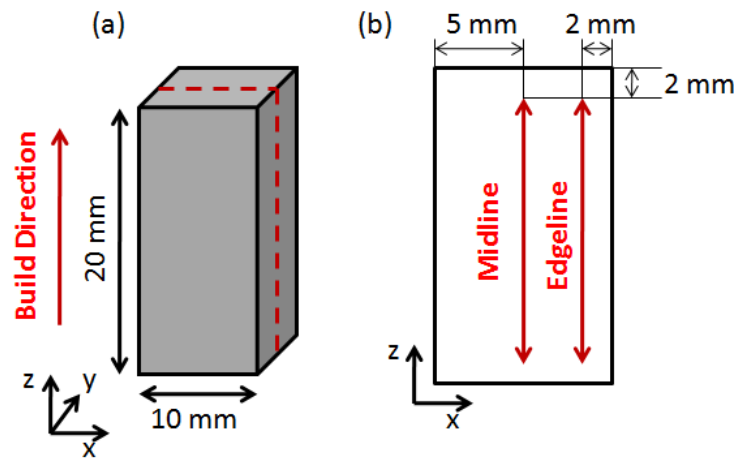


Figure 3.7: Diagram (Not to Scale) illustrating; (a) the sectioning of the sample; (b) the image sampling method for the optimisation study of CM247LC (study (ii)).

iii. SLM Process Optimisation: CMSX486

The image sampling for the quantification of defects was carried out using the XL-30. Samples were sectioned to reveal the X-Z plane as shown in Figure 3.8 (a), and examined as polished. For the CMSX486 study the goal was to rapidly evaluate process parameters so the

midline/edgeline method was abandoned in favour of a grid sampling method to gain an overall view of the defects. 7 BSE images were taken at 2 mm intervals for each of 3 lines running longitudinally down the sample giving an overall sample set of 21 images (covering an area of 5.0 mm²) as illustrated in Figure 3.8 (b).

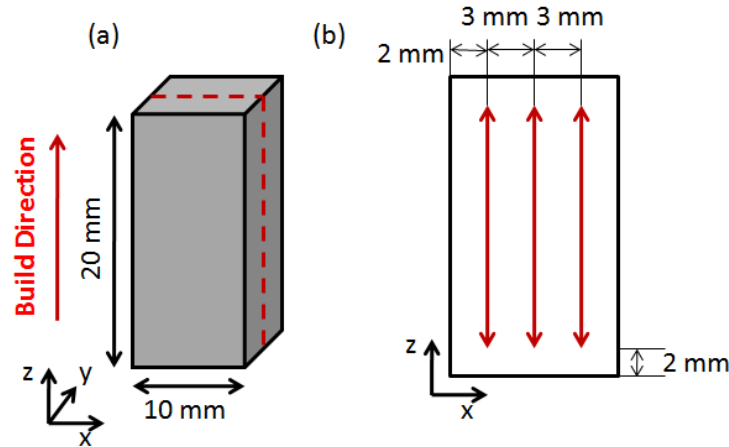


Figure 3.8: Diagram (Not to Scale) illustrating; (a) the sectioning of the sample; (b) the image sampling method for the optimisation study of CMSX486 (study (iii)).

iv. γ' Development Through the Processing Route

In order to examine the evolution of the γ' morphology throughout the processing route (As-Fabricated, HIPed, solution treated and aged), polished and electrolytically etched samples were examined using the Philips XL-30 and SE detector. Micrographs were taken at the following magnifications to allow for direct comparison (4000X, 6000X, 8000X and 16000X).

In order to quantify the size distribution of the γ' particles, a set of 20 micrographs (showing several hundred particles in total) were taken from each sample at 8000X magnification for image analysis.

v. Influence of Laser Scan Strategy on Grain Structure, Orientation and Cracking

In order to study the influence of the Concept Laser island scan strategy on the microstructure of the material, SEM examination was carried out on SLM fabricated CM247LC. Samples etched with Kalling's reagent were examined using the Jeol 6060 in both X-Z and X-Y section to confirm the optical observations of the grain structure.

The FEI Sirion SEM was used to produce EBSD maps showing the crystallographic orientation of the grains within an SLM fabricated and HIPed specimen of CM247LC sectioned in the X-Y plane. A large sample area was obtained by taking 16 EBSD maps, each at 200X magnification, and stitching them together to form an overall map approximately 1.5 mm × 2 mm in size. The data was analysed using HKL Channel 5 Tango and Mambo software [15].

3.10. Image Analysis

Image analysis was used to quantify various features observed during optical and SEM microscopy (Crack density, void area fraction, porosity etc.). Image analysis was performed on the sets of micrographs collected (see sections 3.8 & 3.9) and analysed using the ImageJ software [16]. The image analysis process followed the following standard sequence:

1. Global scale set based on micrograph scale bar (Once per set of micrographs).
2. Background removal (SEM only), 40 pixel ball radius to remove any overall brightness gradient from the image (see documentation for more details [17]).
3. Threshold to produce binary image isolating the relevant features.
4. 'Particle Measurement' to take the various measurements from the particles.

The key particle measurements used in this thesis are:

- **Area:** μm^2
- **Perimeter:** μm
- **Feret Max:** μm , defined as the longest distance between any two points on the boundary [17]
- **Equivalent Diameter:** μm , defined as the diameter of a circle having the same area as the particle
- **Circularity:** Dimensionless measurement of how circular a particle is; a value of '1' indicating a perfect circle moving towards '0' as the shape become increasingly elongated.

These values are further defined in Figure 3.9.

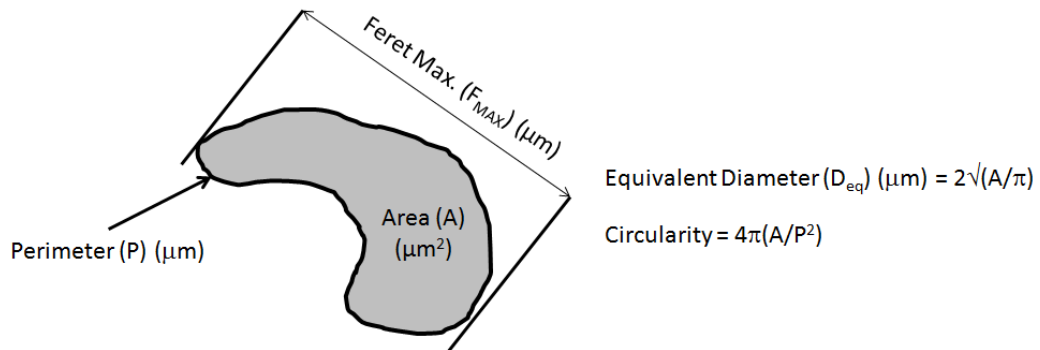


Figure 3.9: Diagram of a ‘particle’ showing the various measurements used in the image analysis.

The specific details of the analysis of images for the different investigations are given below:

i. Crack Quantification of CM247C

Feret Max. (F_{Max}) was used as an approximation to the crack length for crack quantification. Thresholded particles with $F_{\text{MAX}} < 4 \mu\text{m}$ (approximating to one pixel) were classified as image noise and eliminated. Thresholded particles with circularity > 0.7 were eliminated to reduce the effect of occasional small circular porosity.

Total crack length was calculated by summing the F_{MAX} values then averaged this with respect to the total micrograph area to give crack density. The resulting value for crack density was given as mm/mm² (i.e. mm of cracks per mm² of micrograph area).

ii. Crack & Void Quantification of CMSX486

Crack density was calculated as with CM247LC however thresholded particles showing an area > 500 μm^2 were defined as voids. These areas were summed and presented as a % void area fraction of total micrograph area.

iii. Porosity Quantification of IN625

Total pore/void area for IN625 samples was averaged with respect to micrograph area giving a total % area porosity.

iv. Porosity Quantification of Powder Samples (CM247LC/CMSX486/IN625)

Powder porosity was calculated by summing the total particle cross-sectional area, followed by thresholding and summing the total closed porosity within those particles. The overall porosity was presented as a % area of pores to particle cross-sectional area.

v. γ' Particle Size Measurement

The individual γ' particles shown in the micrographs could not be successfully thresholded for measurement. It was therefore necessary to measure each of the particles 'manually' using the imageJ line measurement tool on 300 particles for each sample. The distance between the flat sides of the cuboidal particles was measured in both directions (as shown in Figure 3.10) and the data compiled in a spreadsheet in order to generate size distributions and values for mean particle size.

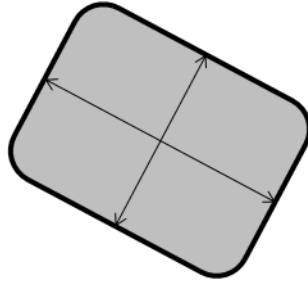


Figure 3.10: Example of a γ' particle measurement. Arrows indicate the distances measured in order to present particles size data.

3.11. Transmission Electron Microscopy (TEM)

TEM was used to visualise very fine γ' precipitates within a sample of SLM fabricated CM247LC in the 'as-fabricated' condition.

Samples were cut using a low speed diamond cutting wheel to a thickness of 0.5 mm and cut to \varnothing 3 mm discs using spark erosion. Samples were then further ground to 150 – 200 μ m thickness using 400 – 800 grit silicon carbide grinding paper.

Polishing was carried out using the twin-jet electropolishing method (Struers Tenupol-5) with a polishing solution of 10% perchloric, 90% methanol. Polishing was carried out at approximately -20°C using 25 – 30 V, 100 – 200 mA.

TEM imaging was carried out using Jeol 2100 laB6 TEM is fitted with Oxford Instruments INCA EDS with an operating voltage of 200 kV.

3.12. MicroCT

In order to visualise the 3D distribution of the cracks within the material and the effectiveness of the HIP treatment, two 'matchstick' samples (2.5 mm diagonal length) were cut from a horizontally fabricated cylinder of SLM powder-bed fabricated CM247LC. The internal crack formation was examined using MicroCT. One sample was in the as-fabricated condition and the second was following a HIP treatment. A schematic diagram for the microCT equipment

is shown in Figure 3.11. The sample is positioned on a rotating table and a sequence of X-ray images are taken as the sample is rotated. The solid material absorbs more of the radiation than the material where there are cracks/voids; these features can be visualised in 3-dimensions by the reconstruction of the image stack. The small sample size allowed for close positioning for the X-ray source giving maximum magnification (determined by the distance ratio a/b as shown in Figure 3.11) and an overall resolution of approximately $2\text{ }\mu\text{m}$.

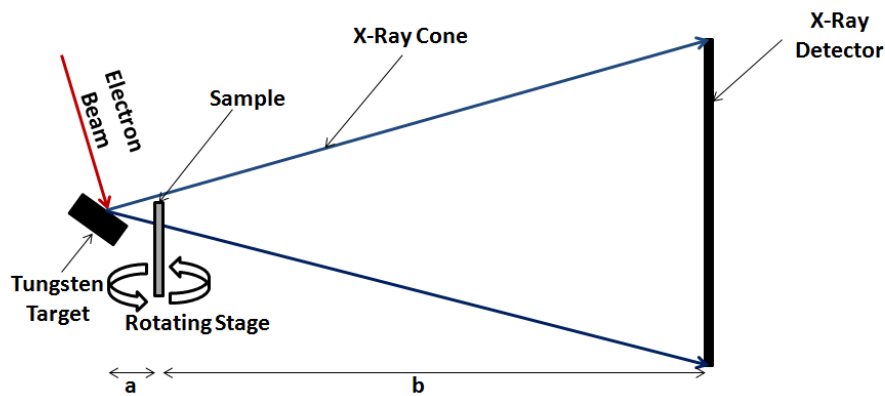


Figure 3.11: Schematic diagram of microCT equipment.

CT scanning was carried out using the Metris Custom Bay MicroCT located at the Henry Moseley X-ray Imaging Facility (HMXIF, Manchester University). Following some initial calibration and testing, the scan used a voltage of 165 kV, a tungsten target and a current of $169\text{ }\mu\text{A}$. A 1 mm Cu filter was positioned between the source and the specimen, this was in order to filter low energy X-rays and prevent them from saturating the detector. A full 360° scan was taken formed of 3142 projections.

The raw data was reconstructed into a 3-dimensional volume using the Metris CT-Pro Software [18]. The volume data analysed using Avizo Standard 6.3 [19] where the cracks and voids were isolated, labelled and could be visualised in three-dimensions. It was not possible to threshold all of the cracks from the data as their width ($< 2\text{ }\mu\text{m}$) was comparable to the

resolution of the CT equipment; however sufficient data was obtained for the purposes of the study. Full details on the MicroCT technique can be found elsewhere [20].

3.13. Differential Scanning Calorimetry (DSC) Thermal Analysis

DSC thermal analysis was carried out using the Netzsch DSC 404 – High Temperature DSC facility (Met. & Mat. UoB). Samples of CM247LC powder (57.38 mg) and solid SLM formed CMSX486 (58.03 mg) were analysed in a recrystallised alumina crucible sealed with a lid in the range between 1000°C and 1400°C at a heating/cooling rate of 10°C/min under argon (flow rate: 100 ml/min). Data analysis to identify γ' solvus, solidus and liquidus temperatures was performed using Microsoft Excel. Full details on the DSC method can be found elsewhere [21].

3.14. Thermo-Calc Phase Diagram Modelling

The chemical composition obtained from the Incotest analysis for CM247LC was used to theoretically model the equilibrium phase composition of the material between 250°C and 1500°C using the commercially available Thermo-Calc Software [22] and the TTNi7 Database.

3.15. Mechanical Testing

The mechanical validation of the SLM processing route was via tensile and creep testing. Bars were built 12 mm diameter and 65 mm long (except where material was limited) using ‘pin-style’ supports. Bars were built both longitudinally and transversely to the build direction (Z-axis) to study the influence of build orientation on mechanical properties.

Following fabrication the bars were subject to different HIP and heat treatments conditions (see Table 3.5 & Table 3.6) before being machined to the appropriate test-sample geometry.

i. Tensile Testing

All tensile testing was carried out in accordance with the ASTM standard (E8/E8M-09 [23]). CM247LC room temperature tensile testing was carried out in the mechanical testing lab (Met. & Mat. UoB); elevated temperature tensile testing and creep testing was carried out externally by Incotest UK. Tensile samples were machined to standard M8 threaded cylindrical test pieces, $\varnothing 4$ mm, test section as shown in Figure 3.12

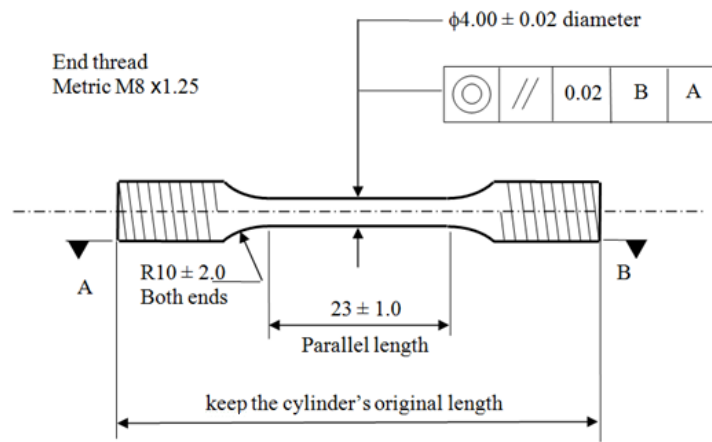


Figure 3.12: Dimensioned drawing of M8 threaded tensile test bar used for room temperature and elevated temperature tensile tests.

All tensile testing was carried out using a physically connected extensometer and the constant crosshead speed method. Crosshead speed was set at 0.35 mm/min to determine yield (upto 0.2% proof stress). This value was determined in accordance with section 7.6.3.3 of the ASTM standard which states that the crosshead speed should be set to 0.015 ± 0.003 mm/mm/min of the original reduced section length (23 mm for the M8 threaded test bar) [23]. Following 0.2% proof stress, the crosshead speed in the elevated temperature tensile tests was increased to 1.5 mm/min in accordance with section 7.6.4 of the ASTM standard [23] which states that to determine tensile strength, the crosshead speed should be set to between 0.05 and 0.5 mm/mm/min of the original reduced section length. Room temperature tests were allowed to continue at 0.35 mm/min until failure.

For each test point, 3 samples following a similar processing route were tested. Room temperature tests were carried out with the aim of demonstrating the differences in build orientation and the application of the HIP treatment whereas the elevated temperature tests were all carried out using vertical test bars with the same process route. IN625 samples were all tested in the as-fabricated condition. Table 3.9 lists the test conditions and the process route for the CM247LC bars, Table 3.10 lists the test conditions and process route for the CMSX486 bars and Table 3.11 lists the test conditions and process route for the IN625 bars.

Table 3.9: Tensile testing conditions for SLM fabricated CM247LC samples.

Temperature	Process Route	Build Orientation	No. of Samples	Test Location
Room Temp.	HT ¹	Vertical	3	UoB
Room Temp.	HT ¹	Horizontal	3	UoB
Room Temp.	HIP & HT ²	Vertical	3	UoB
Room Temp.	HIP & HT ²	Horizontal	3	UoB
700°C	HIP & HT ²	Vertical	3	Incotest
760°C	HIP & HT ²	Vertical	3	Incotest
900°C	HIP & HT ²	Vertical	3	Incotest

1. SLM fabricated and Heat Treated (1260°C, 2h, GQ; 980°C, 5h, AC; 870°C, 20h, AC)
2. SLM fabricated, HIPed (1180°C, 150 MPa, 4h) and Heat Treated (1260°C, 2h, GQ; 980°C, 5h, AC; 870°C, 20h, AC)

Table 3.10: Tensile testing conditions for SLM fabricated CMSX486 samples.

Temperature	Process Route	Build Orientation	No. of Samples	Test Location
Room Temp.	HT ¹	Vertical	3	Incotest
Room Temp.	HT ¹	Horizontal	3	Incotest

1. SLM fabricated and Heat Treated (1318°C, 2h (*see HT section*), GQ; 1140°C, 6h, AC; 871°C, 20h, AC)

Table 3.11: Tensile testing conditions for SLM fabricated IN625 samples.

Temperature	Process Route	Build Orientation	No. of Samples	Test Location
Room Temp.	As- Fabricated	Vertical	3	Incotest
Room Temp.	As- Fabricated	Horizontal	3	Incotest
540°C	As- Fabricated	Vertical	3	Incotest
540°C	As- Fabricated	Horizontal	3	Incotest
760°C	As- Fabricated	Vertical	3	Incotest
760°C	As- Fabricated	Horizontal	3	Incotest

ii. Creep Testing

High temperature creep testing was carried out at Incotest UK in order to establish the effect of the process route and the overall high temperature creep performance of the SLM fabricated material via this process route. 2 samples were tested under each condition for CM247LC and CMSX486, creep testing was in accordance with BS EN 2002-005:2007 [24]. Creep specimens were machined to standard 14G specification with \varnothing 4 mm test section as shown in Figure 3.13.

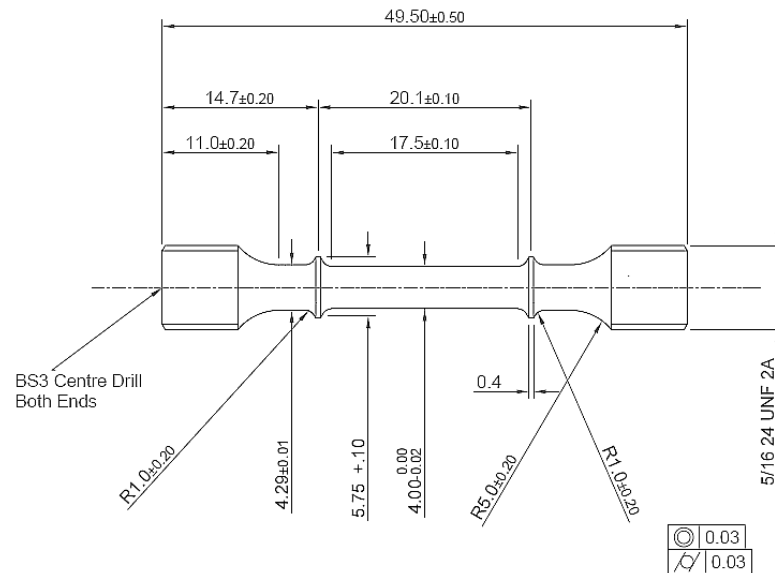


Figure 3.13: Dimensioned drawing showing 14G creep specimen.

All creep tests were carried out at 1050°C, 100 MPa; Table 3.12 and Table 3.13 list specimen conditions for CM247LC and CMSX486 samples respectively.

Table 3.12: Creep test conditions for CM247LC specimens.

Temperature/Stress	Process Route	Build Orientation	No. of Samples	Test Location
1050°C/100 MPa	HT ¹	Vertical	2	Incotest
1050°C/100 MPa	HT ¹	Horizontal	2	Incotest
1050°C/100 MPa	HIP & HT ²	Vertical	2	Incotest
1050°C/100 MPa	HIP & HT ²	Horizontal	2	Incotest

1. SLM fabricated and Heat Treated (1260°C, 2h, GQ; 980°C, 5h, AC; 870°C, 20h, AC)
2. SLM fabricated, HIPed (1180°C, 150 MPa, 4h) and Heat Treated (1260°C, 2h, GQ; 980°C, 5h, AC; 870°C, 20h, AC)

Table 3.13: Creep test conditions for CMSX486 specimens.

Temperature/Stress	Process Route	Build Orientation	No. of Samples	Test Location
1050°C/100 MPa	HT ¹	Vertical	2	Incotest
1050°C/100 MPa	HT ¹	Horizontal	2	Incotest

1. SLM fabricated and Heat Treated (1318°C, 2h (*see HT section*), GQ; 1140°C, 6h, AC; 871°C, 20h, AC)

3.16. Summary

This chapter has presented the key experimental techniques used in the generation of the results presented and discussed in the following chapters. The practical application of the SLM process is further outlined in appendix A and a summary of the central composite design of experiments methodology employed for the parametric studies of CMSX486 and IN625 is presented in Appendix B.

3.17. References

- [1] Thümmel F, Oberacker R. Introduction to Powder Metallurgy. London: The Institute of Materials, 1993.
- [2] LECO. Carbon and Sulfur Determination— LECO Induction Furnace Instruments. 2007.
- [3] LECO. Oxygen and Nitrogen Determination Inert Gas Fusion Instruments. 2007.
- [4] Rouessac F, Rouessac A. Chemical Analysis: Modern Instrumentation Methods and Techniques. New York: Wiley, 2007.
- [5] ESTechnology. ES Technology Website (<http://www.estechology.co.uk>). 2012.
- [6] EOS. EOS Website (<http://www.eos.info/>). 2012.
- [7] Hofmann. Hofmann Innovation Group Website - Concept Laser (<http://www.hofmann-innovation.com/en/technologies/direct-cusing-manufacturing.html>). 2012.
- [8] Donachie MJ, Donachie SJ. Superalloys: A Technical Guide. Ohio: ASM International, 2002.
- [9] Kim IS, Choi BG, Seo SM, Kim DH, Jo CY. Effect of heat treatment on the tensile properties of poly-crystal and DS CM247LC alloy. 2007;124-126:1401.
- [10] Wilson BC, Hickman JA, Fuchs GE. The effect of solution heat treatment on a single-crystal Ni-based superalloy. Journal of Metals 2003;55:35.
- [11] Gabriela B, Lauralice C, George T. Gas Quenching. Quenching Theory and Technology, Second Edition. CRC Press, 2010.
- [12] ASM Speciality Handbook: Nickel, Cobalt, and Their Alloys. Ohio: ASM International, 2000.
- [13] ASM Metals Handbook, Vol. 9 - Metallography and Microstructures. Ohio: ASM International, 1992.
- [14] Reimer L. Scanning Electron Microscopy: Physics of Image Formation and Microanalysis. London: Springer, 1998.
- [15] HKL Channel 5 Tango (Mapping) & Mambo (Pole Figures). HKL.
- [16] Rasband W. ImageJ 1.34u. National institutes of health.
- [17] ImageJ Documentation Webpage (<http://rsbweb.nih.gov/ij/docs/index.html>) 2012.
- [18] CTPro. Metris, 2012.
- [19] Avizo Standard 6.3 Visualisation Sciences Group (VSG)
- [20] Stock SR. MicroComputed Tomography: Methodology and Applications. London: CRC Press, 2008.
- [21] Höhne G, Hemminger W, Flammersheim H-J. Differential scanning calorimetry. London: Springer, 2003.
- [22] Thermo-Calc Software (<http://www.thermocalc.se>). Stockholm Sweden, 2010.
- [23] Standard Test Methods for Tension Testing of Metallic Materials [Metric] Designation: E8/E8M – 09. ASTM International, 2012.
- [24] Aerospace series — Test methods for metallic materials Part 005: Uninterrupted creep and stress-rupture testing (BS EN 2002-005:2007). BSi, 2012.

CHAPTER 4: PROCESS OPTIMISATION: INFLUENCE OF THE SLM PARAMETERS ON THE MICROSTRUCTURE & INTEGRITY

This chapter is concerned with the SLM process optimisation for three Ni-Superalloys. In each case, the study was carried out in a unique fashion based on optimisation criteria for each material. Additionally, microstructure and size distribution of the as-received powder are presented.

4.1 Introduction

Based on the literature survey of weld cracking in high γ' volume fraction nickel superalloys (Chapter 2; Section 2.14) it was anticipated that cracking would be a prominent feature of the SLM-fabricated structures of CM247LC and CMSX486. Preliminary samples of CM247LC SLM-fabricated using the EOSintM270 facility proved this correct and an optical micrograph of the cracks observed can be seen in Figure 4.1.

Studies were undertaken to investigate the influence of the SLM processing parameters on the cracking behaviour and density of the as-fabricated material with the aim of reducing/eliminating this phenomenon as well as identifying a likely mechanism and root cause of this crack formation.

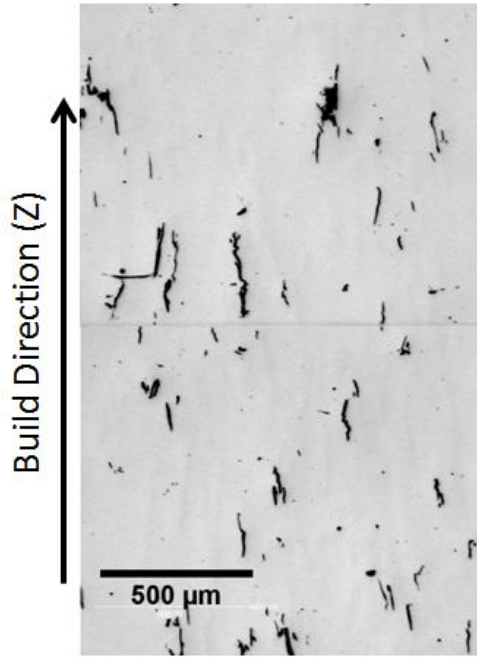


Figure 4.1: Optical micrograph showing cracking within a preliminary SLM-fabricated sample of CM247LC (X-Z plane).

Prior to SLM processing, an examination was carried out on the as-received powder to confirm its size distribution, morphology and chemical composition. Qualitative evidence provided by Concept Laser states that in order for the SLM process to work well, metal powder should be classified within the size fraction of +15-53 μ m and have a regular spherical morphology to ensure good spreading. Powder containing fine particles in the -15 μ m range will bind together and spread poorly during the recoating operation. Over-sized powder particles (+53 μ m) will tend to be swept across the surface of the build into the overflow area when working with 20 μ m slice thickness. Particles up to the 53 μ m size limit can be accommodated within a 20 μ m layer thickness build due to the roughness of the previous build layers and shrinkage in the Z-direction due to the consolidation of the powder following melting.

4.2 CM247LC Parametric Studies

i. Powder Chemical Analysis: Results & Discussion

The powder supplier provided chemical composition information; in order to validate this, independent chemical analysis was carried out on a sample of the as-received CM247LC argon gas-atomised powder as provided by LPW for comparison against the nominal composition provided by Cannon-Muskegon [1]. Additionally, two further samples of SLM consolidated CM247LC were sent for chemical analysis. This was done to investigate the effect of SLM on the material composition to ensure that element vaporisation (See Das [2]) and oxygen pick-up were not significant factors in the processing of nickel alloys. The two SLM samples were processed under conditions considered close to ‘normal’ (150 W, 1500 mm/s, 1.28 J/mm²) and ‘higher-energy’ (200 W, 400 mm/s, 6.29 J/mm²); All other parameters were kept as standard. The results are presented in Table 4.1.

Table 4.1: Chemical analysis result for CM247LC powder, 150 W, 1500 mm/s SLM sample and 200 W, 400 mm/s SLM sample compared against nominal composition [1] (wt.% unless otherwise stated)

	C	Cr	Ni	Co	Mo	W	Ta	Ti	Al	B
Nominal [1]	0.07	8.00	Bal.	9.00	0.50	10.00	3.20	0.70	5.60	0.015
Powder	0.066	8.19	Bal.	9.36	0.46	10.30	3.29	0.71	5.74	0.017
150W, 1500mm/s	0.066	8.10	Bal.	9.22	0.49	10.30	3.32	0.72	5.80	0.018
200W, 400mm/s	0.067	7.77	Bal.	9.21	0.51	10.90	3.52	0.76	5.78	0.018
	Zr	Hf	Si	S	P	Fe	Mg	N	O	
Nominal[1]	0.010	1.40	≤0.03	≤15ppm	N/A	N/A	N/A	N/A	N/A	
Powder	0.011	1.39	0.04	<0.001	0.006	<0.01	<0.001	0.002	0.016	
150W, 1500mm/s	0.012	1.40	0.04	<0.001	0.006	<0.01	<0.001	0.003	0.007	
200W, 400mm/s	0.012	1.47	0.04	<0.001	0.007	<0.01	<0.001	0.003	0.015	

The results presented in Table 4.1 show a generally good agreement between the nominal composition and the supplied CM247LC powder from LPW. The largest discrepancy is that of Co showing a +0.36 wt.% difference when compared to the nominal value. The low levels

of the detrimental S, P, Fe and Mg are particularly encouraging and show a good control of contaminants within the atomisation process.

The only concerning value is the 0.04 wt.% Si which should ideally be lower than 0.03 wt.% however, considering this is only marginally over the nominal value and taking into account the excellent control of all the other potentially detrimental elements, the Si level was considered acceptable. Based on this good correlation between the nominal and the supplied powder, it was decided that the chemistry breakdown supplied with the powder from the manufacturer would be sufficient validation for the CMSX486 and IN625 powders.

Following the SLM process, it can be seen that with the increasing process energy the values for Co and Cr decrease from those seen in the supplied powder (Co: 9.36 wt.% → 9.22 wt.% → 9.21 wt.%; Cr: 8.19 wt.% → 8.10 wt.% → 7.77 wt.%). This can most likely be attributed to the vaporisation of these elements under laser processing, the boiling points under standard pressure for Co and Cr are 2877°C and 2665°C [2] respectively; these boiling points are amongst the lowest in the alloy. The increases seen in some of the other elements are due to their increased concentrations due to the losses of these elements.

Al shows the lowest boiling point of a metallic element within the alloy (2447°C [2]) however the wt.% appears to increase and then decrease with increasing SLM energy conditions; this could be due to Al vaporisation. It is possible that the increase in Al wt.% seen under the 150 W, 1500 mm/s condition (5.74 wt.% → 5.8 wt.%) is the effect of the vaporisation of Cr and Co having greater overall influence than that of the Al vaporisation, whereas the reduction in Al under the 200 W, 400 mm/s (5.8 wt.% → 5.78 wt.%) is the Al vaporisation having a greater overall effect than the vaporisation of Cr and Co.

These compositional changes in the SLM processed material show that vaporisation does have the potential to alter alloy composition following SLM, however considering the small variation between the powder and the 150W, 1500mm/s SLM processed material, it can be concluded that this is not a key area of interest for these studies and was not further investigated.

The oxygen level shows a reduction when compared with the powder under the 150 W, 1500 mm/s SLM conditions, yet an increase under the higher 200 W, 400 mm/s SLM conditions. The exact cause for this is unknown, but it is most likely due to a marginally different oxygen level under the Argon atmosphere which is only maintained through the flooding of the process chamber and controlled down to 0.1%. It was generally concluded however that as the oxygen levels were less than that of the powder under both SLM process conditions and considering that the argon atmosphere cannot easily be improved within the M2 SLM system then the issue of oxide pick-up under laser processing is at this stage not a concern to these investigations.

ii. Powder Size Analysis: Results & Discussion

The particle sizing results are shown in Figure 4.2 which include key size information (Mean, D10, D50, D90).

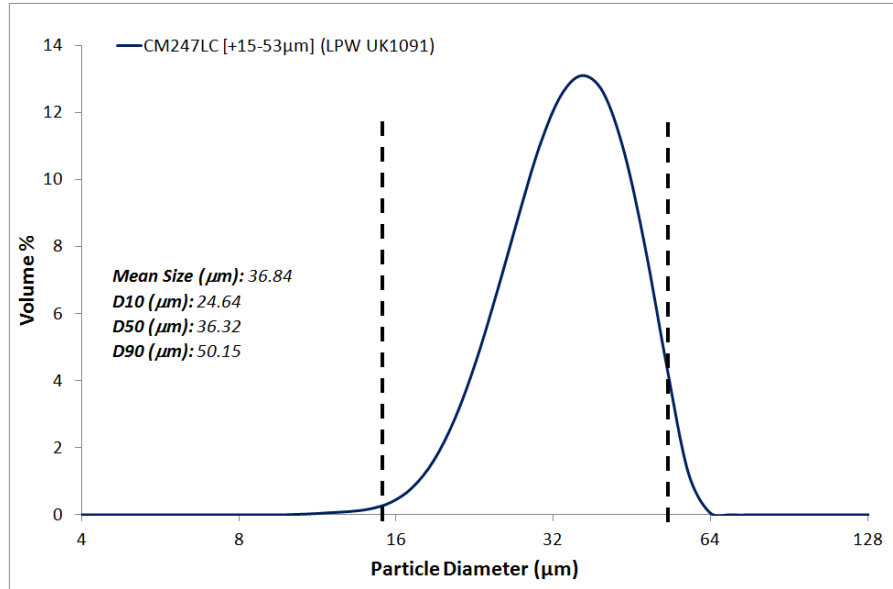


Figure 4.2: Powder size distribution plots for the CM247LC; the vertical dashed lines show the ideal +15-53μm size range.

Figure 4.2 shows that the CM247LC powder has a reasonably good size distribution. The maximum particle size is approximately 64 μm, slightly above the upper ideal limit of 53 μm, likewise the minimum particle size falls slightly below the 15 μm lower boundary. The D10 and D90 values however fall well within these limits and the almost identical Mean and D50 (Median) values combined with the shape of the plot suggests a close to normal distribution of particle size.

The subsequent successful spreading and ease of handling of the powder during SLM confirmed this size distribution as being acceptable.

iii. SEM Powder Examination: Results & Discussion

Micrographs for CM247LC powder are shown in Figure 4.3. Figure 4.4 and Figure 4.5 show further micrographs of the ground and polished CM247LC sample. Powder porosity was calculated by image analysis as a fraction of closed pores compared against overall powder area; a typical micrograph from this set is shown in Figure 4.6 with the key ‘pore-types’ labelled and the porosity data is summarised in Table 4.2. Finally EDS linescans of two

particles (regular spherical and more irregular) are provided in Figure 4.7 and Figure 4.8 respectively in order to show the homogeneous nature of the gas atomised powder.

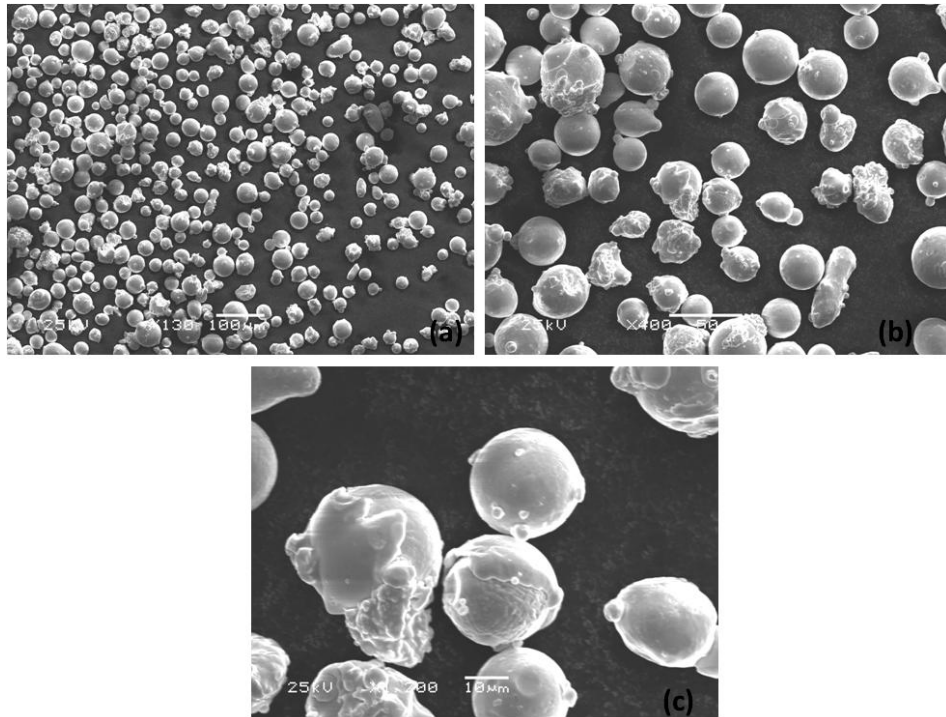


Figure 4.3: Secondary SEM micrographs showing mounted CM247LC powder taken at (a) 130X, (b) 400X, (c) 1200X magnification. Some surface irregularities can be seen on the powder.

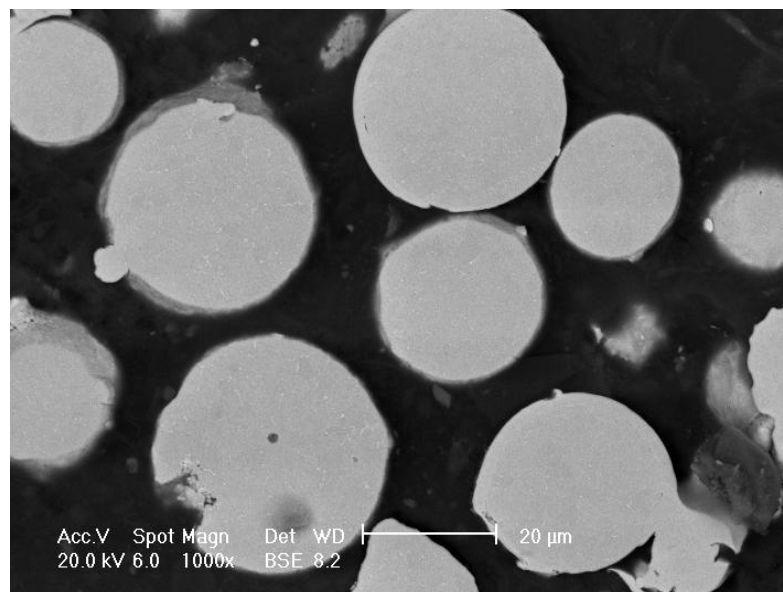


Figure 4.4: Backscattered SEM micrograph showing ground and polished CM247LC powder particles.

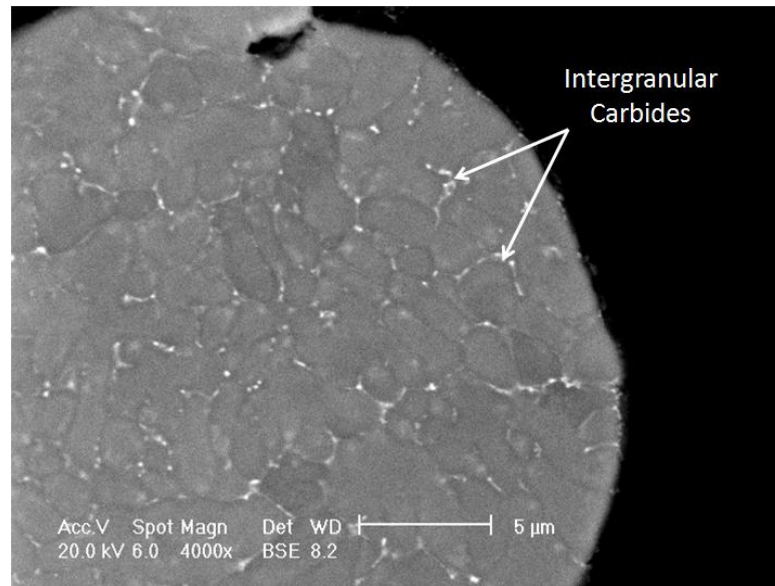


Figure 4.5: Backscattered SEM micrograph showing the grain structure in a single ground and polished CM247LC particle; bright intergranular carbides are labelled.

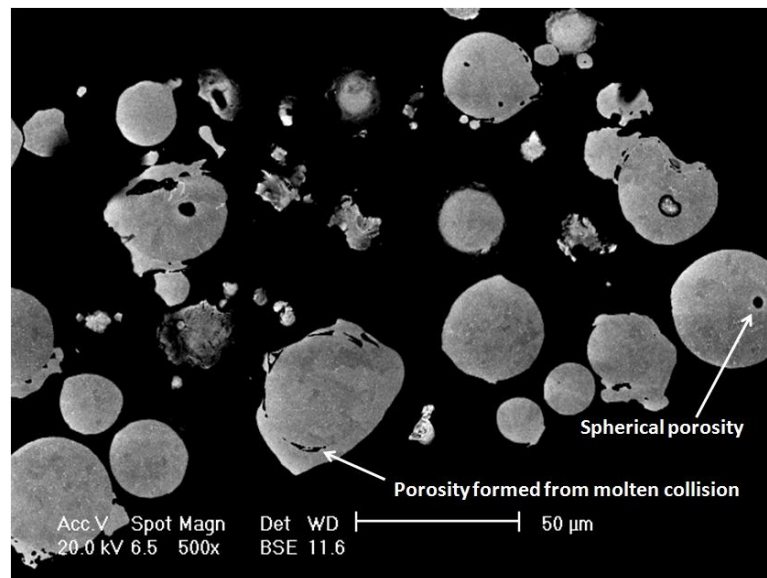


Figure 4.6: Backscattered SEM micrograph typical of the set taken to determine powder porosity via image analysis; key pore features labelled.

Table 4.2: Summary of porosity data calculated by image analysis of ground CM247LC powder.

Total number of particles analysed	585
Minimum pore size to be measured <i>(to eliminate noise)</i>	0.30 μm^2
Total number of pores analysed	462
Mean Pore equivalent diameter	1.79 μm
Maximum Pore equivalent diameter	11.00 μm
% Porosity of the analysed powder	0.88 %

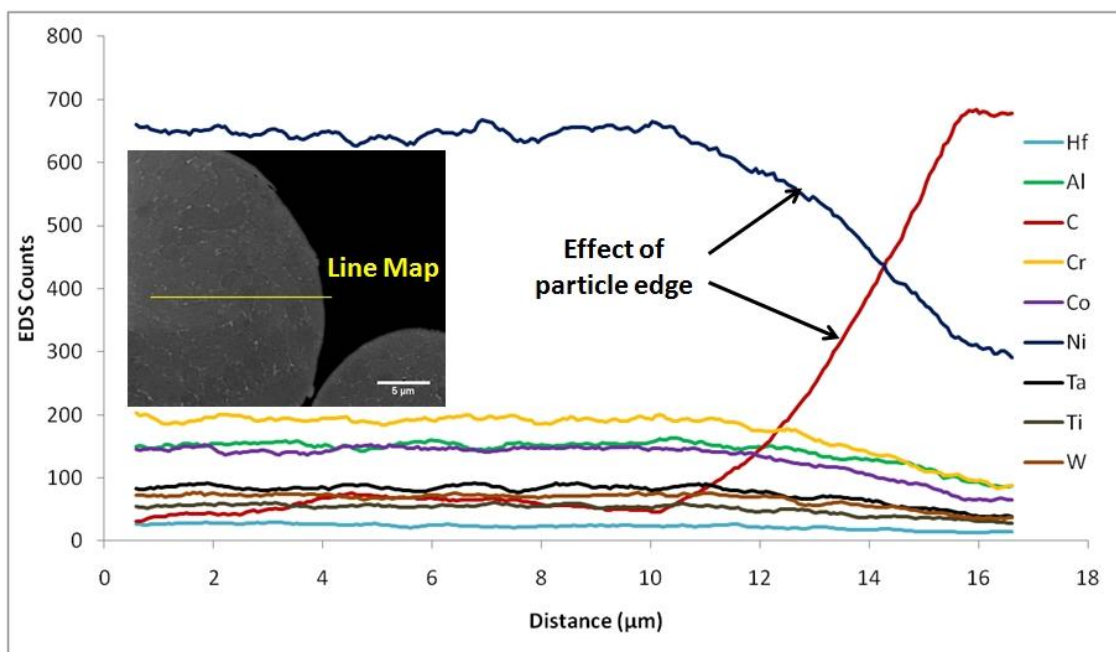


Figure 4.7: EDS linescan for a spherical CM247LC powder particle showing counts against distance across linescan (inset: micrograph of particle with linescan marked in yellow).

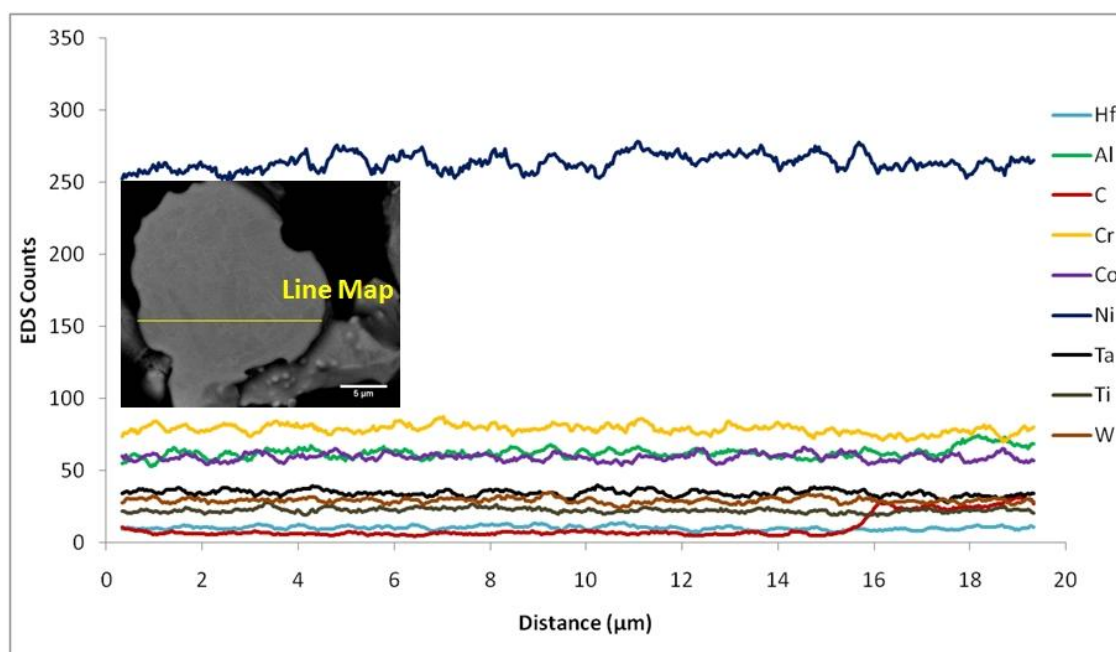


Figure 4.8: EDS linescan for an irregular CM247LC powder particle showing counts against distance across linescan (inset: micrograph of particle with linescan marked in yellow).

Figure 4.3 shows the CM247LC powder to display a reasonably spherical and regular morphology, although no measurement was performed using microscopy, the particle sizes appear to correspond well to the particle size analysis presented previously (Section 4.2.ii.).

Some of the particles display an irregular surface. This has been caused by the collision of a liquid droplet against a solid particle and is more clearly shown in the ground SEM images (Figure 4.6).

The ground and polished SEM micrographs shown in Figure 4.4 and Figure 4.5 illustrate the overall spherical nature of the powder particles although some display fine satellite particles. The backscattered SEM micrograph in Figure 4.5 shows a typical particle to display a fine equiaxed grain structure with bright carbides precipitated along the grain boundaries. There does not appear to be significant elemental segregation or any variation in the grain structure from the edge to the centre of the particle. This is confirmed in Figure 4.7 and Figure 4.8 which shows EDS linescans across individual particles. Neither of these scans appear to show significant variation in composition except for the increase in carbon caused by the mounting Bakelite at their boundary. The small variations in nickel and the heavier elements is due to the detection of the grain boundary carbides and again does not represent solidification segregation.

Figure 4.6 shows a typical micrograph used for the quantification of the porosity within the powder; as with the previous micrographs, some small satellite particles can be seen attached to the outside of the larger spherical particles. Porosity appears to fall into two categories: circular pores which are formed due to the capture of gas within the molten droplet and the subsequent solidification of each particle; this is typically referred to as ‘gas-porosity’ [3]. The second category appears to show a fully formed spherical particle coated in further material. This forms when a molten droplet collides with a fully formed particle and ‘crescent shaped’ porosity may be formed at the interface of these two bodies. It is suggested that this phenomenon is the cause of the irregular outer appearance as seen in some of the particles, Figure 4.3.

Table 4.2 shows a summary of the porosity size analysis. The majority of the pores are small as shown by the mean equivalent pore diameter and the overall porosity (0.88 %) is very low. The larger pores (as represented by the largest equivalent pore diameter of 11 μm) are due to the crescent-type of porosity.

The outer morphology and porosity can be disrupted by molten droplets colliding with solidified particles, however the overall porosity is still small and, without altering the powder preparation method to other more expensive methods (e.g. Plasma Rotating Electrode Process (PREP)), the formation of these types of pores is difficult to eliminate.

iv. SLM Parametric Study: Introduction

The parametric study carried out investigated the influence of three SLM process-parameters on the cracking behaviour: Initially the laser power and scan speed and secondly the influence of the scan spacing. Images were sampled and analysed as discussed in chapter 3 from both the ‘midline’ and ‘edgeline’ of the sample to produce the defect quantification results. Additional micrographs were taken under higher magnification conditions in order to characterise the cracks.

Table 4.3 details the SLM parameters used to produce samples for this analysis and characterisation. Figure 4.9 shows a photograph of one of the typical sets of samples produced in a single build; each sample could be produced using a different parameter set thus reducing the SLM build-time required.

Table 4.3: Parameters used to produce samples for analysis within the parametric study of SLM-fabricated CM247LC.

Laser Power (W)	Laser Scan Speed (mm/s)						
	400	600	800	1000	1250	1500	2000
150	✓	✓	✓	✓	✓	✓	X
180	✓	✓	✓	✓	✓	X	X
200	✓	✓	✓	✓	✓	X	✓

Laser Power/Speed	Scan Spacing (a1)			
	0.53	0.4	0.3	0.2
200W, 2000 mm/s	✓	X	✓	✓
150W, 1500 mm/s	✓	✓	✓	✓

✓ = Built; X = Not Built

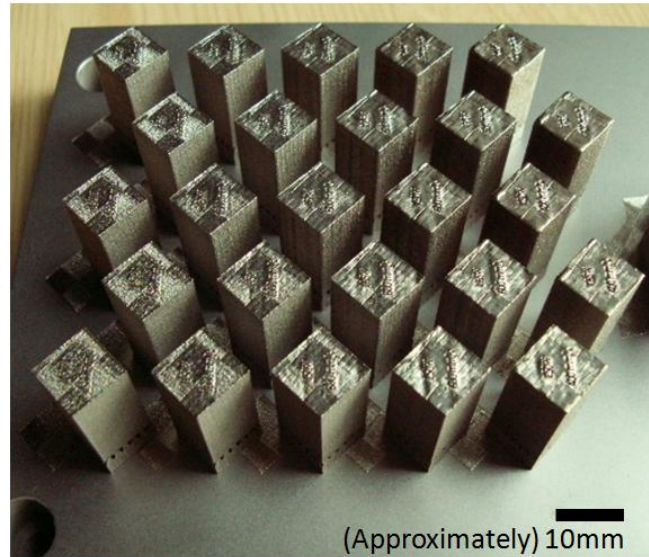


Figure 4.9: Typical set of samples produced during the SLM parametric study for CM247LC.

v. SLM Parametric Study: Microstructural Results

The microstructural observations of the cracking within the SLM-fabricated samples are presented below.

The combination of laser power, scan speed and spacing can give an indication as to energy density (J/mm^2) similar to methods used elsewhere [4, 5], Equation 4-1:

Equation 4-1: Equation defining SLM process energy density (J/mm²) (Note: ‘a1’ is a dimensionless term)

$$\text{Energy Density (J/mm}^2\text{)} = \frac{\text{Laser Power (W)}}{\text{Scan Speed (mm/s)} \times \text{Spacing (a1)} \times \text{Focus Dia. (0.15 mm)}}$$

The cracking observed in the SLM-fabricated CM247LC can be divided into 4 regimes; for the purposes of clarity, these four sample types are initially designated:

- **VHE** - Very High Energy ($\text{VHE} \geq 3.77 \text{ J/mm}^2$)
- **HE** - High Energy ($3.77 \text{ J/mm}^2 > \text{HE} \geq 3.14 \text{ J/mm}^2$)
- **LE** - Low Energy ($3.14 \text{ J/mm}^2 > \text{LE} \geq 1.51 \text{ J/mm}^2$)
- **VLE** - Very Low Energy ($1.51 \text{ J/mm}^2 > \text{VLE}$)

Figure 4.10 shows a typical micrograph from a VHE set of parameters (200 W, 400 mm/s). The micrograph shows a high density of irregular ‘jagged’ cracks which have only a little directionality with respect to the building direction. There also appear to be large pores, typically in the size range of 50-100 μm .

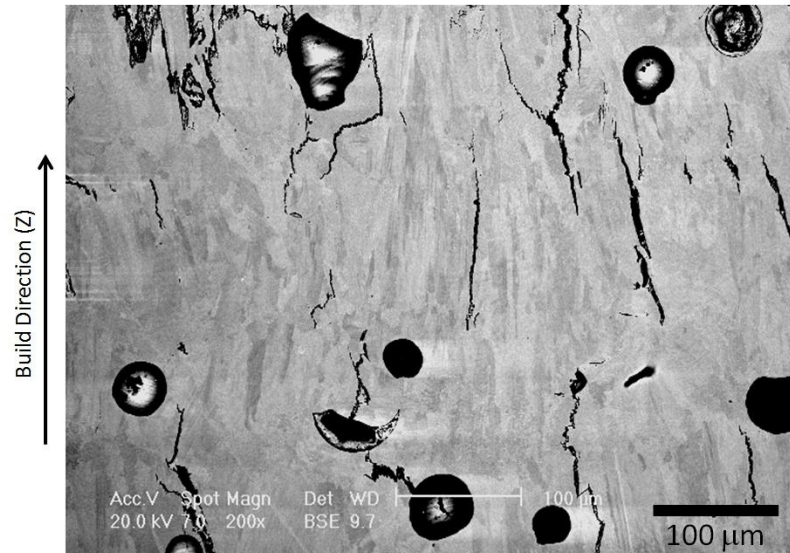


Figure 4.10: Typical BSE SEM micrograph from a VHE sample (200W, 400 mm/s) showing dense jagged cracking and large pores.

Reducing the energy slightly eliminates the occurrence of the large pores as seen in the VHE samples as shown in Figure 4.11 (150 W, 600 mm/s). This regime shows dense ‘jagged’ cracking still only displaying a limited directionality with respect to the build direction.

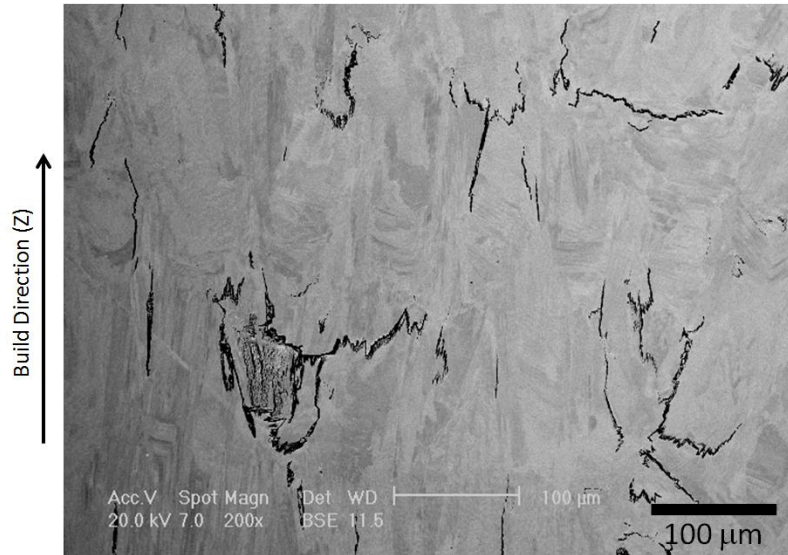


Figure 4.11: Typical BSE SEM micrograph showing HE sample (150 W, 600 mm/s) displaying dense ‘jagged’ cracks with limited directionality with respect to the build direction.

Under high magnification, the ‘jagged’ cracks show an internal surface consisting of tiny dendritic protrusions of only 2-3μm in length as seen in Figure 4.12. Furthermore, in some cases these cracks have formed such a large defect within the material that an entire section of the material has been removed (possibly during sample preparation), Figure 4.13, revealing an entire face consisting of these dendritic protrusions which previously would have constituted the internal surface of a crack.

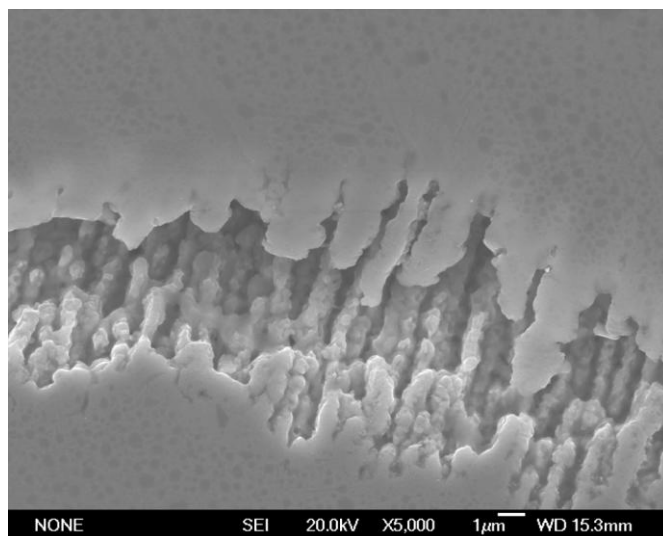


Figure 4.12: SE SEM micrograph showing dendritic protrusions from the internal surface of a ‘jagged’ crack

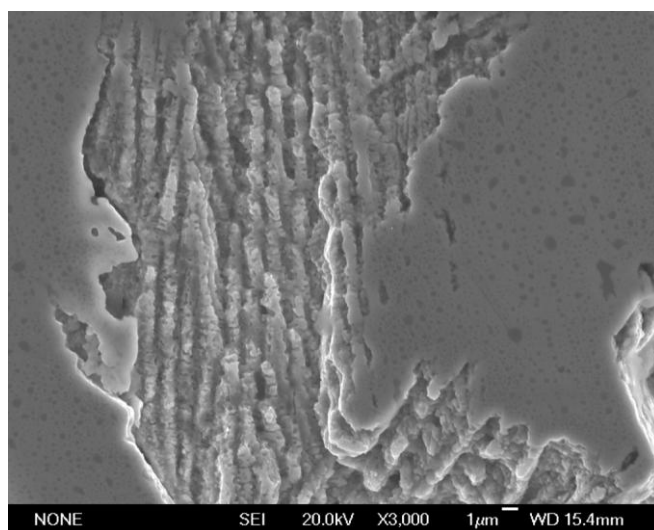


Figure 4.13: SE SEM micrograph showing dendritic protrusions from a ‘jagged’ crack surface

Further reducing the process energy results in a dramatic change in the cracking character as seen in LE samples, Figure 4.14 (150 W, 1000 mm/s). There appear to be generally fewer cracks and they appear to be dominantly smooth rather than ‘jagged’ showing a strong directionality with respect to the build direction. Under high magnification, the smooth cracks do not show the dendritic protrusions on the crack walls as seen in Figure 4.15. Additionally the higher magnification examination (in X-Z and X-Y planes) of some of the finer examples of these cracks shows that they appear to lie along lines of fine carbides with a series of voids

preceding the crack tip, at triple point intersections and along film-like carbides as seen in the series of micrographs presented in Figure 4.16. IPF coloured EBSD maps of three typical examples of these cracks are presented in Figure 4.17.

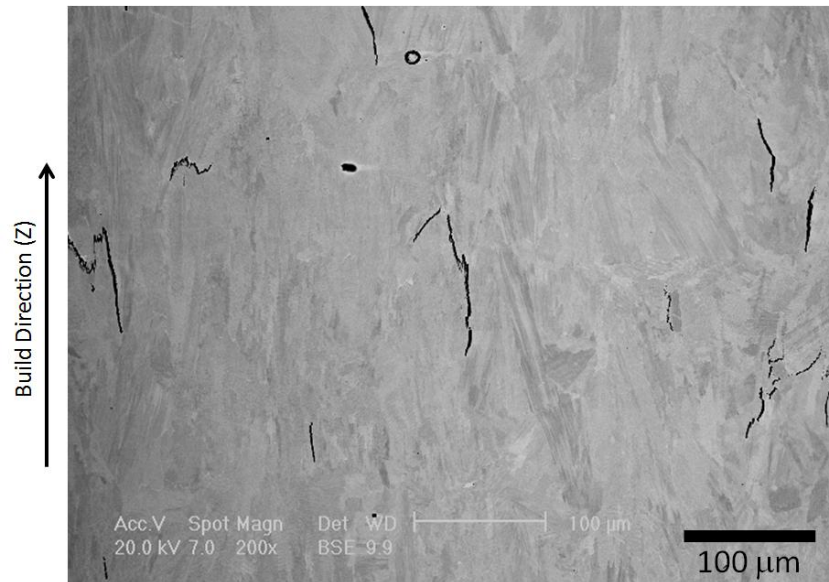


Figure 4.14: BSE SEM micrograph of a typical LE sample (150 W, 1000 mm/s) showing a low occurrence of the ‘jagged’ cracking and a dominant ‘clean’ style of cracking. These cracks show a strong directional alignment to the build direction.

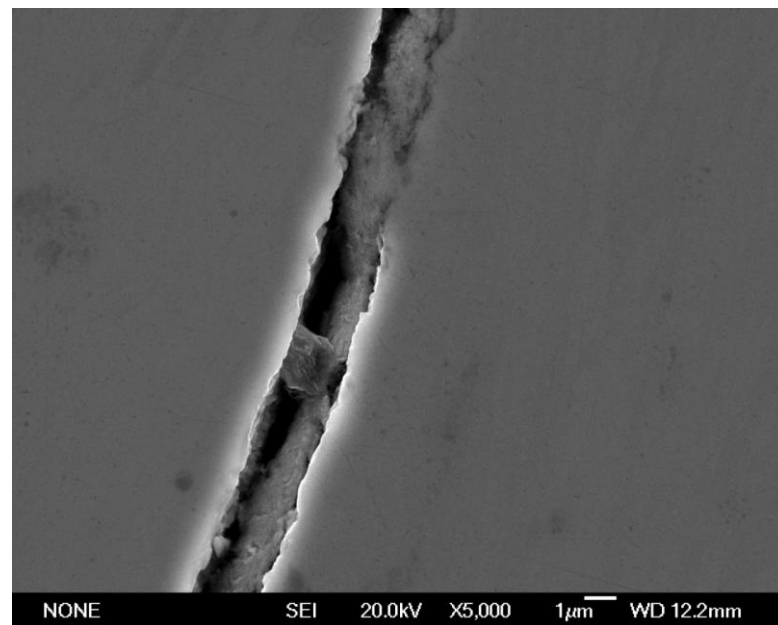


Figure 4.15: SE SEM micrograph showing high magnification detail of a ‘clean’ crack.

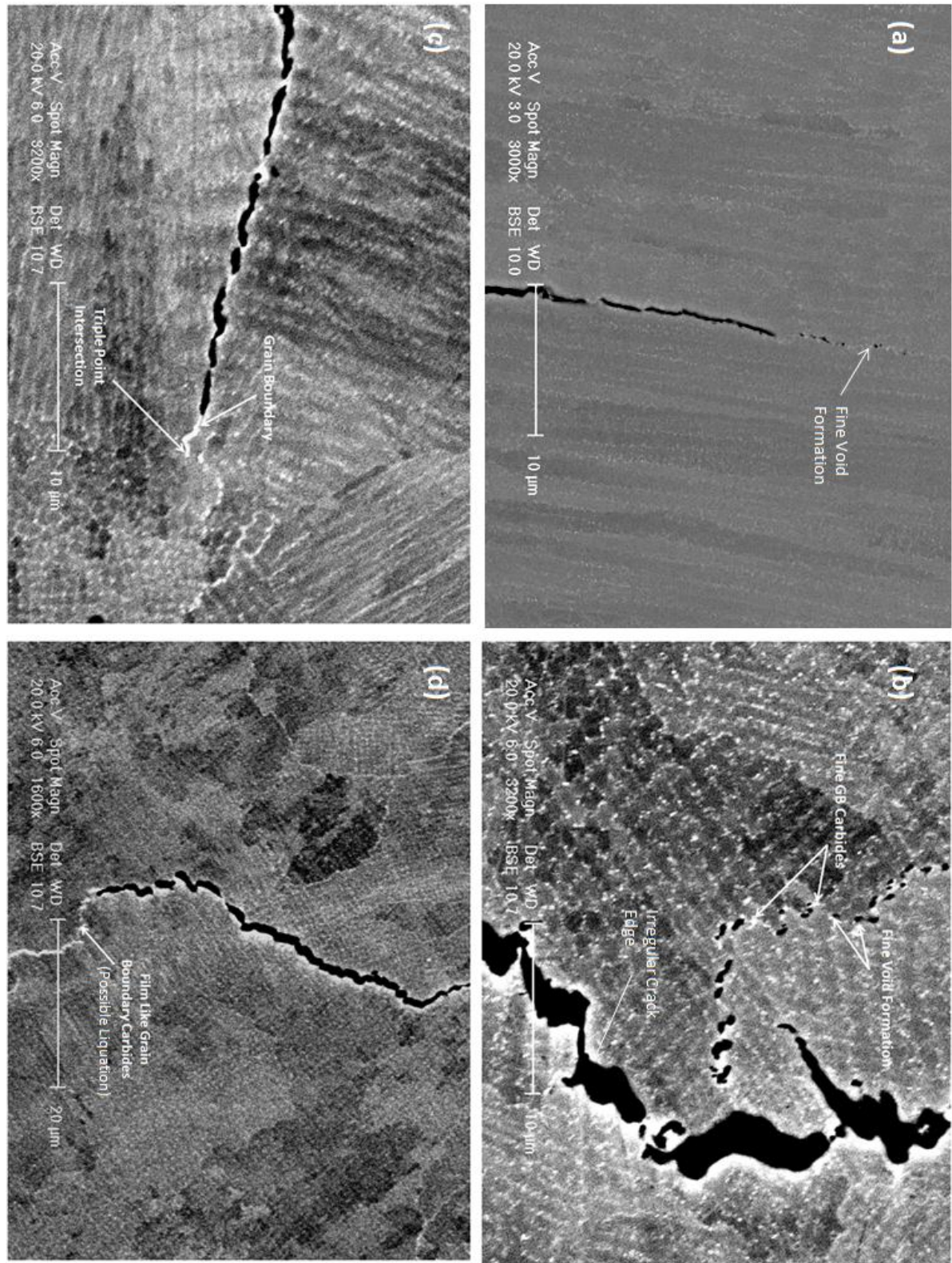


Figure 4.16:BSE SEM micrographs showing grain boundary crack structure: (a) X-Z plane, showing void formation along very fine line of GB carbides; (b) X-Y plane, showing fine void formation along grain boundary next to GB carbides; (c) X-Y plane, showing fine crack-tip with crack lying along a grain boundary originating at a triple-point intersection; (d) X-Y plane, showing crack lying on a grain boundary displaying film-like formation of carbides.

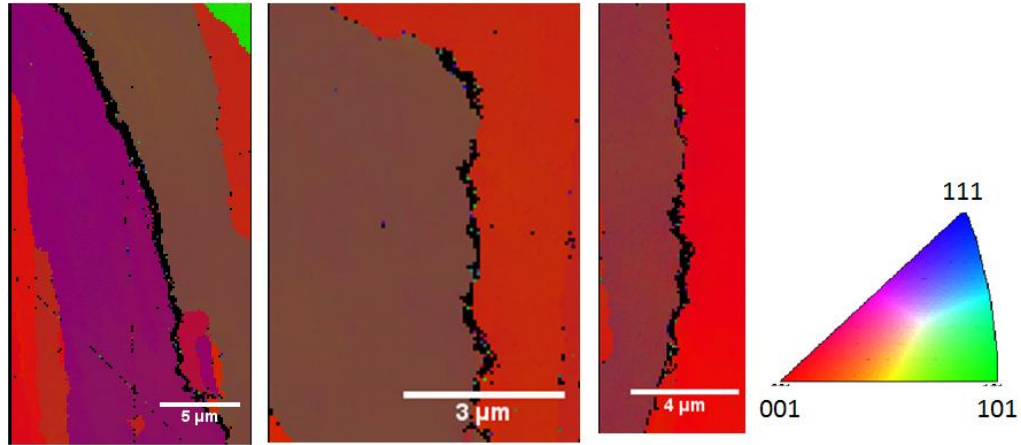


Figure 4.17: IPF coloured EBSD maps of three typical ‘smooth’ style cracks in SLM deposited CM247LC.

Finally, under VLE parameters the crack density appears to be further reduced (retaining the ‘clean’ style) however large volumetric defects open as seen in Figure 4.18 (150 W, 1500 mm/s).

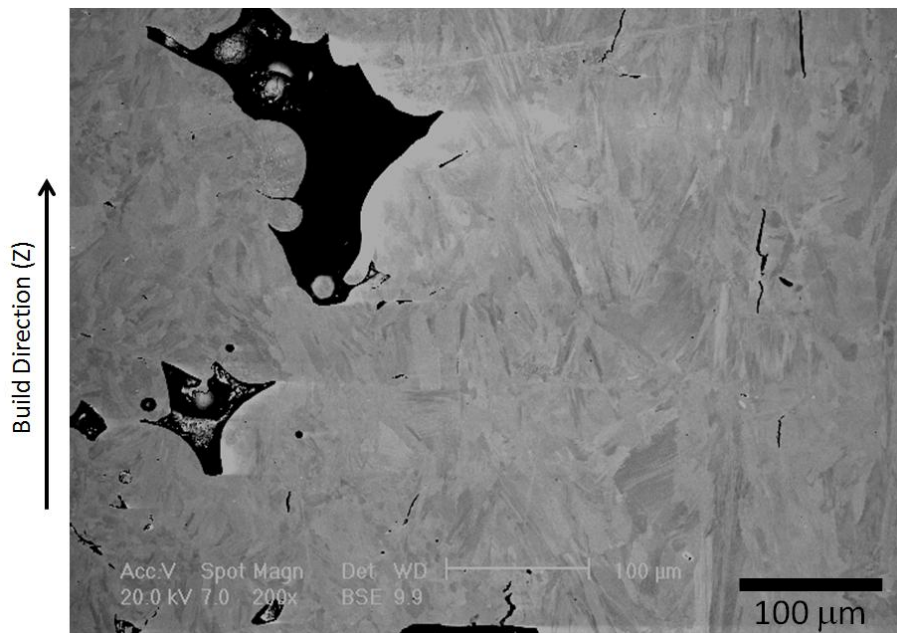


Figure 4.18: BSE SEM micrograph of a typical VLE sample (150 W, 1500 mm/s) showing ‘clean’ style cracks and large volumetric defects.

By examining the micrographs of each of the samples produced for the study it was possible to empirically categorise the cracking within each of them into one of four categories:

- Dense ‘jagged’ cracks with large pores (VHE)
- Dense ‘jagged’ cracks, no large pores (HE)
- ‘Smooth’ cracking style dominant (LE)
- ‘Smooth’ cracking style dominant, large volumetric defects (VLE)

These observations are summarised in Table 4.4:

Table 4.4: Empirical observations of cracking character within SLM-fabricated samples of CM247LC

Laser Power (W)	Laser Scan Speed (mm/s)						
	400	600	800	1000	1250	1500	2000
150							
180							
200							

Laser Power/Speed	Scan Spacing (a1)			
	0.53	0.4	0.3	0.2
200W, 2000 mm/s				
150W, 1500 mm/s				

	Jagged Cracks & Large Pores		Jagged Cracks
	Smooth Cracks		Smooth Cracks & Volumetric Defects
	Not Built		

vi. SLM Parametric Study: Crack Quantification Results

Figure 4.19 and Figure 4.20 show the crack quantification results for the midline and the edgeline respectively. The figures have been labelled showing the boundaries between the different cracking styles observed as dominant within the samples as presented in the previous section. Error bars indicate the standard error determined for each image within that set. The onset of void formation has been labelled showing an artificially raised data-point due to the limitations of the image analysis method resulting in voids being analysed in the same way as cracks. In general terms these plots show a reduction in cracking density with increasing scan speed over all laser powers; this reduction is accompanied with a shift in dominance from the jagged cracks to the smoother cracking style.

Figure 4.21 shows the difference between the midline and edgeline cracking for each sample in terms of a ‘ Δ Cracking’ value where ‘-ve’ indicates a greater level of cracking on the

sample midline and ‘+ve’ indicates a greater level of cracking along the edgeline. In general the midline shows a greater cracking density than the edgeline at higher scan speeds (corresponding to dominance of the smooth cracking style), but no clear trend under lower scanning speeds.

Figure 4.22 shows the variation of cracking density with energy (J/mm^2); the different sample categories, as previously defined, have been labelled. The same general trend as seen in Figure 4.19 and Figure 4.20 is again visible; however the variation within the cracking density over similar energies is high.

Finally Figure 4.23 shows the results for the scan spacing section of the investigation for both power/speed combinations investigated (midline only); this plot has been labelled with relevant microstructural observations. The 150 W, 1500 mm/s line shows how the scan spacing is reduced in order to accommodate the small melt pool and eliminate the volumetric defect formation; however the 200 W 2000 mm/s data shows an increase in cracking density with decreasing scan spacing.

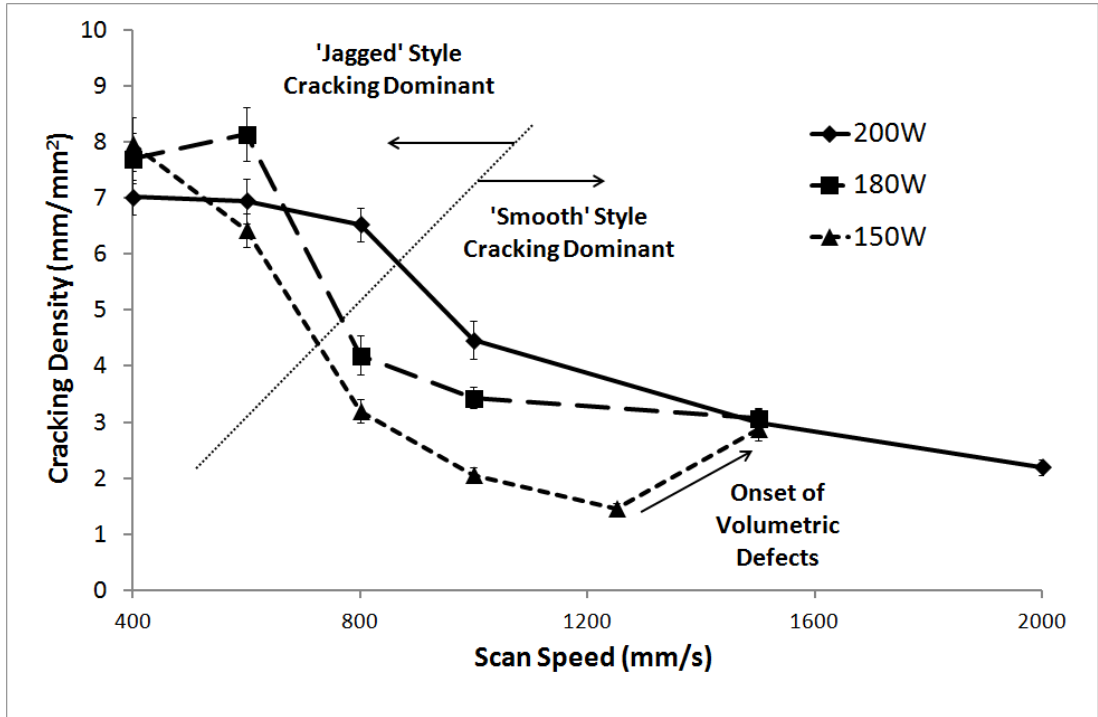


Figure 4.19: Plot showing midline variation of crack density within SLM-fabricated CM247LC samples with respect to scan spacing for three different laser powers. Labels indicate the microstructural observations related to the crack/defect character.

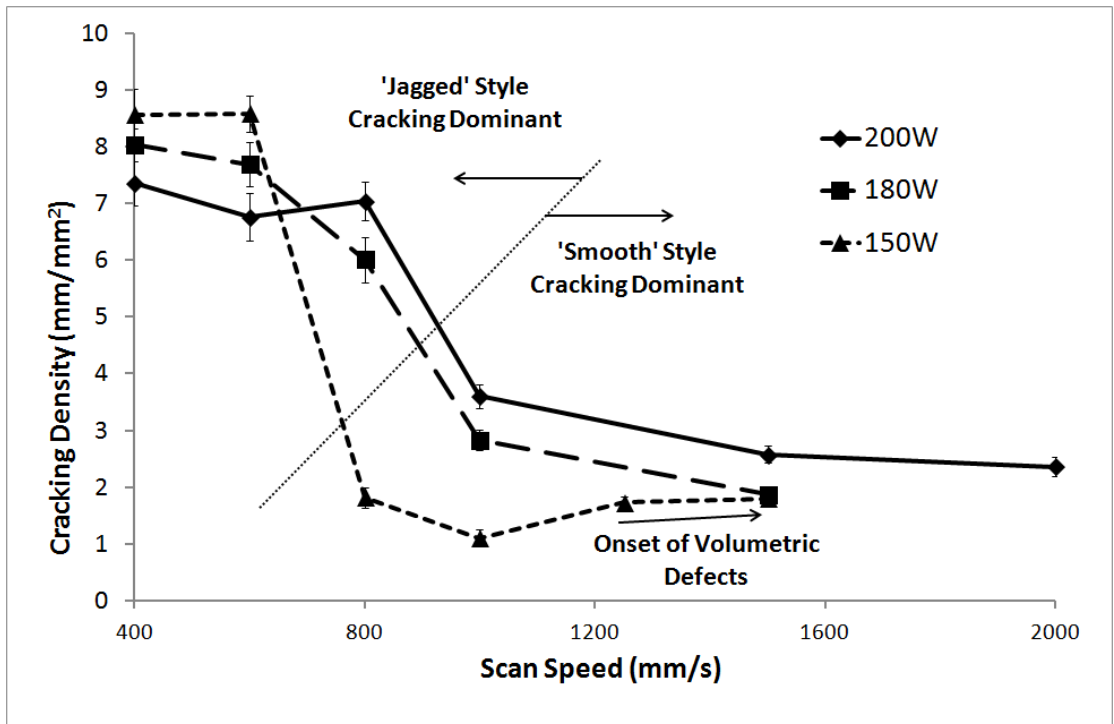


Figure 4.20: Plot showing edgeline variation of crack density within SLM-fabricated CM247LC samples with respect to scan spacing for three different laser powers. Labels indicate the microstructural observations related to the crack/defect character

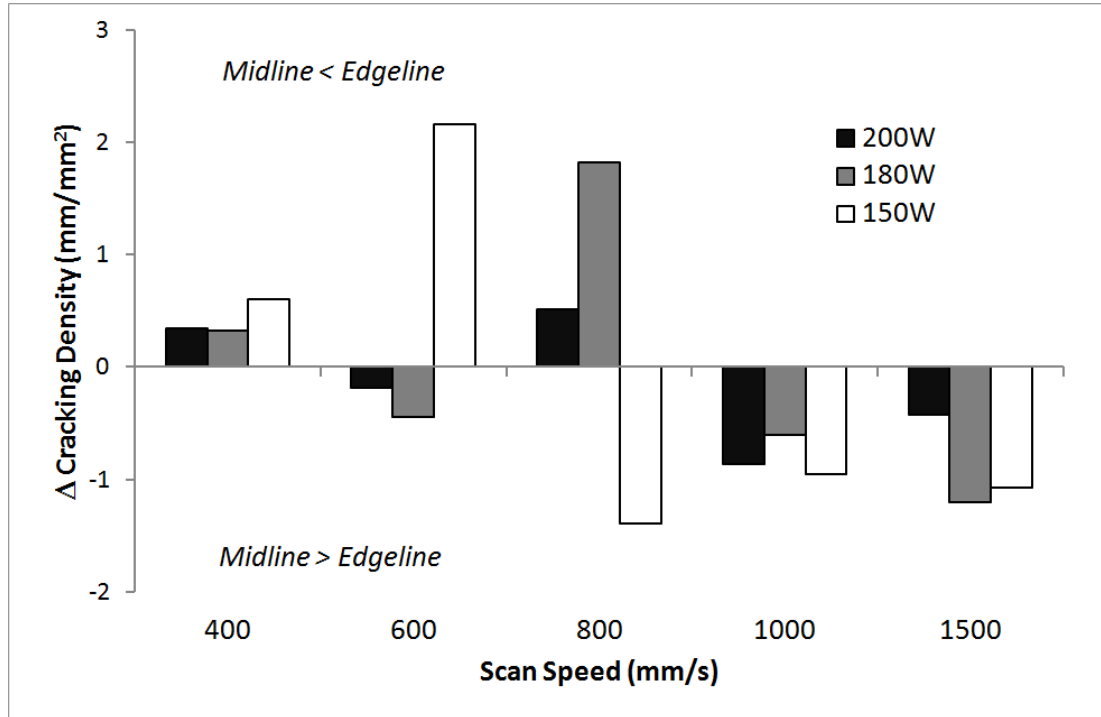


Figure 4.21: Plot showing ‘ Δ Cracking’ values between the edgeline and the midline of SLM-fabricated samples of CM247LC for different scan speeds and laser powers. ‘-ve’ values indicate a greater midline than edgeline cracking density.

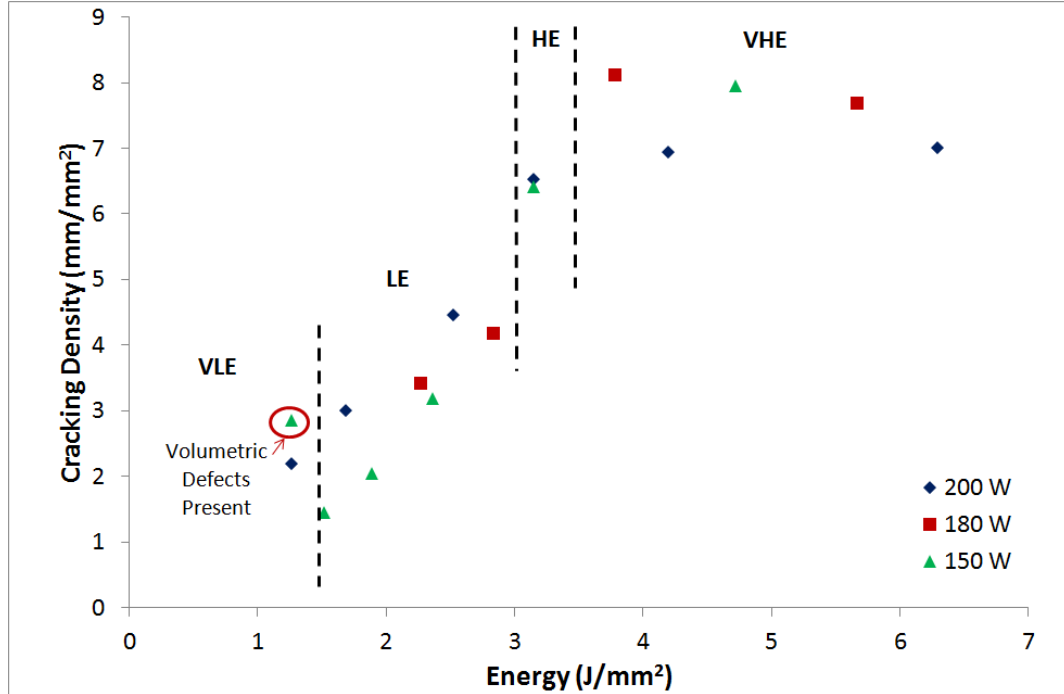


Figure 4.22: Plot showing cracking density variation with energy density (midline samples). Samples previously denoted as VLE, LE, HE and VHE have been labelled.

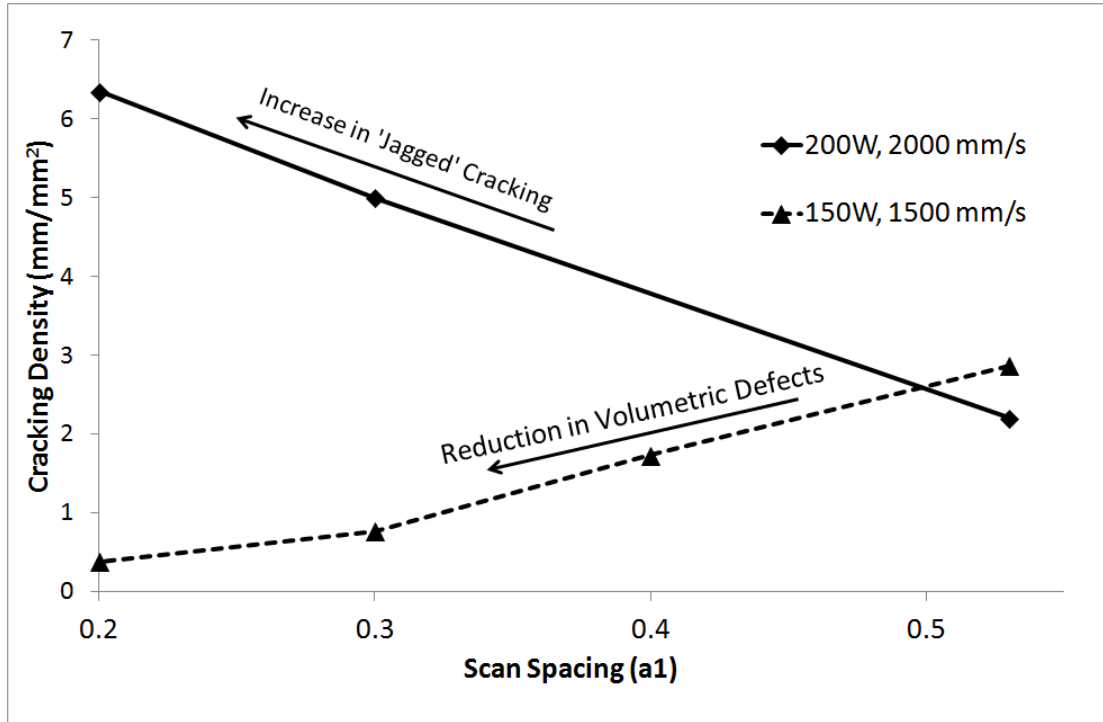


Figure 4.23: Plot showing variation in crack density (midline only) for SLM-fabricated samples of CM247LC with varying scan spacing for two different power/speed parameter sets. Microstructural observations are labelled.

vii. SLM Parametric Study: Discussion

The parametric study has highlighted that the energy input from the laser clearly governs the cracking behaviour within the SLM fabricated material. In general terms the plots in Figure 4.19, Figure 4.20 and Figure 4.22 have all shown that with a reduction in energy density (either via power or scan speed) the cracking decreases and the dominant style shifts from jagged to smooth (grain-boundary). This correlation between the energy density (or ‘heat input’ in welding terminology) and the cracking level is consistent with welding literature. A similar trend showing that decreasing heat input results in a lower incidence of cracking has been reported by several authors, notably Rush *et al.* [6] regarding Rene 80, Egbewande *et al.* [7] and Zhong *et al.* [8] both regarding IN738.

The attempts to standardise the energy in J/mm^2 become less convincing under closer examination. Individual points in Figure 4.22 show very different cracking densities under

similar energy values; this is very apparent in the LE section of the plot where the 200 W points are consistently higher than the 150 W points under similar energies and the 180 W points appear to lie approximately between. Likewise the 200 W, 2000 mm/s point shows the same energy (1.26 J/mm^2) as the 150 W, 1500 mm/s points, however the latter samples showed large volumetric defects unlike the former. Previous studies have suggested the use of standardised energy density equations [4, 5] to combine laser processing parameters; however, in this case these attempts have proved ineffective at providing more than the general trend of cracking density.

Although established in literature regarding SLM [4, 5], the equation combining laser power, scan speed and spacing to give energy density (Equation 4-1) has some assumptions and simplifications that are inappropriate for the evaluation of crack density.

Firstly the use of the product of ‘scan speed (mm/s)’ and absolute scan spacing ($a1 \times \text{Focus Dia. (mm)}$) to represent the area over which the laser scans per second is flawed. This expression suggests that the width of a single laser scan track is equal to the distance between the scan vectors in the raster filled area; however it is known that there is significant overlap (simply due to $a1 < 1$) and remelting of previous scan tracks in the raster filled area and as such the laser radiation is actually distributed over a larger area per second than this expression would suggest.

Secondly the expression fails to take into account the variation of the thermal field within the material with the variation of individual process parameters. It is known from the text by Grong regarding welding [9] that the shape of the weld bead and the associated thermal field is determined by the dimensionless n_3 parameter. For a given material n_3 is proportional to the product of the weld power and speed as shown in Equation 4-2 [9]:

Equation 4-2: Expression for n_3 shape parameter of a weld pool

$$n_3 \propto q_0 v$$

Where ‘ q_0 ’ is the net power and ‘ v ’ is the weld speed. Consider two SLM parameter sets; firstly one with high power, fast scan speed and consequently a high n_3 value, secondly one with low power, slow scan speed and consequently a low n_3 value. Both of these parameter sets may have an equal energy density according to Equation 4-1, for example:

- Set 1 (High n_3): 200 W, 2000 mm/s, $a_1 = 0.5$ (**1.33 J/mm²**)
- Set 2 (Low n_3): 100 W, 1000 mm/s, $a_1 = 0.5$ (**1.33 J/mm²**)

Figure 4.24 [9] shows the typical melt pool shape and associated thermal field for (a) high n_3 and (b) low n_3 value parameters. The close isotherms indicate a high thermal gradient at the leading edge and sides of the high n_3 (Figure 4.24 (a)) melt pool and a much lower thermal gradient at the trailing edge. This is in contrast to the low n_3 (Figure 4.24 (b)) melt pool which shows some variation in thermal gradients, but not the extremes of the former. Although this representation is only diagrammatic, it can be seen that the thermal gradients in these two situations is dramatically different and therefore it is likely that the magnitude and locations of the residual stresses will be different. As the thermal stresses are largely responsible (in conjunction with various mechanisms as discussed later) for the cracking behaviour, it is clear that energy density is not an appropriate parameter by which to evaluate SLM process parameters.

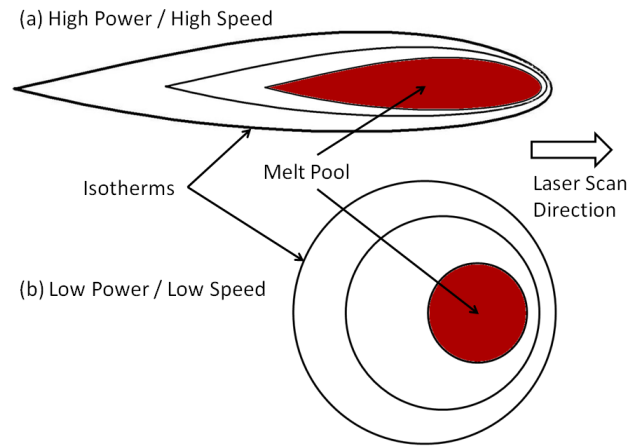


Figure 4.24: Schematic diagram showing typical melt pool shape and associated thermal field for (a) high n_3 and (b) low n_3 welding parameters. [9]

Finally, Equation 4-1 also fails to take into account the scan track length within the raster filled area (or indeed any consideration of the laser scanning strategy). Consider two SLM parameter sets using identical laser power, scan speed and spacing, but one with a short raster track within a simple back-and-forth pattern and the second with a long raster track within a simple back and forth pattern. Within the short path sample the time between each pass within the same region will be very short and as such the material may not have significantly cooled before the laser passes again. In this case it is conceivable that a larger thermal field with a thermal gradient transverse to the laser scan direction may be formed; this scheme is represented diagrammatically in Figure 4.25 (a). Within the long scan path sample there will be significant cooling between each laser pass and as such the only significant thermal field will be that surrounding that of the melt pool; as seen in Figure 4.25 (b). As with the previous example, this thermal field is dramatically different within two parameter sets which are considered identical in terms of energy density.

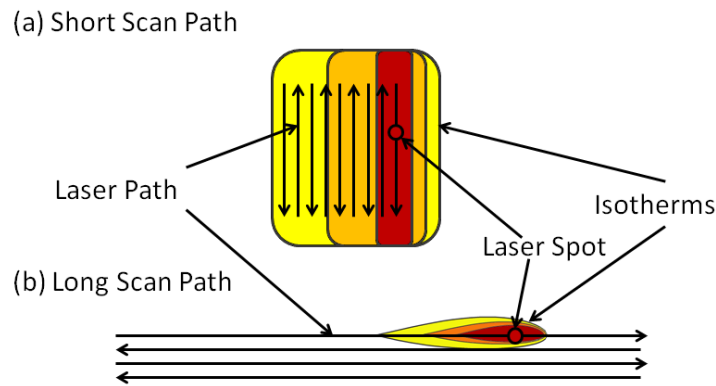


Figure 4.25: Schematic illustration showing the difference in thermal fields between (a) short path and (b) long path raster filled areas in SLM fabrication.

It is for these reasons that the use of energy density (Equation 4-1) should be with caution and why it may not be appropriate for the evaluation of cracking density with the laser fabricated CM247LC. The remainder of the discussion will focus on the influence of the individual process parameters as in Figure 4.19 and Figure 4.20.

Both the cracking character and the crack density results have shown that the laser parameters have a marked influence on the cracking behaviour of the as-fabricated material. These have already been sub-divided into four distinct regimes.

Under the VHE conditions large pores are visible as seen in Figure 4.10. These processing conditions (200 W, 400 mm/s) are the same as those used for the high-energy SLM sample subject to chemical analysis as discussed in section 4.2.i; this sample showed a loss of chromium and cobalt. It is therefore suggested that the large pores observed in this sample are a result of this vaporisation [2] forming gas bubbles within the molten pool during the SLM process and being ‘frozen’ there due to the rapidly cooled nature of the process. These pores appear to act as concentration points for the high levels of residual stress [10] existing within SLM-fabricated material and in many cases appear to be the initiation points for cracks.

‘Jagged’ cracks appear under process conditions categorised as both very high-energy and high-energy. These are very distinctive as seen in Figure 4.11 and can occur both perpendicular and parallel to the build direction. These cracks often appear to be interdendritic in nature although often grain boundary cracks have opened up at the intersection of the grain boundary and the jagged crack due to the residual stresses and the inherent crack susceptibility of grain boundaries. The formation of the ‘jagged’ cracks appears to be due to a solidification cracking mechanism as discussed in chapter 2 (section 2.14.i.).

The occurrence of solidification cracks under the high-energy regime is consistent with weld cracking literature as discussed by Dye *et al.* [11] which states that under high heat input welding conditions a positive stress is induced directly following the weld bead in the solidifying material encouraging this mode of cracking. The research presented by Rush *et al.* [12] also reports some solidification cracking to occur under high heat input welding conditions of Rene 80.

The dendritic protrusions indicate that the crack has formed during solidification where the remaining liquid between the growing dendrites has acted as the crack initiation point under the contraction of solidification [11]. Figure 4.12 shows these dendritic protrusions and in the case of Figure 4.13 where an entire section of the material has been removed (likely by polishing) to reveal the crack surface, the micrograph for crack quantification can show a relatively large area apparently overrun with cracks. This type of effect is discussed further in section 4.5 under the broader section for the limitations of the quantification method. It is also possible that these larger defects are the result of a casting porosity effect (rather than polishing damage) where there is insufficient material to backfill into the interdendritic region [13] however as the mechanisms and resulting structure is very similar (i.e. dendritic protrusions) then distinction between this and solidification cracking is difficult.

Further reduction in process energy results in a crack character as seen in Figure 4.14 which is typical of the LE regime. The dominance of the chaotic solidification type cracks has been significantly reduced and the remaining cracks appear to be relatively aligned to the build direction suggesting grain-boundary cracking. This is confirmed by the EBSD maps in Figure 4.17 which show three of these cracks lying on grain boundaries and the SEM micrographs presented in Figure 4.16 where all cracks examined lie on grain boundaries (although with wider cracks this distinction can be difficult to make due to the relative width of the crack compared to the grain size). Under higher magnification these cracks appear very different from the solidification cracks. Figure 4.15 shows that they do not have the same dendritic protrusions and it is therefore likely that these are formed in the solid state away from the melt pool. The potential mechanisms for the formation of these are discussed in Chapter 2. Due to the suppressed nature of the γ' phase (discussed in Chapter 6) in the as-fabricated state it is unlikely that the strain-ageing mechanism is responsible for the formation of these grain-boundary cracks.

It is therefore suggested that Ductility-Dip Cracking (DDC) or liquation mechanisms are responsible (in conjunction with high residual stresses) for this cracking behaviour. Based on the evidence, DDC is a potential cracking mechanism as the reheating of the material during each subsequent layer of deposition could allow for grain boundary sliding but not dynamic recrystallisation (either because the reheat temperature is not high enough, or the reheat is too brief). The micrographs in Figure 4.16 (a,b) show the cracks lying on a line of fine carbides appearing to originate from a series of linked pores. This is very similar to the research presented by Lippold & Ramirez [14] which shows voids forming due to stress concentrations around locking carbides and tortuous grain boundaries where temperatures have been elevated allowing grain boundary sliding. The crack in Figure 4.16 (c) also clearly lies on a grain

boundary and could be said to originate at a triple-point intersection, again reported as a typical DDC initiation point.

Although many of the cracks show evidence of DDC, as discussed in the previous paragraph, there is also some indication that liquation may also contribute to the formation of some of the grain boundary cracks. Figure 4.16 (d) shows a thin-film like carbide at a grain boundary lying at the tip of a crack. This is very similar to the research presented by Egbewande *et al.* [7] and Zhong *et al.* [8] which both show similar thin film carbides preceding crack tips due to the liquation of low-melting point carbides during heating by laser welding processes. Furthermore the ‘irregular’ morphology of the crack edge shown in Figure 4.16 (b) does not appear to be either a jagged solidification crack seen in the HE specimens, or the ‘clean’ grain boundary style crack associated with DDC. It is however somewhat similar to the irregular surfaces reported by Rush *et al.* [12] when discussing the liquation cracking within Rene 80.

It has therefore been concluded that the grain boundary cracks are a combination of both DDC due to stress concentrations around carbides and liquation of the low-melting point grain boundary phases manifesting as thin film carbides located at the crack tips. This is consistent with welding research as presented by Dye *et al.* [11] in which weldability maps of IN718 show that liquation cracking is the mechanism prominent in low heat input welds.

The final mechanism is the formation of large volumetric defects as seen in Figure 4.18 for a typical very low-energy condition. This type of defect is not a crack; however it does constitute a serious defect within the material. These large defects are caused by incomplete consolidation at low-energy due to the reduction in melt pool size under these conditions.

When comparing the crack character to the crack density results, it can be seen that there is a clear step down in crack density which corresponds to the shift from a dominance of

solidification cracks to that of grain-boundary cracks. This shift is indicated by the dotted line in Figure 4.19 and Figure 4.20 for the midline and edgeline of samples respectively. For the section of the study varying power and speed only, the sample with the least cracking is that of 150 W, 1250 mm/s for the midline and 150 W, 1000 mm/s for the edgeline.

The comparison of midline to edgeline presented in Figure 4.21 shows that for the higher-energy samples there is no consistent trend for the difference between these values. For the lower-energy samples however where grain-boundary cracking is dominant, there is a trend showing that the crack density is greatest within the middle of the sample. Without further investigation it is difficult to conclude much more with regards to this variation across the sample. It is suggested that this effect is likely to be due to a greater residual stress within the core of the samples and is most likely to be heavily dependent on the sample geometry. From this point onwards the study focuses on the midline results only as the poorer of the two in the region of interest (i.e. grain-boundary cracking dominant region of the process window).

The final section of the study focussed on the reduction of the scan-spacing from the default $a_1 = 0.53$. The midline plot in Figure 4.19 shows an anomalous point for the sample processed at 150 W, 1500 mm/s, this point appears to show an increase in crack density, however examination of the micrographs revealed that this increase is artificial and results from the onset of the large volumetric defects which are also quantified as cracks (see Section 4.5 for further discussion on the limitations of the image analysis method). Other than these defects the crack density appeared to be very low so the further study to reduce the scan spacing and therefore accommodate for the reduction in melt pool size was undertaken.

Figure 4.23 shows that for the 150 W, 1500 mm/s condition the crack density reduced with the reduction in scan spacing and corresponded to a gradual elimination of the occurrence of

the large volumetric defects. These defects were fully eliminated when the scan was reduced to $a_1 = 0.3$. A similar experiment was carried out on a fully consolidating (ie. containing cracks, but not volumetric defects) parameter set, 200 W, 2000 mm/s. This sample showed a marked increase in cracking with the reduction in spacing and even a shift back from the grain-boundary style cracking to solidification cracking. It can be concluded that the reduction in scan spacing can eliminate the volumetric defects within the material, however there is a penalty induced under higher power conditions of increased cracking caused by the increased energy density. It is the belief of the author that further understanding of these complex relationships could be gained with accurate high-resolution thermal data from the melt pool or extensive modelling taking into account the varying absorption and thermal behaviour specific to the geometry and process conditions.

At this point the parametric study was drawn to a close as further reductions in power and scan spacing would result in prohibitively slow processing. It is obvious from the results gained and the review of the relevant literature that a full elimination of cracks in the as-fabricated SLM processed CM247LC is not feasible for the Concept Laser M2 without extensive system modification and further research; this is outside the scope of this thesis which aims to focus on the establishment of a process route with currently available technology.

The parametric study did manage to show distinct windows of operation and relate them to the cracking behaviour as well as significantly reducing the cracks within the as-fabricated samples compared with preliminary work. The process conditions of 150 W, 1500 mm/s, $a_1 = 0.2$ resulted in the lowest crack density. In practice the conditions 150 W, 1500 mm/s, $a_1 = 0.3$ were used for all subsequent CM247LC processing as the resultant cracking for these parameter sets is very similar yet the processing time using $a_1 = 0.3$ is significantly shorter.

4.3 CMSX486 Parametric Studies

CMSX486 was also suggested as a potential candidate for the high-temperature application, however due to its similarity in composition to CM247LC it is susceptible to similar cracking behaviour and problems. As an extension to the CM247LC parametric study, the CMSX486 study aimed to assess the ability to rapidly achieve a reasonable set of operating parameters through a statistical design of experiments (DOE) methodology to reduce the number of samples produced and establish a quantitative relationship between the parameters and the crack density.

i. Powder Size Analysis: Results & Discussion

The CMSX486 argon gas atomised powder was supplied by Carpenters in the size fraction of -50 μm . This powder was subsequently re-sieved by LPW Technology Ltd. to the size fraction of +15-53 μm . Figure 4.26 shows the particle size distributions both before (labelled as ‘Carpenters’) and after (labelled as ‘reclassified’) the re-sieving.

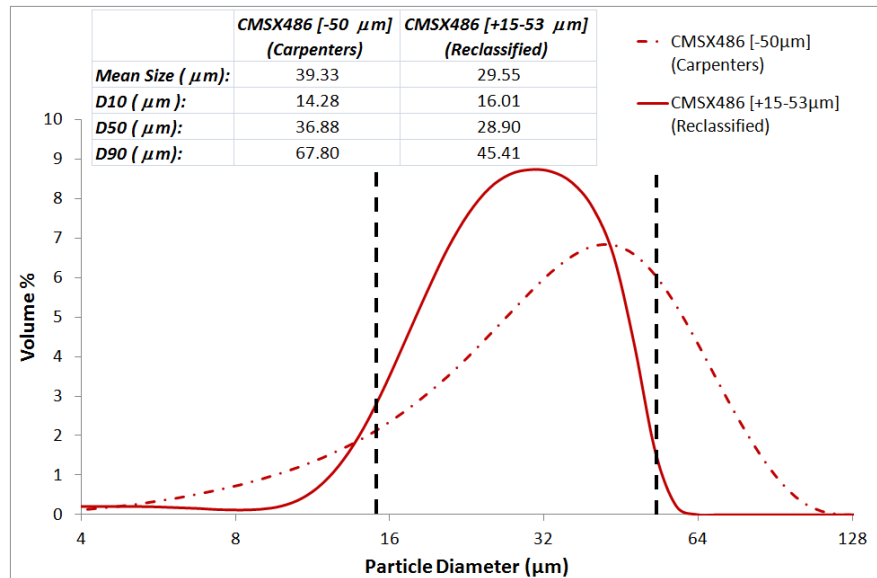


Figure 4.26: Particle size distribution for argon gas atomised CMSX486 powder as supplied (Carpenters, Chain dashed line) and following re-sieving (Reclassified, Solid line); black dashed lines indicate the ideal size distribution boundaries. Key sizing data is provided in the inset table.

Figure 4.26 clearly shows that the as-received powder displays a very poor size distribution compared with the ideal. The maximum particle size is approximately 128 μm and the minimum is $< 4 \mu\text{m}$. The D10 and D90 values both lie outside the ideal range for SLM processing at 14.28 μm and 67.80 μm respectively and the greater mean (39.33 μm) compared to the D50 (Median, 36.88 μm) indicates a skewing of the distribution towards the larger particle sizes. This powder was loaded into the Concept laser M2, however processing was not carried out due to the poor spreading and hence the re-sieving was necessary.

Following the re-sieving the powder classification was significantly improved; the maximum and minimum particle sizes for this powder are approximately 60 μm and 10 μm respectively. These are still just outside the ideal range, but as the D10 and D90 lie within the ideal range at 16.01 μm and 45.41 μm respectively it was considered to be acceptable. Additionally difference between the mean and D50 values (29.55 μm and 28.90 μm) was also significantly reduced by the re-sieving therefore reducing the skew of the distribution towards the larger particle size. This re-sieved powder handled acceptably when spread in the SLM process

ii. SEM Powder Examination: Results & Discussion

Figure 4.27 shows a secondary SEM micrograph of the CMSX486 powder in the as-supplied state. The powder shows a large distribution of particle sizes confirming the results in the previous section.

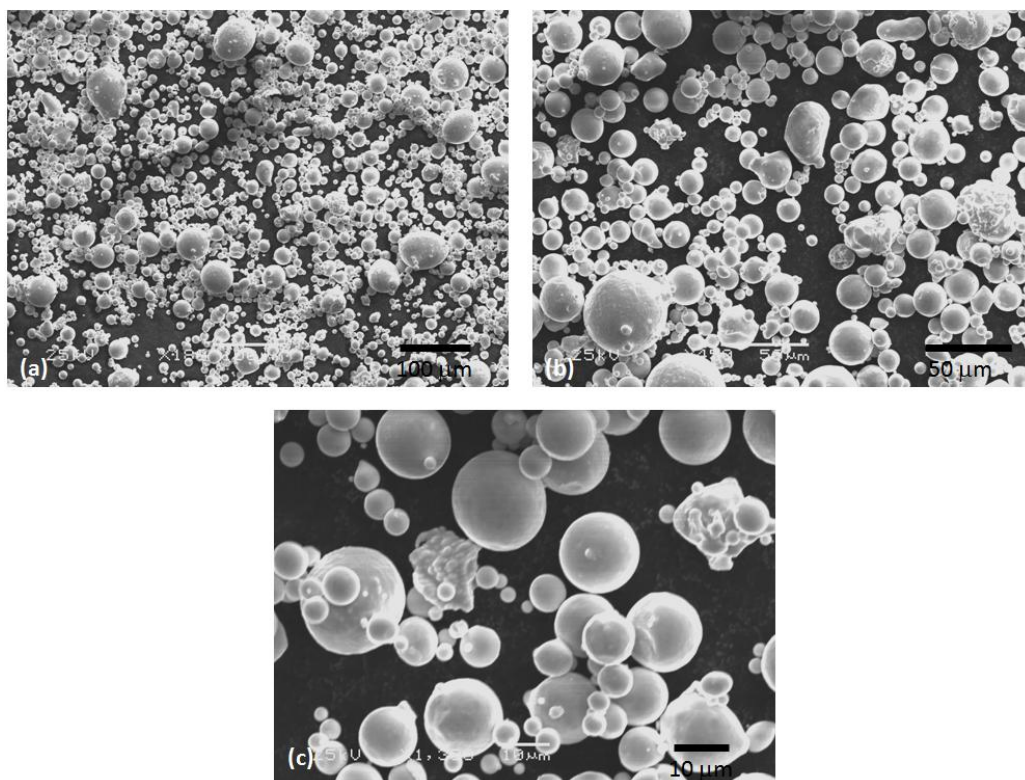


Figure 4.27: SE SEM micrographs of the as-supplied gas atomised CMSX486 powder at increasing magnifications ((a)-(c)).

Figure 4.28 shows an individual particle of the gas atomised CMSX486 powder. The particle appears to show a fine equiaxed grain structure with fine carbide precipitates at the grain boundaries. The backscattered micrograph does not show any elemental segregation across the diameter of the particle; the EDS linescans shown in Figure 4.29 confirm this.

Figure 4.30 shows a typical micrograph taken from the set used for porosity quantification of the re-sieved powder. The particles appear to show much more irregular shapes compared with the CM247LC powder discussed in Section 4.2.iii. Many of the larger particles appear to be formed from the joining of two particles during solidification.

The pores are similar to those seen in CM247LC and can similarly be divided into gas porosity formed during solidification and crescent shaped porosity formed from the collision between a solid particle and molten droplet.

Table 4.5 shows the porosity results obtained from the image analysis of the ground CMSX486 sample. The overall powder porosity is 0.87% and overall the porosity sizes and range is very similar to that seen in the CM247LC samples.

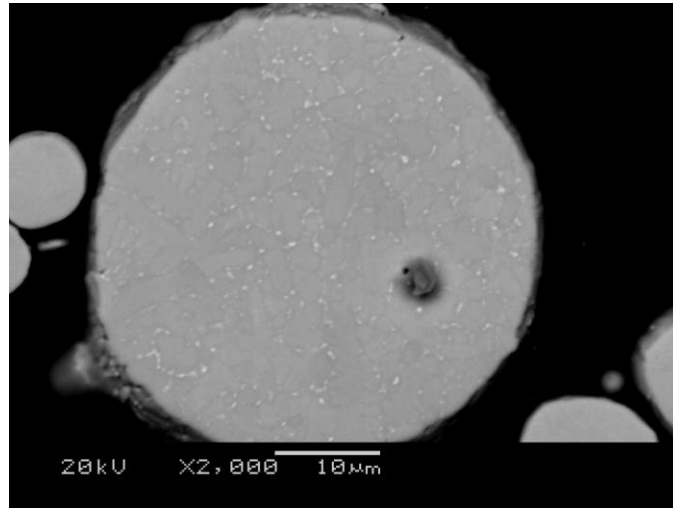


Figure 4.28: BSE SEM micrograph showing an individual ground and polished powder particle of CMSX486.

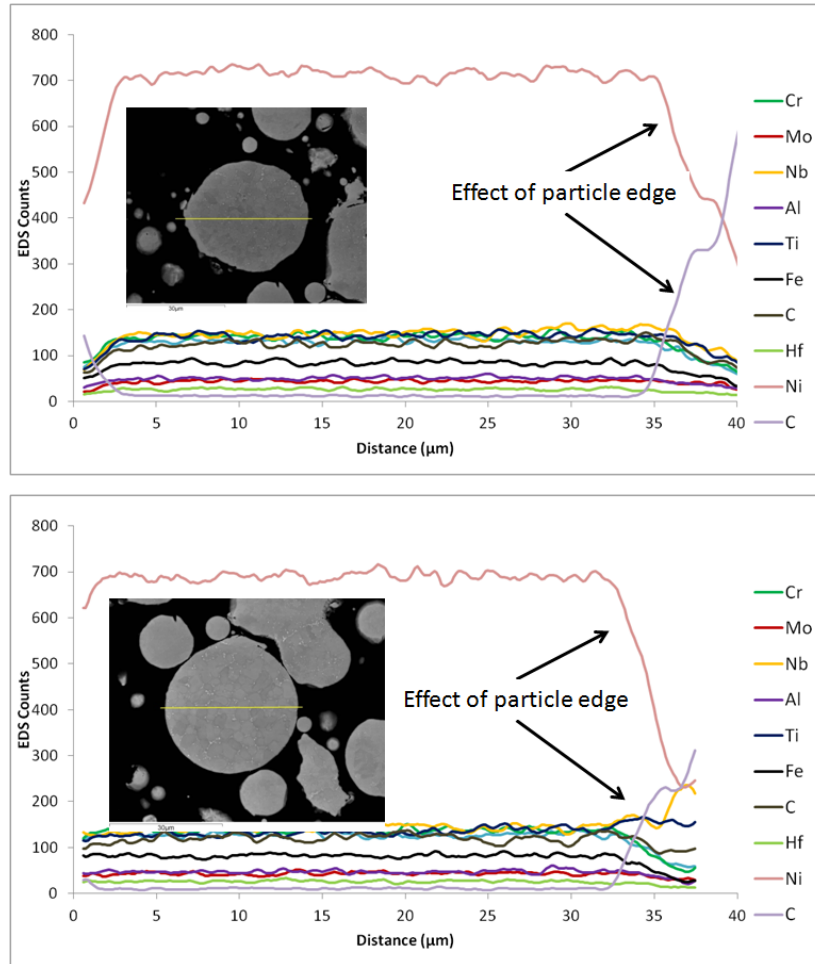


Figure 4.29: EDS linescans across two CMSX486 particles (inset – linescan shown by yellow line) showing no significant variation across the particle diameter. Note the drop in Ni and increase in C due to the edge of the particle and the mounting Bakelite.

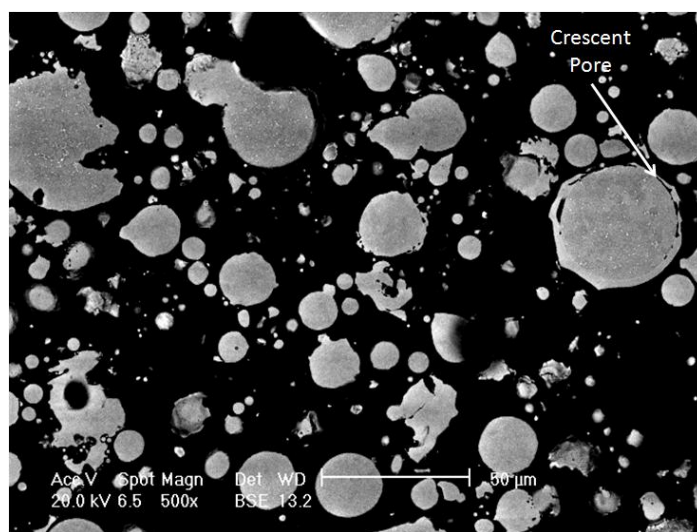


Figure 4.30: BSE SEM micrograph of a ground CMSX486 powder sample (Re-sieved). Note the irregular particle shapes from the joined of particles in the molten state and the crescent pores formed from droplets colliding with solidified particles.

Table 4.5: Porosity quantification results for CMSX486 (re-sieved) powder.

Total number of particles analysed	695
Minimum pore size to be measured <i>(to eliminate noise)</i>	0.30 μm^2
Total number of pores analysed	500
Mean Pore equivalent diameter	1.74 μm
Maximum Pore equivalent diameter	9.07 μm
% Porosity of the analysed powder	0.87 %

iii. Statistical DOE Introduction

A central composite design model was used to examine 4 design variables (Laser Power, Laser Speed, Scan Spacing and Island Size). The methodology for using a central composite design of experiments is outlined in Appendix B. The values determined by images analysis for crack density and void fraction were measured as responses as outlined in chapter 3 section 3.10.ii. The statistical DOE software “Design-Expert” [15] was used to analyse the raw data to give values of statistical significance for each of the variables (and 1st order interactions) on both of the responses; produce empirical equations relating the process parameters to crack density and void fraction; Provide an R^2 value (confidence level) for the equation and finally determine process parameters to eliminate the voids (Void fraction \rightarrow 0%) whilst reducing the cracking as much as possible.

iv. SLM Parametric Study: Crack & Void Quantification Results

The raw data for the responses for each design point investigated are listed in Table 4.6. The DOE was carried out for the following ranges of parameters: Laser Power (100 - 200 W); Scan Speed (500 - 2000 mm/s); Scan Spacing (a1, 0.2–0.8); Island Size (2 – 8 mm). Figure 4.31 shows the raw data for cracking density and void fraction plotted against energy density (J/mm^2) calculated using Equation 4-1.

For crack density Table 4.7 summarises the analysis of variance and highlights the statistically significant terms ($P < 0.05$). The empirical relationship is presented in Equation 4-3 with the R^2 value and Figure 4.32 shows a comparison of the model to the actual results. Figure 4.33, Figure 4.34, and Figure 4.35 show the predicted influence of laser power, laser speed and the interaction of scan spacing and scan speed.

Table 4.6: Raw experimental results for the parametric study of CMSX486.

Std	Run	Factor 1: Laser Power (W)	Factor 2: Scan Speed (mm/s)	Factor 3: Scan Spacing (a1)	Factor 4: Island Size (mm)	Response 1: Cracking Density (mm/mm ²)	Response 2: Void Area Fraction (%)
27	1	150	1500	0.5	5	6.07	0.33
23	2	150	1500	0.5	2	8.16	0.50
17	3	100	1500	0.5	5	3.80	7.14
8	4	175	2000	0.65	3.5	5.32	6.48
22	5	150	1500	0.8	5	3.76	4.49
11	6	125	2000	0.35	6.5	3.92	3.18
5	7	125	1000	0.65	3.5	6.83	1.00
24	8	150	1500	0.5	8	6.05	0.07
1	9	125	1000	0.35	3.5	5.37	0.11
26	10	150	1500	0.5	5	5.87	0.04
16	11	175	2000	0.65	6.5	4.05	4.64
7	12	125	2000	0.65	3.5	2.41	22.43
15	13	125	2000	0.65	6.5	3.75	16.22
4	14	175	2000	0.35	3.5	6.57	0.32
18	15	200	1500	0.5	5	8.81	0.27
19	16	150	500	0.5	5	7.79	0.52
10	17	175	1000	0.35	6.5	5.96	0.73
20	18	150	2500	0.5	5	3.71	4.57
6	19	175	1000	0.65	3.5	8.66	0.21
14	20	175	1000	0.65	6.5	8.59	0.47
2	21	175	1000	0.35	3.5	5.86	0.21
12	22	175	2000	0.35	6.5	6.30	0.20
13	23	125	1000	0.65	6.5	4.03	0.26
9	24	125	1000	0.35	6.5	4.50	0.11
25	25	150	1500	0.5	5	6.88	0.10
3	26	125	2000	0.35	3.5	2.64	6.95
21	27	150	1500	0.2	5	6.81	0.27

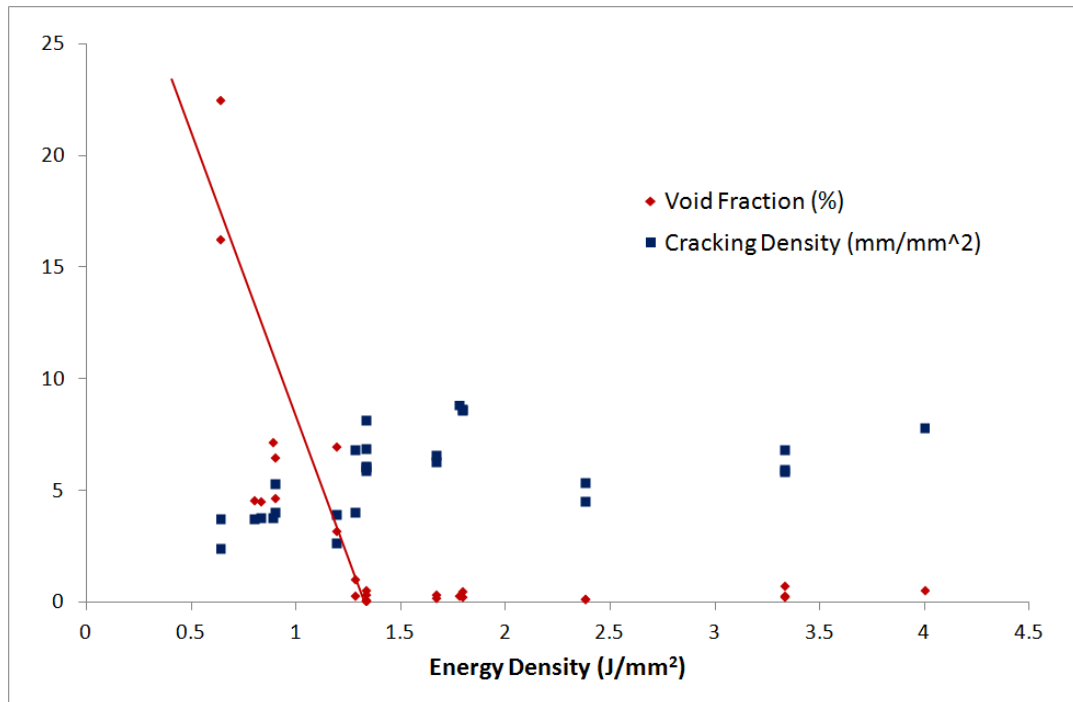


Figure 4.31: Plot showing raw void fraction and cracking density data for SLM fabricated CMSX486 plotted against energy density (mm/mm²)

Table 4.7: ANOVA for crack density of CMSX486. Blue rows indicate significant terms and red row indicates overall model significance.

Source	Sum of Squares	df	Mean Square	F - Value	P- Value (Prob>F)
Model	70.74	14	5.05	3.45	0.0189
Power (A)	32.41	1	32.41	22.16	0.0005
Speed (B)	22.05	1	22.05	15.07	0.002
Scan Spacing (C)	0.54	1	0.54	0.37	0.5561
Island Size (D)	1.92	1	1.92	1.31	0.2746
AB	0.086	1	0.086	0.059	0.8126
AC	0.11	1	0.11	0.078	0.7843
AD	0.013	1	0.013	8.70E-03	0.927
BC	6.65	1	6.65	4.55	0.0543
BD	1.39	1	1.39	0.95	0.3489
CD	0.58	1	0.58	0.4	0.5401
A ²	0.35	1	0.35	0.24	0.6357
B ²	1.51	1	1.51	1.03	0.3295
C ²	3.11	1	3.11	2.13	0.1702
D ²	0.11	1	0.11	0.077	0.7857

Equation 4-3: Empirically determined relationship between the process parameters and the crack density for CMSX486 with corresponding R^2 value.

$$\begin{aligned} \text{Cracking Density} = & \\ & -9.96920 \\ & +0.091257 * \text{Laser Power} \\ & +2.73149\text{E-}003 * \text{Scan Speed} \\ & +29.73059 * \text{Spacing} \\ & -0.56473 * \text{Island Size} \\ & +5.86117\text{E-}006 * \text{Laser Power} * \text{Scan Speed} \\ & +0.022574 * \text{Laser Power} * \text{Spacing} \\ & -7.53981\text{E-}004 * \text{Laser Power} * \text{Island Size} \\ & -8.59812\text{E-}003 * \text{Scan Speed} * \text{Spacing} \\ & +3.92954\text{E-}004 * \text{Scan Speed} * \text{Island Size} \\ & -0.84737 * \text{Spacing} * \text{Island Size} \\ & -2.03613\text{E-}004 * \text{Laser Power}^2 \\ & -1.06447\text{E-}006 * \text{Scan Speed}^2 \\ & -16.97932 * \text{Spacing}^2 \\ & +0.032365 * \text{Island Size}^2 \end{aligned}$$

$$R^2 = 80.12\%$$

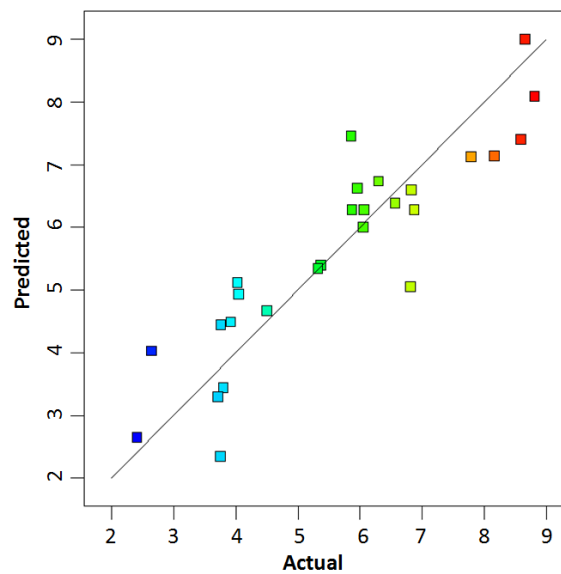


Figure 4.32: Plot showing comparison of predicted values against actual results for the crack density of SLM-fabricated CMSX486.

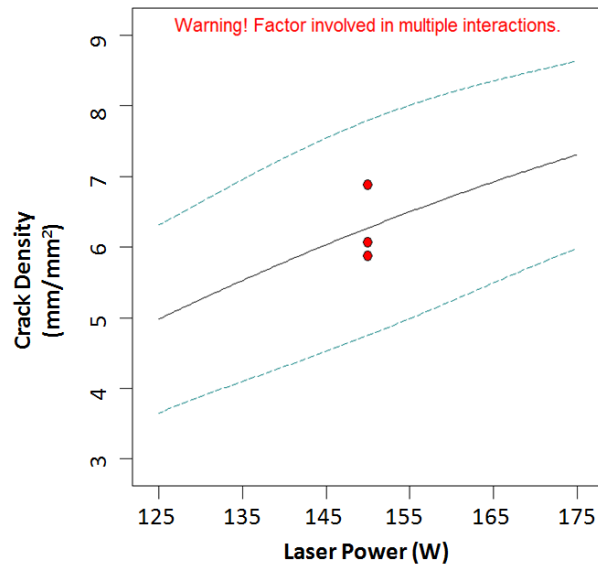


Figure 4.33: Plot showing predicted influence of laser power on crack density for CMSX486 (scan speed = 1500 mm/s, scan Spacing = 0.5, island size = 5 mm). Red points indicate the design points measured and the dashed lines indicate the 95% confidence limits of the model.

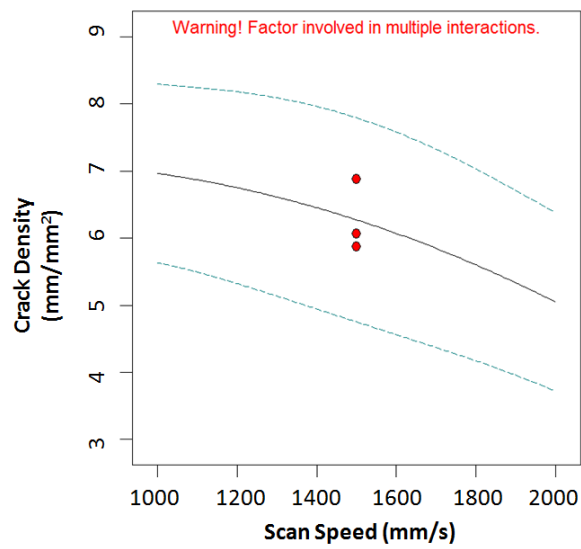


Figure 4.34: Plot showing predicted influence of laser scan speed on crack density for CMSX486 (laser power = 150 W, scan Spacing = 0.5, island size = 5 mm). Red points indicate the design points measured and the dashed lines indicate the 95% confidence limits of the model.

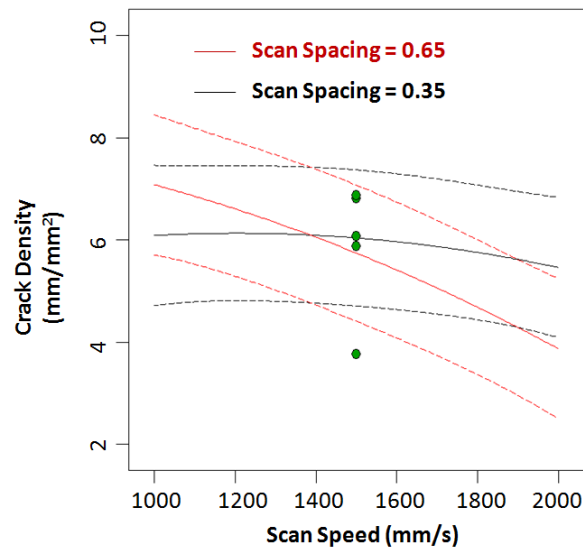


Figure 4.35: Plot showing the predicted interaction between the scan spacing and the scan speed for CMSX486. The red plot indicates the predicted influence of scan speed on crack density for a scan spacing = 0.65 and the black for a scan spacing = 0.35. The dashed lines indicate the respective 95% confidence limits and the green dots are the measured design points.

For void fraction; Table 4.8 summarises the analysis of variance and highlights the statistically significant terms ($P < 0.05$). The empirical relationship is presented in Equation 4-4 with the R^2 value and Figure 4.36 shows a comparison of the model to the actual results. Figure 4.37, Figure 4.38, and Figure 4.39 show the influence of laser power, laser speed and laser spacing respectively. Figure 4.40 and Figure 4.41 show the interaction between scan speed and laser power and that of scan spacing and scan speed respectively.

Table 4.8: ANOVA for void fraction of CMSX486. Blue rows indicate significant terms and red row indicates overall model significance.

Source	Sum of Squares	df	Mean Square	F - Value	P- Value (Prob>F)
Model	648.02	14	46.29	6.37	0.0014
Power (A)	107.34	1	107.34	14.77	0.0023
Speed (B)	178.33	1	178.33	24.54	0.0003
Scan Spacing (C)	97.29	1	97.29	13.39	0.0033
Island Size (D)	6.81	1	6.81	0.94	0.3522
AB	86.89	1	86.89	11.96	0.0047
AC	23.06	1	23.06	3.17	0.1001
AD	5.69	1	5.69	0.78	0.3938
BC	91.92	1	91.92	12.65	0.0039
BD	8.97	1	8.97	1.23	0.2882
CD	1.66	1	1.66	0.23	0.641
A ²	29.59	1	29.59	4.07	0.0665
B ²	16.79	1	16.79	2.31	0.1543
C ²	15.29	1	15.29	2.1	0.1725
D ²	2.22	1	2.22	0.31	0.5906

Equation 4-4: Empirically determined relationship between the process parameters and the void fraction for CMSX486 with corresponding R² value.

$$\begin{aligned}
 \text{Void area fraction} = & \\
 & +21.96806 \\
 & -0.28966 \cdot \text{Laser Power} \\
 & +0.011782 \cdot \text{Scan Speed} \\
 & -16.95462 \cdot \text{Spacing} \\
 & -1.95925 \cdot \text{Island Size} \\
 & -1.86429\text{E-}004 \cdot \text{Laser Power} \cdot \text{Scan Speed} \\
 & -0.32016 \cdot \text{Laser Power} \cdot \text{Spacing} \\
 & +0.015897 \cdot \text{Laser Power} \cdot \text{Island Size} \\
 & +0.031958 \cdot \text{Scan Speed} \cdot \text{Spacing} \\
 & -9.98496\text{E-}004 \cdot \text{Scan Speed} \cdot \text{Island Size} \\
 & -1.43259 \cdot \text{Spacing} \cdot \text{Island Size} \\
 & +1.88435\text{E-}003 \cdot \text{Laser Power}^2 \\
 & +3.54910\text{E-}006 \cdot \text{Scan Speed}^2 \\
 & +37.62707 \cdot \text{Spacing}^2 \\
 & +0.14338 \cdot \text{Island Size}^2
 \end{aligned}$$

$$R^2 = 88.14\%$$

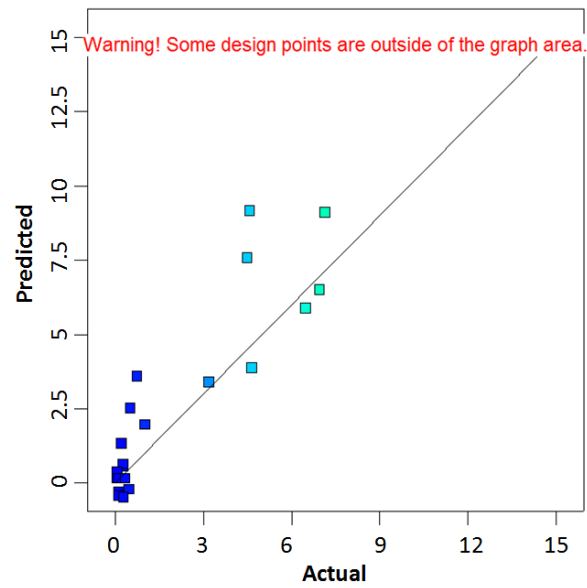


Figure 4.36: Plot showing comparison of predicted values against actual results for the void fraction of SLM-fabricated CMSX486

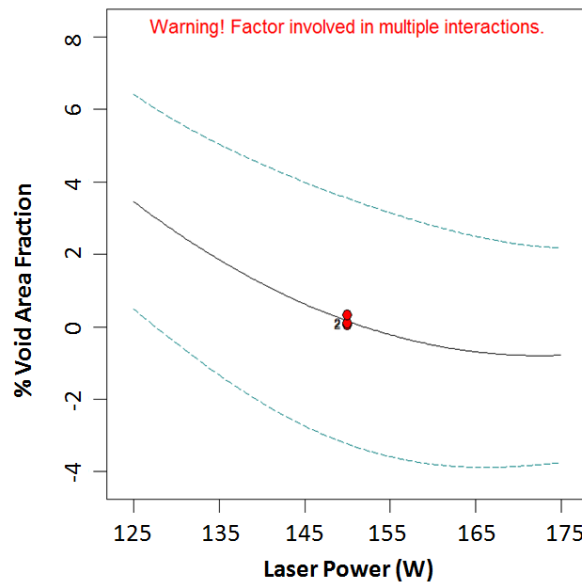


Figure 4.37: Plot showing predicted influence of laser power on void fraction for CMSX486 (scan speed = 1500 mm/s, scan Spacing = 0.5, island size = 5 mm). Red points indicate the design points measured and the dashed lines indicate the 95% confidence limits of the model.

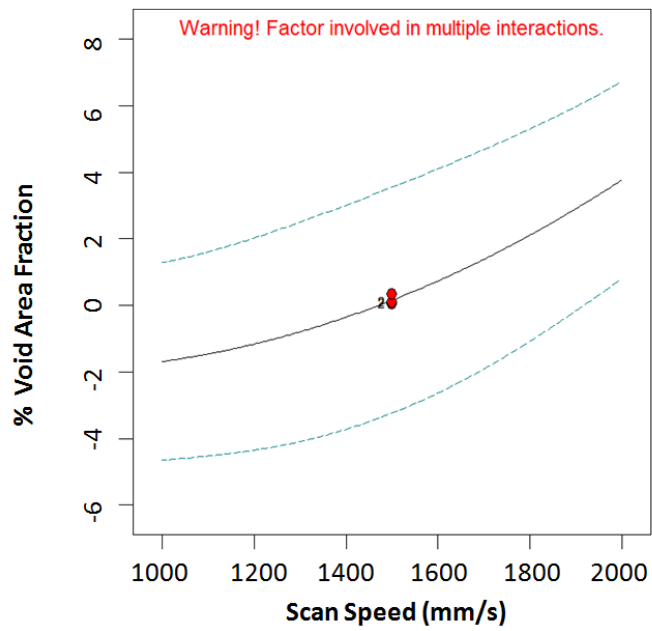


Figure 4.38: Plot showing predicted influence of laser scan speed on void fraction for CMSX486 (laser power = 150 W, scan Spacing = 0.5, island size = 5 mm). Red points indicate the design points measured and the dashed lines indicate the 95% confidence limits of the model.

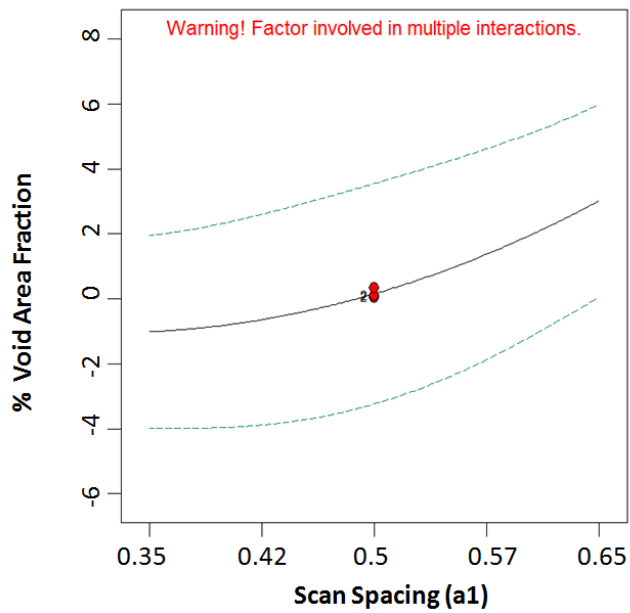


Figure 4.39: Plot showing predicted influence of scan spacing on void fraction for CMSX486 (laser power = 150 W, Scan Speed = 1500 mm/s, island size = 5 mm). Red points indicate the design points measured and the dashed lines indicate the 95% confidence limits of the model.

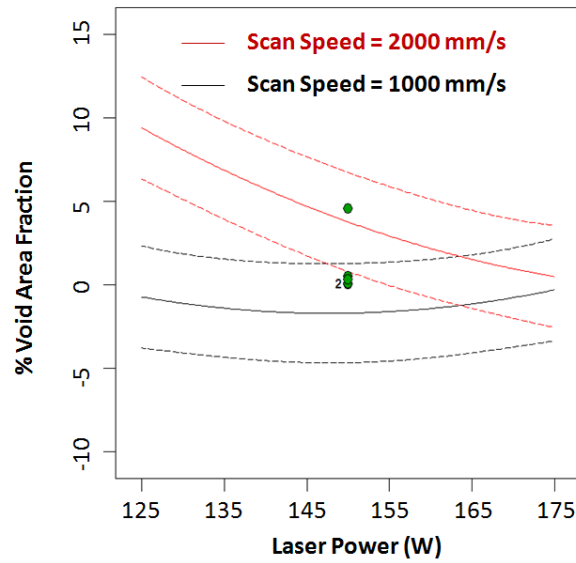


Figure 4.40: Plot showing the predicted interaction between the scan speed and the laser power for CMSX486. The red plot indicates the predicted influence of laser power on void fraction for a scan speed = 2000 mm/s and the black for a scan speed = 1000 mm/s. The dashed lines indicate the respective 95% confidence limits and the green dots are the measured design points.

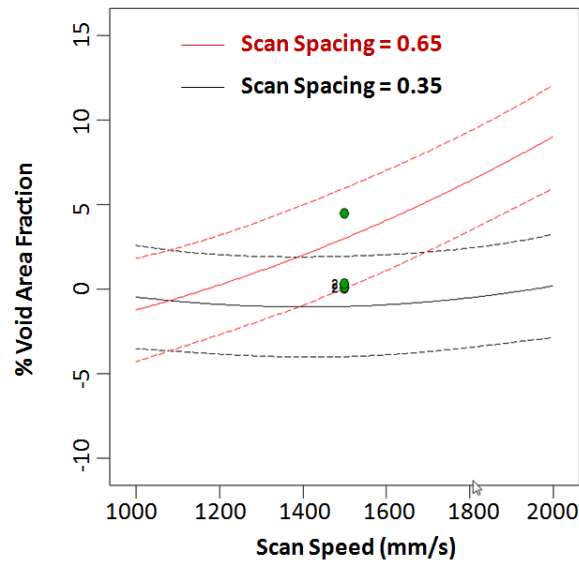


Figure 4.41: Plot showing the predicted interaction between the scan spacing and the scan speed for CMSX486. The red plot indicates the predicted influence of scan speed on void fraction for a scan spacing = 0.65 and the black for a scan spacing = 0.35. The dashed lines indicate the respective 95% confidence limits and the green dots are the measured design points.

Figure 4.42 and Figure 4.43 show surface plots for predicted (based on Equation 4-3 and Equation 4-4) crack density and void fraction respectively, these are plotted against laser

power and scan speed for fixed values of scan spacing and island size. Figure 4.44 shows both predicted crack density and void fraction.

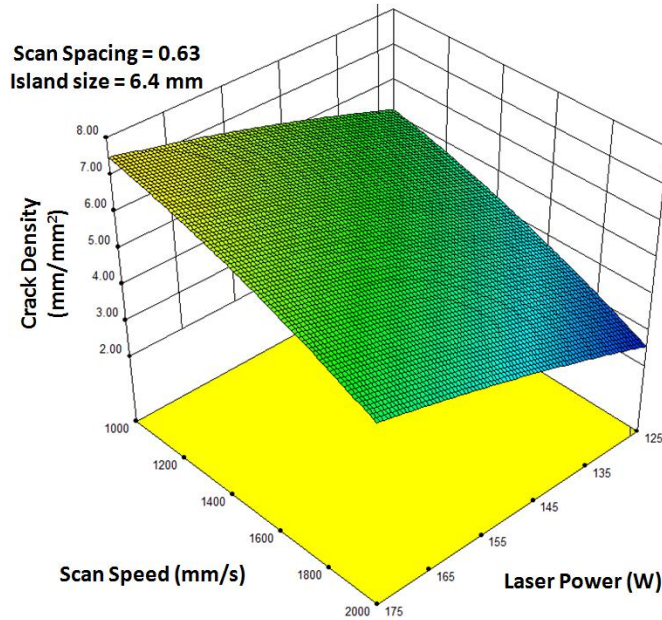


Figure 4.42: Surface plot showing predicted crack density against scan speed and laser power for CMSX486. Scan spacing fixed at 0.63; island size fixed at 6.4 mm.

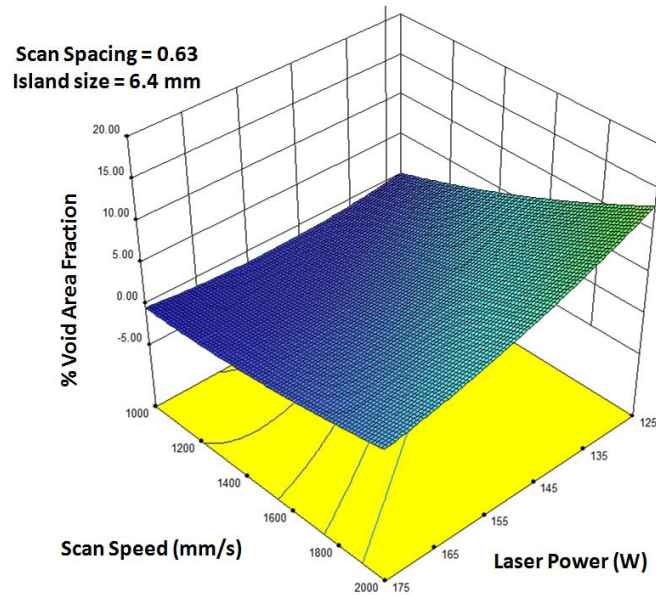


Figure 4.43: Surface plot showing predicted void area fraction against scan speed and laser power for CMSX486. Scan spacing fixed at 0.63; island size fixed at 6.4 mm.

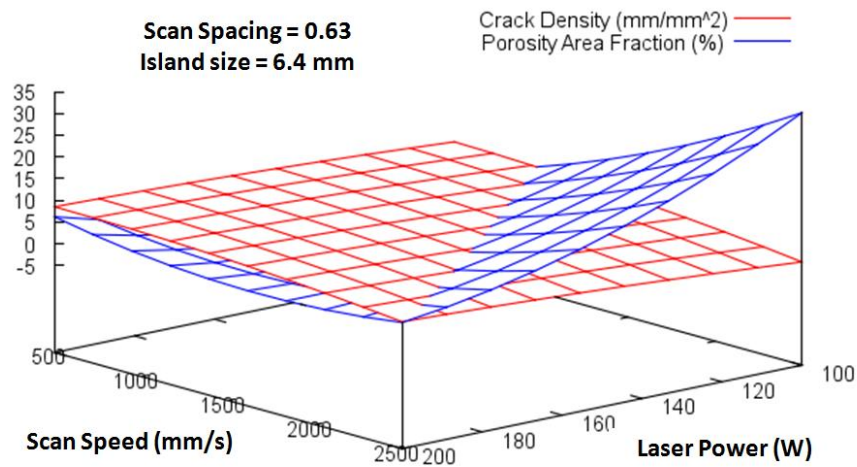


Figure 4.44: Surface plot showing both predicted crack density (red) and void area fraction (blue) for CMSX486. Scan spacing fixed at 0.63; island size fixed at 6.4 mm.

The target condition for the statistical analysis was a full consolidation (i.e. no void fraction) whilst having the lowest possible crack density. The Design-Expert Software predicted an optimised set of processing conditions of:

- **Laser Power:** 128 W
- **Scan Speed:** 1007 mm/s
- **Scan Spacing (a1):** 0.63
- **Island Size:** 6.4 mm

For these conditions a void fraction of 0.01% (effectively 0%) is predicted and a crack density of 5.4 mm/mm². Following this optimisation three similar samples were SLM-fabricated under these conditions. For these three samples both crack density and void fractions were evaluated. The results of this validation are presented in Table 4.9.

Table 4.9: Crack density and void fraction results from the three validation samples compared against the model results for CMSX486.

	Crack Density (mm/mm ²)	Void Area Fraction (%)
<i>Model Result</i>	<i>5.40</i>	<i>0.01</i>
Validation 1	2.95	0.01
Validation 2	8.18	0.21
Validation 3	2.24	0.00

v. SLM Parametric Study: Discussion

The parametric study into the cracking of CM247LC involved several SLM builds as each new direction of investigation was based on the results from the previous. This allowed for a good understanding of the defects and cracking behaviour within the material, however it was time consuming and only investigated three operating parameters without considering interactions between them. Conversely the CMSX486 parametric study aimed to rapidly assess the material and find a reasonable set of operating parameters quickly. This was effectively achieved in one SLM build with a second being used to validate the results.

The parametric build involved the analysis of 27 samples chosen based on the central composite design for four variables. The raw results of this are shown in Table 4.6 however these numbers do very little to illustrate the trends in cracking and void fraction. The plot in Figure 4.31 illustrate the general trends; however, it is only following the statistical analysis that the significant factors become clear.

For crack density Table 4.7 shows the ANOVA results. Laser power, scan speed and the combined 'scan spacing \times scan speed' (despite having a P value of 0.0543, slightly over the 0.05 considered to show significance) were shown to be the significant factors for crack density. This corresponds broadly to the findings presented for CM247LC. Equation 4-3 shows the fitted equation to model the crack density based on the operating parameters. The comparison of this model to the actual data can be seen in Figure 4.32; the data shows a reasonable fit to the model, however there is some significant scatter.

Following the generation of this model, the variation of the crack density with each of the significant terms can be predicted. Figure 4.33 shows that the model predicts crack density to decrease with a corresponding decrease in laser power and Figure 4.34 shows the crack

density to decrease with increasing scan speed. Both of these predictions agree with the general overall scheme shown for CM247LC which in broad terms shows a decrease in crack density with decreasing energy density; however the design of experiments methodology fails to reveal insight into the character or mechanisms behind the crack behaviour.

Further to these single parameter influences, Figure 4.35 reveals a distinct advantage of the statistical method. It can be seen that the scan spacing has a marked effect on the influence of scan speed on crack density. For a high scan spacing ($a_1 = 0.65$) crack density decreases with increasing scan speed, however for a low scan spacing ($a_1 = 0.35$) the crack density barely varies with scan speed. This kind of multiple parameter interaction cannot be obtained by the methodology used for the evaluation of CM247LC.

Table 4.8 shows the ANOVA for the void fraction within CMSX486. For this analysis the parameters of laser power, scan speed and scan spacing were found to be significant as well as the interaction terms of ‘power \times speed’ and ‘speed \times spacing’. A model equation was determined (Equation 4-4) and the comparison of the actual results against the model are shown in Figure 4.36. This comparison is much harder to evaluate than the corresponding plot for the crack density model as many of the experimental results yielded very low void fraction.

The model predictions for the variation of void fraction with power and scan speed are shown in Figure 4.37 and Figure 4.38 respectively. The model predicts a trend completely opposite to that of cracking with void fraction decreasing with increasing laser power and increasing with increasing scan speed. Furthermore, these plots (and the subsequent ones) illustrate how this ‘model’ is a purely empirical relationship as it predicts negative void fraction in certain cases which is impossible.

Figure 4.39 shows a predicted increase in void fraction with increasing scan spacing which agrees strongly with the results obtained during the CM247LC study where the scan spacing was reduced in order to eliminate voids.

In terms of the interactions, Figure 4.40 shows that a low scan speed (1000 mm/s) appears to almost eliminate the influence of laser power on the void fraction maintaining it at effectively zero, whereas under a high scan speed the laser power greatly affects the void fraction. Similarly, Figure 4.41 shows that a low scan spacing ($a_1 = 0.35$) effectively reduces the void fraction to zero and eliminates the effect of the scan speed and conversely a high scan spacing (0.65) makes the void fraction highly dependent on the scan speed. Of course these results are only valid for the range of parameters investigated, but they reveal that there is a threshold of energy input for which full consolidation will occur; $\approx 1.3 \text{ J/mm}^2$ as seen in Figure 4.31. This threshold can be achieved either through laser power, scan speed or scan spacing, however once it has been passed then the material will be fully consolidated (ignoring the effect of cracks) and the other parameters will have no further influence on the void fraction; this use of energy density as a standardised measure of energy input to evaluate consolidation is consistent with current theory of SLM processing of Al alloys [4].

The surface plots in Figure 4.42 and Figure 4.43 illustrate the response for crack density and void fraction respectively and Figure 4.44 reveals, what was previously stated, that the two curves are opposite in terms of slope direction. This conclusively shows that for the parameter range investigated there is no condition where the voids can be eliminated whilst also eliminating the cracks. This supports the similar conclusion made for the parametric study of CM247LC.

The final ‘optimised’ process parameters are therefore a compromise predicting a crack density of 5.4 mm/mm^2 whilst still giving a void fraction of 0.01% (effectively 0%). The validation build results shown in Table 4.9 show that for validation sample 1 and 3 the void fraction prediction was very good and for sample 2 there was only a very small void fraction (0.21%) The results for crack density however were much more scattered varying by approximately $\pm 3 \text{ mm/mm}^2$. This shows that there is clearly a much greater scatter in the system than predicted by the 95% confidence bands shown in the previous results. The scatter is confirmed by the energy density plot of raw data (Figure 4.31) which shows high scatter and little distinct trend.

Overall the statistical method has shown that the void fraction can be successfully modelled. It appears however that there is significant scatter in the crack density results; an explanation for this scatter is suggested in Chapter 5. The overall trends support those found for CM247LC and validates the methods used with CM247LC for reducing the cracks and eliminating the voids within the samples. The statistical DOE also supports the conclusion that for the current SLM facility a condition where cracking and voids are eliminated in the as-fabricated condition for these high γ' volume fraction materials is un-achievable.

The statistical method has provided a rapid evaluation of the material process parameters; however, where this statistical DOE fails is in the understanding of the microstructural mechanisms responsible for the cracking.

4.4 IN625 Parametric Studies

The parametric investigation of IN625 was carried out in a very similar way to the previous CMSX486 study. Literature (see Chapter 2) suggests that IN625 is a good candidate for laser processing as it does not show the same susceptibility to weld-induced cracking.

This parametric study again aimed to rapidly assess the process parameters for IN625 however in this case the central composite design method was used for only three parameters: laser power, scan speed and scan spacing. The island size did not show any significance in the previous study and so was eliminated from this DOE. Also based on an initial examination of the samples, there was no cracking observed in the as-fabricated sate so the results were obtained for void area fraction only and utilised optical (rather than SEM) microscopy to aid the rapid nature of the investigation.

i. Powder Size Analysis Results & Discussion

As with the previous studies, the powder size distribution was measured. The argon gas-atomised IN625 powder was supplied by LPW Technology Ltd. in the size fraction +15-53 μm . Figure 4.45 shows the verified size distribution.

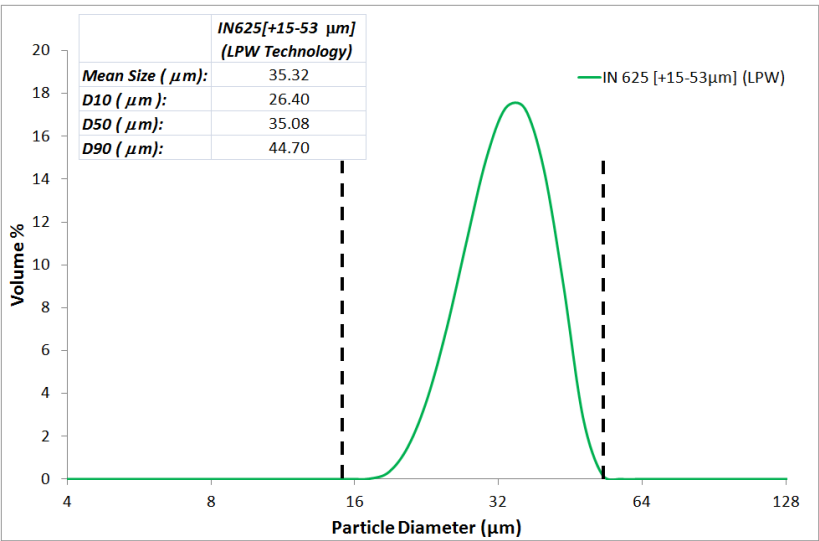


Figure 4.45: Particle size distribution for argon gas atomised IN625 powder as; black dashed lines indicate the ideal size distribution boundaries. Key sizing data is provided in the inset table.

The powder size distribution lies clearly within the ideal boundaries showing a maximum at almost exactly 53 μm and a minimum particle size slightly greater than 16 μm . The particle

sizes appear to show a good normal distribution with little skew as indicated by the similar mean and D50 (median) values.

ii. SEM Powder Examination: Results & Discussion

Examination of the ground and polished powder was carried out in a similar way to that of CM247LC and CMSX486. Figure 4.46 shows a typical image from the set taken for porosity measurement; it shows similar morphologies to the previous powders examined. There appear to be some poorly shaped particles caused by the attachment of two individual particles and evidence of liquid droplets colliding with solid particles causing misshaping and the characteristic crescent voids as seen previously.

Figure 4.47 shows a BSE SEM micrograph of an individual particle. It appears to show a finely dendritic morphology; however there does not appear to be any significant elemental segregation across the diameter of the particle as seen in the EDX linescans presented in Figure 4.48.

The overall porosity quantification is presented on Table 4.10. In general the IN625 powder appears to show much lower porosity in terms of average pore size and overall porosity area fraction than the previous two powders.

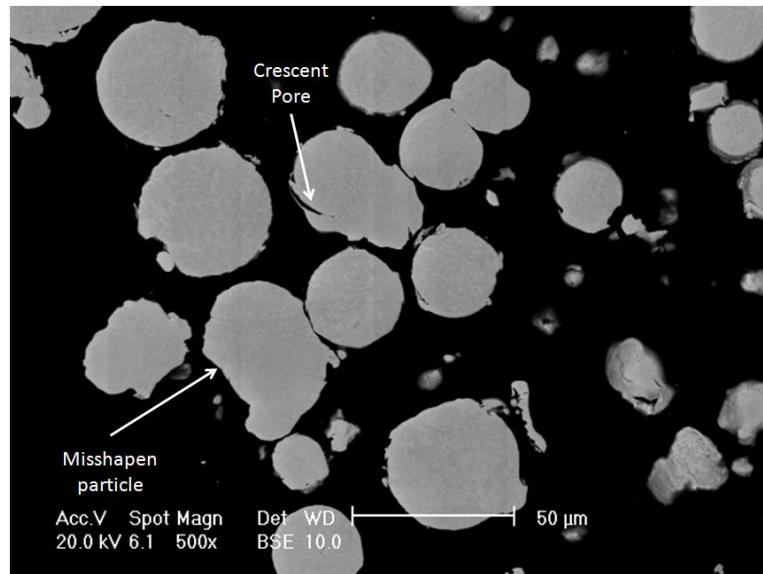


Figure 4.46: BSE SEM micrograph showing a typical sample of ground and polished IN625 as used for the porosity quantification. Note the misshapen particles due to particle joining during solidification and the ‘crescent’ shaped pores formed by particle collision during solidification.

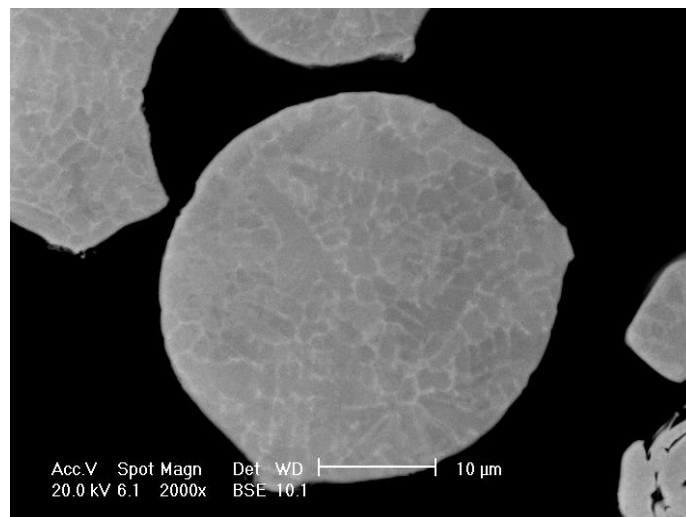


Figure 4.47: BSE SEM micrograph of an individual ground and polished particle of IN625 argon gas atomised powder.

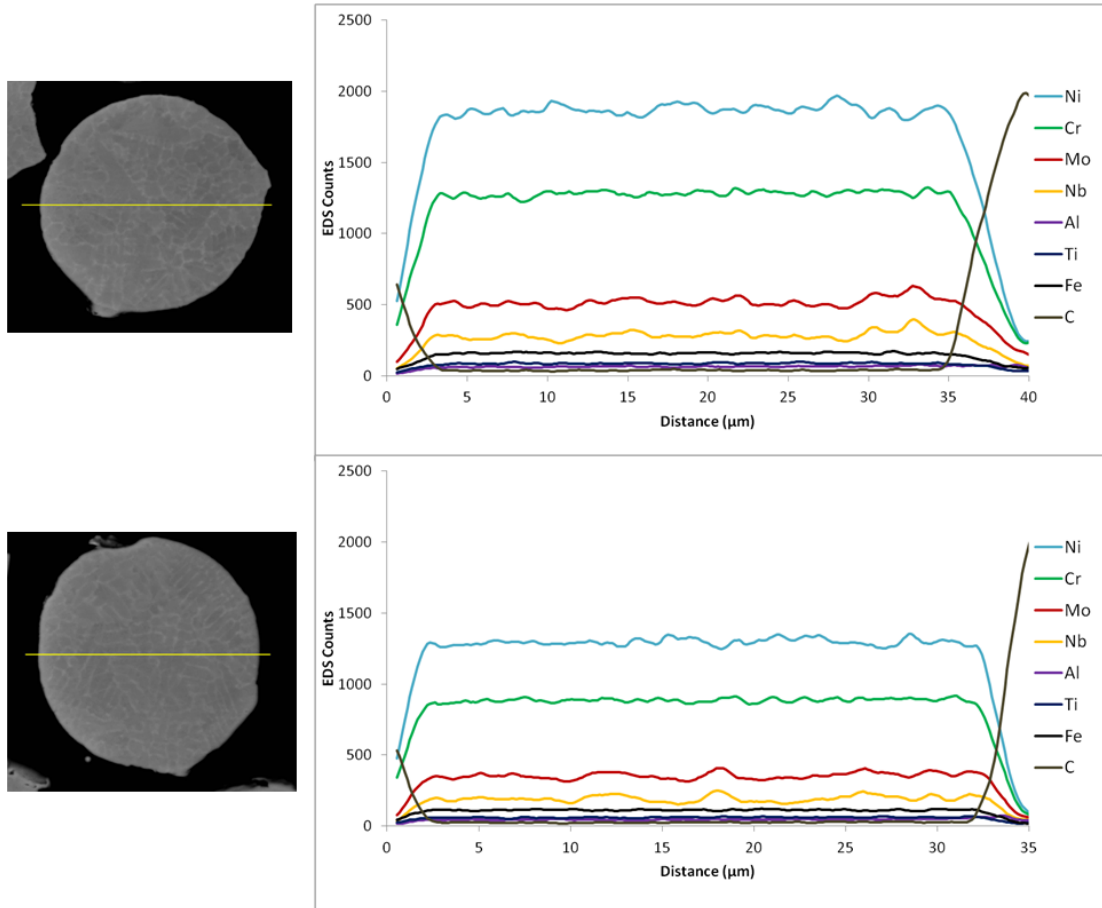


Figure 4.48: EDS linescans across two individual IN625 powder particles (Yellow line on micrograph denoting linescan profile). EDS results show no significant segregation across the particle. Note: The increase in C and decrease in Ni towards either end of the scan is due to the onset of the particle edge and the effect of the mounting Bakelite.

Table 4.10: Porosity quantification results for In625 powder.

Total number of particles analysed	447
Minimum pore size to be measured <i>(to eliminate noise)</i>	0.30 μm^2
Total number of pores analysed	203
Mean Pore equivalent diameter	1.19 μm
Maximum Pore equivalent diameter	2.97 μm
% Porosity of the analysed powder	0.14%

iii. SLM Parametric Study: Void Quantification Results

The raw results for the parametric study carried out for IN625 are presented in Table 4.11. the study investigated laser power (100 – 200 W); scan speed (1000 - 3000 mm/s) and scan

spacing (a1; 0.2-0.8). the raw data has been plotted against energy density (J/mm^2 , Equation 4-1) Figure 4.49.

Table 4.11: Parametric DOE study results for the SLM processing of IN625 investigating 3 parameters measuring porosity only.

ID		Factor 1: Laser Power (W)	Factor 2: Speed (mm/s)	Factor 2: Spacing (a1)	Response 1 (Porosity - % area)
1	Centre Points	150	2000	0.5	8.34
2		150	2000	0.5	7.43
3		150	2000	0.5	7.84
4	Axial Points	100	2000	0.5	15.54
5		200	2000	0.5	0.53
6		150	1000	0.5	0.11
7		150	3000	0.5	13.57
8		150	2000	0.2	0.35
9		150	2000	0.8	12.87
10	Cube Points	125	1500	0.35	1.53
11		125	1500	0.65	9.63
12		125	2500	0.35	8.4
13		125	2500	0.65	16.62
14		175	2500	0.35	2.42
15		175	2500	0.65	15.7
16		175	1500	0.35	0.13
17		175	1500	0.65	1.12

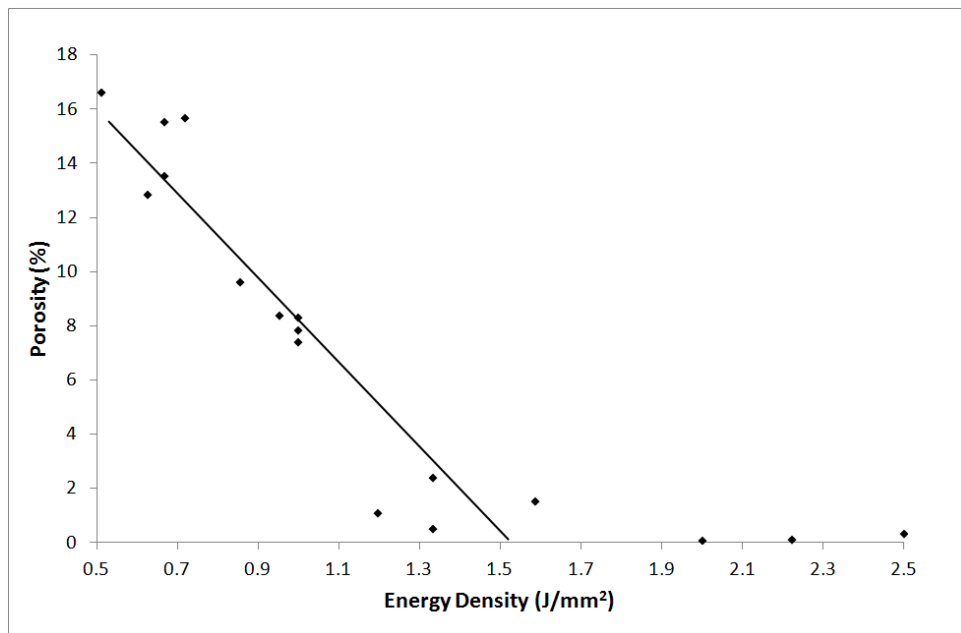


Figure 4.49: Plot showing porosity (%) against energy density (J/mm^2) for SLM of IN625.

The Design-Expert predicted an R^2 value of 83% when fitting these results to a linear model. In this case only the individual parameters laser power, scan speed and scan spacing were

examined for statistical significance. The ANOVA table is presented in Table 4.12 and shows that all of these parameters have a P-value of <0.05 and so are all significant.

Table 4.12: ANOVA for void area fraction of IN625. Blue rows indicate significant terms and red row indicates overall model significance.

Source	Sum of Squares	df	Mean Square	F - Value	P- Value (Prob>F)
Model	538.2	3	179.4	40.35	<0.0001
Power (A)	137.07	1	137.07	30.83	<0.0002
Speed (B)	207.72	1	207.72	46.72	<0.0003
Scan Spacing (C)	193.42	1	193.42	43.51	<0.0004

The linear model produced for these results is given in Equation 4-5.

Equation 4-5: Empirically determined relationship between the process parameters and the void fraction for IN625.

$$\text{Void Area Fraction (\%)} = -1.25672 - (0.11707 \times \text{Laser Power}) + (7.20625\text{E-}003 \times \text{Scan Speed}) + (23.17917 \times \text{Scan Spacing})$$

The comparison of the model against the actual void fraction values is shown in Figure 4.50.

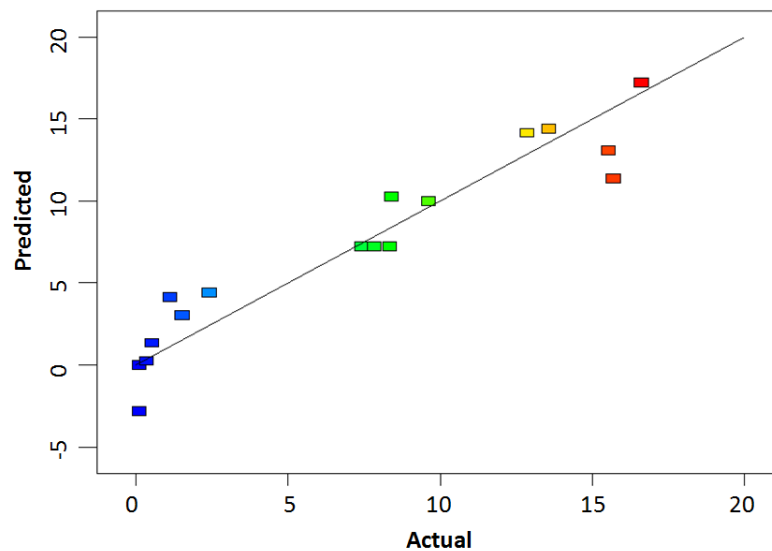


Figure 4.50: Plot showing comparison of predicted values against actual results for the void fraction of SLM-fabricated IN625.

Figure 4.51, Figure 4.52 and Figure 4.53 show that the void fraction increases with increasing scan speed and scan spacing, but decreases with increasing laser power.

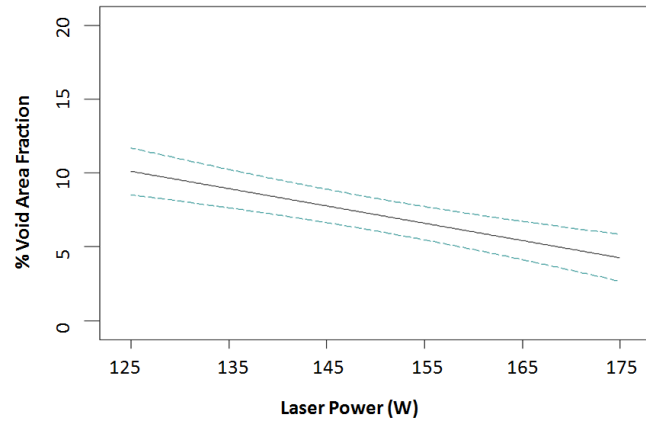


Figure 4.51: Plot showing predicted influence of laser power on void fraction for IN625. Dashed lines indicate the 95% confidence limits of the model.

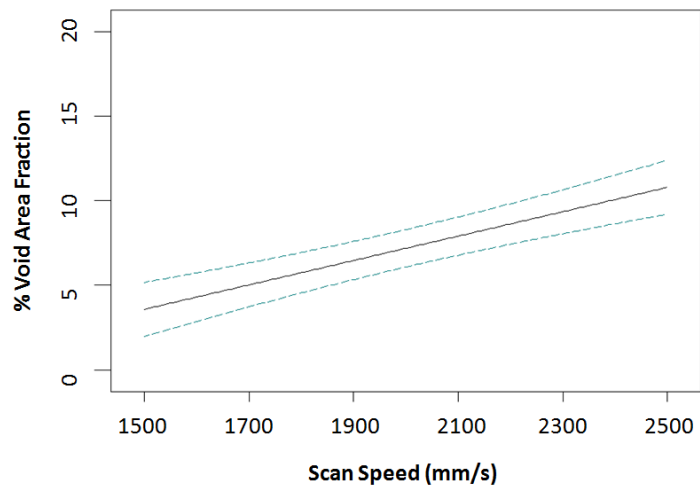


Figure 4.52: Plot showing predicted influence of scan speed on void fraction for IN625. Dashed lines indicate the 95% confidence limits of the model.

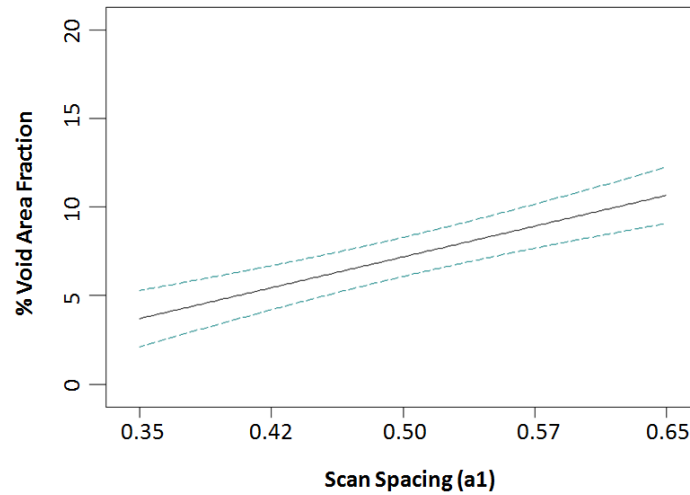


Figure 4.53: Plot showing predicted influence of scan spacing on void fraction for IN625. Dashed lines indicate the 95% confidence limits of the model.

The predicted limit of 0% void fraction with respect to scan speed and spacing for various laser powers is shown in Figure 4.54. Parameters falling below the line for their laser power are predicted to have a 0% void fraction (full consolidation).

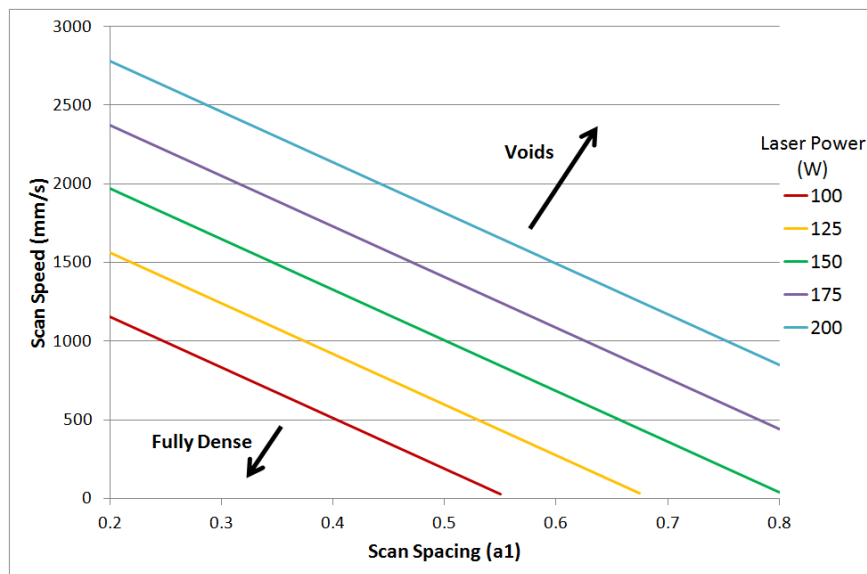


Figure 4.54: Plot showing the predicted limits of 0% void fraction for the SLM of IN625 for different laser powers in terms of scan speed and spacing. Processing parameters falling below the line specific to their laser power are predicted to produce fully dense material.

To further evaluate the processing parameters an approximation of the time to laser-scan each island (and so an indication of the overall process speed) was calculated using Equation 4-6

and the plotted values for each of the zero void fraction lines presented in Figure 4.54. This time-map is shown in Figure 4.55 and assumes a standard island size of 5mm × 5mm and the spot size of 0.15 mm.

Equation 4-6: Approximation to the time (s) to selectively laser melt one island.

$$Time (s) = \frac{\left(\frac{Island Width(mm)}{Laser Spot Diameter (mm) \times Scan Spacing(a1)} \right) \times Island Length(mm)}{Scan Speed (mm/s)}$$

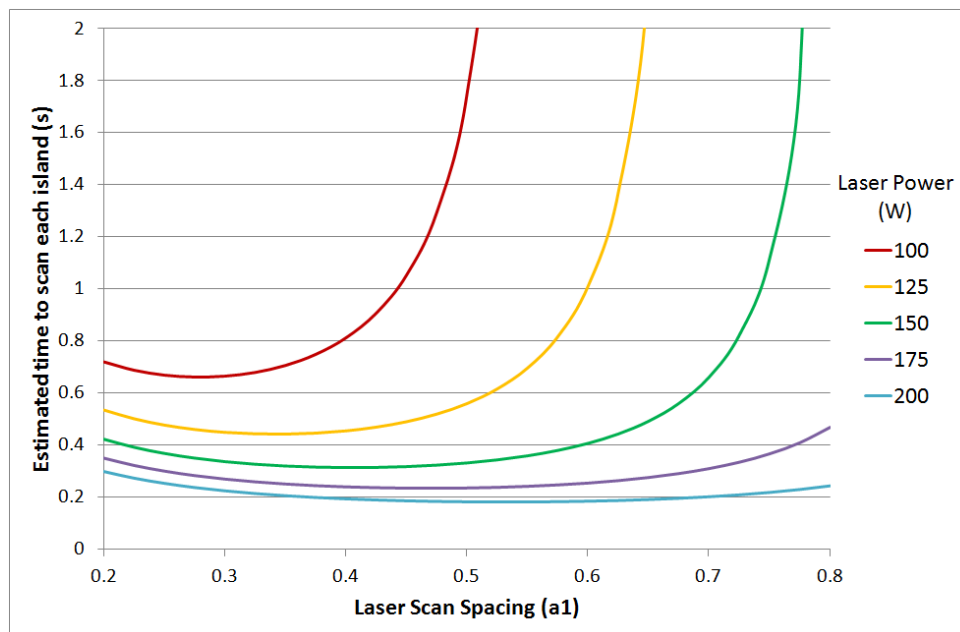


Figure 4.55: Predicted time-map for IN625 showing time to scan a single island for lines representing 0% void fraction samples for different laser powers and the corresponding required scan spacing. The corresponding scan speeds can be found by referring to Figure 4.54.

The optimum condition was found using a power of 200 W processing to produce fully dense samples in the shortest time; this corresponded to a scan speed of 1734 mm/s and a scan spacing of 0.525. The scan speed was rounded to 1700 mm/s (still corresponding to a predicted 0% void fraction) for simplicity.

Three validation samples were processed under these conditions and their void area fractions calculated. The results for this validation are shown in Table 4.13.

Table 4.13: Validation results for the optimised IN625 SLM parameters based.

	Void Area Fraction (%)
Validation 1	0.26
Validation 2	0.36
Validation 3	0.31

iv. SLM Parametric Study: Discussion

The reduced susceptibility for IN625 to cracking over CM247LC and CMSX486 lies in its improved ductility. Based on the literature data provided in Chapter 2 (sections 2.6 & 2.8) it can be seen that at room temperature IN625 shows up to 50% elongation to failure compared with only 10% for CM247LC. This improved ductility allows for greater accommodation of the residual stresses formed due to the SLM process. Additionally IN625 does not suffer from the same strain ageing effects as CM247LC as it is not a γ' hardenable alloy. There is hardening via γ'' however this occurs much more slowly and in the rapid heating and cooling of the laser process this is unlikely to have any influence. It should be noted that any distortion due to the internal stresses was not measured and further research with this alloy would need to address this issue.

It is for these reasons that cracking is not observed in any of the SLM-fabricated samples of IN625 and the parametric study instead focussed solely on the elimination of voids (volumetric defects) caused by incomplete consolidation. The Design-Expert software determined that a simple linear fit (Equation 4-5) was the most accurate to model the data with each of the three parameters being significant (Table 4.12). This model appears to show a reasonably narrow band of scatter when compared with the actual results in Figure 4.50. the plot of the raw data, Figure 4.49 confirms that the use of energy density (J/mm^2) as a normalised parameter can be used in the case of porosity (incomplete consolidation) which

supports the similar conclusion found for CMSX486 (and literature regarding SLM of Al [4]) and again appears to show a threshold for incomplete consolidation ($\approx 1.6 \text{ J/mm}^2$)

The previous studies into CM247LC and CMSX486 showed that the void formation behaviour is governed strongly by energy density and the results presented in Figure 4.51, Figure 4.52 and Figure 4.53 for IN625 confirm this. The void area fraction reduces with increasing laser power (more energy density), but increases with increasing scan spacing and scan speed (less energy density).

By plotting the modelled 0% void fraction boundaries as in Figure 4.54 for several laser powers it can be clearly seen that as the laser power is increased, the processing window for full consolidation is also increased. With such a wide range of parameters it was necessary to further constrain the limits to establish a 'best' processing parameter set. Therefore the approximation for the selective laser melting of a single island (Equation 4-6) was established as a method for reducing the processing time. For each of the 0% void fraction boundary lines this single-island time was calculated and plotted against the scan spacing for each laser powers (The appropriate scan speed could be found by substituting back in to Equation 4-5 or referring to Figure 4.54). Clearly the maximum laser power of 200 W produces the fastest processing times and due to the trade-off between scan speed and scan spacing, a minimum processing time was found at: 200 W, 1734 mm/s, $a1 = 0.525$. For simplicity the scan speed was rounded down to 1700 mm/s for practical processing. This is still predicted to yield a 0% void fraction.

The validation of this parametric study was carried out by SLM processing three further samples at the optimised conditions; the results for this are presented in Table 4.13. These samples did show a higher than predicted void fraction, but on average the material density by

optical examination was 99.69% which is overall reasonable. A high number of the pores observed appeared to be spherical implying that they were retained from gas porosity within the atomised powder; however some of the pores were irregular in shape indicating possibly poor bonding between layers or incomplete consolidation.

It is suggested that if further work were to take place on this alloy then as the window for complete consolidation is so large, the process parameters should be adjusted to allow for any scatter not predicted with the model by applying a ‘safety factor’ to the scan speed or spacing ensuring the best possibility for full material consolidation. For all other samples of this material produced in this thesis however, the parameters used for the validation (as stated above) were used for the SLM processing of the material.

4.5 Validity & Limitations of the Image Analysis Method Used for the Quantification of Crack Density

The image analysis method used for quantification of the crack density was selected to provide a repeatable and versatile solution to the problem of measuring a crack density within the material which shows different crack character depending on the process conditions. The results were required to present to overall ‘damage’ within the fabricated rather than just the maximum damage region (as would be the case using a maximum crack length measurement traditional in fatigue studies). It is for this reason that a ‘crack density’ method was used where the amount of cracking in total crack length was normalised with respect to the micrograph area.

One limitation of this has already been outlined; the image processing method considers all defects to be cracks. This inaccuracy was discussed in Section 4.2.vi. where voids were interpreted as cracks for the condition 150 W, 1500 mm/s and therefore an artificially high

value for cracking was reported. This type of limitation stresses the importance of examining the micrographs rather than simply relying on a fully automated routine to interpret the results.

The second limitation revolves around the use of Feret diameter which simply measures the maximum point to point length of a thresholded particle. This is a good approximation where the cracks are reasonably straight such as in the grain boundary cracking condition illustrated in Figure 4.14. However where the cracks are highly interlinked and do not show the same directionality such as in the solidification case shown in Figure 4.11 this approximation becomes increasingly inaccurate. Possibly underestimating or overestimating the crack density depending on which sections are ‘linked’ once the threshold has been applied. However these regions would also cause problems if a classical grid intercept method was used and the decision as to where or what constituted an individual crack would then fall to operator judgement. Similarly a simple ‘crack count’ method would suffer with the same problems as well as not providing any indication as to the crack density.

The image analysis method also only examines the crack density within a single plane and ideally a three-dimensional consideration would be taken. A microCT method, as presented in Chapter 5, would be able to produce this however to carry this out for the amount of samples needed for this parametric study is currently impractical due to time and budget.

Although this image analysis method does suffer from some limitations, it should be emphasised however that it does give a good approximation to crack density under the grain boundary cracking condition which is where the interest in this particular study lies. It should also be noted that the accuracy of this method increases as the crack density approaches zero. Under the solidification dominant conditions the method provides a consistent method of

quantifying the crack density and although the results are not as reliable as those produced for the low energy samples, they can still be presented as long as the limitations are fully understood.

4.6 Conclusions & Summary

Overall the CM247LC study has shown that the character of the cracking can be related to the processing conditions within the SLM process however for both of the γ' hardenable materials (CM247LC and CMSX486) it has not been possible to eliminate the cracking in the as-fabricated condition. The study has instead focussed on reducing the cracking as much as is possible whilst retaining a 'fully consolidated' (i.e. no voids) structure.

Through microstructural examination of the cracks, different mechanisms have been suggested as responsible for their formation. Under the optimised processing conditions for CM247LC grain boundary cracking is dominant and based on the microstructural observations a combination of the DDC and liquation mechanisms are suggested for their formation.

The statistical methods used for CMSX486 and IN625 have supported the findings of the CM247LC study in terms of the overall trends with respect to consolidation and cracking as well as showing that this type of method can be used to rapidly assess a material and obtain reasonable processing conditions. The scatter in these models should not be overlooked however and the 'real-life' component geometry is also likely to have a huge impact on the process. It is therefore clear that although these types of studies can be used to initially assess a material, it should be a long-term goal that the process be tailored to the specific component and ideally an all encompassing model should be developed to dynamically vary the processing parameters to best suit each slice of the build.

The use of a normalised energy parameter to combine the input parameters remains as a contentious issue. The incomplete consolidation/porosity can be linked strongly to a normalised parameter showing that the energy density input provides a good method of assessing the ability of a parameter set to fully consolidate the material, however the more complex issue of cracking does not appear to relate well to this normalised parameter as highlighted by the CM247LC parametric study and the scatter in the CMSX486 cracking results. The cracking phenomenon will be highly dependent on the formation of residual stresses, the complex material laser interactions and the thermal behaviour of the material.

The work presented in Chapter 5 continues to discuss a ‘retro-fix’ HIPping solution to eliminate the remaining cracks within the material.

Finally it should be noted that these parametric studies have highlighted the stark differences in processability between the different nickel-base superalloys investigated. IN625 has shown excellent processability and does not display the high crack-susceptability of CM247LC and CMSX486. This emphasises the need for appropriate material selection by designers and engineers when considering SLM as a processing route but also the need to develop high-temperature materials specifically suited to the SLM process if this is to be a viable manufacturing option in the future.

4.7 References

- [1] Cannon-Muskegon. C-M Group Website. www.c-mgroup.com, vol. 2009, 2009.
- [2] Das S. Physical Aspects of Process Control in Selective Laser Sintering of Metals. *Advanced Engineering Materials* 2003;5:701.
- [3] Thümmel F, Oberacker R. *Introduction to Powder Metallurgy*. London: The Institute of Materials, 1993.
- [4] Olakanmi EO, Cochrane RF, Dalgarno KW. Densification mechanism and microstructural evolution in selective laser sintering of Al-12Si powders. *Journal of Materials Processing Technology* 2011;211:113.
- [5] Wu X, Wang F, Clark D. On direct laser deposited Hastelloy X: dimension, surface finish, microstructure and mechanical properties. *Materials Science and Technology* 2011;27:344.
- [6] Sidhu RK, Ojo OA, Chaturvedi MC. Microstructural response of directionally solidified Rene 80 superalloy to gas-tungsten arc welding. *Metallurgical and Materials Transactions A (Physical Metallurgy and Materials Science)* 2009;40:150.
- [7] Egbewande AT, Buckson RA, Ojo OA. Analysis of laser beam weldability of Inconel 738 superalloy. *Materials Characterization* 2010;61:569.
- [8] Zhong M, Hongqing S, Wenjin L, Xiaofeng Z, Jinjiang H. Boundary liquation and interface cracking characterization in laser deposition of Inconel 738 on directionally solidified Ni-based superalloy. *Scripta Materialia* 2005;53:159.
- [9] Grong O. *Metallurgical Modelling of Welding* (2nd Edition). London: Institute of Materials, 1997.
- [10] Shiomi M, Osakada K, Nakamura K, Yamashita T, Abe F. Residual stress within metallic model made by selective laser melting process. *CIRP Annals - Manufacturing Technology* 2004;53:195.
- [11] Dye D, Hunziker O, Reed RC. Numerical analysis of the weldability of superalloys. *Acta Materialia* 2001;49:683.
- [12] Rush MT, Colegrove PA, Zhang Z, Broad D. Liquation and post-weld heat treatment cracking in Rene 80 laser repair welds. *Journal of Materials Processing Technology* 2012;212:188.
- [13] Institute IC. *Atlas of casting defects / Investment Casting Institute*. (2nd Edition): Montvale, N.J. : The Institute, 2004.
- [14] Ramirez AJ, Lippold JC. High temperature behavior of Ni-base weld metal Part II - Insight into the mechanism for ductility dip cracking. *Materials Science and Engineering A* 2004;380:245.
- [15] Design-Expert Software. Stat-Ease.

CHAPTER 5: INFLUENCE OF LASER SCAN STRATEGY ON GRAIN STRUCTURE, ORIENTATION AND CRACKING

Results and discussion are presented in this chapter examining the influence of the Concept Laser ‘Island Scan Strategy’ (as defined in Chapter 3) used during SLM. This strategy is found to have an impact on the grain structure, orientation and three-dimensional crack distribution within the material. A small study designed to compare the island scan pattern against a simple ‘back-and-forth’ scan pattern is also presented.

5.1. Introduction

The Concept Laser ‘Island Scan Strategy’ is used as standard during the M2 operation. Full details of this method are found in Chapter 2; in summary: the filled area of each slice is laser scanned in small square sections referred to as ‘islands’. Each island (5 mm × 5 mm) is formed with a regular ‘back-and-forth’ laser path; however the order in which the islands are scanned is randomised. The overall island pattern is moved by 1 mm in its X and Y axes with each layer. The following sets of results have been collated to illustrate the influence of this strategy on SLM fabricated CM247LC.

5.2. Grain Structure

Optical and SEM microscopy was performed on etched samples in both the X-Y (transverse) and X-Z (longitudinal) planes in order to examine the grain structure.

Figure 5.1 shows an optical micrograph of the X-Y plane, clearly visible is a repeating ‘square’ shaped pattern of lightly and heavily etched regions. The darker regions appear to be at the borders of each ‘square’ with the more lightly etched regions lying in the middle of the

‘square’. This pattern is a repeating feature across the entire plane with each square having a side-length of 1 mm as shown in the annotated micrograph, Figure 5.2.

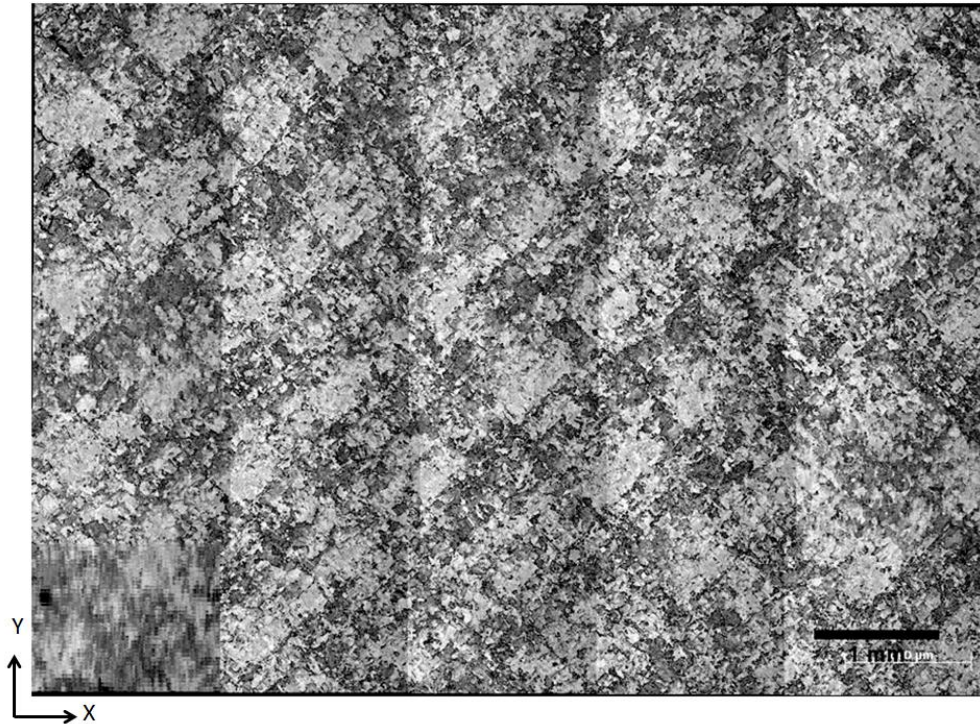


Figure 5.1: Optical Micrograph (Stitched) showing etched microstructure in the X-Y plane; vertical lines are an artefact of micrograph stitching.

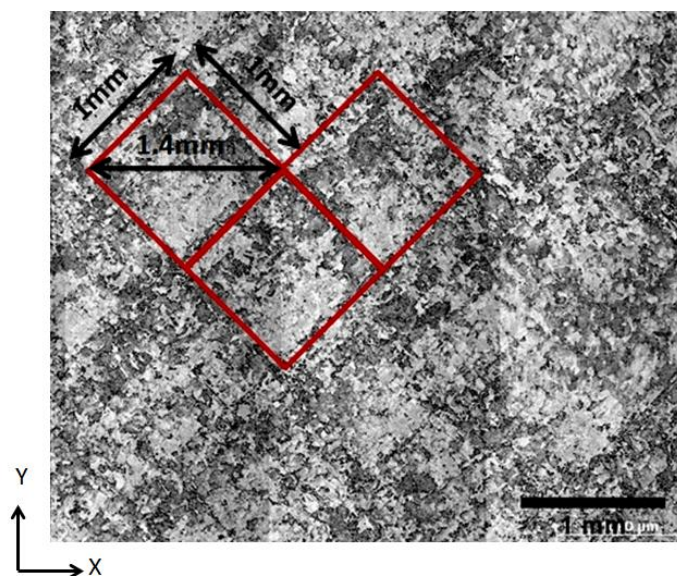


Figure 5.2: Annotated optical micrograph showing the 1 mm repeating 'square' pattern in the X-Y plane.

Figure 5.3 shows a backscattered SEM micrograph taken from the boundary region between these two differently etched regions. The more heavily etched area shows a region of fine-elongated grains, whilst the more lightly etched region shows larger grains appearing to be more equiaxed.

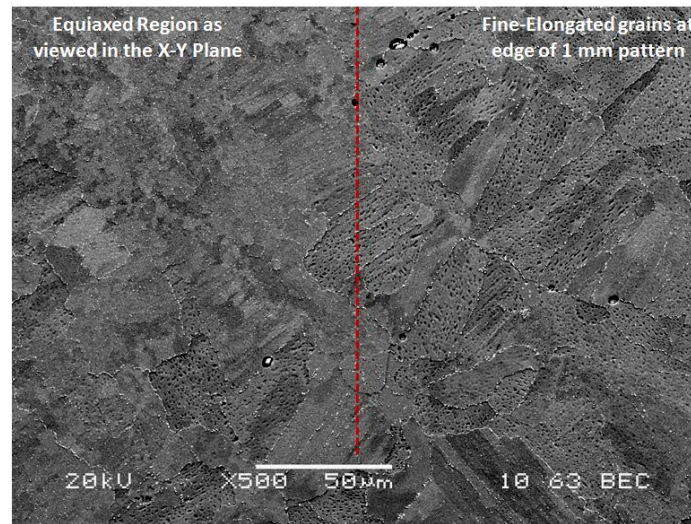


Figure 5.3: Backscattered SEM Micrograph showing the fine elongated grain structure at the pattern boundary region (Right of the dashed line) of the 1 mm pattern contrasting with the more equiaxed grains in the central region (left of the dashed line).

Figure 5.4 shows an optical micrograph of an etched specimen in the X-Z (longitudinal) plane. The grain structure shows long elongated ‘plumes’ of columnar grains typically associated with laser processing (see literature review, Chapter 2). There is also a secondary fine grained region lying between the long columnar areas. This bimodal structure is confirmed under SEM observation as shown in Figure 5.5.

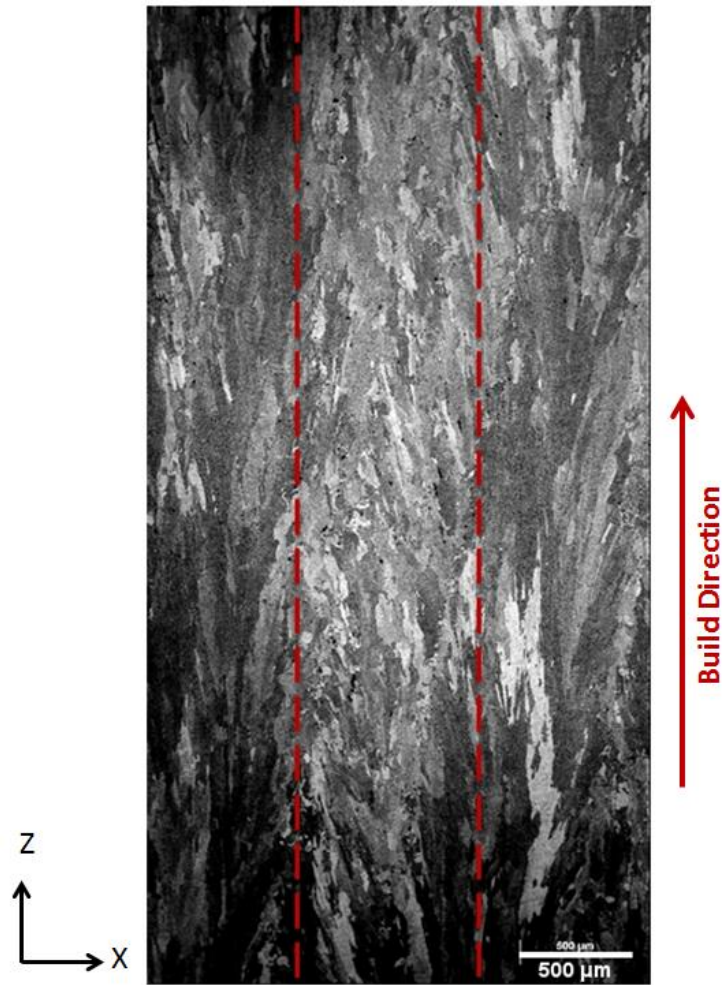


Figure 5.4: Optical micrograph in the X-Z plane showing the long ‘plumes’ of elongated grains with the fine grained region running down the middle of the image in the build direction (between dashed lines).

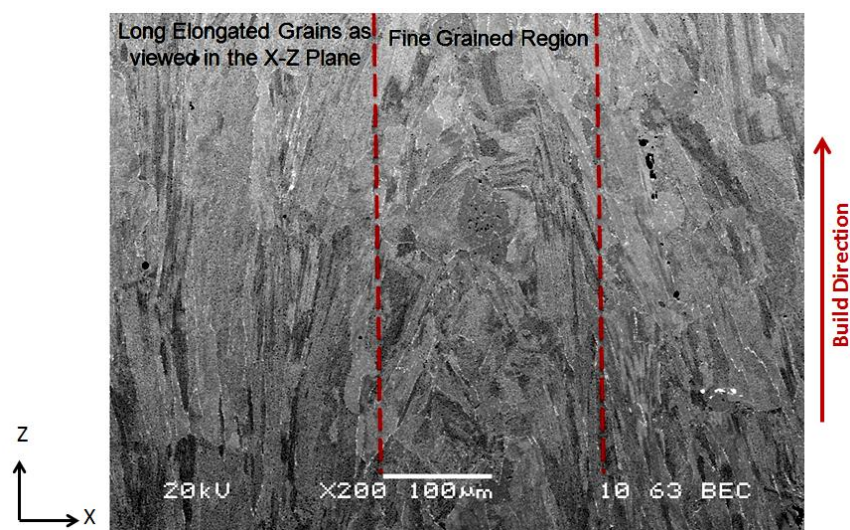


Figure 5.5: Backscattered SEM micrograph showing the elongated and fine grained regions in the X-Z plane (denoted by dashed lines).

The micrographs of the X-Y and X-Z planes can be considered simultaneously to form an understanding of the 3-dimensional grain structure. The SLM processed material consists of regions of columnar grains elongated in the build direction (Z axis), but appearing equiaxed in the X-Y plane. These columnar zones are separated by fine grained regions which form a macro $1\text{ mm} \times 1\text{ mm}$ square pattern when viewed in the X-Y plane and projects downwards throughout the Z-axis; these fine grains also display some elongation, but in directions perpendicular to the build direction. This bi-modal grain structure is shown diagrammatically in Figure 5.6 (a) imposed on a cuboid. An overall schematic representation can be seen in Figure 5.6 (b) with the blue and red regions representing the columnar and fine grains respectively.

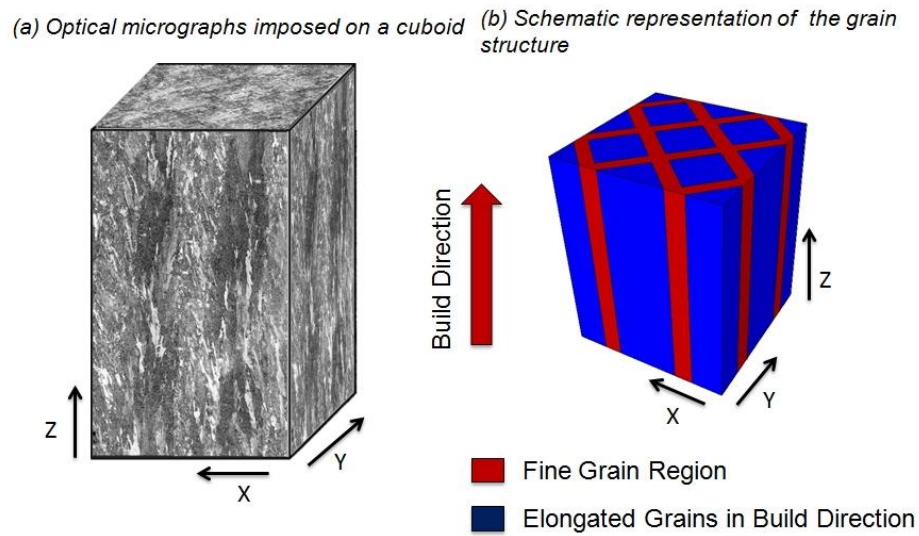


Figure 5.6: Diagram showing how the grain structure in the transverse (X-Y) and longitudinal (X-Z) planes relate to each other; (a) is a 3D representation constructed from micrographs and (b) shows this relationship schematically. This suggests a bimodal grain structure consisting of coarse elongated grains surrounded by fine grained regions in a repeating square pattern.

5.3. EBSD Mapping

A large area (approx. $1.5\text{ mm} \times 2\text{ mm}$) inverse pole figure (IPF) coloured EBSD map of the X-Y plane is presented in Figure 5.7. The same bimodal grain pattern can be seen in the

EBSD map. The elongated columnar grains correspond to the ‘red’ regions of the map and represent a strong $\langle 001 \rangle$ texture with respect to the normal. The secondary fine-grained regions do not show a specific orientation and in general display a much more random texture. The $\{100\}$ pole plots shown in Figure 5.8 correspond to each of these two regions: Figure 5.8 (a) to the columnar grained region and Figure 5.8 (b) to the fine grained region. Figure 5.8 (a) shows a strong $\{100\}$ texture misaligned to the sample normal by approximately 45° . Figure 5.8 (b) shows some weak crystallographic alignment of the $\{100\}$ poles, but in general terms there is no strong texture and a high level of misalignment between grains both internally and to the surrounding strongly textured region.

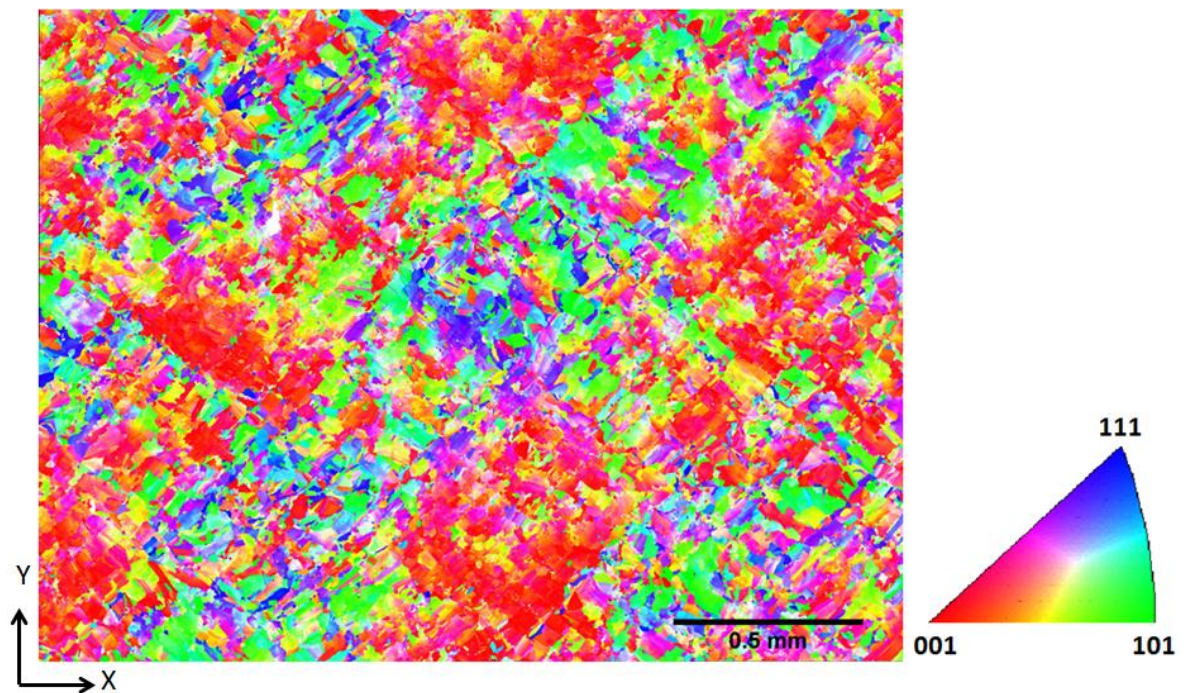


Figure 5.7: IPF EBSD map showing the X-Y plane of SLM fabricated CM247LC highlighting the repeating square pattern.

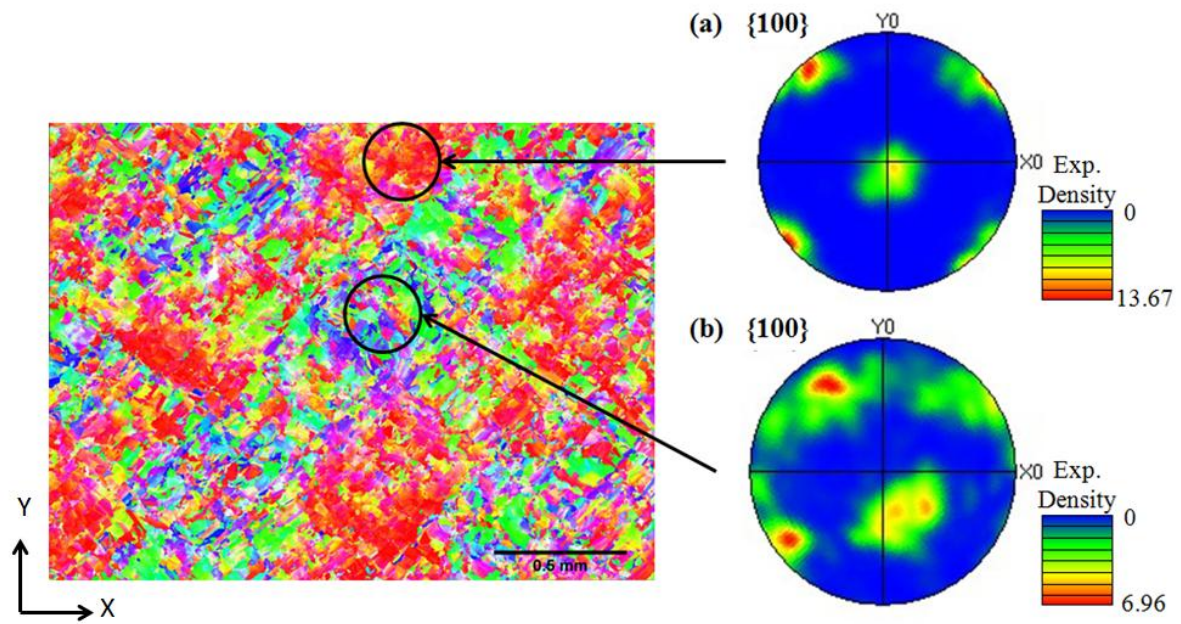


Figure 5.8: Localised pole figures corresponding to (a) area of strong texture, (b) less defined orientation.

Figure 5.9 shows the grain boundaries $> 5^\circ$ for the same EBSD mapped region, for clarity an enlarged area showing one of the repeating pattern units is provided in Figure 5.9 (b) whilst the full map is shown in Figure 5.9 (a). Figure 5.10 shows the frequency plot for the occurrence of the different misorientation angles for the entire mapped area. The bar chart in Figure 5.11 shows the misorientation angle frequencies for the different regions (the ‘core’ and ‘boundary’ regions of the repeating pattern) of the mapped area. It should be noted that the bounding of these regions has been determined by the author’s judgement and the results are presented only as an indication of the trend of misorientation angles in these regions.

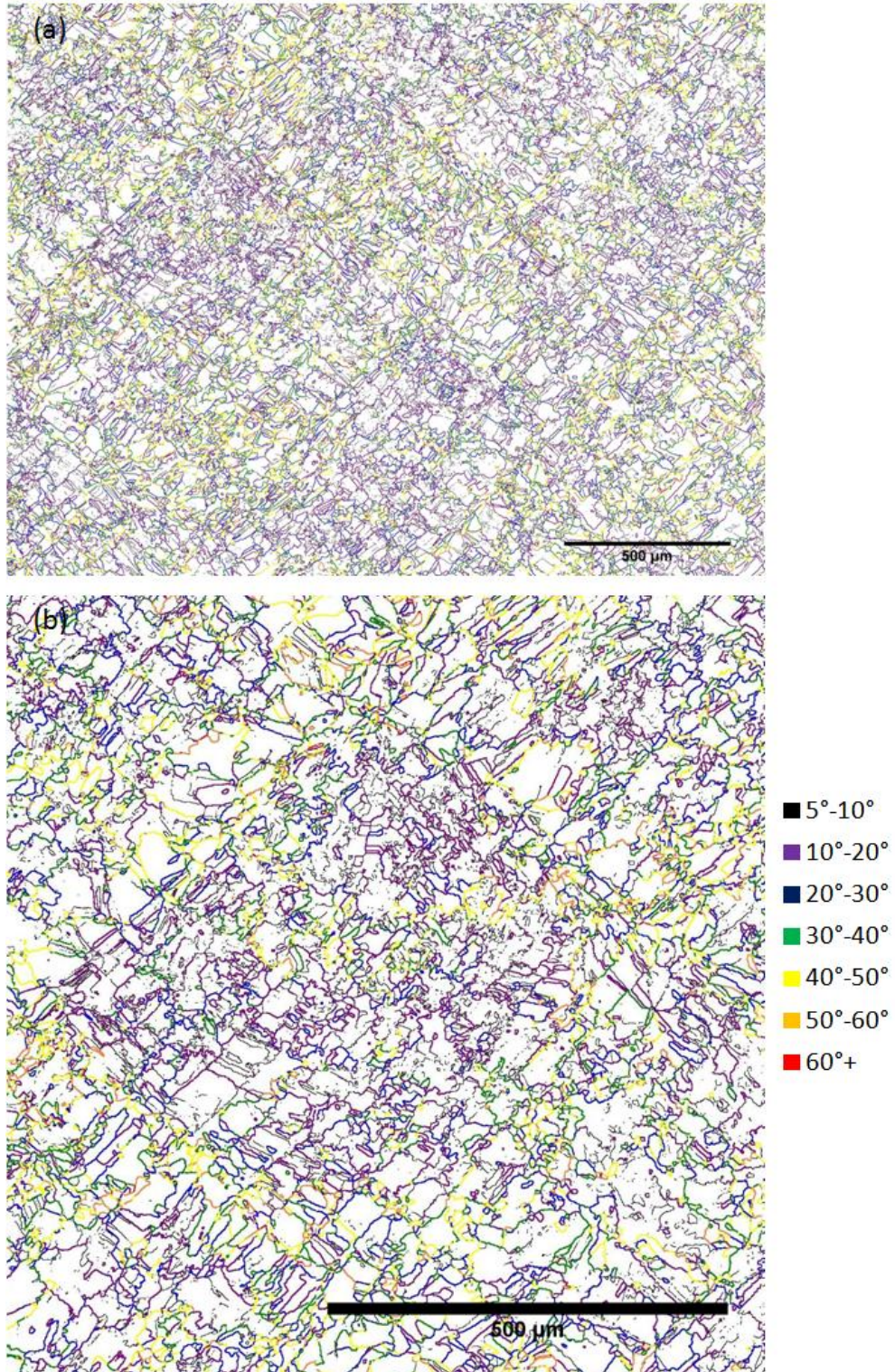


Figure 5.9: Grain boundary misorientation of the EBSD mapped area for misorientation $> 5^\circ$; (a) shows the entire area; (b) shows a single unit of the repeating pattern.

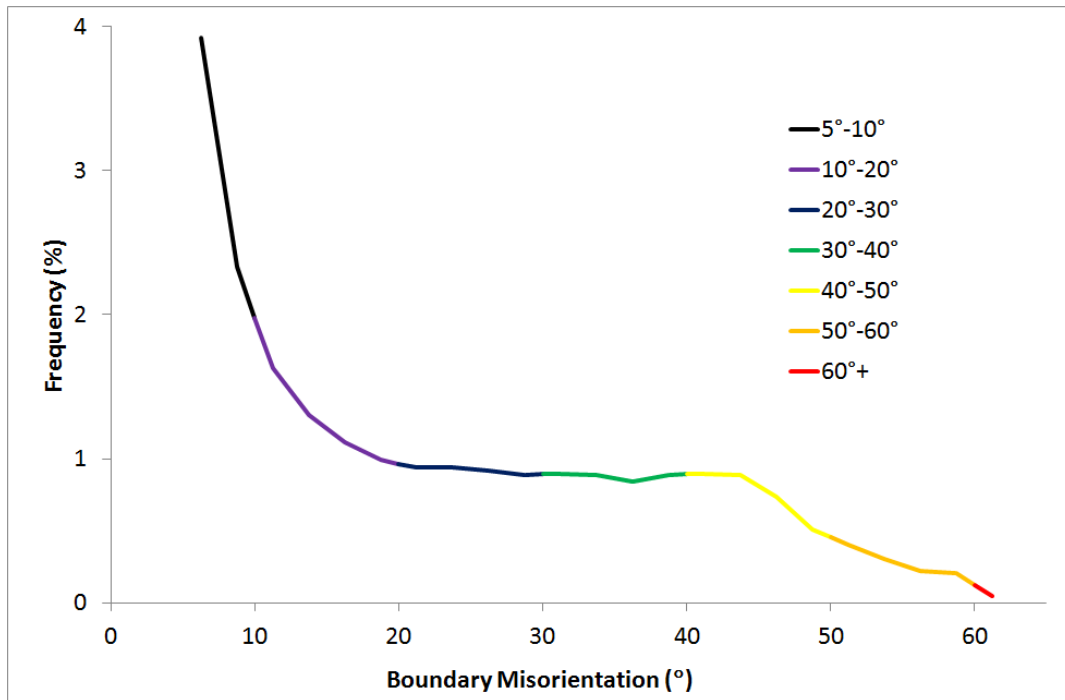


Figure 5.10: Frequency distribution of grain boundary misorientation for the entire EBSD mapped area (misorientation > 5° only).

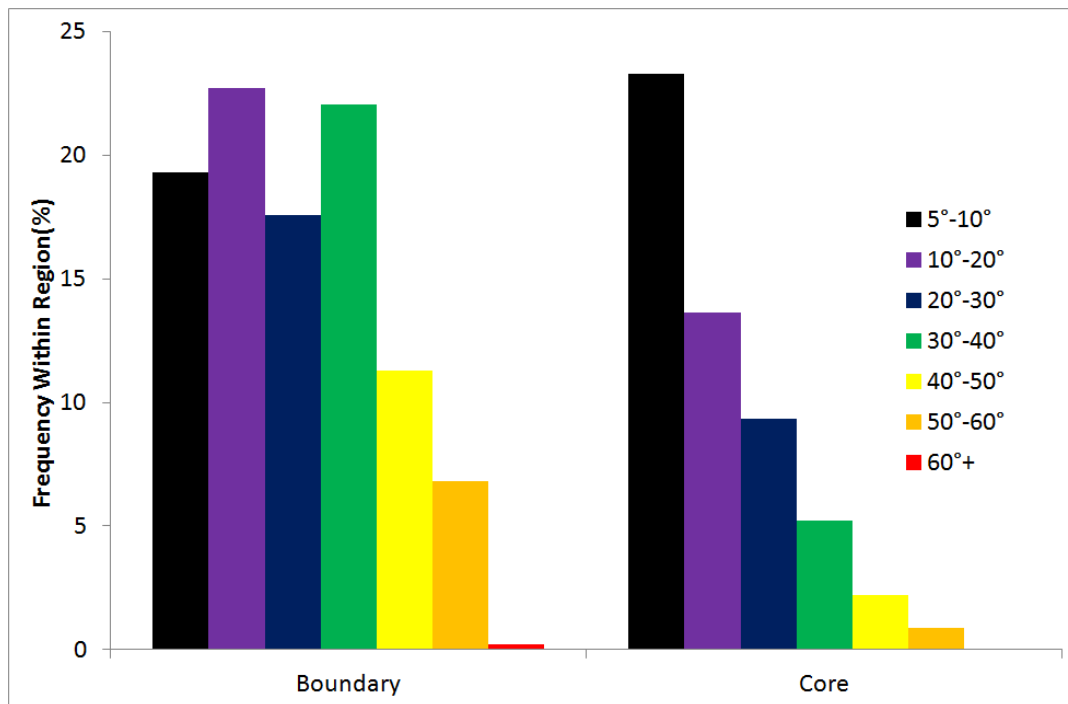


Figure 5.11: Relative frequency of grain boundary misorientation within the boundary and core regions of the repeating pattern (regions were divided using by author's judgement).

5.4. MicroCT & SEM Visualisation of Cracks and Voids

Figure 5.12 shows a 3-dimensional visualisation of the cracks within the as-fabricated CM247LC sample cut from the surface of a cylindrical test specimen. The red shapes represent the cracks whereas the yellow shapes represent larger void-like defects within the structure.

Figure 5.13 (a) shows the same sample as viewed at the X-Y plane (down the Z axis). The cracks appears to lie in very specific regions and boundaries between the more heavily cracked and lightly cracked material as labelled in the annotated Figure 5.13 (b). It is suggested that these heavily and less heavily cracked regions also follow the same $1\text{ mm} \times 1\text{ mm}$ pattern as seen in the previous microscopy and EBSD results, although the sample size is too small to see a complete pattern unit.

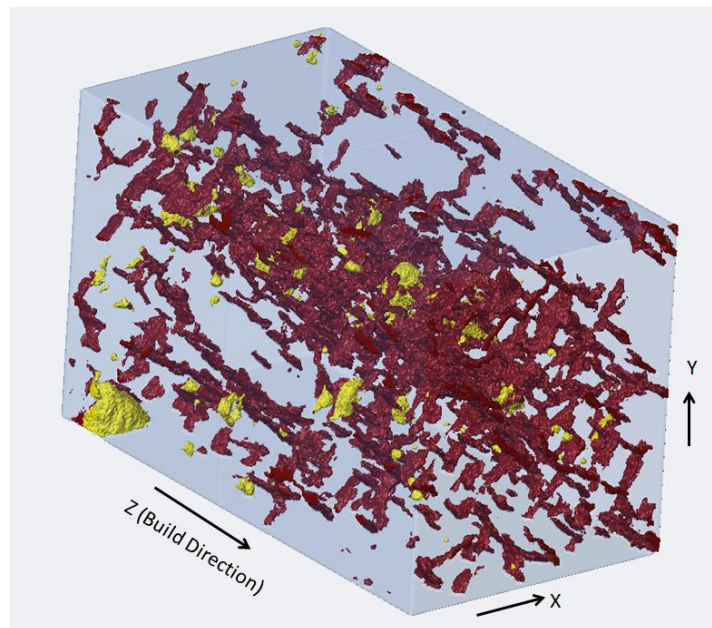


Figure 5.12: MicroCT 3-dimensional visualisation of SLM fabricated CM247LC showing cracks (red) and voids (yellow); note the band of heavy cracking running through the entire length of the sample. Sample measuring 2.5 mm across X-Y diagonal.

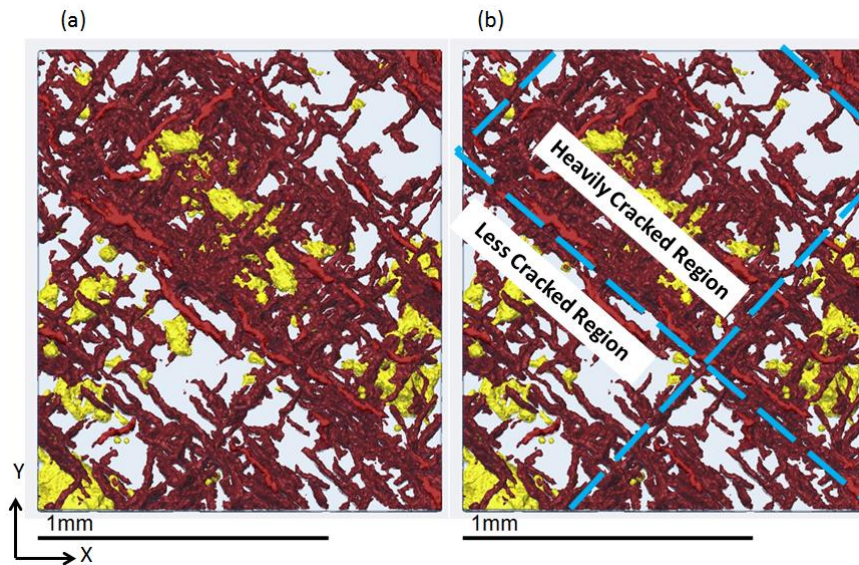


Figure 5.13: MicroCT 3-dimensional visualisation of SLM fabricated CM247LC of the X-Y plane showing cracks (red) and voids (yellow). (a) standard visualisation; (b) annotated image showing the boundaries between the well defined heavily and less cracked regions denoted by the dashed lines.

SEM observations of the X-Y plane were used to support the MicroCT observations. Figure 5.14 shows a backscattered SEM micrograph with annotations indicating the heavily cracked boundary regions.

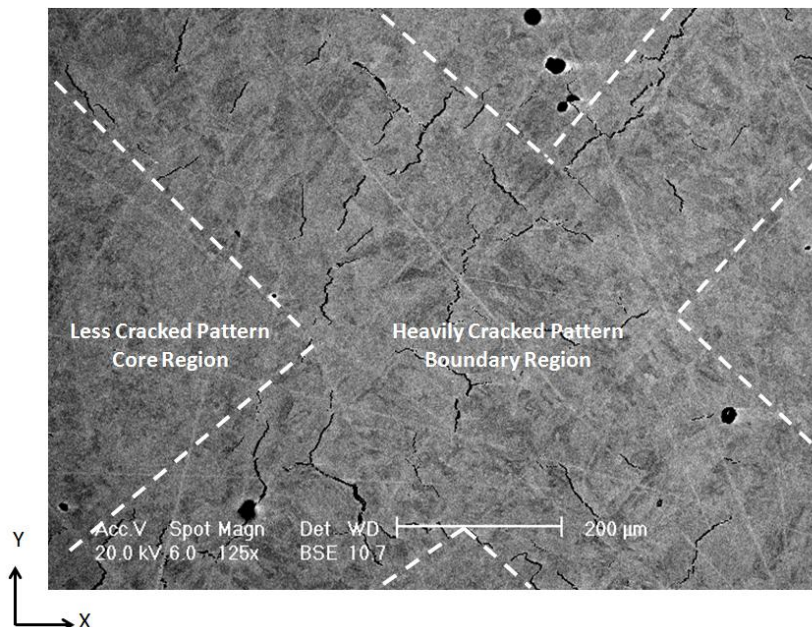


Figure 5.14: BSE SEM micrograph showing the as-fabricated transverse (X-Y) plane with annotations indicating the heavily cracked and less cracked regions of the repeating pattern.

As a ‘retro-fix’ solution to the cracks, samples were HIPped (as described in Chapter 3) with the aim of closing the cracks and producing a fully dense material. Figure 5.15 shows the microCT visualisation of the cracks within the HIPped sample; the few remaining cracks (red) are all connected to the sample surface. An SEM micrograph of a similar sample is shown in Figure 5.16 confirming the crack closure.

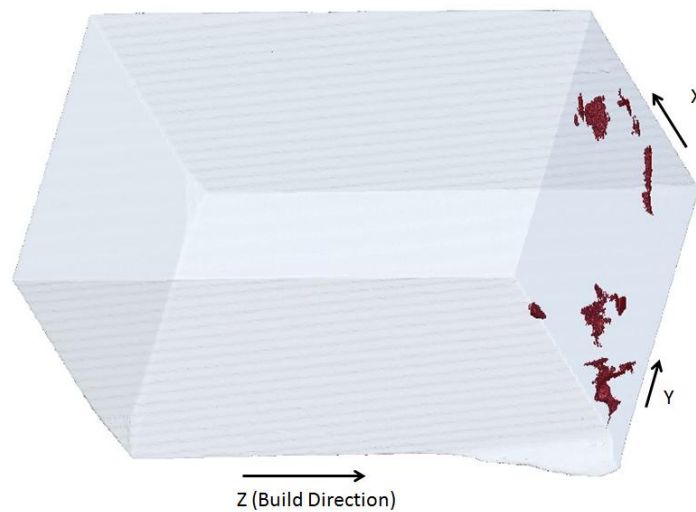


Figure 5.15: MicroCT 3-dimensional visualisation of SLM fabricated and HIPped CM247LC showing cracks (red).

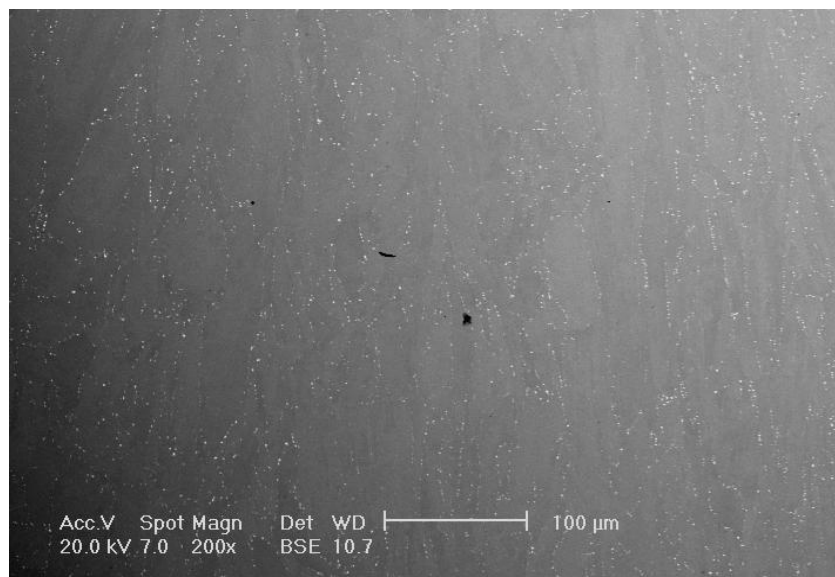


Figure 5.16: BSE SEM Micrograph showing SLM fabricated and HIPped CM247LC. Note the elimination of cracks with only minor isolated porosity remaining.

5.5. Discussion

The square patterned bi-modal grain structure is clearly not a naturally occurring property of the material and can only be a result of the SLM process. The pattern takes the form of a repeating square shape of 1 mm side-length rotated by 45° to the X axis. As previously stated, the island scan strategy uses a 5 mm island size, so the origins of this 1 mm pattern are not immediately obvious, yet it becomes apparent by considering several layers and the movement of the island pattern. Figure 5.17 shows how the position of a single 5 mm island moves over 5 slices. With each slice the entire island pattern is shifted by 1 mm in the X and Y of their local co-ordinate system. Considering that the ‘red’ island in Figure 5.17 represents the position of the island in the 1st slice, the ‘blue’ outline being the 2nd slice position and so on, it can be seen that there is a square 1 mm repeating ‘interference’ pattern caused by the overlapping island borders. In real terms, this island pattern is spread throughout the X-Y plane and after 6 slices the island borders lie exactly as they did in the 1st slice so this pattern also stretches through the entire height (Z) of the build.

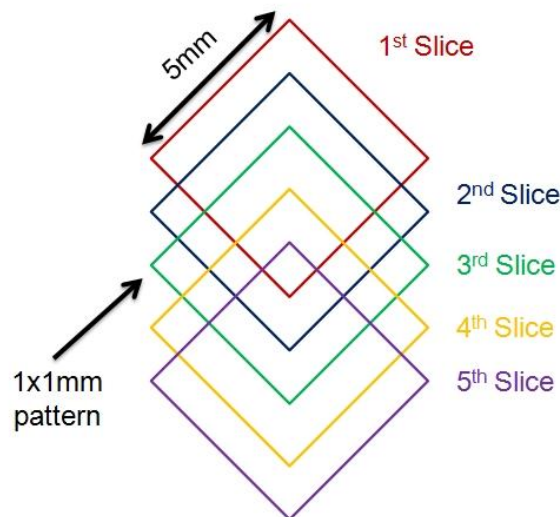


Figure 5.17: Schematic representation of how the 5mm island pattern with a 1mm shift each layers can result in the observed 1mm repeating pattern in the grain structure caused by the effect of the edges of the islands realigning every 6 slices.

Large columnar grains are widely reported to occur in laser fabricated materials [1-4] as discussed in Chapter 2 (section 2.12) due to the partial remelting of the preceding build layers and the highly directional nature of the heat flow vertically downwards through the previously deposited material and build plate. The research by Liu et al. [5] presents a bi-modal grain structure within DLF deposited IN718; this structure is attributed to the rapid cooling at the edge of each of the laser scan tracks forming fine grained regions.

The affinity of nickel to show a strong $\langle 001 \rangle$ orientation with respect to the axis of heat flow (as exploited in DS and SC casting) supports the finding that it is the large columnar grains which correspond to the highly $\langle 001 \rangle$ textured regions of the EBSD maps. This is characteristic of FCC alloys cooled directionally due to the competitive grain growth effect; a fuller explanation of this phenomenon is available elsewhere relating to DS casting [6]. Similar texture has been observed in the previously discussed (See Chapter 2) research regarding DLF of IN718 by Zhao et al. [7].

By considering both the observations of the grain structure and the EBSD results it is apparent that the columnar regions have been formed in a relatively slowly cooled region with a strong vertical direction heat flow ($-Z$) where epitaxial growth occurs. By contrast, the fine grained regions occurring at the boundary of the pattern have been formed by rapid cooling in a direction other than vertically downwards ($-Z$) creating a high degree of misorientation between the two regions.

Traditionally the heating within a single island would be assumed to occur as a moving point heat source following the back-and-forth pattern as illustrated in Figure 5.18 (a). However, within a single island, the movement of the laser spot is very rapid and there is a high degree of overlap between each scan line (determined by scan spacing). Considering this, it is

suggested that an entire ‘band’ of material could be heated almost simultaneously. As such the laser scanning of an island could be considered to be a ‘band’ of heat moving from one edge across the island where the procession speed is governed by the scan spacing if the scan speed remains constant. This procession speed will remain constant so long as a complete square island is being processed. A diagrammatic representation of the ‘band-heating’ concept is shown in Figure 5.18 (b).

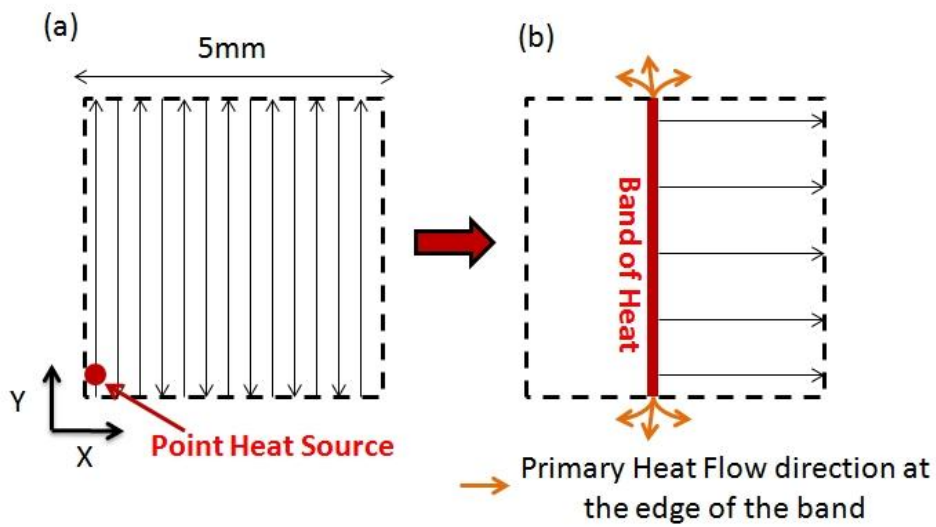


Figure 5.18: Diagram showing how a rapidly moving point heat source (a) could be considered to be a band of heat moving across the island (b) with a speed determined by the scan speed and scan spacing.

It is clear that for material being heated by the middle of the band the primary heat flow direction will be downwards ($-Z$) as the surrounding material in the X-Y plane will be of a similar temperature therefore forming the large columnar grains and $\langle 001 \rangle$ texture.

At the boundary of the island however, only the edge of the heating band passes over and there is a large amount of cold material surrounding in the X-Y plane. This effect is responsible for the rapid cooling and fine grained regions found at the 1 mm pattern boundaries.

By considering basic heat transfer principles it becomes clear why the cooling rates in these two regions are different. Firstly the situation is simplified by assuming that the heat band is at a constant temperature along its length. Considering a point somewhere in the middle of the band of heat, there will be negligible heat transfer in the Y-direction (Figure 5.18) as the heat band is constant and therefore for the X-Z thermal fields along the central portion of the band will be identical. The rate of heat transfer for this point can therefore be considered using the standard expression for biaxial heat conduction [8], Equation 5-1, where ‘T’ is temperature (°C), ‘t’ is time (s), ‘a’ is thermal diffusivity (mm²/s) and X/Z are the directions of heat flow:

Equation 5-1: Biaxial heat conduction equation [8]

$$\frac{\partial T}{\partial t} = a \left[\frac{\partial^2 T}{\partial x^2} + \frac{\partial^2 T}{\partial z^2} \right]$$

This biaxial model however breaks down upon reaching the end portion of the band of heat where the cooler surrounding regions mean that the heat flow in the Y-direction (along the axis of the band) can no longer be ignored. The expression for heat flow in the Y-direction away from the band must therefore be included and as such the triaxial expression [8], Equation 5-2, for heat conduction is in effect at the edge regions:

Equation 5-2: Triaxial heat conduction equation [8]

$$\frac{\partial T}{\partial t} = a \left[\frac{\partial^2 T}{\partial x^2} + \frac{\partial^2 T}{\partial z^2} + \frac{\partial^2 T}{\partial y^2} \right]$$

With this additional ‘Y’ contribution it is clear that the cooling rates at the regions at the edge of the heat band will be significantly greater than those in the centre therefore resulting in the fine-grained regions. Without in-depth computational modelling this behaviour cannot be accurately predicted although it remains an interesting avenue for future investigation.

The microCT crack visualisations, supported by SEM as shown in Figure 5.14, have shown that areas of dense cracking also occur at the pattern boundaries which coincide with the fine grained and highly misoriented regions; the misorientation map presented in Figure 5.9 confirms this. The overall GB misorientation frequency plot in Figure 5.10 shows a large number of low angle grain boundaries which would correspond to the highly textured ‘core’ regions of the repeating pattern, but also some much greater misorientation with some boundaries being misaligned by over 60°. When roughly divided into ‘boundary’ and core regions (as in Figure 5.11) it can be seen that the core region has a high percentage of low misorientation whereas the boundary region has a higher percentage of boundaries misaligned by 20°-60° confirming the result shown in the IPF coloured map and pole figures.

In Chapter 4 it is concluded that one of the primary mechanisms of crack formations is DDC. Fundamental literature on this subject by Lippold *et al.* [9, 10] has reported that DDC susceptibility is increased on highly misoriented grain boundaries (>15°) such as those observed in the fine grained regions thereby supporting the conclusion that DDC is a primary mechanism for crack formation. The work of Lippold *et al.* [9] also goes on to discuss the influence of low- Σ CSL (Coincident Site Lattice) boundaries on DDC occurrence and propagation; without EBSD data relating to an as-fabricated sample it is difficult to comment on the influence of these special boundaries on DDC occurrence, however it remains an interesting avenue for future work.

The occurrence of dense cracking in ‘bands’ also explains the scatter in the crack density observed in the parametric study of the various alloys, particularly CMSX486 (reported in Chapter 4). Sample sets of 2-dimensional SEM micrographs were used to quantify the crack

density and it is possible the scatter in the results was introduced due to some micrographs being taken on the heavy bands of cracking and some within the area of less cracking.

The microCT visualisation also reveals some voids present within the SLM fabricated CM247LC sample whereas parametric study results in Chapter 4 showed the elimination of voids for these processing conditions. It is difficult to compare the two sets of results as the sample geometry was different in each case (cuboidal for the parametric study, cut from a horizontally built test piece for microCT), however it is likely that the 3-dimensional visualisation has provided a more accurate representation of the remaining cracks/voids in the material rather than the simple 2-dimensional slice observed under SEM during the parametric study. Ideally therefore the parametric study would be conducted using microCT rather than SEM to quantify the remaining defects, however this is impractical due to the time-consuming and costly nature of both the collection of data and post-processing to visualise the defects.

It has been shown that the island scan strategy is responsible for the bi-modal grain structure; bands of heavy cracking and fine grained, highly misoriented regions. It is obvious that these features will have a detrimental effect on the overall material properties. Ideally a different laser scan strategy would be employed to produce a much more homogeneous structure, however such a scan strategy would need to take into account the varying geometry throughout the build and adjust the laser processing parameters accordingly. For example, if a simple ‘back-and-forth’ scan strategy was used and the parameters optimised using cuboidal samples then it is very unlikely that the same parameters would be appropriate for a large cross-sectional area geometry as the time interval between each laser scan line would be increased. Likewise, a geometry progressing from a small to large cross-sectional area with increasing Z-height would have different heat transfer properties from one moving from a

large to small cross-sectional area. Taking all these factors into consideration would require an ‘all encompassing’ model of the process and constantly varying parameters to keep the processing in the optimum window.

As this is not possible in the scope of the current work, a retro-fix solution of HIPping the SLM fabricated sample has been adopted to close the internal cracks and defects. The effectiveness of using HIPping has been proven in literature for other materials [3, 11, 12] (See Chapter 2). During the microCT work the HIPped sample showed a very good crack and defect closure with only the surface-connected cracks remaining as seen in Figure 5.15 and was confirmed by SEM examination of a similar sample as seen in Figure 5.16. The HIPping does not however eliminate the bi-modal grain structure.

5.6. Simple Scan Pattern: A Preliminary Study

At this point the optimisation of a simple scan strategy is not practical for a complex component as discussed in the previous section, however for the purposes of comparison, a single sample produced using a simple ‘back-and-forth’ scan pattern (in the Y-direction) was produced (using the same laser power, speed and spacing as derived in Chapter 4 for CM2247LC). Figure 5.19 illustrates the difference between the laser scan path of the island scan strategy (a) and the simple scan strategy (b) for a single slice of the samples examined. This sample was examined in the X-Y plane only using optical microscopy and EBSD mapping.

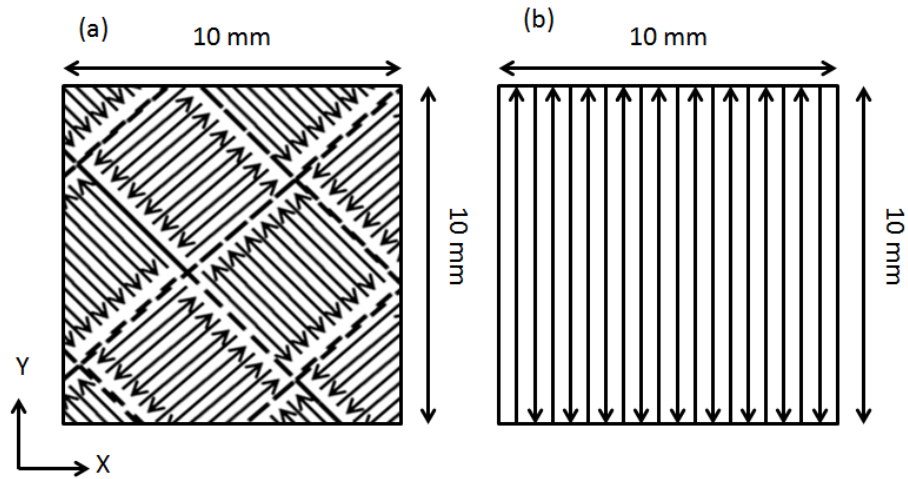


Figure 5.19: Schematic illustration showing the difference between (a) the island scan strategy and (b) the simple scan strategy for the laser path of a single slice.

i. Results

Figure 5.20 shows an optical micrograph of a typical region of the simple scan pattern sample of CM247LC in the X-Y plane.

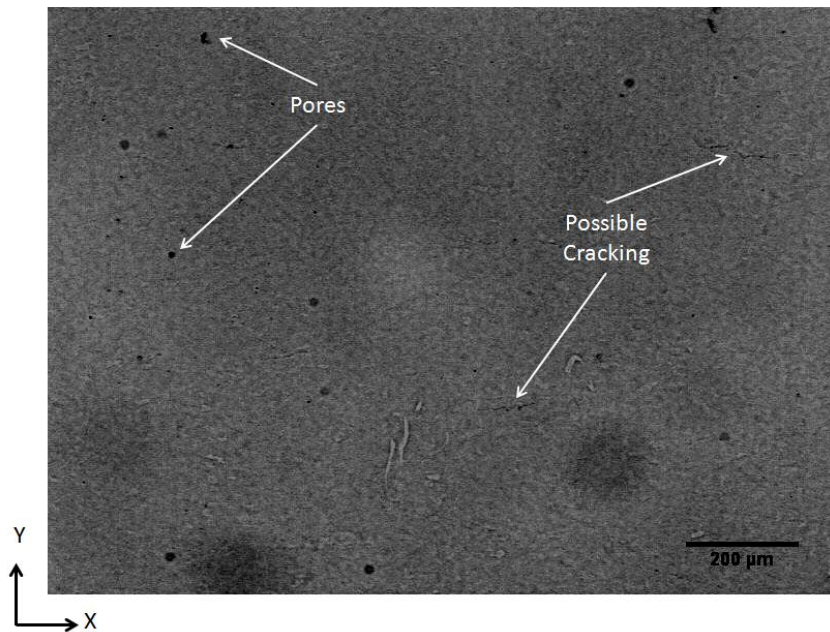


Figure 5.20: Optical micrograph showing simple scan pattern produced CM247LC in the X-Y plane. Possible cracks and pores are labelled.

Figure 5.21 shows a large-area stitched EBSD map of the simple scan pattern CM247LC, IPF coloured with respect to (a) the Z (build) direction and (b) the Y (laser scan) direction.

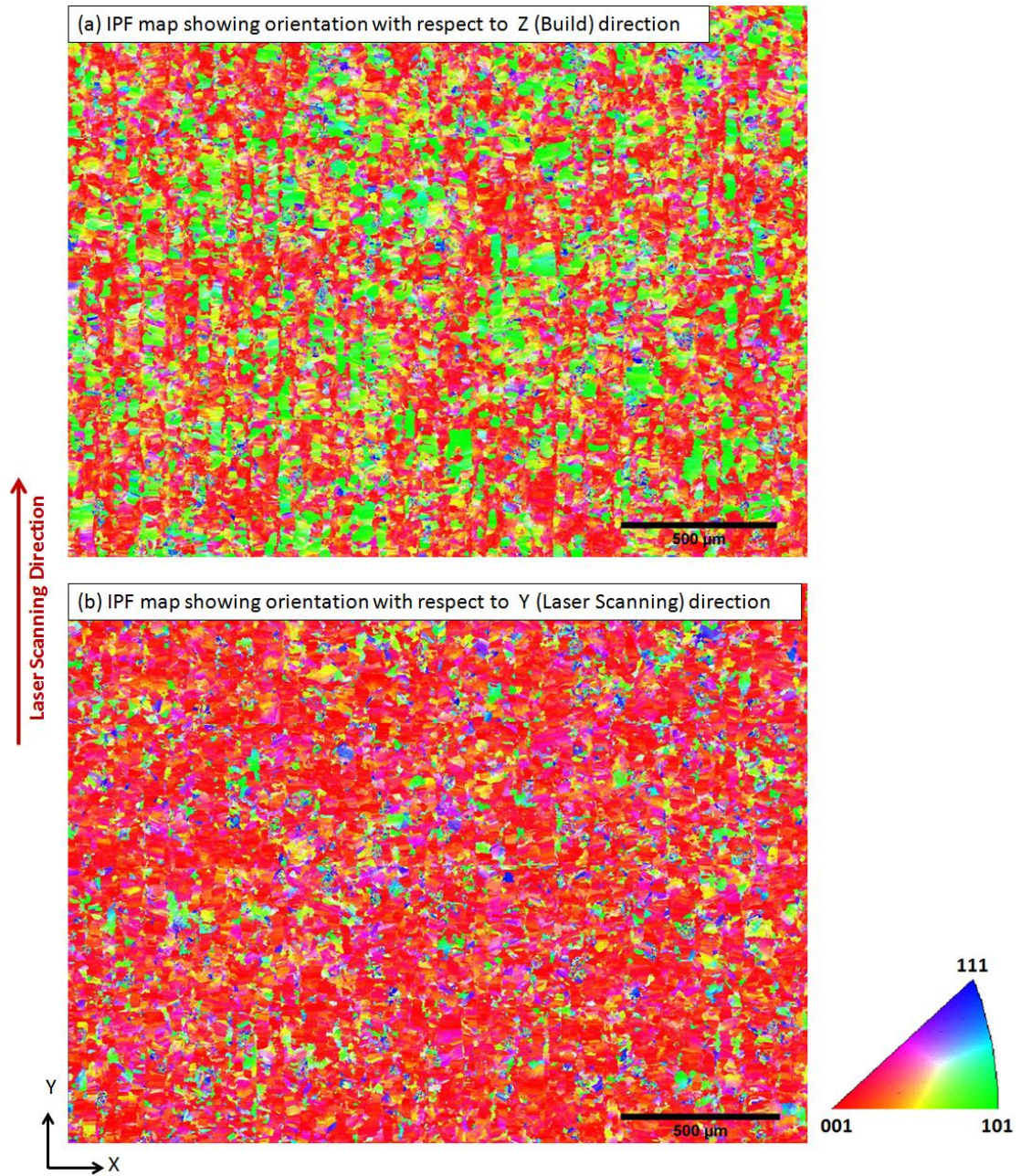


Figure 5.21: EBSD map of simple scan pattern CM247LC with IPF colouring showing crystallographic orientation with respect to the (a) Z (build) direction and (b) Y (laser scan) direction.

Figure 5.22 shows the corresponding $\{100\}$ pole figures generated from a typical area within the map with respect to the (a) Z (build) direction and (b) Y (laser scan) direction.

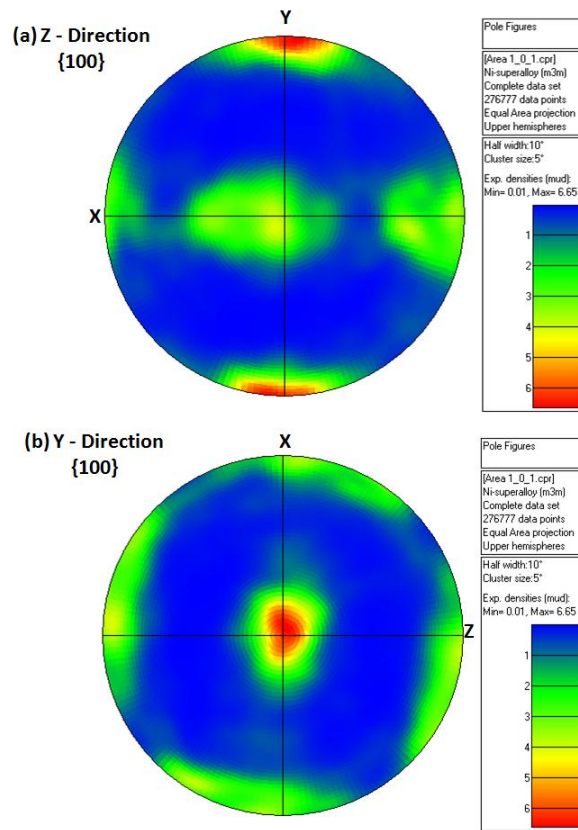


Figure 5.22: {100} pole figures for the simple scan pattern CM247LC with respect to the (a) Z (build) direction and (b) Y (laser scan) direction.

Figure 5.23 shows a frequency plot for grain boundary misorientation within the simple scan CM247LC.

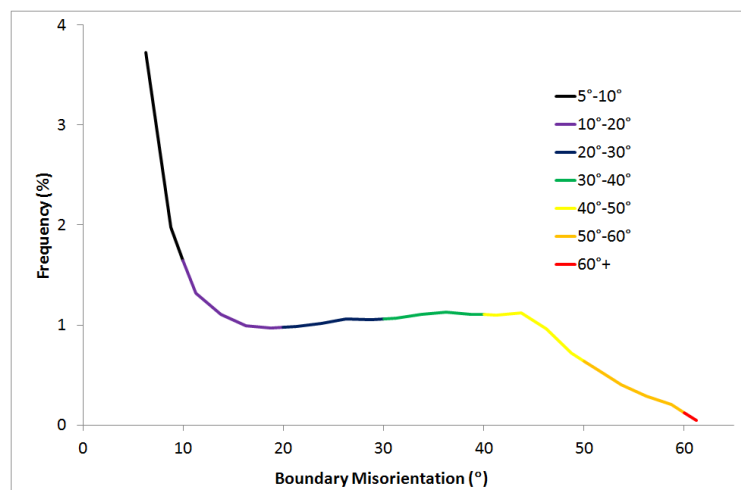


Figure 5.23: Frequency plot showing grain boundary misorientation frequency for the simple scan pattern CM247LC.

ii. Discussion

The optical microscopy examination of the simple scan pattern CM247LC revealed an apparently very low cracking density as seen in the typical micrograph presented in Figure 5.20; there is also no obvious evidence that these cracks are forming in specific regions of the sample unlike the previously discussed island strategy. Without further study to quantify and characterise the cracks it is impossible to draw further conclusions however this cursory examination does appear to support the suggestion that the cracking density is increased with the use of the island scan strategy.

The EBSD maps presented in Figure 5.21 show a much more homogeneous structure produced by the simple scan pattern than the island scan strategy. Initial mapping examining the normal (Z) map revealed a mix of strong $\langle 001 \rangle$ and $\langle 101 \rangle$ crystallographic alignment show by the dominance of red and green in Figure 5.21 (a), however by mapping the crystallographic orientation with respect to the Y (laser scan) direction a very strong affinity for the $\langle 001 \rangle$ direction is present as seen in Figure 5.21 (b). This is further supported by the $\{100\}$ pole figures in Figure 5.22 which again show a very strong alignment of the $\{100\}$ pole with the Y direction but some variation in the rotation about this axis. The strong alignment suggests that solidification is occurring in the direction of the laser scan path; this is in sharp contrast to that seen for the island scan pattern where the strongest alignment of the $\{100\}$ pole was within the large columnar grains in the Z-direction.

Finally the grain boundary misorientation plot shown in Figure 5.23 is very similar to the overall plot presented for the island scan pattern (Figure 5.10).

Without further characterisation, examination and mechanical testing it is impossible to fully understand the overall influence of this simple scan pattern on CM247LC however the EBSD

maps presented here do show that the laser scan pattern has the ability to produce vastly different microstructures in the same material under the same nominal operating conditions; the author suggests this an area for further future investigation.

5.7. Conclusions & Summary

The studies into the effect of the island scan strategy have isolated by optical and SEM microscopy the presence of a bi-modal grain structure. This takes the form of defined regions of large columnar grains separated by thin regions of fine grains forming a $1\text{ mm} \times 1\text{ mm}$ ‘lattice’ pattern in the X-Y plane. The large columnar regions have shown a strong $\langle 001 \rangle$ texture whilst the fine grained regions show a chaotic texture with highly misaligned grain boundaries. MicroCT and SEM investigations have shown that the fine grained and heavily cracked regions correspond as is consistent with the conclusion reached in Chapter 4 that the cracks are intergranular and form via the DDC mechanism.

‘Band-heating’ has been suggested to explain the formation of the bi-modal structure where the rapidly scanning laser within a single island could better be considered as a ‘band’ of heat moving from one edge to the opposite. The high thermal gradients at the edge of the band caused by the cool surrounding material are responsible for the fine grained and highly misoriented grains.

A brief examination of a simple scan pattern sample of CM247LC has revealed that the scan strategy can dramatically influence the microstructure however without extensive modelling/experimentation it is not currently feasible to implement this simple method in the SLM-fabrication of a complex component; therefore the ‘island’ scan-strategy has been used for the remainder of the research presented within this thesis.

Without the ability to dynamically control the laser processing parameters using an all-inclusive model, a retro-fix solution to the cracking has been implemented. A HIPping treatment has been applied to the samples in order to close the internal defects and has proven very successful as no remaining non-surface connected cracks/voids were observed in the microCT data of the HIPped sample. This retro-fix however does not remove the bimodal grain structure or surface connected defects.

5.8. References

- [1] Vilaro T, Colin C, Bartout JD, Naze L, Sennour M. Microstructural and mechanical approaches of the selective laser melting process applied to a nickel-base superalloy. *Materials Science and Engineering A* 2012;534:446.
- [2] Amato KN, Gaytan SM, Murr LE, Martinez E, Shindo PW, Hernandez J, Collins S, Medina F. Microstructures and mechanical behavior of Inconel 718 fabricated by selective laser melting. *Acta Materialia* 2012;60:2229.
- [3] Wu X, Wang F, Clark D. On direct laser deposited Hastelloy X: dimension, surface finish, microstructure and mechanical properties. *Materials Science and Technology* 2011;27:344
- [4] Das S. Physical Aspects of Process Control in Selective Laser Sintering of Metals. *Advanced Engineering Materials* 2003;5:701.
- [5] Liu F, Lin X, Huang C, Song M, Yang G, Chen J, Huang W. The effect of laser scanning path on microstructures and mechanical properties of laser solid formed nickel-base superalloy Inconel 718. *Journal of Alloys and Compounds* 2011;509:4505.
- [6] Reed RC. *The Superalloys: Fundamentals and Applications*: Cambridge, 2006.
- [7] Zhao X, Chen J, Lin X, Huang W. Study on microstructure and mechanical properties of laser rapid forming Inconel 718. *Materials Science and Engineering A* 2008;478:119.
- [8] Grong O. *Metallurgical Modelling of Welding* (2nd Edition). London: Institute of Materials, 1997.
- [9] Collins MG, Ramirez AJ, Lippold JC. An investigation of ductility-dip cracking in nickel-based weld metals - Part III. *Welding Journal* (Miami, Fla) 2004;83:39/S.
- [10] Collins MG, Ramirez AJ, Lippold JC. An Investigation of Ductility Dip Cracking in Nickel-Based Weld Metals - Part II. *Welding Journal* (Miami, Fla) 2003;82:348S.
- [11] Blackwell PL. The mechanical and microstructural characteristics of laser-deposited IN718. *Journal of Materials Processing Technology* 2005;170:240.
- [12] Zhao X, Lin X, Chen J, Xue L, Huang W. The effect of hot isostatic pressing on crack healing, microstructure, mechanical properties of Rene88DT superalloy prepared by laser solid forming. *Materials Science and Engineering A* 2009;504:129.

CHAPTER 6: HEAT TREATMENT, γ' STRUCTURE & MECHANICAL TESTING

This chapter focuses on the heat treatment of the SLM-fabricated and HIPped CM247LC to produce a fine cuboidal γ' microstructure. Results from an oil-quenched investigation, DSC and Thermo-Calc modelling are presented during the determination of the solution treatment temperature.

The γ' structure throughout the process route has been examined and quantified and a small investigation into the combination of the HIPping and solution treatment steps suggested as a means of reducing the number of steps in the processing route.

The correct heat treatment is necessary in order to produce good mechanical properties; creep and tensile data is presented for the final material. This includes comparisons of horizontally and vertically built specimens, HIPped against non-HIPped and the SLM-fabricated material against literature values.

Finally the mechanical properties of the SLM-fabricated CMSX486 and IN625 are assessed in a similar way.

6. 1. Establishing Solution Treatment for SLM & HIPped CM247LC

As reported in the literature review (Chapter 2), the suggested solution treatment temperature for cast CM247LC varies depending on the literature source. The first batch of samples used a conservative temperature of 1230°C (based on Donachie [1]). Following this further investigations were carried out to accurately determine a suitable treatment for SLM & HIPped CM247LC using an oil-quenched trial and microstructural observations to see when

γ' solution had occurred and this was supported by DSC results of CM247LC powder and the Thermo-Calc phase diagram modelling of the material.

i. Initial Gas Quench (GQ) Results (1230°C)

Figure 6.1 shows the coarse γ' structure following the 1230°C (1230°C, 2h, GQ) solution treatment of the SLM-fabricated & HIPped CM247LC under 2000x (a) and 6000x (b) magnification. The γ' particles are coarse ($\sim 1\text{--}2\text{ }\mu\text{m}$ across) and show an irregular morphology. In certain regions of the sample an elongation of the γ' particles into coarse ‘raft-like’ structures can be seen as shown in Figure 6.2.

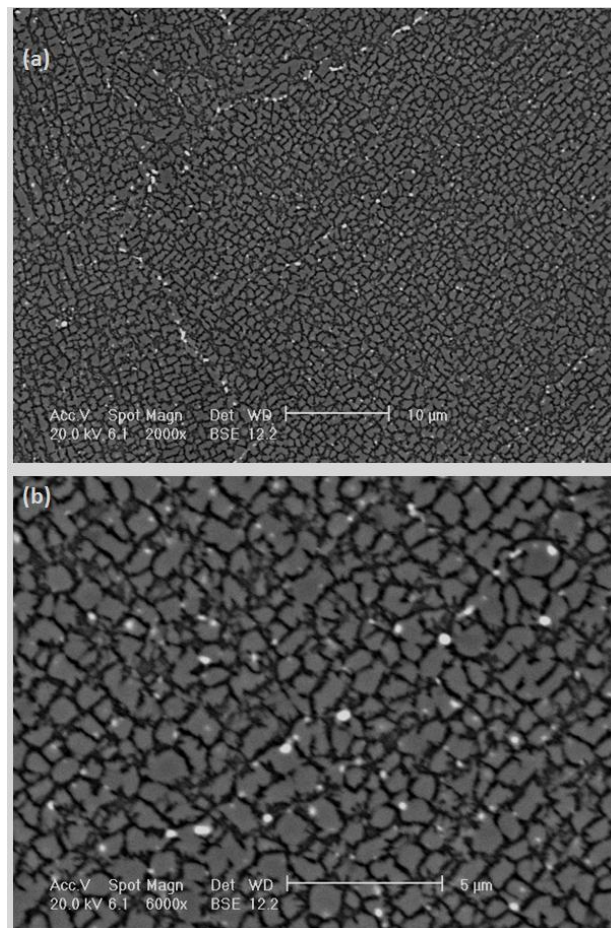


Figure 6.1: BSE SEM micrographs of etched CM247LC revealing coarse γ' structure. Sample was SLM-fabricated, HIPped and solution treated (1230°C, 2h, GQ); (a) 2000x magnification, (b) 6000x magnification.

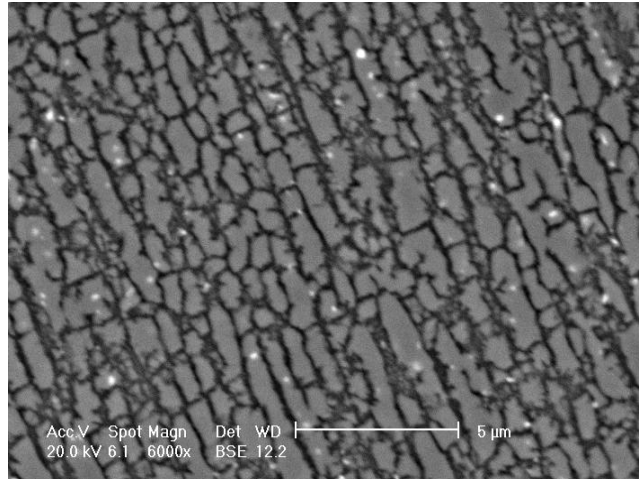


Figure 6.2: BSE SEM micrograph of etched CM247LC revealing coarse ‘raft-like’ γ' structure. Sample was SLM-fabricated, HIPped and solution treated (1230°C, 2h, GQ).

ii. Oil Quench Investigation Results

Figure 6.3 shows etched micrographs revealing the γ' structure of oil quenched samples following 2h dwell in an air furnace at 1260°C (a), 1280°C (b), 1300°C (c). All samples show a very similar fine ($\sim 0.2\text{-}0.5\text{ }\mu\text{m}$) cuboidal γ' structure.

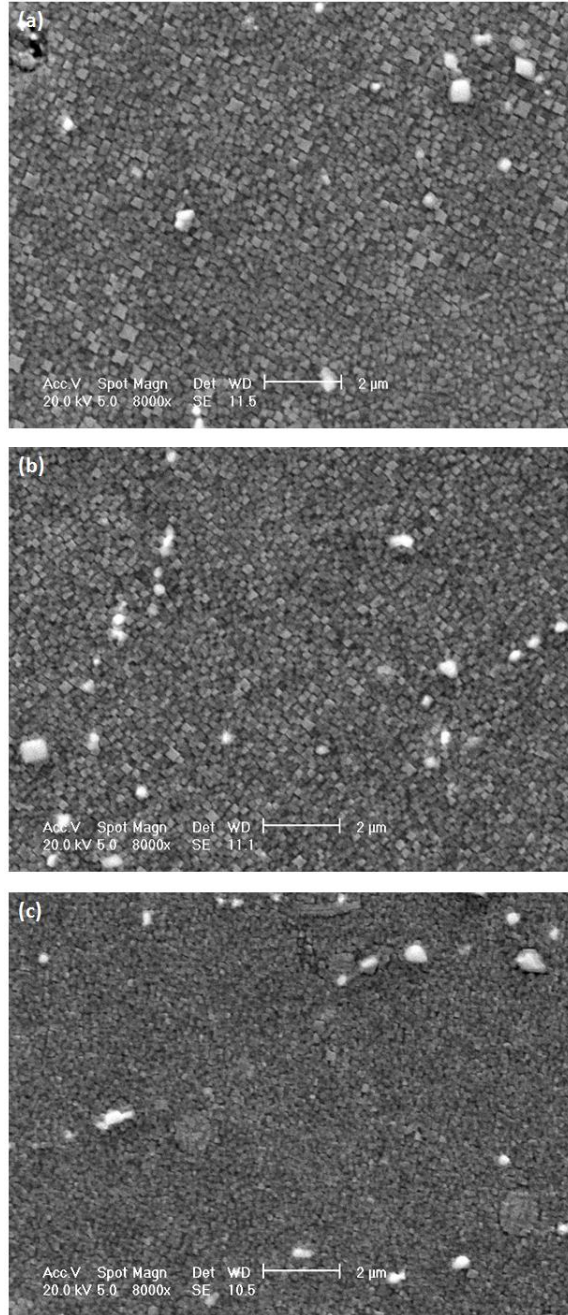


Figure 6.3: SE SEM micrographs showing oil quenched SLM-fabricated CM247LC & HIPped samples following 2h hold at (a) 1260°C, (b) 1280°C and (c) 1300°C. Samples are etched to reveal fine γ' structure.

iii. DSC Results of CM247LC Powder

The DSC results for the heating and cooling of CM247LC powder are shown in Figure 6.4. The plot is annotated with the solidus (determined by extrapolation of the linear portions of the plot) at 1331°C, liquidus at 1373.5°C and the onset of the γ' formation on the cooling

curve at 1269°C. Although the energy change for the γ' formation is small, it has been identified as the correct peak by comparison with the DSC curves presented by Zhao et al. [2].

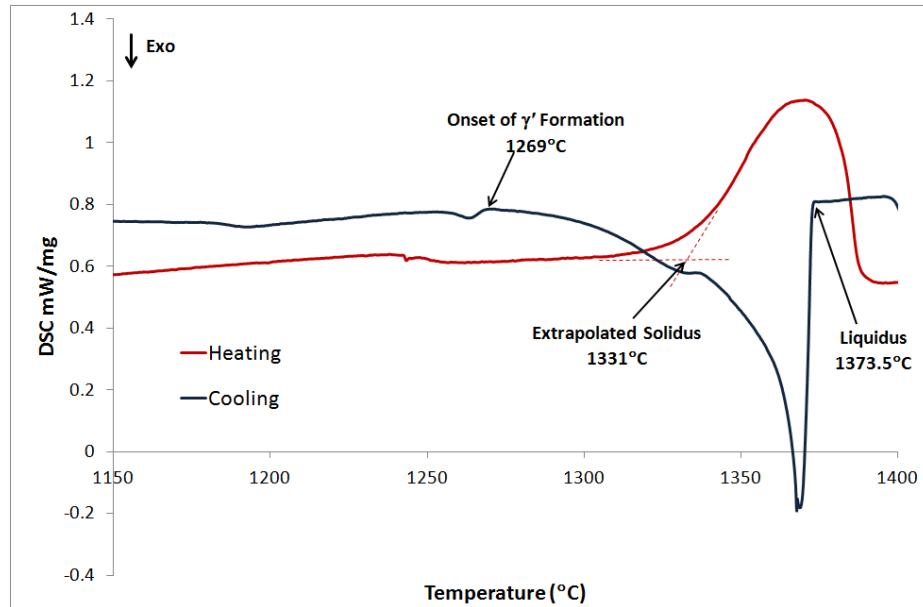


Figure 6.4: DSC results for the heating (red) and cooling (blue) of CM247LC powder (UK1091) annotated with solidus, liquidus and onset of γ' formation (Heating/Cooling = 10°C/min).

iv. Phase Diagram Modelling of CM247LC (Thermo-Calc)

The modelled temperature-phase fraction plot for CM247LC is shown in Figure 6.5 based on the material composition obtained from analysis. The model shows full dissolution of the γ' phase at approximately 1288°C, a solidus of approximately 1344°C and a liquidus of approximately 1412°C.

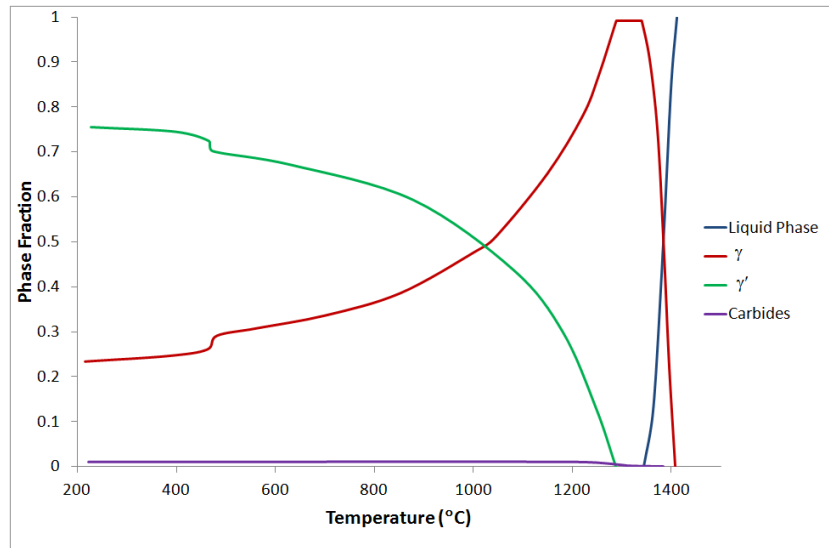


Figure 6.5: Thermo-Calc temperature-phase fraction model of CM247LC.

v. Discussion

The 1230°C (GQ) solution treatment showed a coarse γ' structure indicating incomplete dissolution of the γ' phase within the γ matrix as seen in Figure 6.1; this structure is far from the desired fine cuboidal structure for optimum mechanical properties. In certain areas a distinct directionality within the coarse structure is visible where the γ' precipitates appear to form ‘raft-like’ structure shown in Figure 6.2. This cannot be truly called rafting as the material has not been exposed to the extended periods of stress and temperature typically associated with raft formation however it is suggested that this structure forms via a similar mechanism to rafting where the precipitation of the γ' phase occurs whilst the material is subject to residual stress. This type of structure has been observed previously by Pierret et al. [3] in stressed regions of cast materials before any service exposure.

The oil quench investigation aimed to determine the temperature needed to obtain a good solution treated structure whilst maintaining the 2h dwell time. The range 1260°C - 1300°C was selected as literature has reported a solution treatment for CM247LC at 1260°C (e.g. Kim et al. [4]) and below the melting point range reported by Cannon-Muskegon

(1310°C-1375°C [5]). The three samples showed a much finer γ' structure than the 1230°C GQ sample and also a regular cuboidal structure as desired; this can be seen in Figure 6.3. The sample held at 1300°C shows a marginally finer γ' structure to those held at 1260°C and 1280°C; however all three are comparable and the variation could simply be due to human variation introduced during in the quench process.

This result is consistent with the DSC data (Figure 6.4) that show the onset of γ' precipitation to occur at 1269°C in the cooling curve; the corresponding peak for the onset of dissolution in the heating curve occurs gradually and cannot be distinguished.

The Thermo-Calc model of the material differs slightly and shows a complete dissolution of the γ' phase to occur theoretically at 1288°C. At 1260°C however there is only a predicted ~9% volume fraction of γ' compared with ~75% when fully precipitated.

The solution treatment temperature should lie in the narrow window between the boundary for fully dissolved γ' and the solidus. The solidus temperature determined by DSC was extrapolated as 1331°C from the two linear portions of the plot as is standard practice (see Höhne et al. [6]) however as the curve does begin to rise before this point, it is possible that liquid phases may start to form at a marginally lower temperature; possibly closer to the 1310°C reported by Cannon-Muskegon [5]. For this reason the solution treatment temperature of 1260°C was considered to be sufficient to produce a fine γ' structure (confirmed by the oil quench investigation) whilst avoiding the formation of liquid phases during the treatment. It is however clear from the DSC data and Thermo-Calc modelling that this temperature is unlikely to produce a complete dissolution of the γ' phase.

6.2. Evolution of γ' Structure through the Processing Route of CM247LC

The proposed processing route consists of several stages; the SLM-fabrication to produce the desired geometry; HIPping to eliminate the internal cracks and pores; solution & 2-stage ageing heat treatment to refine the γ' structure in order to improve the mechanical properties of the material. This sequence is illustrated in Figure 6.6.

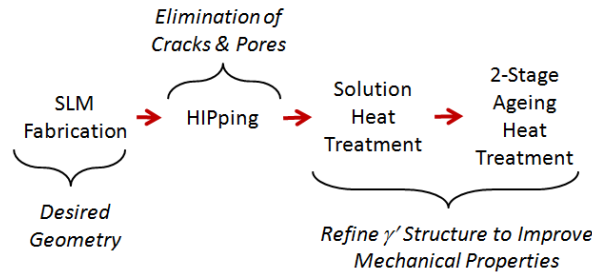


Figure 6.6: Diagram illustrating the steps in the proposed processing route for SLM-fabricated CM247LC components.

i. Microstructure Observations & Results

Typical micrographs showing the γ' structure are presented showing CM247LC following each of the processing steps within the processing route.

As-Fabricated γ' Structure

Figure 6.7 shows an SEM micrograph of the as-fabricated CM247LC; the sample was etched to reveal the γ' structure (Note: γ' not visible). Figure 6.8 (a) shows a TEM diffraction pattern for the as-fabricated CM247LC. The weak 010 diffraction spot would be forbidden in a pure γ matrix and is therefore solely formed due to the γ' phase. This 010 superlattice γ' reflection was selected to produce the dark field TEM micrograph shown in Figure 6.8 (b) thus revealing the γ' as the bright phase (estimated particle size < 5 nm).

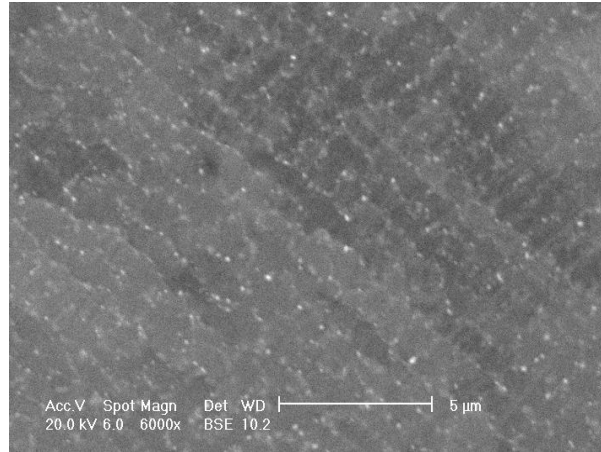


Figure 6.7: BSE SEM micrograph of as-fabricated CM247LC, etched to reveal γ' phase. Light phase represented fine carbide precipitates, γ' phase not visible.

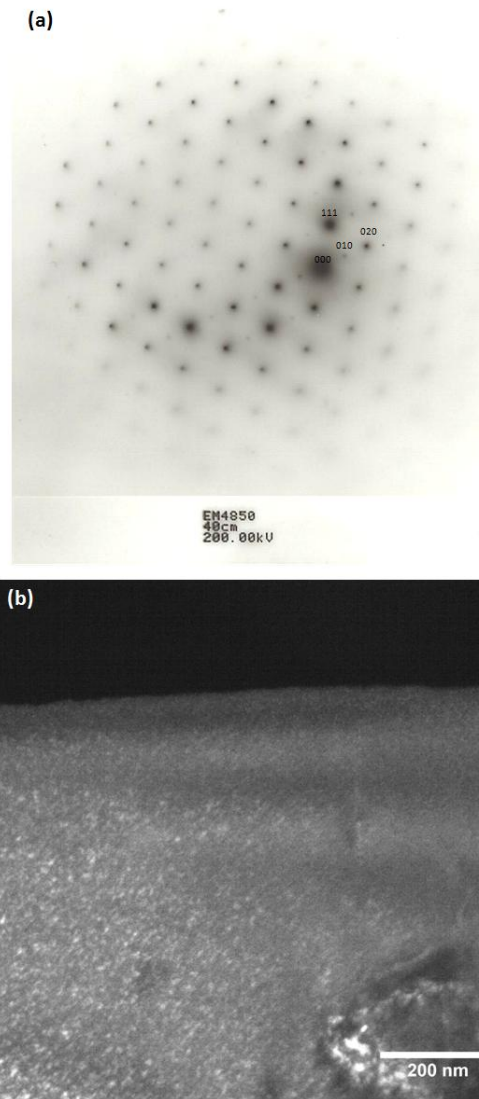


Figure 6.8: TEM Micrographs of as-fabricated CM247LC. (a) Diffraction pattern showing the indexed weak 010 γ' superlattice spot. (b) Corresponding dark field TEM micrograph revealing γ' as the bright 'speckled' phase (obvious in the lower left corner).

SLM-fabricated & HIPped γ' Structure

Figure 6.9 shows the typical coarse γ' structure in the SLM-fabricated and HIPped CM247LC.

(HIPped at 1180°C, 150 MPa, 4h dwell – standard 5°C/min heating & cooling)

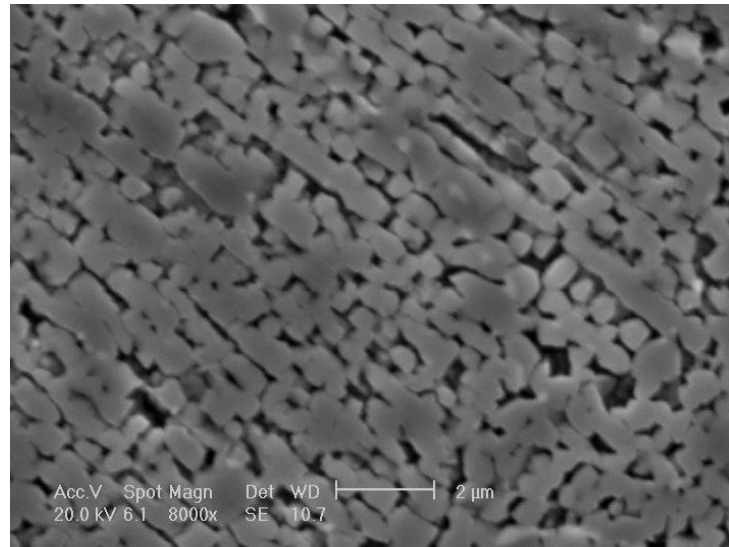


Figure 6.9: SE SEM micrograph showing SLM-fabricated & HIPped CM247LC etched to reveal γ' phase; γ' shows a very coarse structure.

SLM-fabricated, HIPped & Solution Treated γ' Structure

Figure 6.10 shows reasonably fine cuboidal γ' structure of SLM-fabricated, HIPped & solution treated CM247LC (Solution Treatment: 1260°C, 2h dwell, Gas Quenched); some particles show a tendency towards ‘arrowhead’ morphology in the particle corners and there are occasionally split-cube style particles.

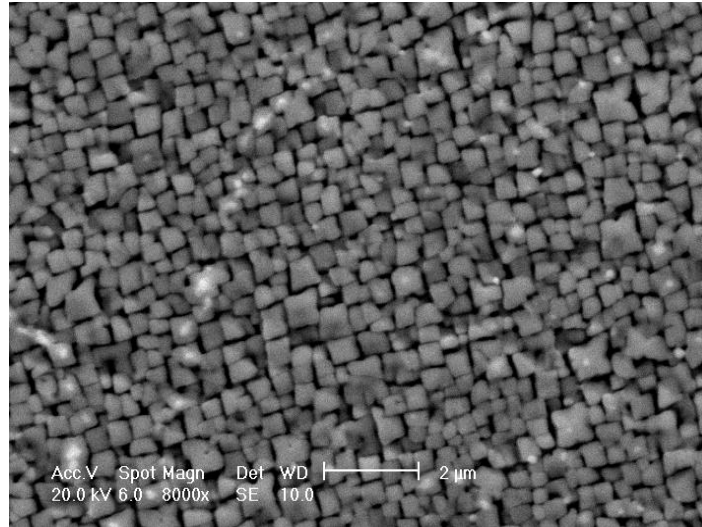


Figure 6.10: SE SEM micrograph showing SLM-fabricated, HIPped & solution treated CM247LC etched to reveal γ' phase; γ' shows reasonably fine cuboidal γ' structure.

SLM-fabricated, HIPped, Solution & 1st Ageing Treated

Figure 6.11 shows the cuboidal γ' structure of SLM-fabricated, HIPped, solution and 1st ageing treated CM247LC (1st ageing: 980°C, 5h dwell, Air Cooled [4]). Many particles show arrowhead and 'split-cube' morphology associated with over-ageing.

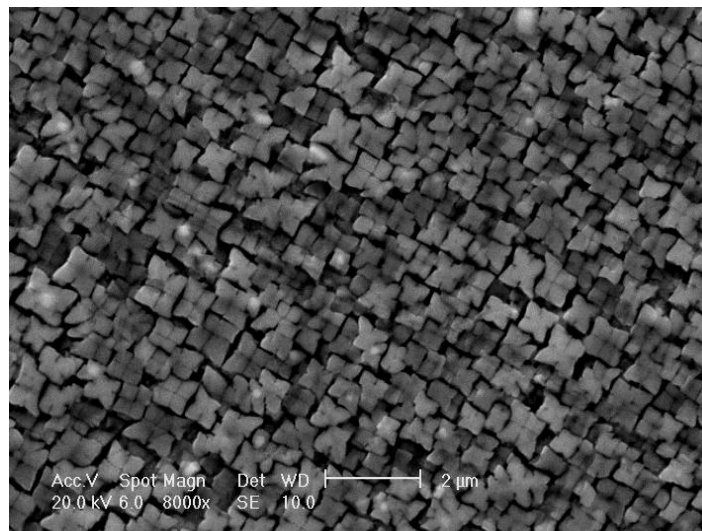


Figure 6.11: SE SEM micrograph showing SLM-fabricated, HIPped, solution & 1st ageing treated CM247LC etched to reveal γ' phase; γ' shows cuboidal structure with some 'split-cube' style particles.

SLM-fabricated, HIPped, Solution, 1st & 2nd Ageing Treated

Figure 6.12 shows the coarse cuboidal γ' structure of SLM-fabricated, HIPped, solution, 1st and 2nd ageing treated CM247LC (2nd ageing: 870°C, 20h dwell, Air Cooled [4]). Particles are coarse and have merged together in many cases. Many particles show irregular and the 'split-cube' morphology associated with over-ageing.

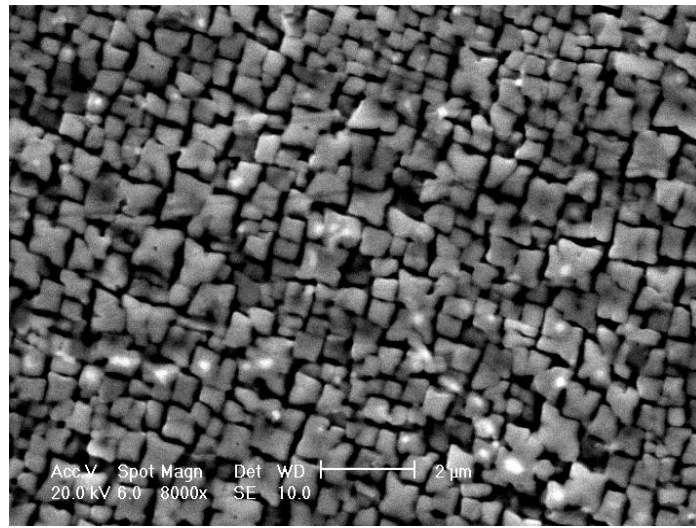


Figure 6.12: SE SEM micrograph showing SLM-fabricated, HIPped, solution, 1st & 2nd ageing treated CM247LC etched to reveal γ' phase; γ' shows coarse with many irregular and 'split-cube' style particles.

ii. Quantification of Particle Size & Shape

Figure 6.13 shows frequency plots of particle size for the measured γ' particles following (a) solution treatment, (b) 1st ageing and (c) 2nd ageing; 300 particles were measured for each plot and each are annotated with the maximum particle size, mean particle size and the mean aspect ratio (longer side length/shorter side length). Figure 6.14 shows the moving average (over 3 bins) of all three frequency plots for direct comparison.

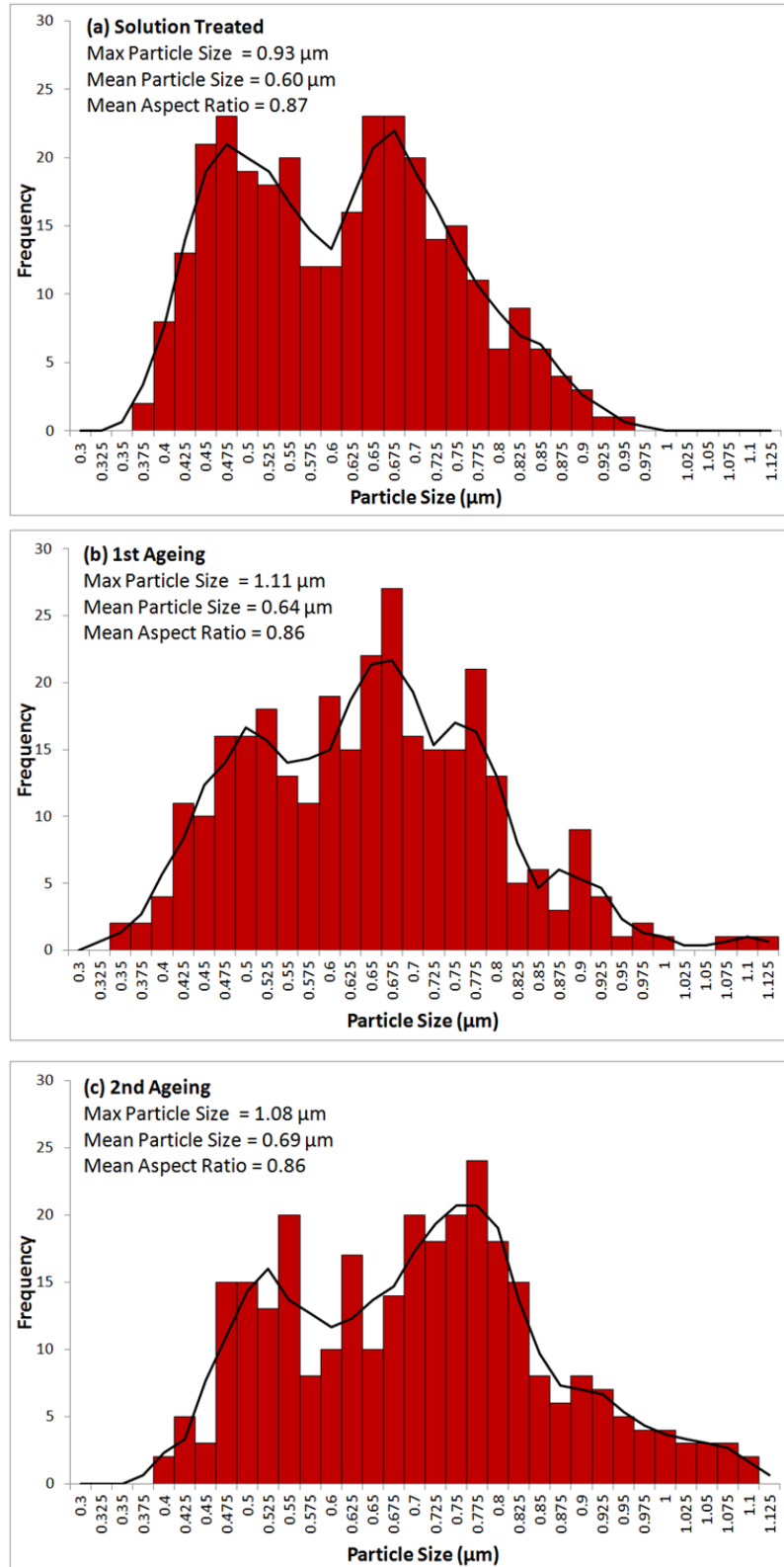


Figure 6.13: Frequency plots showing γ' particle size distributions in SLM-fabricated & HIPed CM247LC following (a) solution treatment, (b) 1st ageing and (c) 2nd ageing; plots are annotated with the maximum particle size, mean particle size and the mean aspect ratio. Black line shows moving average over 3 bins.

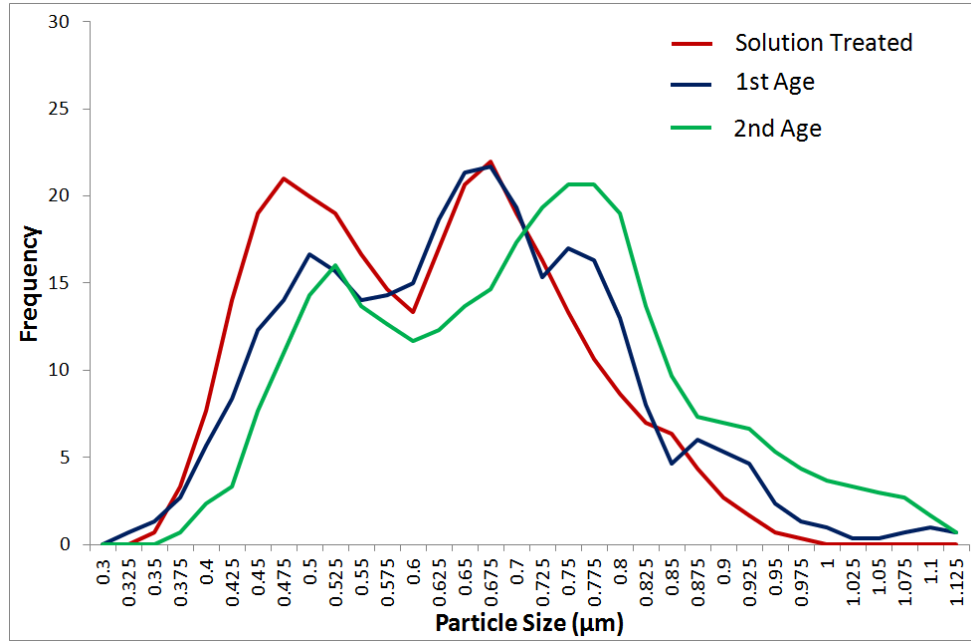


Figure 6.14: Plot showing moving average line for frequency of γ' particle size in the solution treated (red), 1st aged (blue) and 2nd aged (green) conditions.

iii. HIPped & Rapidly Cooled Microstructure

In an attempt to reduce the number of steps in the processing route of the SLM-fabricated CM247LC, it was proposed that the HIP and solution steps could be combined by HIPping at the solution temperature (1260°C) and applying gas ‘jet-cooling’ to mimic the gas-quench.

Figure 6.15 shows the thermocouple data for the standard HIP cycle, the ‘jet-cooled’ HIP and the TAV furnace gas-quenched solution treatment; the plot is annotated with the cooling rates for each cycle based on the linear sections of the cooling curve. This data was measured using the closest integrated thermocouple to the samples within the HIP/furnace however thermocouples could not be situated on or directly next to the samples so data may not be representative of the actual cooling rates experienced by the material.

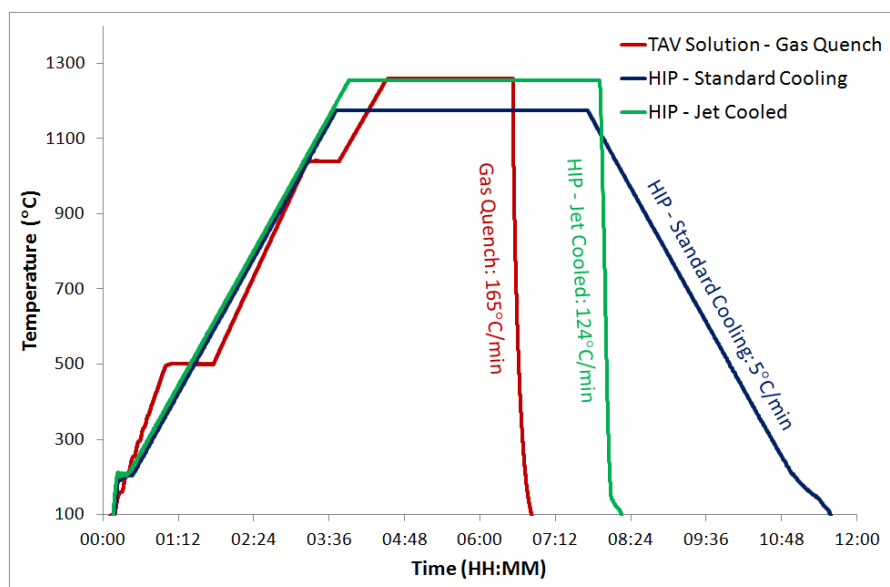


Figure 6.15: Plot showing measured temperature against time for the gas-quenched solution treatment, HIP with jet-cooling and standard HIP cycles. Curves are annotated with cooling rates determined by the linear portions of the falling curve.

The micrograph in Figure 6.16 shows the etched γ' structure of SLM-fabricated CM247LC following the HIP & jet-cooling; the material shows a coarse irregular structure.

Measurement of particle size distribution was difficult as most particles did not show a distinct cuboidal structure, so edge-to-edge measurement could not be carried out. For comparison however, an attempt was made to measure 300 particles using a similar method to that used to obtain the previous results. These results for particle size distribution are presented in Figure 6.17 annotated with the maximum and mean particle size; it should be noted however that this is based on operator judgement in measuring the width of each particle.

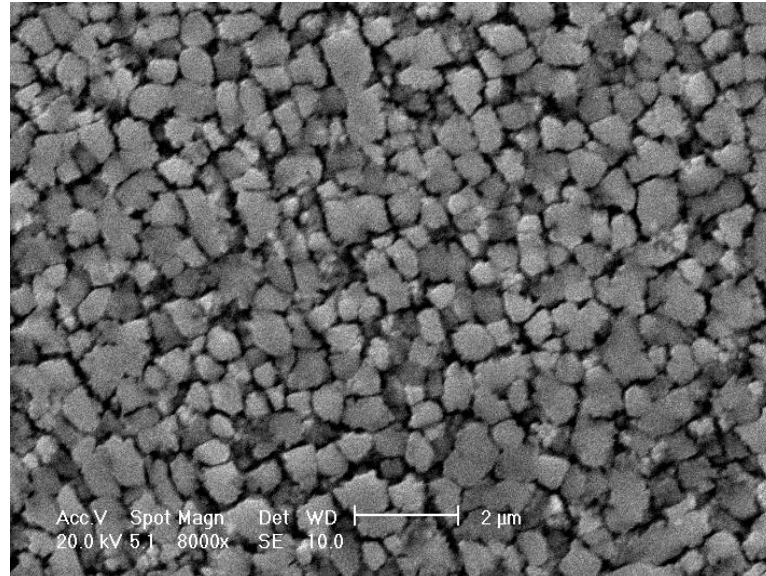


Figure 6.16: SE SEM micrograph showing SLM-fabricated, HIPped & jet-cooled CM247LC etched to reveal the coarse γ' structure.

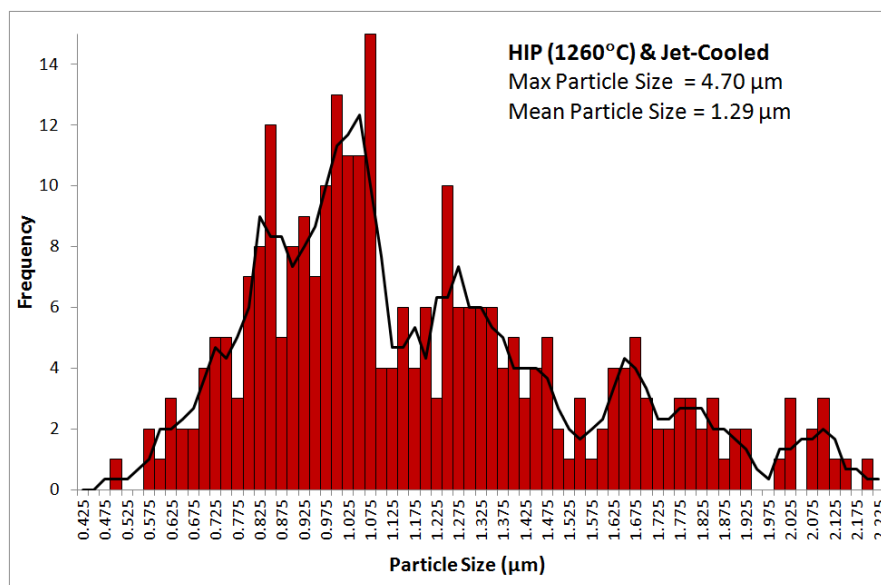


Figure 6.17: : Frequency plot showing γ' particle size distribution in SLM-fabricated, HIPped and jet-cooled CM247LC. Plot is annotated with the maximum & mean particle size; black line shows moving average over 3 bins.

iv. Discussion

The SLM-fabricated CM247LC in the as-fabricated condition does not reveal any γ' particles under SEM examination and appears to be a completely solution treated microstructure. The very rapid localised melting and solidification of the material acts as a rapid quench for the

melt-pool thereby suppressing the γ' phase. Figure 6.7 shows the result of several attempts to etch the material to reveal the γ' structure under SEM examination, however any γ' is too small to resolve.

The γ' phase was revealed under TEM examination, however only by using the superlattice γ' reflection in the dark field. These extremely fine γ' precipitates are approximately 5 nm in size are shown in Figure 6.8 as the bright phase. This illustrates the degree to which the material is in a solutionised condition following SLM.

Ideally at this point within the processing route the material would be aged in order to further precipitate the γ' phase, however due to the cracks (as previously discussed), the material must be HIPped to close these internal defects. Figure 6.9 shows how the slow cooling rates (5°C/min) within the HIPping process over-age the material leaving very coarse γ' where individual particles have grown and merged together to form large blocky rafts. In this condition the material is crack and pore free, however the further heat treatment is clearly necessary in order to refine the structure to fine cuboidal particles and so produce the best possible mechanical properties.

Following solution treatment and cooling by gas-quench, the γ' shows a fine cuboidal structure as can be seen in Figure 6.10. This structure is fairly promising, however it clearly shows a greater particle size than that achieved by the oil quench as seen in Figure 6.3. This difference in particle size can be related to the difference in cooling rates between the quenching media as discussed in the experimental chapter (Chapter 3). Although the gas-quenched structure is not ideal, this process is necessary for the heat treatment of the material under vacuum to avoid oxidation of the components.

Following the 1st ageing treatment the γ' particles begin to show the characteristic split-cube morphology (see Figure 6.11) associated with the over-aged material and this effect is accentuated following the 2nd ageing (see Figure 6.12) with the additional negative characteristic that the larger particles have grown to merge with their neighbours in some cases.

The γ' particle size distributions were measured and plotted in order to further understand the evolution of this structure through the heat treatment section of the processing route; these distributions are shown in Figure 6.13. The solution treated distribution shown in (a) has a distinct double-peak; the first peak at approximately 0.5 μm and the second at approximately 0.7 μm . Based on the microstructural observation it can be determined that the 0.5 μm peak corresponds to the regular cuboidal particles whilst the second peak corresponds to those that have grown into the arrowhead and split-cube particles. Both of these peaks show approximately the same frequency.

The particle distribution following the 1st ageing is shown in Figure 6.13 (b) has a similar double peak distribution, with both peaks at approximately the same points (0.5 μm & 0.7 μm). The 0.7 μm peak is now significantly larger than the 0.5 μm indicating that more of the particles have aged into the larger arrowhead and split-cube morphologies following the ageing treatment.

Finally the particle distribution for the material following the 2nd ageing is shown in Figure 6.13 (c). Again this shows the double-peak distribution with the larger peak representing the large particle size. In this case however both peaks have shifted slightly and now occur at approximately 0.55 μm and 0.8 μm respectively. This shift could indicate a general coarsening of all the γ' particles.

The three distributions are directly compared in Figure 6.14 which serves to emphasise the change in particle size. Overall the mean particle size varies only slightly across the heat treatment stages from $0.6\ \mu\text{m} \rightarrow 0.64\ \mu\text{m} \rightarrow 0.69\ \mu\text{m}$. These mean sizes fall within the ranges found in the literature (see Chapter 2) for those typically used in mechanical testing of γ' hardenable nickel superalloys – albeit generally near the upper limit of these ranges. Based on the morphological observation however, the more ideal cuboidal structure was achieved following the solution treatment only and if future research continues in this area then a recommendation of simply a solution treatment could be advised in order to obtain a ‘good’ γ' structure.

Keeping this in mind an investigation into the use of a gas ‘jet-cooled’ HIPping treatment was proposed. The HIPping conditions were set at 1260°C , with a 4h dwell time (same time & temperature as the solution treatment), under 150 MPa with the jet-cooling applied rather than the controlled $5^\circ\text{C}/\text{min}$ cooling. The plot in Figure 6.15 shows the thermocouple data from these three different treatments; from this data it is clear that there is only a difference of $41^\circ\text{C}/\text{min}$ between the gas-quench and jet-cooled HIPping ($165^\circ\text{C}/\text{min}$ & $124^\circ\text{C}/\text{min}$ respectively). The micrograph in Figure 6.16 shows the γ' structure following the HIP & jet-cooling to be particulate, but coarse and only partially cuboidal. The particle size distribution in Figure 6.17 shows mean particle size of $1.29\ \mu\text{m}$ which is more than double that obtained following the solution treatment. Considering the difference in the cooling rates, this particle size difference seems to be disproportionately large; it is suggested that the cooling rate of the samples within the HIP is not as rapid as that measured. This is speculation as it is not possible to position a thermocouple closer to the samples within the gas-quench furnace or the HIP chamber.

The structure of the γ' phase following the HIP & jet-cooling is promising however and has proven the feasibility that a HIPping treatment combined with a rapid enough quench could produce the desired γ' structure making the SLM manufacture using CM247LC a two-step rather than five-step process. This would significantly reduce processing time and cost making it an attractive option for netshape manufacture.

6.3. Mechanical Testing of CM247LC

The mechanical testing conditions were largely influenced by the requirements of the industrial sponsor; all samples were fully heat treated before being machined and tested, however the inclusion of HIPping and the build orientation were investigated. Room temperature tensile testing was used to determine the effect of HIPping against non-HIPped material and vertically built (tension axis parallel to the build direction) against horizontally built (tension axis perpendicular to the build direction); these factors were also investigated in the creep testing. Further elevated temperature tensile tests were carried out on the vertically built, HIPped and fully heat treated samples as the configuration predicted to give the best results.

i. Tensile Results

For room temperature tensile testing, 3 samples were tested in each condition: vertically built, HIPped & heat treated; horizontally built, HIPped & heat treated; vertically built & heat treated only; horizontally built & heat treated only. Bar plots showing UTS, 0.2% Proof Stress (approximating to yield stress) and % strain to failure are shown in Figure 6.18, Figure 6.19 and Figure 6.20 respectively; all plots also show the appropriate data presented by Kim et al. [7] for conventionally cast (CC'd) CM247LC for comparison. Due to the failure of some samples in the 1st build, 2 samples (Horizontally fabricated & heat treated only) were built in

a 2nd batch and tested at a later date; the data relating to these is shown as hatched in the bar plots.

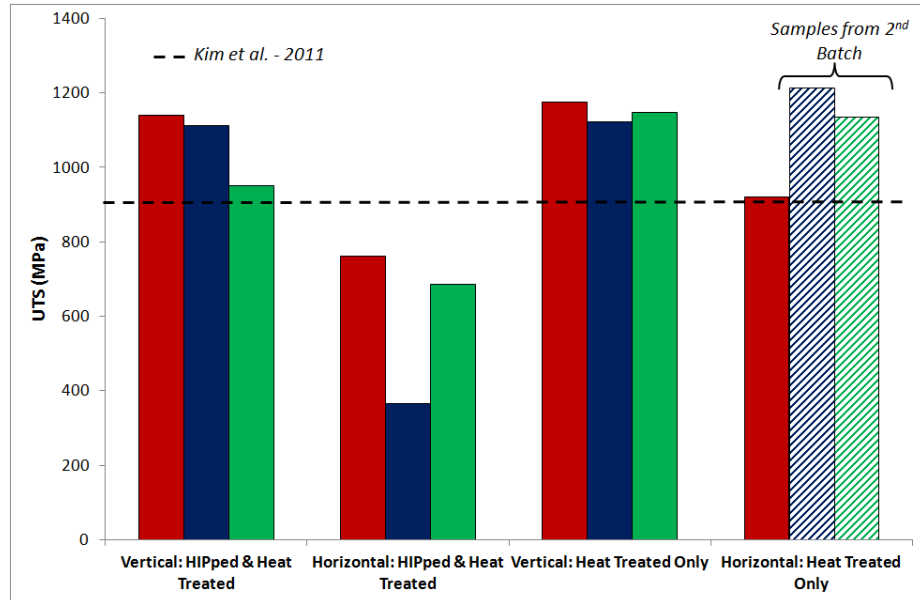


Figure 6.18: Bar plot showing UTS at room temperature for SLM-fabricated CM247LC for 4 different processing conditions; 3 samples were tested for each condition. Dashed line shows data for CC'd CM247LC presented by Kim et al. [7] for comparison. Hatched bars show samples SLM-fabricated in a 2nd batch and tested at a later date.

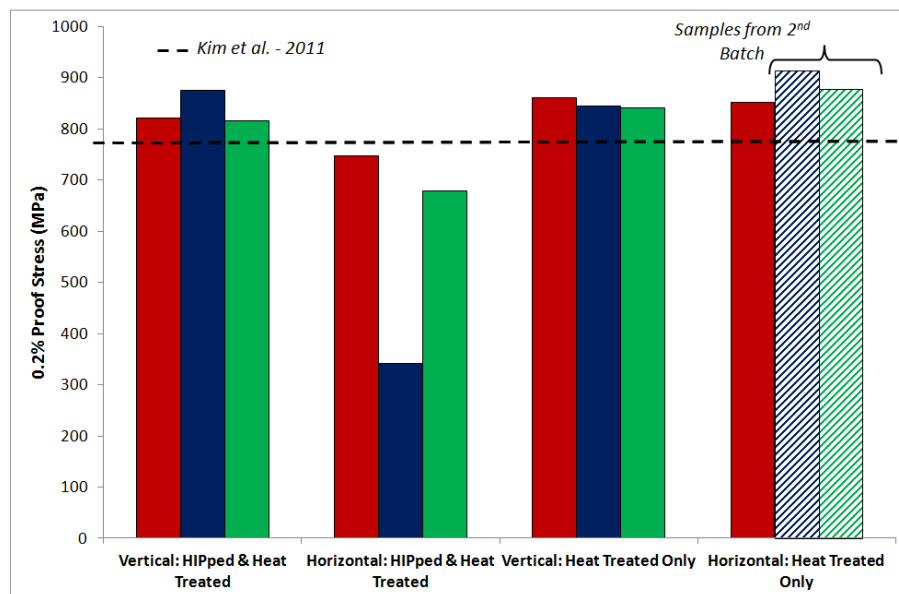


Figure 6.19: Bar plot showing 0.2% proof stress at room temperature for SLM-fabricated CM247LC for 4 different processing conditions; 3 samples were tested for each condition. Dashed line shows data for CC'd CM247LC presented by Kim et al. [7] for comparison. Hatched bars show samples SLM-fabricated in a 2nd batch and tested at a later date.

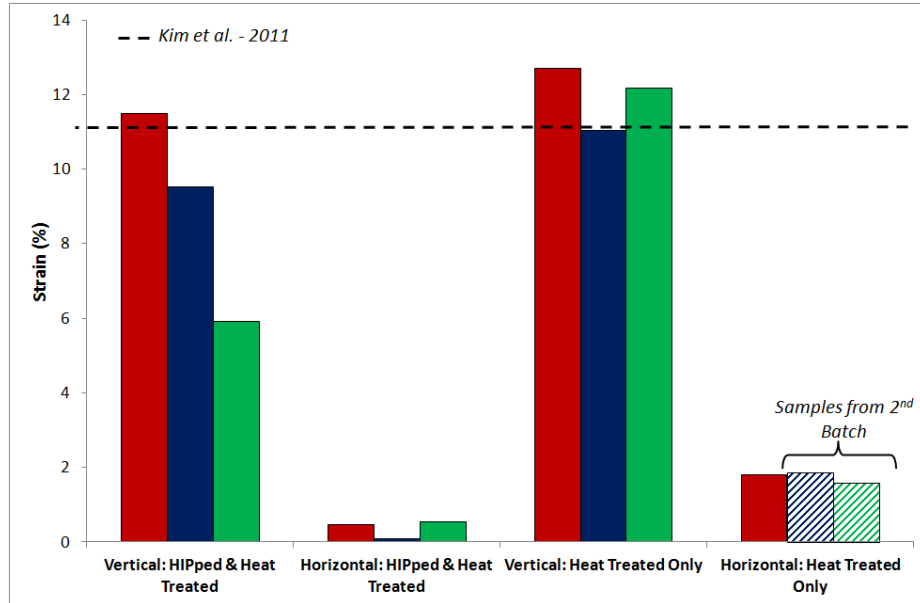


Figure 6.20: Bar plot showing % strain to failure at room temperature for SLM-fabricated CM247LC for 4 different processing conditions; 3 samples were tested for each condition. Dashed line shows data for CC'd CM247LC presented by Kim et al. [7] for comparison. Hatched bars show samples SLM-fabricated in a 2nd batch and tested at a later date.

Elevated temperature tensile testing was carried out at 700°C, 760°C and 900°C on vertically built, HIPped & heat treated samples; 3 samples were tested at each temperature. The UTS and 0.2% proof stress are shown in Figure 6.21 and the % strain to failure is shown in Figure 6.22. Individual data points have been plotted and the mean values were used to construct the line in each case; circled data points were ignored as outliers for the calculation of the mean. The corresponding data for cast CM247LC presented by Kim et al. [7] is also shown for comparison.

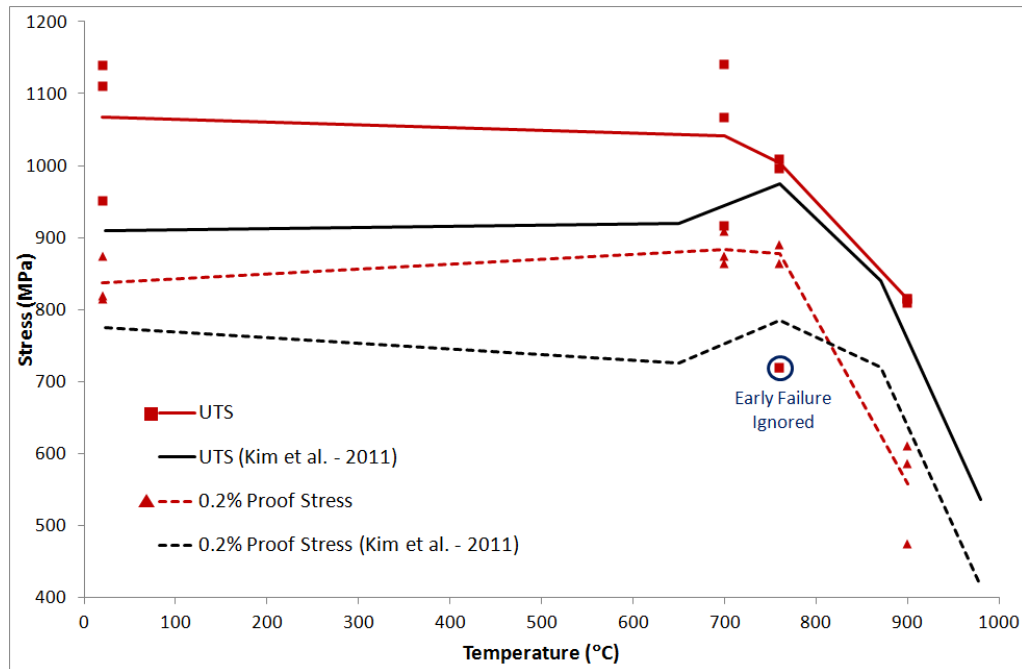


Figure 6.21: Elevated temperature tensile test results for vertically built SLM-fabricated, HIPped & heat treated CM247LC showing UTS (square points & solid line) and 0.2% proof stress (triangular points & dashed line). Data presented by Kim et al. [7] for CC'd CM247LC (black lines) is also presented for comparison.

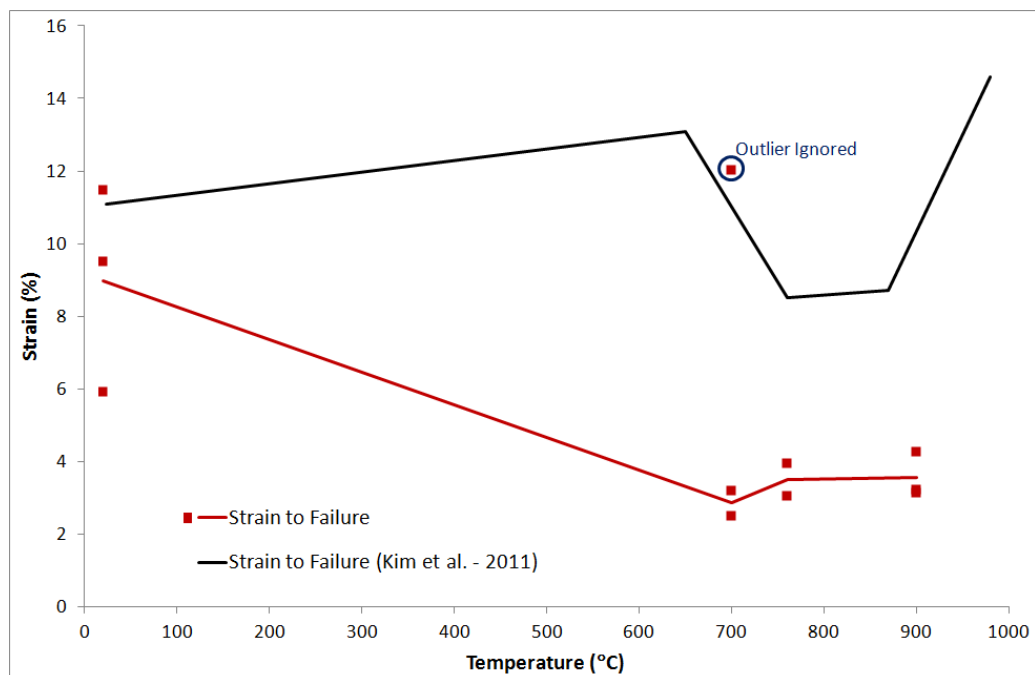


Figure 6.22: Elevated temperature tensile test results for vertically built SLM-fabricated, HIPped & heat treated CM247LC showing % strain to failure. Data presented by Kim et al. [7] for CC'd CM247LC (black line) is also presented for comparison.

ii. Creep Results

Creep results are presented for 1050°C, 100 MPa. Two samples were tested in each condition: vertically built, HIPped & heat treated; horizontally built, HIPped & heat treated; vertically built & heat treated only; horizontally built & heat treated only. The creep curves for the vertically built samples are shown in Figure 6.23 (a) and the horizontal curves shown in Figure 6.23 (b). A bar plot showing a summary of the creep life and creep strain to failure are shown in Figure 6.24 and Figure 6.25 respectively.

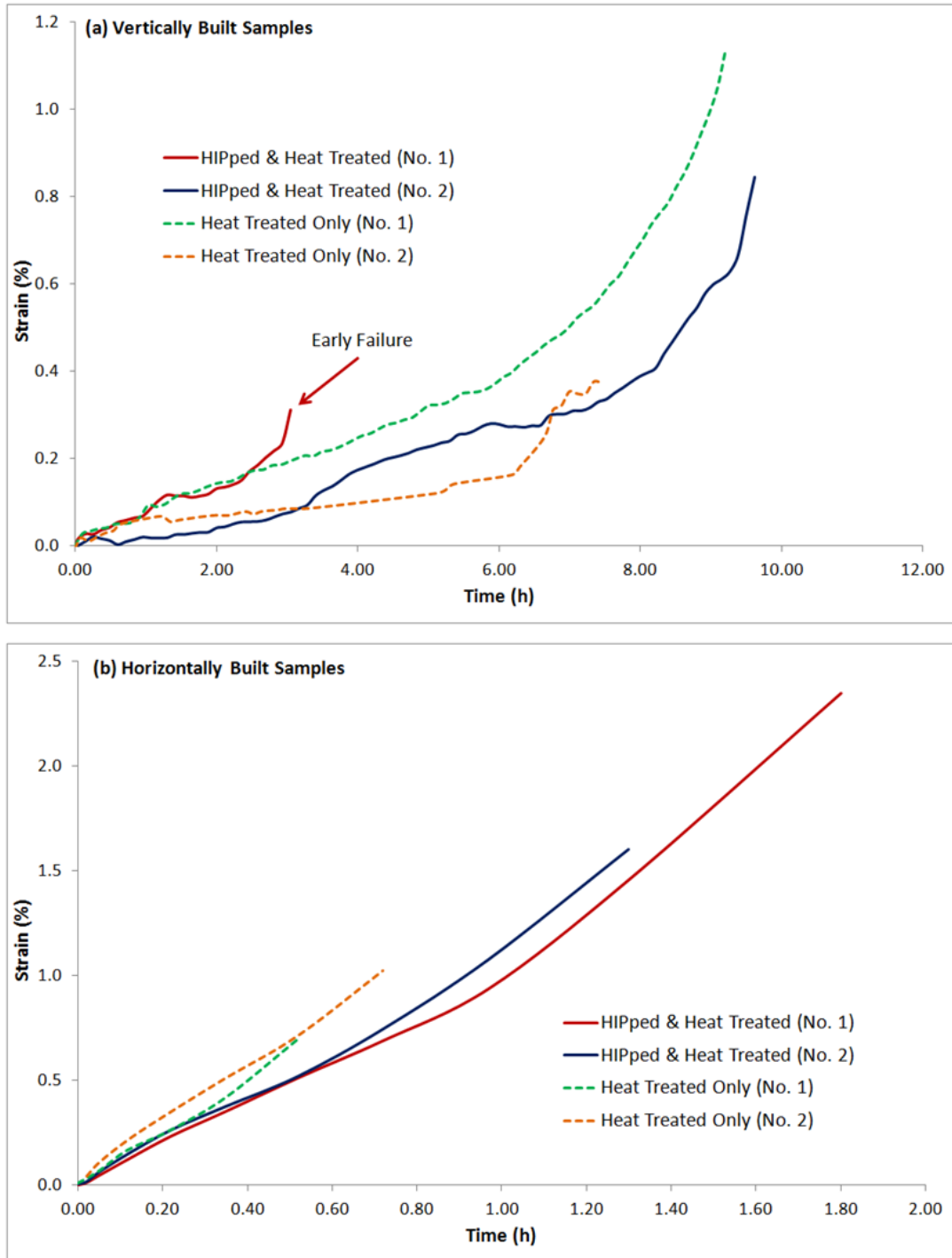


Figure 6.23: Creep curves for SLM-fabricated CM247LC in various conditions tested at 1050°C, 100MPa. Vertical sample results are shown in (a) and horizontal in (b); two samples tested for each condition (Note: Different time axis scale on (a) and (b)).

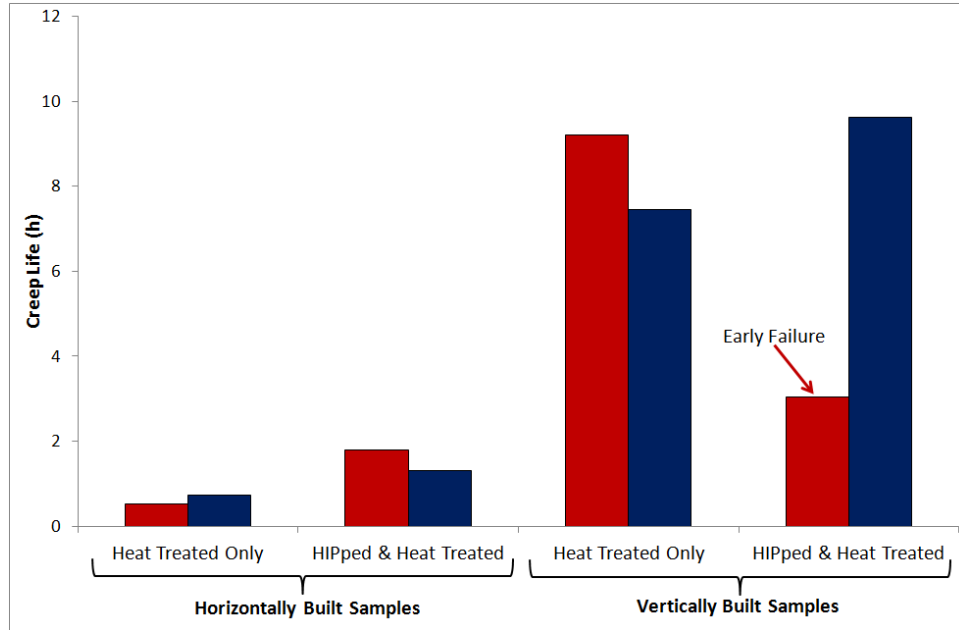


Figure 6.24: Bar plot showing 1050°C, 100 MPa creep life for SLM-fabricated CM247LC following various processing conditions.

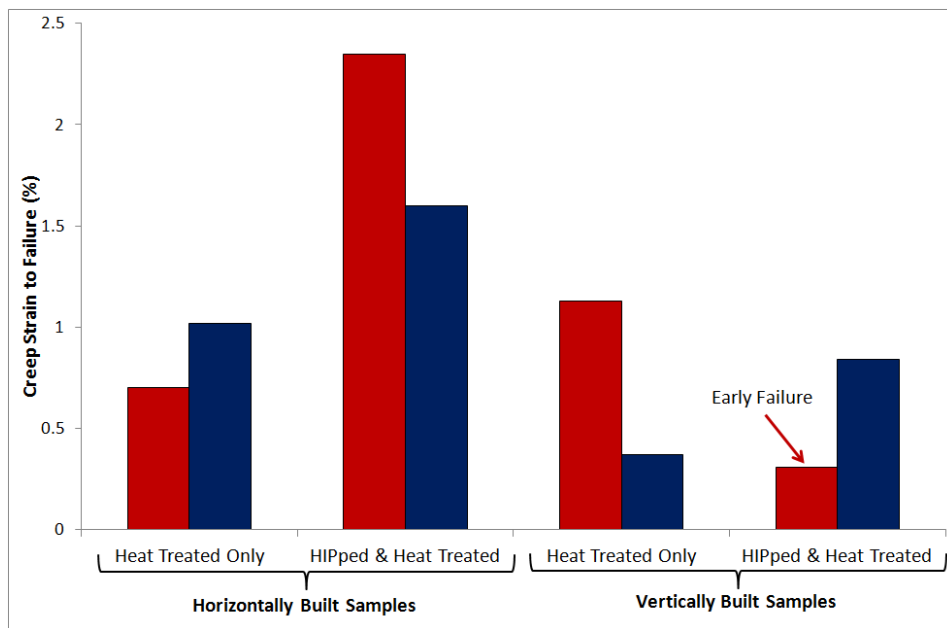


Figure 6.25: Bar plot showing 1050°C, 100 MPa creep strain to failure for SLM-fabricated CM247LC following various processing conditions.

iii. Discussion

There are three key areas for discussion regarding these mechanical test results for the SLM-fabricated CM247LC. Firstly the tensile results and how the different process routes have influenced the properties. Secondly the creep results and finally how both these sets of results compare against the conventionally cast data published by Kim et al. [7] for tensile and by Donachie [1] for creep.

The room temperature tensile results showed one anomalous early failure in the horizontally fabricated HIPped & heat treated condition and the creep results showed a similar result for a vertically fabricated HIPped & heat treated sample. These are believed to be caused by some internal defect within the sample; without extensive fractography the cause of this cannot be determined.

The room temperature 0.2% proof stress results (Figure 6.19) are fairly consistent across all the processing routes. This behaviour is governed by the elastic rather than plastic deformation characteristics of the material and as such the build orientation (mainly influencing the grain structure) is of little impact. The samples HIPped prior to the heat treatment show a marginally lower 0.2% proof stress than the non-HIPped samples which could be attributed to a slightly coarser γ' structure existing in the HIPped samples despite the attempt to mitigate this using the solution heat treatment.

The room temperature % strain to failure results (Figure 6.20) show a much more dramatic difference between the processing routes. Here the once again the HIPped samples appear to show a marginally poorer performance (lower ductility) than the non-HIPped ones, but much more striking is the difference made by the build orientation with the horizontally built samples showing extremely low ductility compared to the vertically built samples. The

elongated grains in the build direction reduce significantly the number of grain boundaries (and cracks) perpendicular to the loading direction which typically act as fracture initiation points dramatically increasing the ductility whereas the opposite is true in the horizontally built samples.

The UTS results (Figure 6.18) again seem to show a marginally poorer performance of the HIPped samples to their non-HIPped counterparts in both build orientations; this appears to indicate that the elimination of cracks only has a slight impact on the stressed cross-sectional area and hence no significant change to the tensile properties with or without HIPping. The horizontally built and HIPped specimens show the lowest average UTS, however the horizontal non-HIPped specimens compare very favourably to the vertically built ones. Overall it seems as though build orientation affects the ductility of the material, but has a much less significant effect on the strength of the material.

The creep curves for all the samples tested are shown in Figure 6.23. In all cases the samples seem to show entirely tertiary creep which is consistent with published literature showing only tertiary creep at temperatures above 980°C (see Satyanarayana et al. [8] as discussed in Chapter 2). The curves for the vertical samples in Figure 6.23 (a) seem to be ‘uneven’ which could indicate points of sudden grain boundary slipping and locking. It is suggested that the cause for this is the lack of consistency in grain structure in the direction of loading (as discussed in Chapter 5). By contrast the horizontal creep curves seen in Figure 6.23 (b) are much smoother.

The creep life of the samples is generally very poor. The vertically built samples had a creep life 4-5 times longer than the horizontal samples. HIPping resulted in a slight increase in creep life believed to be due to the elimination of rupture initiation points. HIPping in the

horizontally fabricated samples resulted in a significantly improved creep life as the majority of the crack faces are perpendicular to the loading direction. The elimination of these cracks resulted in an increase of the loaded cross-sectional area and a reduction in potential rupture initiation points.

It can be seen that the tensile testing results (for the best processing conditions) outperform the conventionally cast material in terms of UTS and 0.2% proof stress up to the 900°C temperature where the 0.2% proof stress drops slightly below the literature values. The room temperature ductility of the vertically built samples is comparable to that of the conventionally cast material however it marginally underperforms at the higher temperatures, most likely due to any remaining defects within the samples. Overall it shows that any remaining defects within the material do not seem to greatly influence the tensile properties. The horizontally built samples significantly underperform compared to the cast material in terms of room temperature ductility but surprisingly show comparatively good UTS and yield strength.

The creep results however significantly underperform against the literature data; the Larson-Miller data provided by Donachie [1] predicts a creep life of approximately 236 hours at 1050°C, 100 MPa for DS CM247LC which shows the tested creep life maximum of 9.6 hours to be very poor by comparison. The reasons for this are likely to include the existence of defects within the material (i.e. possible inclusions of oxides caused by HIPping), the high temperature testing conditions which result in partial dissolution of the γ' phase and the poor grain structure. It must also be noted that predictions from Larson-Miller data become less accurate at the limits of the material performance.

6. 4. Mechanical Testing of CMSX486

The intention of the mechanical testing of CMSX486 was to evaluate the properties of the material in a similar way to that discussed for CM247LC (i.e. the influence of HIPping and build orientation on room temperature tensile properties; elevated temperature performance of vertically built and HIPped material; influence of build orientation and HIPping on creep properties). All samples were heat treated prior to testing as described by Wilson et al. [9] and discussed in Chapter 3. In order to confirm correct solution treatment, DSC analysis was carried out on a solid piece (58.03 mg) of the as-fabricated CMSX486 to determine the γ' solvus temperature, solidus and liquidus.

Following machining the HIPped and heat treated samples had to be abandoned due to extensive cracking visible to the naked eye; this can be seen in Figure 6.26.



Figure 6.26: Photograph showing SLM-fabricated CMSX486 following HIPping, heat treatment and machining to test specimen geometry. Note the extensive cracking visible along the length of the sample.

Testing was therefore not carried out on the HIPped samples as they all displayed similar faults. Due to time, material and cost constraints, it was not possible to reproduce these samples or further investigate the cause for the significant cracking pictured here. It is suggested that due to the very high γ' fraction of the material, large residual stress and slow cooling rates in the HIP that these may be reheat cracks caused by the strain-ageing effect although further investigation would be needed to confirm this.

i. DSC Results

The DSC results for the heating and cooling of the solid sample of SLM-fabricated CMSX486 powder are shown in Figure 6.27. The plot is annotated with the solidus (determined by extrapolation of the linear portions of the plot) at 1337°C, liquidus at 1388.5°C and the onset of γ' formation on the cooling curve at 1312°C.

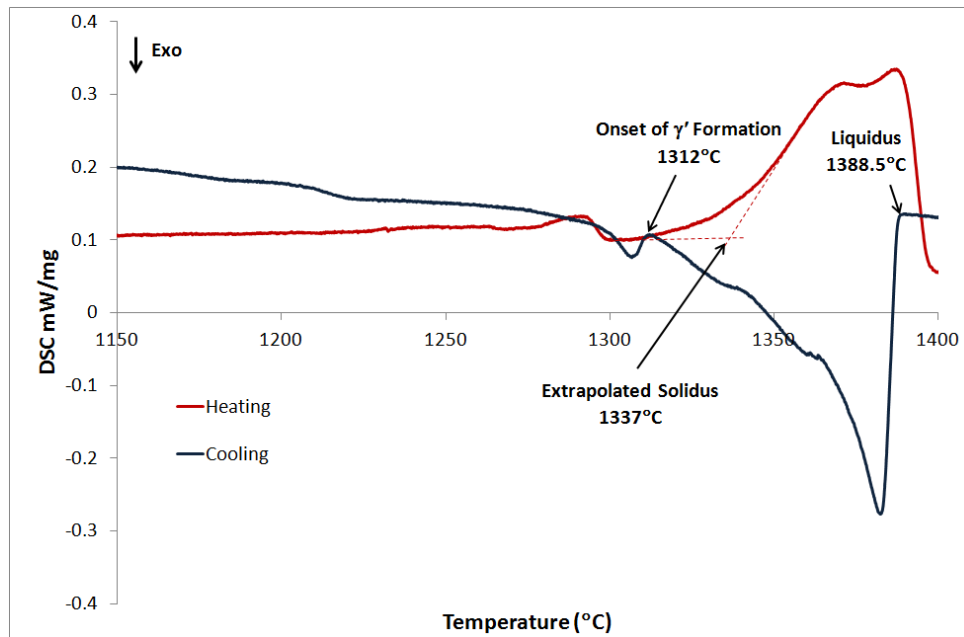


Figure 6.27: DSC results for the heating (red) and cooling (blue) of a solid sample of CMSX486 annotated with solidus, liquidus and onset of γ' formation (Heating/Cooling = 10°C/min).

ii. Tensile Results

Tensile testing of SLM-fabricated CMSX486 was carried out at room temperature in the heat treated condition. Three samples were tested in both the horizontal and vertical build orientation. Bar plots showing UTS, 0.2% proof stress and % strain to failure are presented in Figure 6.28, Figure 6.29 and Figure 6.30 respectively.

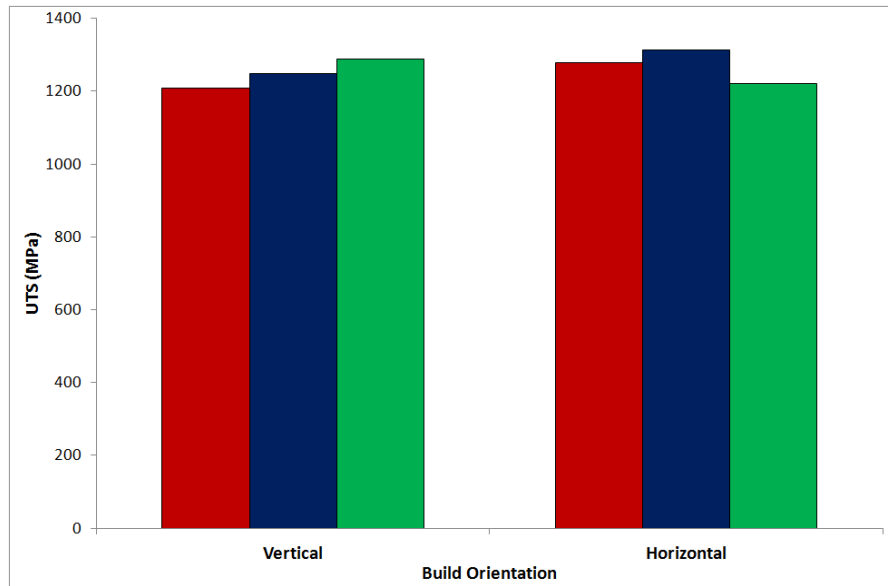


Figure 6.28: Bar plot showing UTS for SLM-fabricated and heat treated CMSX486. Three samples were tested in both vertical and horizontal build orientation.

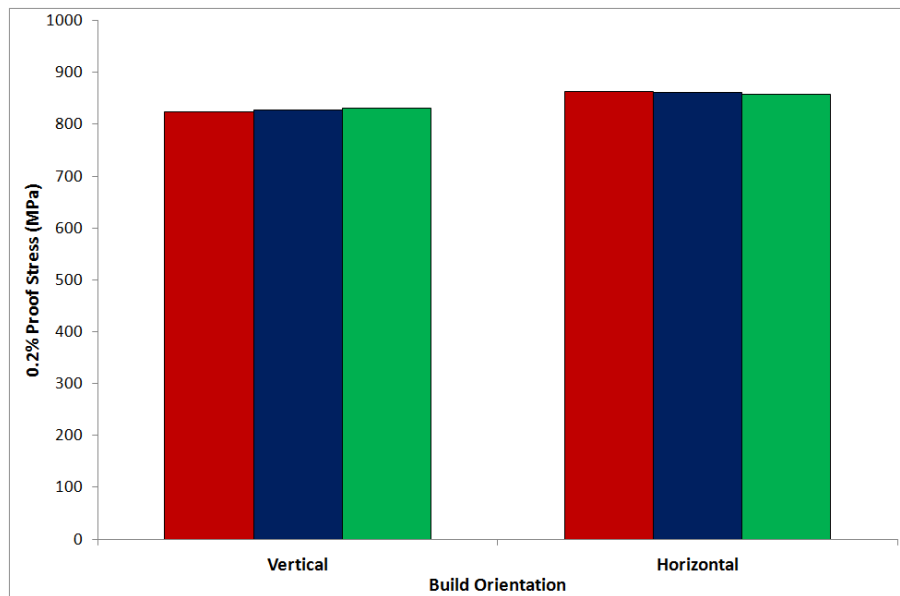


Figure 6.29: Bar plot showing 0.2% proof stress for SLM-fabricated and heat treated CMSX486. Three samples were tested in both vertical and horizontal build orientation.

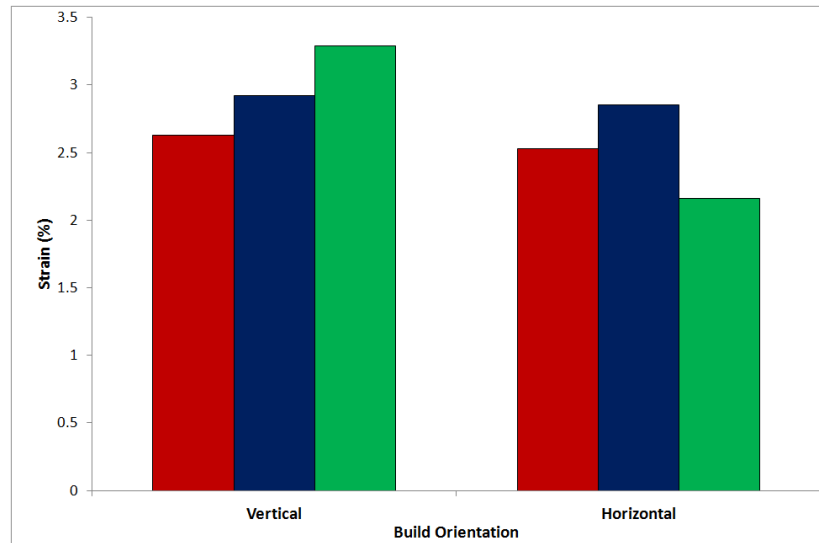


Figure 6.30: Bar plot showing % strain to failure for SLM-fabricated and heat treated CMSX486. Three samples were tested in both vertical and horizontal build orientation.

iii. Creep Results

CMSX486 samples were tested at 1050°C and 100 MPa in the SLM-fabricated and heat treated condition. Two samples were subject to testing for both the vertical and horizontal build orientations; however the horizontally built samples failed under hot loading, therefore only the vertical results are presented. The creep curves annotated with the creep life for the vertically built and heat treated samples is shown in Figure 6.31.

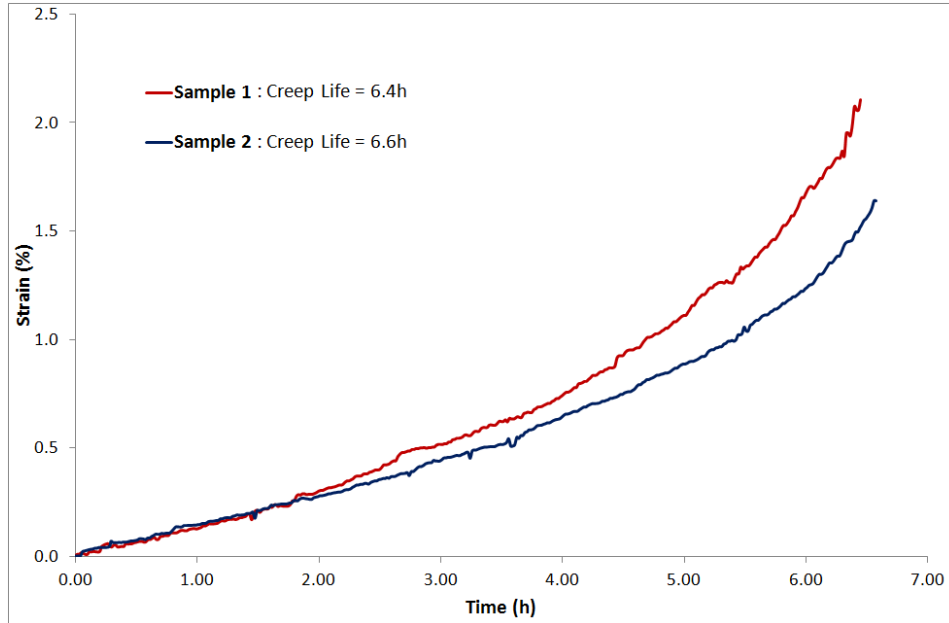


Figure 6.31: Creep curves for SLM-fabricated and fully heat treated CMSX486. Samples tested at 1050°C and 100 MPa loading. The plot is annotated with the creep life of each sample.

iv. Discussion

Due to the lack of available tensile data for cast CMSX486 and the failure of the HIPped samples, it is difficult to draw any significant conclusions from the room temperature testing of the material presented here.

Both the 0.2% proof stress and UTS are consistent for both the vertically and horizontally built specimens. The % strain to failure shows particularly low ductility for the samples and again very little variation between the horizontally and vertically built specimens.

The shape of the creep curves is similar to that seen for CM247LC and comparing the creep life to that presented by Harris & Wahl [10] (predicting a creep life in the region of 1000h) it performs very poorly. This is most likely a result of the heavy cracking within the material which (as discussed in Chapter 4) is much more significant than that seen in CM247LC; this is accentuated by the failure of the horizontal samples under hot loading.

6.5. Mechanical Testing of IN625

Only the tensile properties of the as-fabricated (without heat treatment of HIPping) IN625 were assessed in accordance with the requirements of the industrial sponsor.

i. Tensile Results

The UTS and 0.2% proof stress results for the as-fabricated IN625 are presented in Figure 6.32; data published by Donachie [1] is presented for cast IN625 providing a benchmark comparison. Similarly, the results for the % strain to failure are presented in Figure 6.33.

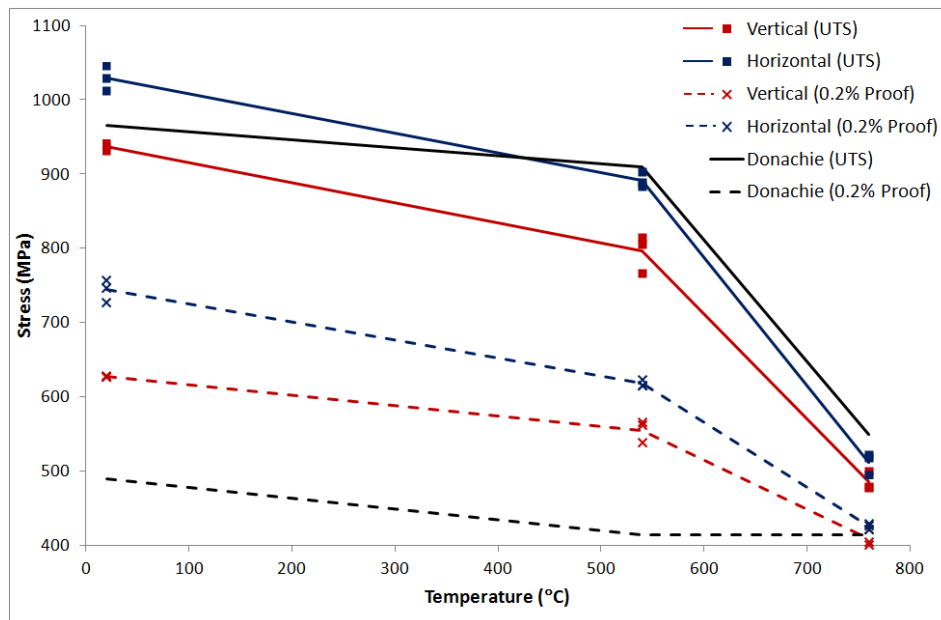


Figure 6.32: Plot showing UTS and 0.2% proof stress for as-fabricated IN625 in both the horizontal and vertical build conditions against temperature. Data published by Donachie [1] for cast IN625 is shown in black.

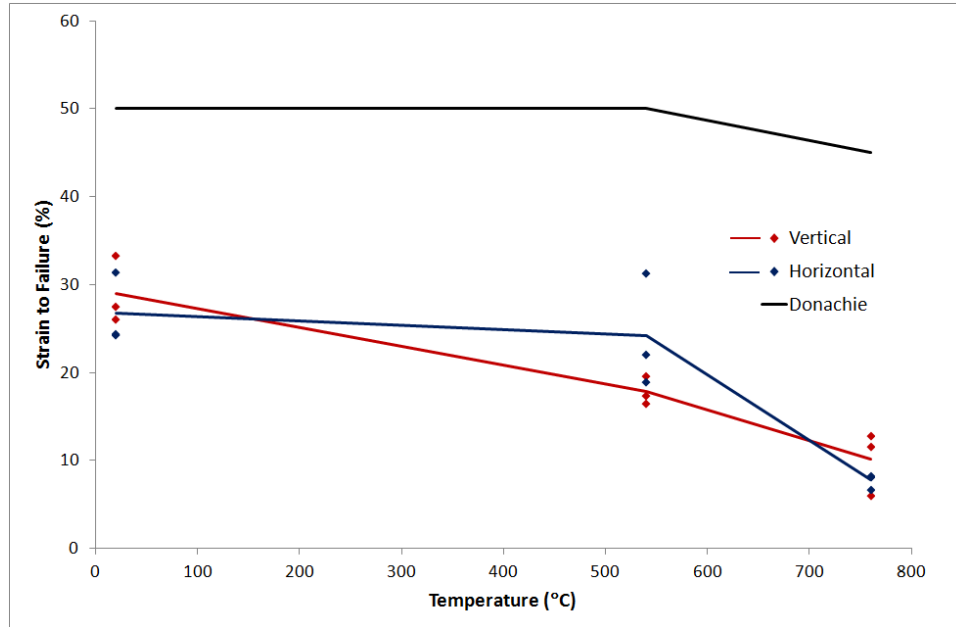


Figure 6.33: Plot showing % strain to failure for as-fabricated IN625 in both the horizontal and vertical build conditions against temperature. Data published by Donachie [1] for cast IN625 is shown in black.

ii. Discussion

The results in Figure 6.32 and Figure 6.33 show that overall the SLM-fabricated IN625 performs well when compared to the cast material. The UTS results are very similar to the cast material, particularly the horizontal results and the yield strength of the SLM-fabricated material is consistently higher than the cast material. Like the SLM fabricated CM247LC, IN625 shows a poorer ductility when SLM-fabricated than cast however this performance is reasonably consistent between the horizontal and vertical samples and does not drop to the very low ductility levels seen in the CM247LC results.

The striking feature of these results is the consistently higher UTS and yield of the horizontal over the vertically built samples. In Chapter 4 it is discussed that there is some remaining porosity even with these optimised process parameters and they appear to be due to some isolated poor bonding between layers. This could explain the performance of the vertical samples where the loading axis is perpendicular to the build layers.

Overall these results are very encouraging and confirm what has been previously stated that IN625 is a good candidate material for SLM-fabrication without some of the limitations of the γ' hardenable materials. It is the author's opinion that further improvement to the mechanical properties could be made by HIPping the IN625 samples in order to ensure a fully dense material; however further study into the microstructural effects of this would be required.

6. 6. Overall Discussion & Conclusions

Overall the tensile properties of CM247LC compare well to the conventionally cast material in terms of UTS and 0.2% proof stress, however the ductility of the material seems to be largely influenced by the build orientation. The creep results are much less encouraging and although improved by the HIP and in vertical build orientation they are still significantly lower than anticipated however with such a limited number of results it is difficult to draw firm conclusions.

The CMSX486 results were disappointing stemming from a combination of the high cracking susceptibility of the material and the extensive reheat cracking caused by HIPping. At this point it seems as though this material is certainly an unsuitable candidate material for SLM manufacture based on the difficulties encountered during this investigation.

The application of HIPping requires further investigation and the overall heat treatment of the material (although a method has been outlined here) could be refined and streamlined to reduce the processing steps. The HIPped CM247LC did show an improvement in creep performance, however the HIPped samples also showed slightly poorer tensile properties than their non-HIPped counterparts and the significant cracking observed in the HIPped CMSX486 samples suggests that HIP heating/cooling rates need further investigation which has not been possible within the timescale of this research.

The final point to note is the good mechanical properties achieved from the as-fabricated IN625. This was anticipated based on the review of the literature and the parametric study (Chapter 4) however the proof of this processability is given with the very good tensile properties of the material compared with cast IN625 and illustrates that the SLM process can produce mechanically sound components in an as-fabricated condition given the correct starting material.

6. 7. References

- [1] Donachie MJ, Donachie SJ. Superalloys: A Technical Guide. Ohio: ASM International, 2002.
- [2] Zhao K, Lou LH, Ma YH, Hu ZQ. Effect of minor niobium addition on microstructure of a nickel-base directionally solidified superalloy. *Materials Science and Engineering A* 2008;476:372.
- [3] Pierret S, Evans A, Ania P, Anders K, Thomas E, Van Swygenhoven H. Combining neutron diffraction and imaging for residual stress analysis in single crystal turbine blades. *Euromat 2011*. Montpellier, France, 2011.
- [4] Kim IS, Choi BG, Seo SM, Kim DH, Jo CY. Effect of heat treatment on the tensile properties of poly-crystal and DS CM247LC alloy. 2007;124-126:1401.
- [5] Cannon-Muskegon. C-M Group Website. www.c-mgroup.com, vol. 2009, 2009.
- [6] Höhne G, Hemminger W, Flammersheim H-J. Differential scanning calorimetry. London: Springer, 2003.
- [7] Kim IS, Choi BG, Hong HU, Yoo YS, Jo CY. Anomalous deformation behavior and twin formation of Ni-base superalloys at the intermediate temperatures. *Materials Science and Engineering A* 2011;528:7149.
- [8] Satyanarayana DVV, Omprakash CM, Jagadeesan B, Das N. Effect of section thickness on creep and stress rupture behaviour of DS CM247 nickel base superalloy. *Materials at High Temperatures* 2008;25:17.
- [9] Wilson BC, Hickman JA, Fuchs GE. The effect of solution heat treatment on a single-crystal Ni-based superalloy. *Journal of Metals* 2003;55:35.
- [10] Harris K, Wahl JB. Improved single crystal superalloys, CMSX-4 (SLS)[La+Y] and CMSX-486. Champion, PA, United states: Minerals, Metals and Materials Society, 2004. p.45.

CHAPTER 7: CONCLUSIONS, EVALUATION & FUTURE WORK

This chapter briefly summarises the main conclusions presented in Chapters 4, 5 & 6. Included is an evaluation of the processing route and the current viability of using SLM as an alternative to casting for the production of high temperature CM247LC and suggestions for future research are also presented.

7.1. Overall Conclusions

The parametric studies presented in Chapter 4 have shown that for the γ' hardenable alloys (CM247LC & CMSX486) it is not possible to eliminate the cracks in the as-fabricated condition using technology currently available (Concept Laser M2). It has been possible however to pinpoint a set of processing parameters within the larger processing window where the cracking is significantly reduced. The likely cracking mechanisms have been investigated and can be related to the processing parameters – the lowest levels of cracking (and least damaging) were found to occur when grain boundary cracking was dominant. It has been concluded through the microstructural examination of the cracks that they form via a combination of two mechanisms. Ductility-Dip Cracking (DDC) as observed in welds of nickel alloys where stress concentrations around grain boundary carbides lead to the formation of voids and cracks and liquation cracking caused by liquation of low melting point grain boundary phases forming weak liquid films as a result of reheating.

Microstructural investigations and microCT results have been presented in Chapter 5 to show that HIPping can close the cracks to provide a possible retro-fix solution to the cracking problem but add a time consuming additional step to the processing route.

The use of a statistical method to obtain good process parameters for CMSX486 and IN625 was a partial success as it was able to generate a reasonable set of parameters, although the cracking density for CMSX486 showed much more variability than this approach predicts. Given the current necessity for HIPping to close internal defects and the unknown impact of applying blanket parameters to any given geometry however, the statistical method does allow a set of processing parameters to be rapidly obtained and used as a starting point for further investigations.

The study of the grain structure and orientation of the SLM-fabricated CM247LC presented in Chapter 5 has shown that the island scan strategy used by the Concept Laser M2 produces a bi-modal structure with some strong grain elongation along the build axis. EBSD has shown that the fine grained regions at the boundary of each island are misaligned to the elongated grains; subsequent microCT investigation has revealed the fine grained regions to be particularly susceptible to cracking. A limited investigation into a simple ‘back-and-forth’ scan strategy has illustrated the potential to influence the grain structure by varying the laser path.

The application of a heat treatment in order to produce a desirable γ' structure within CM247LC has been investigated in Chapter 6. Micrographs have been presented to show the γ' structure at the various stages during the processing route. The solution treatment has been established and a full heat treatment based on the standard treatment available in the literature has produced a coarse cuboidal γ' structure; this treatment was concluded to be acceptable. A limited trial illustrated the potential to reduce the number of processing steps by combining the HIP and solution treatments.

Finally, mechanical testing has been used to evaluate the SLM processing route. The tensile properties (both room temperature and elevated) of CM247LC are comparable to those published in literature; however the creep performance is significantly worse. Additionally the HIPped samples do not perform significantly better than the non-HIPped samples in tensile testing indicating that the closure of cracks is not a key governing factor although by disregarding the poor overall creep performance, it can be stated that HIPping does improve the creep properties of the material. The build orientation significantly affects the ductility of the material and the creep performance, both being greater in the vertical orientation; however it does not influence the overall tensile strength of the material.

The poor creep performance of the material is of great concern when considering the primary application (high-temperature; high-stress components) and the suggested cause is discussed in Chapter 6. In general it is believed that the poor (non-homogeneous) grain structure is likely to be a large contributing factor, but additionally the testing conditions are extreme for the particular material and it is possible that partial dissolution of the γ' phase (as predicted by the thermocalc model in Chapter 6. Unfortunately the industrial requirements for creep testing specified these conditions (1050°C, 100 MPa) and there was insufficient time and finance to conduct a more thorough creep testing program in order to better characterise the material against the literature data.

The concurrent work on CMSX486 was aimed at rapidly assessing a similar material without the use of in-depth microstructural examination using statistical methods, published heat treatment data and DSC. The mechanical testing of this material was disappointing and showed firstly that the HIPping of SLM fabricated CMSX486 needed significant investigation due to the occurrence of what is believed to be reheat cracking caused by the slow

heating/cooling rates of the HIPping process. The as-fabricated samples seemed to show consistent tensile strength, but low ductility and the creep results were particularly poor for what is regarded as a high-temperature creep resistant material. This poor performance can be attributed to the very high cracking susceptibility (even compared to CM247LC) as seen in Chapter 4 and as such CMSX486 cannot be recommended as a candidate material for SLM fabrication using the current process route and techniques.

The IN625 study was aimed to show that, by selecting a much more appropriate alloy (i.e. greater ductility and γ'' hardenable – see Chapter 2 & 4), the SLM process can produce a nickel superalloy in a crack-free state (although any distortion of the material due to internal stress has not been measured). The mechanical properties have shown that even without further heat treatment this material performs very well when compared with conventionally cast material.

7.2. Evaluation of the SLM Processing Route

As stated in previous chapters, the process route incorporates SLM fabrication, HIPping and the heat treatment. This brief evaluation will first consider the use of SLM as a method of forming high temperature nickel superalloy components and secondly the overall processing route incorporating all the steps required to produce the final component.

The potential advantages to the SLM method are stated in Chapter 1. The method allows for the production of complex geometries to be produced directly from a CAD file without the need for expensive tooling; this is of particular importance in aerospace components which often require complex internal geometries difficult to form by other methods. The results presented in this thesis however have shown that the SLM process is far from being production-ready for components made from CM247LC.

The cracks in the as-fabricated condition are a cause for concern and are aggravated by the island scan-strategy employed by the Concept Laser M2. Concept Laser report that this strategy is aimed at reducing the overall residual stress in components by more evenly heating each slice [1]. The evidence presented in this thesis has shown that for the γ' hardenable material CM247LC, the island strategy is responsible for the formation of a bi-modal grain structure with dense areas of cracking occurring at the fine grained regions on the island boundaries; this is a key area of concern for any future work in this area.

The overall processing route also has several points that are of concern when considering its application in a production environment. The number of processing steps starts to eliminate the potential gains in time and cost of using SLM; this is further emphasised when considering the initial casting and atomisation of the starting material prior to SLM and the subsequent surface finishing operations required by the majority of aerospace components.

These concerns are compounded by the poor creep performance of the processed CM247LC and its lack of physical consistency (shown by the early failure of individual samples in both the creep and tensile testing sets).

This thesis has investigated the viability of using of the commercially available Concept Laser M2 for the production of components from the nickel superalloy CM247LC. Using the available facilities the SLM-processed material has been studied, refined and the detrimental microstructural features (cracks, grain structure etc.) examined. On the basis of this work it is concluded that the process route is not currently viable for the production of CM247LC components with properties comparable to traditionally cast equivalents.

In more general terms SLM may be a viable method for the production of components using more suitable materials (as highlighted by the IN625 studies). The technique has the ability to

produce structures and geometries which would otherwise be hugely difficult to produce however the potential application of this technique for weight saving and design refinement for functionality has not in general been exploited. In order for this to occur designers and engineers must strive to further understand the abilities and limitations of the technique in order to accept it as a viable manufacturing alternative rather than regarding it with an air of novelty as is currently the case.

In the next section the future areas of research required to make SLM a viable processing route for CM247LC are outlined.

7.3. Proposed Areas of Future Work

Listed below are research areas needed in order to develop SLM as a processing route for γ' hardenable materials:

i. Simulation of the SLM process

The development of an accurate model of the SLM process could be achieved through close collaboration of a physical metallurgist and modelling specialist. Based on measurements of variables (such as heat transfer through the powder bed, cooling rates & thermal gradients etc.), the model should be gradually increased in complexity being validated wherever possible by experimental data. The data obtained as a result of the current research (e.g. quantification of cracking etc.) would provide the basis for an initial validation of the model.

The final model should be able to predict the following:

- Precipitation/morphology of the various phases within the material
- The occurrence/structure of cracks
- The grain structure within the material

Ultimately it is envisaged this simulation could be used to “reverse-model” the process by providing a final target microstructure and the geometry to be produced and obtaining process parameters as the output. This is more than likely to be a dynamic set of process parameters where a suitable laser path, power, speed etc. are all constantly varying throughout the build.

ii. Specific Investigation into the Influence of the Laser Scan-Strategy

Linked to the previous proposal (possibly as a component of the same research project), a full study examining the influence of the laser scan-strategy on the microstructure of the material should be undertaken. This should include the following specific areas of research:

- Characterisation of the microstructure for a range of geometries and range of scan strategies
- Thermal measurement either by thermocouple, pyrometer or high resolution/frame rate thermal camera of the melt pool and surrounding material during the process.
- Theoretical calculations incorporating the measured data and validated against the characterised grain structure.
- Finally the reverse working of the calculations in order to predict processing parameters resulting in a specific microstructure.

iii. Refinement of the SLM process to reduce residual stress

As a significant contributing factor in the formation of the cracks in the as-fabricated material, research into reduction of residual stress must be undertaken in conjunction with the above two research areas in order to reduce cracking and to predict distortion. This must initially be an investigatory piece of research to quantify the residual stress currently within SLM-fabricated material and should then shift focus to possible methods of reduction (e.g. bed-heating, secondary laser etc.). It is suggested that to adequately evaluate the residual

stress fields around features such as carbides or individual scan tracks that synchrotron stress measurement, possibly combined with synchrotron tomography should be employed to achieve the required resolution.

iv. Further Cracking Mechanism Investigation

The occurrence of cracking within CM247LC has been suggested as a DDC-like mechanism based on the microstructural observations, however a full investigation into the structure of these crack using should be carried out and should include a micro-modelling component. The research should cover the following broad topics:

- Full characterisation of the crack structure including extensive TEM examining the GB particles
- Quantification of the occurrence of particles at the different grain boundaries and investigation into the influence on the grain misorientation angle, the occurrence of GB particles and the occurrence of cracking
- Micro-modelling into the precipitation of the GB particles and the stress generated by this precipitation as well as the influence of residual stresses in order to disambiguate DDC from other cracking mechanisms
- Synchrotron measurement of stress fields around grain boundaries of different misorientations and around the GB precipitates.

v. Post Fabrication HIPping & Heat Treatment

The post fabrication treatments applied to CM247LC within this study are lengthy and awkward. The streamlining of this process must be a priority if it is to become an economically viable process. As such research including the following broad topic areas should be undertaken:

- Examination and study of the closed crack surfaces following HIP
- The extensive microstructural characterisation of the material during each processing step.
- The assessment of the HIP to result in PWHT cracking due to the residual stress within high volume γ' fraction alloys (e.g. CMSX486)
- The further investigation of using a combined HIP & HT in order to eliminate the need for so many post production steps.

vi. Alloy Development for SLM

The IN625 study has shown that using a more appropriate alloy the SLM process can produce non-cracked material. The main results in this thesis have been regarding CM247LC which itself was developed for thin-wall castings. Development of a nickel superalloy specifically tailored to processes using SLM is an obvious area for future research.

vii. Engineering for SLM

Although not specifically an area of metallurgy research, improved understanding of engineering and design for SLM-fabricated components is currently being largely overlooked. The constraints with SLM design are vastly different from those seen in traditional casting/machining and research must be carried out into design optimisation for this processing route to fully capitalise on the potential gains of this method in terms of efficient and innovative design.

This would also include a full evaluation of the dimensional accuracy of the process, distortion measurement and the development of a process of surface refinement which can be applied to SLM fabricated structures as standard.

7.4. Final Remarks

This thesis represents an initial attempt to take an existing material and an existing technology and study the combination of the two. The ‘future work’ suggestions have highlighted the need for a much greater body of research to be carried out before such a combination is viable. Engineers creating future SLM systems and material scientists must work together to overcome the challenges raised by this research; only then can the rewards of this technique be fully realised.

7.5. References

- [1] Hofmann. Hofmann Innovation Group Website - Concept Laser (<http://www.hofmann-innovation.com/en/technologies/direct-cusing-manufacturing.html>). 2012.

APPENDIX A: CONCEPT LASER M2 OPERATION

This appendix outlines the standard practices used during SLM by the Concept Laser M2 system within the research presented in this thesis; it is not intended to be a system operating manual which is available elsewhere [1, 2]. Details include the CAD preparation, support structures, parameter definitions (including the standard parameters used) and the practical operation of the system.

i. File Preparation

File preparation for the SLM process follows these general steps:

- CAD files are prepared using commercially available CAD software (SolidWorks [3] within UoB) or provided by the industrial partner.
- CAD files are exported in the industry standard *.stl (Standard Tessellation Language) format. This format approximates the geometry to a closed surface defined by connected triangles; the export settings can be used to increase the number of triangles and so the accuracy of the final product. Conversely low resolution *.stl files may result in visibly faceted components.
- CAD geometry (*.stl format) is imported into the commercially available Magics 15.0 [4] software including Concept Laser Slicer module.
- Orientation and position are defined within Magics
- Automatically generated supports are applied at this stage if supports were not manually generated within the CAD geometry
- Concept Laser module used to slice the CAD files. At this stage the following parameters are defined:

- Slice Thickness
- Beam Compensation
- Contour Inset
- Island Size (X & Y)
- Island Rotation
- Island Shift (X & Y)
- Slice files for the component (filename.cls) and the support structure (s_filename.cls) are generated to be transferred to the M2 PC.

ii. Support Structures

Support structures are applied as standard to all components to be manufactured by SLM for the following reasons:

- Supports are required to physically connect the component to the build plate as the powder cannot securely provide support during building
- Supports anchor sections during building to reduce the chance of deformation due to residual stress which can result in failure
- Support structures provide a route for heat transfer in overhanging sections to prevent ‘over-melting’ of powder which can result in a very poor underside surface finish.
- Components are offset by 3 mm – 5 mm from the build plate as standard and attached by only support structures. This allows for easier removal, a more homogenous final material (reducing the significant heat sink effect of the build plate) and the elimination of the potentially inconsistent first few build layers from the component.

Supports are either designed into the CAD file (referred to as ‘manual’ supports; see Chapter 3 for details) or generated using the SG module in Magics (referred to as ‘automatic’ supports).

The Magics SG module examines each surface of the CAD and those with an overhang angle greater than a user defined threshold value (typically 45°) are assigned a support. Automatic supports consist of a thin lattice structure in the X-Y plane generated by single laser scan vectors and a bounding outer wall. Supports are attached to the component by teeth to allow for easy removal; this type of support structure can be seen in Figure 1. Parameters affecting the form of these supports can be adjusted and the generation of appropriate supports requires a certain degree of operator judgement; typical parameters used for demonstration components produced during research as listed in Table 1.

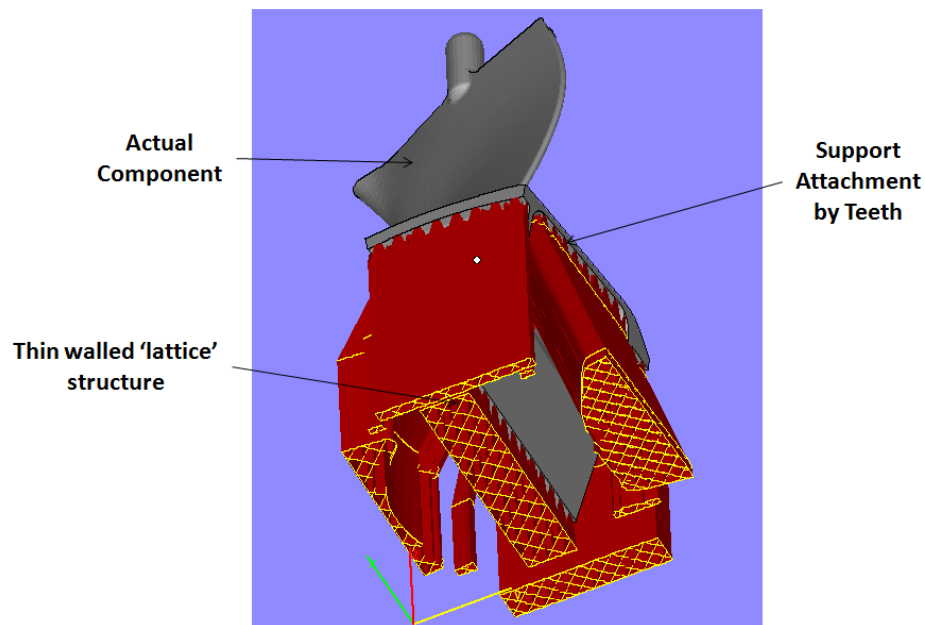


Figure 1: Screenshot from Magics [4] showing the automatically generated support structure attached to the actual component geometry.

Table 1: Typical automatic support parameters used for SLM of CM247LC, CMSX486 & IN625

Support Type	Block
Hatching X/Y	0.5 mm
Hatching Rotation	45°
Hatching/Border Teeth	Upper
Hatching/Border Teeth Height	1.5 mm
Hatching/Border Teeth Top Length	0.6 mm
Hatching/Border Teeth Base Length	1.5 mm
Hatching/Border Teeth Base Interval	0.2 mm
Fragmentation	Yes
Fragmentation Interval X/Y	4 mm
Fragmentation Separation Width	0.5 mm
Border Fragmentation	No
Borders	Yes
Perforations	No

iii. Physical Setup and Operation of the M2 System

The Concept Laser M2 is shown in Figure 2 (a); it consists of two halves: the handling chamber on the left allows for powder loading/unloading and the levelling of the bed to take place under an argon atmosphere and processing chamber on the right where the laser aperture is located and the SLM takes place. The hidden external details of the processing chamber are shown in Figure 2 (b). The technology module contains the powder and build platforms and the recoater blade and can be moved between the handling and processing chamber; a schematic diagram of this unit can be seen in Figure 3.

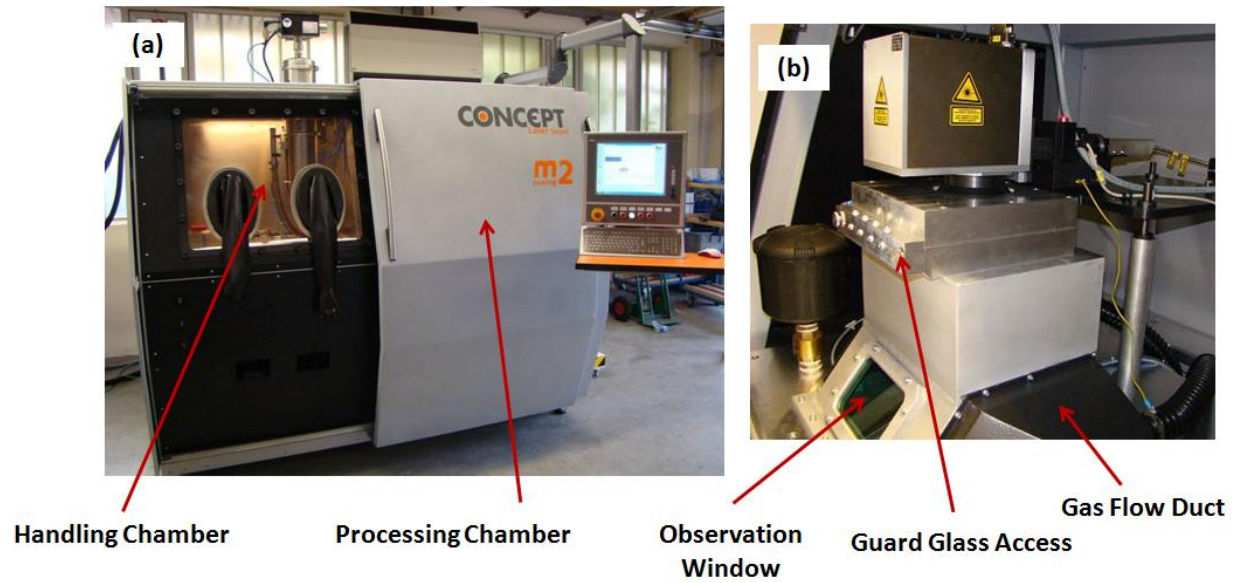


Figure 2: Photograph showing different views of the Concept Laser M2 system: (a) Front view of machine showing handling chamber; (b) Exterior view of the processing chamber.

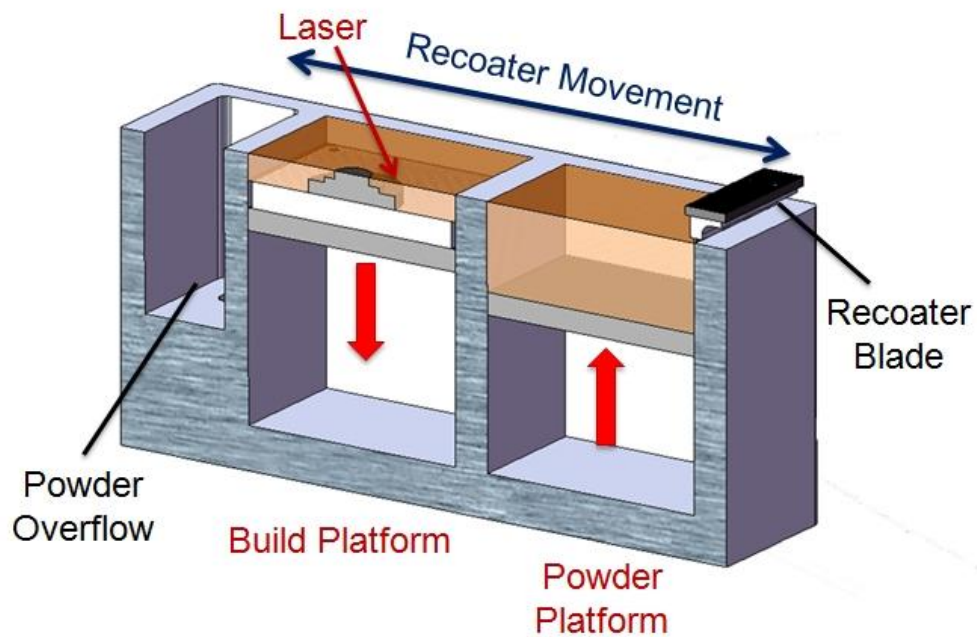


Figure 3: Schematic cross-section of the technology module of the Concept Laser M2 system.

Machine Cleaning

Prior to each build, the Concept Laser M2 SLM system is cleaned in order to reduce the chance of contamination from previous build materials. The following key points relate to the cleaning of the M2:

- In general cleaning consists of initially using an ATEX approved vacuum cleaner to remove any visible remaining powder followed by wiping with ethanol.
- Particular care is paid to bolt holes and screw caps which can accumulate hard-to-remove powder.
- Within the handling chamber the gloves and surrounding lips are of particular importance.
- Within the processing chamber access is particularly difficult so special care and attention must be taken to clean the ledges, entry and exit port of the gas flow duct and the observation window.
- The guard glass (protecting the laser aperture) is cleaned using lens cloth to ensure no contamination which can lead to the failure of this component.
- The build and powder platforms within the technology module contain many screw caps and bolt holes and as these come into direct contact with the powder must be carefully cleaned.
- The felt seals surrounding the moving platforms in the technology module can hold powder and this is removed by moving both platforms up and down several times and cleaning between each movement.

Build Plate

- All build plates are ground flat prior to SLM.

- The build surface is sand blasted to provide a matt finish with the aim of reducing reflectivity and encouraging powder to be retained during the first few build layers.
- Plates are cleaned with ethanol prior to SLM processing.

Recoater Blade

- The flexible rubber recoater blade is examined following the completion of every build for signs of wear and damage and replaced as necessary.
- The blade is also replaced following any change in build material.

Bed Levelling

The sequence for the final preparation of the powder-bed is listed below:

- Powder is loaded into onto powder platform under argon atmosphere.
- Using the manual controls of both the platforms and recoater blade; the powder is levelled across both platforms.
- The powder is thinned on the build plate by incrementally raising the build platform and moving the recoater blade across.
- The bed is ready when a very fine spread of powder (the surface of the plate clearly visible) lies across the build plate and the powder reservoir is completely flat.

Build Start

The sequence for starting the build is listed below:

- The technology unit is moved to the processing chamber
- The argon supply and fan are both activated to maintain a clean inert atmosphere
- The laser can only be activated once the atmosphere has dropped to <1% O₂.

- Two laser exposures of the first slice are carried out prior to starting to ensure the plate is free of contamination and ensure good bonding between the build and plate.
- Following this the process is started and allowed to continue until completion without further operator intervention.

iv. SLM Process Parameters

The key process parameters for the raster-filled area are provided and defined in Chapter 3. Figure 4 defines the parameters governing the location of the contour vector relative to the raster scanned area and the desired edge of the component; the influence of the contour scan has not been investigated within this thesis.

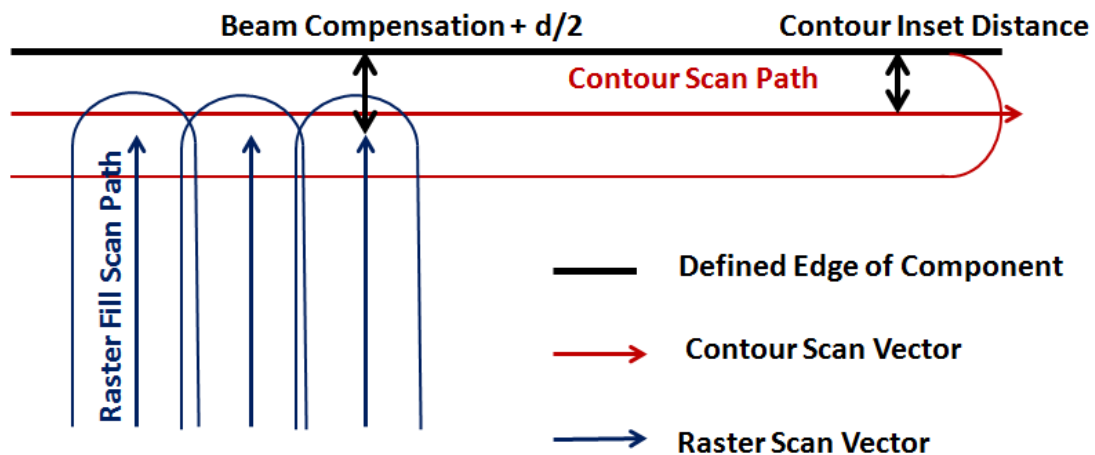


Figure 4: Diagram defining the contour inset and beam compensation with respect to the defined part edge and scan vectors.

Figure 5 shows the standard parameters used when slicing the CAD models in Magics. Figure 6, Figure 7 and Figure 8 show the laser parameters, process parameters and machine parameters assigned when SLM processing CM247LC following the optimisation (See Chapter 4). Other than the laser power, laser speed and scan spacing of the 'skin' (relating to

the raster scanned area) these are identical to those used for CMSX486 and IN625. Laser power, speed and scan spacing for CMSX486 and IN625 are provided in Chapter 4.

Files

Model	Slice Files
P 10_10_cube_legs	Test.cls

Selected Directory

E:\CAD_Slice\Blocks_Bars

Predefined parameter sets

Predefined

NewUpdateDeleteSet Default

Slice Model

Slice Thickness0.020mm

Beam Compensation0.020mm

Slice Support

Slice Thickness0.020mm

Skin-Core

☒ No Core☐ No Skin☐ Skin

Wall Thickness1.000mm

Additional Contours

☒ Inside☐ Outside

Number of Contours:10

Distance:0.075mm0.100mm

Island

☒ Enable Island

X Size5mm

X Shift1mm

Y Size5mm

Y Shift1mm

Angle45Deg

Figure 5: Screen capture showing parameters used when slicing in the Magics software.

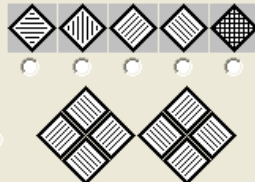




<input checked="" type="checkbox"/> fill vectors exposure	<input checked="" type="checkbox"/> contours exposure <input type="checkbox"/> additional contours exposure <input type="checkbox"/> over mass contours exposure	<input checked="" type="checkbox"/> support exposure
skin : laser power : Power : 150 [W] sp 1500 mm/s focus dia 0,15 mm operation mode : <input checked="" type="radio"/> cw <input type="radio"/> puls frequency : 0 kHz	contures : laser power : Power : 200 [W] sp 1500 mm/s focus dia 0,15 mm operation mode : <input checked="" type="radio"/> cw <input type="radio"/> puls frequency : 0 kHz	Support : laser power : Power : 200 [W] sp 2000 mm/s focus dia 0,15 mm operation mode : <input checked="" type="radio"/> cw <input type="radio"/> puls frequency : 0 kHz
hatching : 	overlapp :  a : 0,25 x d contour :  contour width : 150 µm over mass :  contour width : 38 µm Belichtung : <input checked="" type="radio"/> exposure every slice <input type="radio"/> exposure every 2. slice <input type="radio"/> exposure every 3. slice <input type="radio"/> exposure every n. slice	exposure : <input checked="" type="radio"/> exposure every slice <input type="radio"/> exposure every 2. slice <input type="radio"/> exposure every 3. slice <input type="radio"/> exposure every n. slice
overlapp :  a1 : 0,3 x d a2 : 0,15 x d exposure : <input checked="" type="radio"/> exposure every slice <input type="radio"/> exposure every 2. slice <input type="radio"/> exposure every 3. slice <input type="radio"/> exposure every n. slice		

Figure 6: Screen capture showing standard laser parameters assigned for the SLM of CM247LC

proces parameter : cusing_default exposure sequence : vectors->contours	
scanning system : waiting time beam off : 0,3 [0.0-100.0 ms] waiting time beam on : 0,08 [0.0-100.0 ms] waiting time at edges : 0 [0.0-100.0 ms] waiting time after laser jump max. : 1 [0.0-100.0 ms] waiting time after laser jump min. : 0,5 [0.0-100.0 ms] saturation afer in mm : 5 [0.0-100.0 mm]	powder delivering height : dose step : 180 % startslices : 3 [slices] factor : 180 % additional slices : additional slices : 0 slices

Figure 7: Screen capture showing standard process parameters assigned for the SLM of CM247LC

speed	
coater current :	100 [%]
coater in process :	80 [mm/s]
coater manual :	80 [mm/s]
extra coating :	200 [mm/s]
fan :	
revolution process :	45 [%]
fan on : <input checked="" type="checkbox"/>	
nitrogen on : <input checked="" type="checkbox"/>	
clean blow :	
time interval for blow :	4999 [min]
number of cleans :	1
break between :	1000 [ms]
Ventilator abschalten : <input checked="" type="checkbox"/>	

Figure 8: Screen capture showing standard machine parameters assigned for the SLM of CM247LC

v. References

- [1] M2 Cusing Operation Manual: Cyclone Version (www.concept-laser.de): Concept Laser - Hoffman Innovation Group, 2010
- [2] M2 Cusing Software: Software Magics; Software Concept Laser (www.concept-laser.de): Concept Laser - Hoffman Innovation Group, 2010
- [3] SolidWorks 2012 - Dassault Systems (<http://www.solidworks.com>). SolidWorks Corp., 2012.
- [4] Magics v15.0 - Materialise (<http://www.materialise.com/>). 2011.

APPENDIX B: CENTRAL COMPOSITE DESIGN

METHODOLOGY

This appendix aims to describe the Central Composite Design (CCD) methodology used in the statistical DOE of the CMSX486 and IN625 parametric studies. The overall principle of the response surface method and the general meaning of the P-value and R^2 terms are described. The commercially available software Design-Expert [1] was used to generate the results and as such full discussion of how the values are generated is not presented and can be found in traditional texts on the subject [2].

i. Central Composite Design

Central Composite Design (CCD) is the most popular choice for the fitting of second order response surface models. Far from a full factorial method; CCD, and the subsequent response surface fit, allows for the generation of a model to predict an optimum set of processing conditions for a given response whilst keeping the number of experimental runs to a minimum. The generation of the design points used in CCD is presented below:

As an example a three-factor design space is considered (P_1, P_2, P_3) and for each factor, five equally spaced levels (L_{1-5}) are selected spanning the region of interest. The CCD design space is shown in Figure 1 and consists of three different types of design points.

Axial Points: Each axial point uses the limit of the range for one parameter and the mid-points of the other two parameters (e.g. $P_1(L_{1,5}); P_{2,3}(L_3)$).

Cube points: The cube points form a cube using L_2 and L_4 of each parameter as the corner points (e.g. $P_{1-3}(L_{2,4})$).

Centre point: Three runs are carried out at the mid-point in order to assess the confidence band of the results (e.g. $P_{1-3}(L_3)$).

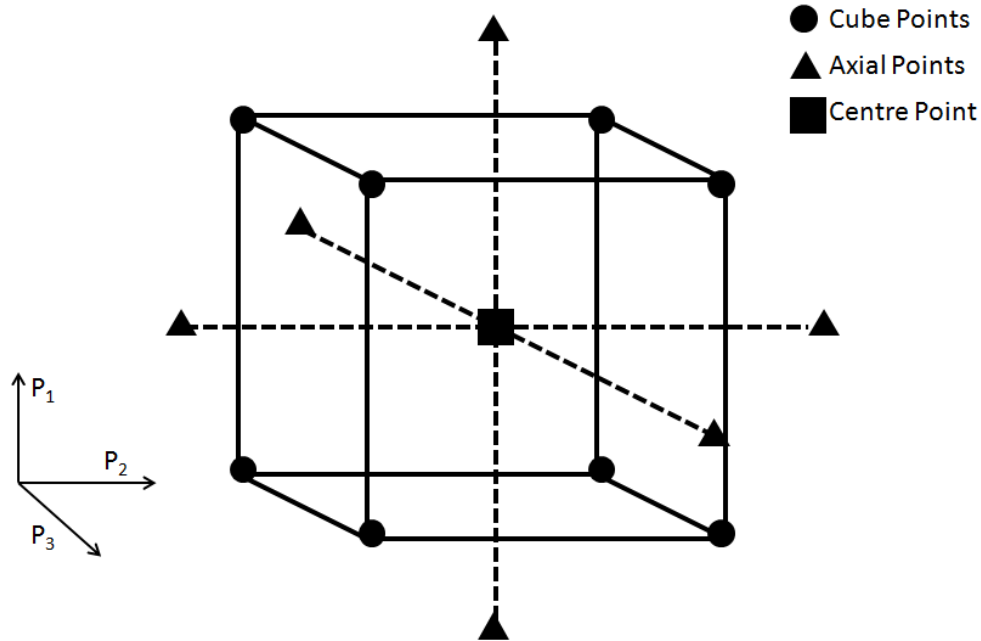


Figure 1: CCD space for three factors

In total the CCD only requires 17 experimental runs whereas a full factorial method for five levels of three factors would require 125 runs; this type of experimental design can be used to dramatically reduce the experimental work and therefore rapidly evaluate and optimise parameters for a specific measured response.

ii. Fitting Response Surface

The response surface is fitted to create a continuous surface to connect the responses of the measured design points. For the work presented in this thesis and 2nd order polynomial is fitted for CMSX486 and a 1st order for IN625. The fitted curve should not be used to predict responses outside of the design space but can be used to predict optimum processing points for a specific response.

iii. Definitions of the P-Value and R^2 Value

The P-value is defined as “*the probability that the test statistic will take on a value at least as extreme as the observed value of the statistic when the null hypothesis is true*” [2]. Therefore for each term investigated by Analysis of Variance (ANOVA) the P-value is assessed. A P-value of <0.05 leads to a rejection of the null hypothesis and the term is determined to be statistically significant.

R^2 can interpreted as “*the proportion of variability in the data explained by the model*” [2]. Therefore the greater the R^2 value, the closer the model is to predicting the variation of the data with changing parameters.

iv. References

- [1] Design-Expert Software. Stat-Ease.
- [2] Montgomery DC. Design and Analysis of Experiments (4th Edition). New York: John Wiley & Sons, 1997.